eman ta zabal zazu

Universidad del País Vasco
Euskal Herriko Unibertsitatea

RELATIVISTIC AND TOPOLOGICAL DOMAIN WALL SIGNATURES IN SPIN SPACE

AUTHOR: RICARDO RAMA EIROA

SUPERVISOR: RUBÉN MIGUEL OTXOA DE ZUAZOLA
SUPERVISOR: KOSTYANTYN GUSLIYENKO

ADVISOR: JULIÁN MARÍA GONZÁLEZ ESTÉVEZ

DOCTORAL PROGRAM: PHYSICS OF NANOSTRUCTURES AND ADVANCED MATERIALS

October 24, 2022. San Sebastián, Spain

Abstract

The recently discovered possibility of manipulating, through current-induced spin-orbit fields, the order parameter of a certain family of metallic antiferromagnets, such as Mn2Au, whose magnetic state can be characterized through conventional magnetoresistive effects, has attracted the attention of the spintronics community. This is due to the advantages that they present with respect to their ferromagnetic counterparts, such as the absence of stray fringing fields, inherent frequencies in the elusive THz band, and high critical Néel temperatures. Furthermore, the fact that the propagating antiferromagnetic solitons are not prone to deformation during their ultrafast dynamic processes allows envisioning full-antiferromagnetic all-spintronics devices that beat current von Neumann architectures in terms of operating speeds, energy efficiency, and miniaturization. In this context, we have investigated the relativistic and topological signatures of domain walls in spin space using analytical tools and atomistic spin dynamics simulations. In this sense, we have been able to verify that emulating the in-plane magnetization stability of antiferromagnetic systems through strong hard-axis axis anisotropies in ferromagnets allows to delay the Walker breakdown and access to relativistic magnetic texture dynamics. On the other hand, focusing on the case of the antiferromagnet Mn_2Au, it has been possible to reduce the analytical description of quasistatic magnetic soliton dynamics to a Newton-like second-order differential expression which highlights its pseudoparticle behavior as well as to predict its after-pulse displacement based on its steady-state relativistic mass. Moreover, it has been proven that in this antiferromagnetic material it is possible to access a highly nonlinear dynamic domain wall regime under sufficiently large external stimuli, producing the appearance of additional pairs of magnetic textures preserving the overall topological charge as well as the transient propagation of one of the nucleated magnetic solitons at supermagnonic velocities. Additionally, the total or partial release of the exchange-based self energies of two antiferromagnetic domain walls with different relative chiralities through topologically-mediated collisions has been analyzed, being possible to obtain information about their topological charges through the induced thermal footprint in the electronic and phononic reservoirs.

Extracto

La recientemente descubierta posibilidad de manipular, a través de campos de tipo espín-órbita inducidos por corrientes eléctricas, el parámetro de orden de una cierta familia de materiales antiferromagnéticos metálicos, tales como Mn_2Au, cuyo estado magnético puede ser caracterizado a través de efectos magnetorresistivos convencionales, ha atraído la atención de la comunidad científica en el campo de la espintrónica. Esto se debe a las ventajas que presentan este tipo de sistemas en comparación con sus contrapartes ferromagneticas, tales como inexistencia de campos demagnetizantes significativos, frecuencias inherentes en la banda elusiva del THz y altas temperaturas críticas tipo Néel. Además, debido a que los solitones antiferromagnéticos no tienden a deformarse durante sus procesos dinámicos ultrarrápidos, es posible hipotetizar su inclusión en aparatos puramente espintrónicos conformados por materiales antiferromagnéticos que puedan superar el rendimiento actual de las arquitecturas de tipo von Neumann en términos de velocidad de operación, eficiencia energética y miniaturización. En este contexto, hemos investigado las trazas relativistas y topológicas de paredes de dominio en el espacio de espín, empleando, para ello, herramientas analíticas y simulaciones dinámicas de espines átomicos. En este sentido, hemos sido capaces de verificar que, asegurando la estabilidad de la magnetización en el plano en reposo en materiales ferromagnéticos, lo cual ocurre en materiales antiferromagnéticos de forma natural, a través de fuertes anisotropías de eje díficil, es posible retrasar la ruptura tipo Walker y obtener textures magnéticas que se propagan en el marco relativista. Por otro lado, centrándonos en el caso del material antiferromagnético Mn_2Au, hemos podido reducir la descripción analítica de solitones magnéticos en regímenes dinámicos cuasiestacionarios a una expresión diferencial newtoniana de segundo orden, lo cual pone de manifiesto que se comportan como pseudopartículas y, además, hemos hallado que es posible predecir el desplazamiento que estos experimentan tras apagarse el pulso magnético de tipo espín-órbita a través de su masa relativista en estado estacionario. Adicionalmente, hemos demostrado que, en este sistema antiferromagnético, las paredes de dominio pueden acceder a una régimen dinámico altamente no lineal bajo la acción de estímulos externos lo suficientemente grandes, lo cual da como resultado la aparición de pares adicionales de texturas magnéticas, preservando la carga topológica global, así como la propagación transitoria de uno de los solitones magnéticos nucleados a velocidades supermagnónicas. Asimismo, hemos analizado la liberación total o parcial de las autoenergías de canje de dos paredes de dominio antiferromagnéticas con diferenes quiralidades relativas a través de colisiones mediadas por topología, pudiéndose conocer cuáles eran sus cargas topológicas a través de las huellas térmicas inducidas en los reservorios de electrones y fonones.

Acknowledgments

Looking back, it is difficult to disentangled my personal experiences of the academic training during the years through which my doctoral journey has been extended. This is due not only to the fact that my habitual residence has been transferred from my hometown, A Coruña, to Donosti for work reasons, but also because the people with whom I have interacted on a daily basis have also changed. Furthermore, the perpetual shadow of the COVID-19 pandemic has become a looming presence, not only because of restrictions and isolation, but also due to a generalized feeling of sadness and introspection that has changed the lives of many people. Within this context, having entered a PhD program has allowed me to face internal fears such as making my first trips outside the Iberian Peninsula, with the inherent helplessness on language basis, as well as dedicating all my working time to research, which implies writing and exposing the work in which I have been involved. In this journey, I would like to thank, first of all, my advisor, Julián González, from whom I have always felt a genuine predisposition to help me in any field so that I could concentrate as much as possible on physics. On the other hand, I would like to express my most sincere admiration and respect for my two supervisors, Rubén M. Otxoa and Konstantin Y. Guslienko, who have had the patience to instruct and guide me throughout this long road that is now complete, and of which I want to think that I am taking something that I hope will last throughout my life. From Rubén I think I have learned to love what you do, and I hope one day to be able to transmit it in a similar way as he does with those around him, while from Konstantin I take the perspective that it is always possible to reduce a problem until it is manageable enough to draw valuable conclusions. I hope that, if in the future, I manage to establish a scientific career, I can do an honest and quality work to honor the effort that my supervisors have invested to train me as well as possible.

Concerning my experiences abroad, I would like to highlight that, during the celebration of the European School of Magnetism in Brno, Czech Republic, in 2019, I had the opportunity to learn and meet great scientists in my field, as well as touring a wonderful city that I have greatly enjoyed in the company of Carla Muñoz-Rodríguez and Daniel Casaleiz, with whom I have also had the opportunity to coincide in some meetings of the Spanish Club of Magnetism. From my short stay at the Freie Universität Berlin, Germany, I feel very grateful to Unai Atxitia for his warm treatment and the opportunities he has given me to be involved in projects with him, as well as the direction of the Department of Physics of the aforementioned university who made it easy for me to return to Spain when the pandemic broke out. From my time at the Department of Physics at the University of York, United Kingdom, I would like to highlight the treatment and respect, both human and scientific, that my hosts, Richard F. L. Evans and Roy W. Chantrell, have always given me, with whom I maintain collaborations that have allowed me to grow at all levels. In this line, I would like to thank the PhD candidates of their group, Jack Collings, Jackson Ross and, especially, David Papp, for their warm welcome and conviviality during

the months that I shared an office with them, as well as Noemí Gesteiro, with whom I had the opportunity to explore and learn more about the city and its surroundings. Also, I would like to mention my gratitude to Sarah Jenkins for her professionalism and patience in discussing the results of her simulations with me. All these experiences would not have been possible without the financial support from the Donostia International Physics Center, the University of the Basque Country, the Spanish Ministry of Science and Innovation, the Deutsche Forschungsgemeinschaft, and the Hitachi Cambridge Laboratories. Finally, I would like to remember all those who have collaborated with me and who have contributed to improve all the work in which I have been involved.

During my years in Donosti I have met incredible people like Josu Mendizabal, who has not only always given me a calm and reliable coexistence, but has also taught me important automatisms to illustrate my papers and presentations, Irati Arzuaga and Michelle Rojas, from whom I have always received unspeakable love and indispensable support, and all the people of Kuraia Fight Club, whom have helped me to maintain a good physical and mental balance. However, this entire journey would not have been possible if I had not been accepted into the Master in Nanoscience taught by the Materials Physics Center and the University of the Basque Country, for which I am grateful to the selection committee for giving me the opportunity, and to all the professors I have met there for their valuable time. Additionally, I have had the great fortune of having the friendship of Miguel Ángel J. Herrera and Elena H. Sánchez, two irreplaceable people with whom I have shared fantastic moments and from whom I have learned a great deal through their lines of research. From a scientific point of view, I am very grateful to those people who, selflessly, have responded to emails that I may have sent to clarify scientific doubts that may have arisen during these years, among whom I would like to highlight Alexey Kimel, André Thiaville, Olivier Fruchart, Luis López Díaz, and Michele Voto. At this point, I would also like to express my gratitude to the people who have scientifically supervised me in the past, Manuel Vázquez Ramallo, F. Sebastián Bergeret, and Joaquín Fernández-Rossier, whom I hope to have honored over the years for their incontestable efforts to train me under their tutelage. Likewise, I would like to wish Javier Vélez, who shares supervisors with me, the best possible experience and successes in his PhD journey in the coming years, with whom I hope to collaborate at some point. Moreover, I would like to remember my friends from A Coruña, who have helped me throughout my adult life to get here, among whom I would like to highlight Víctor González, Miguel Carballo, Lucía Papaleo, Isabel Suárez, and Iria Louzán, as well as the Galician institutions in which I have been academically trained, the IES Eusebio da Guarda and the University of Santiago de Compostela. Finally, I would like to thank from the bottom of my heart the enormous support and unconditional love of my family, help without which it would have been possible to get here. Many thanks to my mother, Alejandra Eiroa, my aunt, Fátima Eiroa, and my grandfather, Julio Eiroa, for always believing in me.

Statement of originality

University of the Basque Country
Donostia International Physics Center

Title: Relativistic and topological domain wall signatures in spin space

Author: Ricardo Rama Eiroa

Supervisor: Rubén Miguel Otxoa de Zuazola
Supervisor: Kostyantyn Gusliyenko

Advisor: Julián María González Estévez

Tribunal member: María Aranzazu Eceiza Mendiguren
Tribunal member: Burkard Hillebrands
Tribunal member: Agustina Asenjo Barahona
Tribunal member: Luis López Díaz
Tribunal member: Célia Tavares de Sousa
Tribunal member: Fernando Sebastián Bergeret Sbarbaro
Tribunal member: María Blanco Rey
Tribunal member: Gleb Nicolai Kakazei

External reader: Elton Jose Gomes Santos
External reader: Richard Francis Llewelyn Evans

I hereby declare that this manuscript submitted to the University of the Basque Country, Spain, to qualify for the Degree of Doctor in Physics of Nanostructures and Advanced Materials has been written solely by me, the text having been inspected by my supervisors, not having been deposited without their express consent. I certify that the scientific papers that constitute my work during the years that my PhD has lasted have not been included in another thesis presented successfully for another degree. In those cases in which, in the construction of this text, it has been required to include information extracted from external sources, these have been conveniently cited. Everything exposed in this thesis is in accordance with the Code of Good Practice in Research promoted by the University of the Basque Country. The authorship rights of this manuscript enjoy the protection regulated in the Real Decreto Legislativo 1/1996, de 12 de abril, under which the intellectual property of this thesis belongs to the author. No quotation is allowed without full acknowledgment.

November 14, 2022. San Sebastián, Spain.

List of publications

Discussed in this doctoral dissertation

[1] **R. Rama-Eiroa**, R. M. Otxoa, P. E. Roy, and K. Guslienko
Steady one-dimensional domain wall motion in biaxial ferromagnets: mapping of the Landau-Lifshitz equation to the sine-Gordon equation
Phys. Rev. B **101**, 094416 (2020) arXiv:1910.13266 (2019)

[2] R. M. Otxoa, P. E. Roy, **R. Rama-Eiroa**, J. Godinho, K. Y. Guslienko, and J. Wunderlich
Walker-like domain wall breakdown in layered antiferromagnets driven by staggered spin–orbit fields
Commun. Phys. **3**, 190 (2020) arXiv:2002.03332 (2020)

[3] R. M. Otxoa, **R. Rama-Eiroa**, P. E. Roy, G. Tatara, O. Chubykalo-Fesenko, and U. Atxitia
Topologically-mediated energy release by relativistic antiferromagnetic solitons
Phys. Rev. Res. **3**, 043069 (2021) arXiv:2106.05804 (2021)

[4] **R. Rama-Eiroa**, P. E. Roy, J. González, K. Y. Guslienko, J. Wunderlich, and R. M. Otxoa
Inertial domain wall characterization in layered multisublattice antiferromagnets
J. Magn. Magn. Mater. **560**, 169566 (2022) arXiv:2109.09003 (2021)

Additional works produced during the PhD period

[5] **R. Rama-Eiroa**, R. M. Otxoa, and U. Atxitia
Temperature-dependent critical spin-orbit field for orthogonal switching in antiferromagnets
Appl. Phys. Lett. **121**, 132401 (2022) arXiv:2207.09563 (2022)

[6] J. B. Collings, **R. Rama-Eiroa**, R. M. Otxoa, R. F. L. Evans, and R. W. Chantrell
Generalised form of the magnetic anisotropy field in micromagnetic and atomistic spin models
arXiv:2210.10916 (2022)

[7] S. Jenkins, **R. Rama-Eiroa**, J. B. Collings, U. Atxitia, O. Chubykalo-Fesenko, K. Everschor-Sitte, R. M. Otxoa, R. W. Chantrell, and R. F. L. Evans
Temperature dependent properties of the antiferromagnet Mn_2Au
In preparation

Contributions to congresses, conferences, and seminars

Oral talks

[1] *Supermagnonic Domain Wall Dynamics in Layered Antiferromagnets*
PhD Seminar Series organized by the Materials Physics Center (MPC/CFM). San Sebastián, Spain. June 12, 2019

[2] *Walker-Like Domain Wall Breakdown in Layered Antiferromagnets Driven by Staggered Spin-Orbit Fields*
Scientific Session of Young Researchers, Spanish Club of Magnetism and Spanish Chapter of IEEE Magnetics Society Annual Meeting. Pamplona, Spain. October 17, 2019

[3] *Inertial Domain Wall Motion Driven by Staggered Spin-Orbit Fields in Uncompensated Antiferromagnets*
Joint Meeting of the Condensed Matter Divisions of the Spanish Royal Physics Society (RSEF-GEFES) and of the European Physical Society (EPS- CMD). Madrid, Spain. Online. August 31, 2020

[4] *Inertial Domain Wall Motion Driven by Staggered Spin-Orbit Fields in Layered Antiferromagnets*
2020 Annual Conference on Magnetism and Magnetic Materials (MMM2020). Palm Beach, United States. Online. November 5, 2020

[5] *Spin-Orbit Field-Induced Domain Wall Dynamics in the Complex Antiferromagnet Mn2Au*
SolSkyMag 2021 congress. San Sebastián, Spain. Online. June 22, 2021

[6] *Relativistic Topologically-Mediated Energy Release by Antiferromagnetic Solitons*
SolSkyMag 2021 congress. San Sebastián, Spain. Online. June 22, 2021

Poster presentations

[1] *Steady One-Dimensional Motion in Biaxial Anisotropic Ferromagnets*
SolSkyMag 2019 congress. San Sebastián, Spain. June 25, 2019

[2] *Inertial Domain Wall Motion Driven by Staggered Spin-Orbit Fields in Uncompensated Antiferromagnets*
Ultrafast Spintronic Phenonema and Materials 2020, PhD conference. Ostrov, Czech Republic. March 3, 2020

[3] *Inertial Domain Wall Motion Driven by Staggered Spin-Orbit Fields in Uncompensated Antiferromagnets*
Joint European Magnetic Symposia (JEMS) 2020 congress. Lisbon, Portugal. Online. December 7-11, 2020

List of figures

List of abbreviations and acronyms

Abbreviations	
Chap(s).	chapter(s)
Eq(s).	equation(s)
Fig(s).	figure(s)
Sec(s).	section(s)

Acronyms	
1D	one-dimensional
2D	two-dimensional
AFM	antiferromagnet(s), antiferromagnetic
AMR	anisotropic magnetoresistance
ASDS	atomistic spin dynamics simulations
DMI	Dzyaloshinskii-Moriya interaction
DW	domain wall(s)
EE	Edelstein effect
EL	Euler-Lagrange
FM	ferromagnet(s), ferromagnetic
GMR	giant magnetoresistance
HDD	hard-disk drive(s)
HM	heavy metal(s)
LL	Landau-Lifshitz
LLG	Landau-Lifshitz-Gilbert
MR	magnetoresistive
MRAM	magnetoresistive random-access memory/memories
MTJ	magnetic tunnel junction(s)
NM	non-magnetic
RKKY	Ruderman-Kittel-Kasuya-Yosida
SG	sine-Gordon
SH	spin Hall
SHE	spin Hall effect
SO	spin-orbit
SOC	spin-orbit coupling
SOT	spin-orbit torque(s)
SPE	spin Peltier effect
STT	spin-transfer torque(s)
SV	spin valve(s)
SW	spin wave(s)
TB	tunnel barrier(s)
TMR	tunnel magnetoresistance
WB	Walker breakdown

Table of contents

Chapter 1

Introduction

Nowadays the ever-increasing information production trend is accompanied by its processing in big data centers and its online digital-based storage. To the current demand could be added in the near future the envisioned internet-based interconnectivity in the search for a smart way of living, known as Internet-of-Things. The main problem resides in that currently the 11% of the annual global electricity consumption is destined for the information and communication sector. This, in conjunction with the inherent greenhouse gas emission, motivate the search for more efficient industrial processes with the smallest possible environmental footprint [1].

Modern semiconductor-based computers rely on von Neumann-like architectures, where information processing and storage take place in different locations, resulting in detrimental speed and efficiency [2, 3]. In the case of transistor-dominated schemes, the implementation of computation-in-memory schemes such as bioinspired neural networks becomes highly unfathomable due to the required on-chip densities [4, 5]. It is precisely due to these miniaturization limitations that the irruption of the actual spintronics-based non-volatile energy-efficient computer memories occurred [6]. Beyond this, all-spintronics-based computers could overcome the current parallel computing and multiprocessor paradigms [7, 8], which could be done through the combination of state-of-the-art magnetic memories with spin-based logic circuits, which would reduce the current power leakage and heat dissipation [9–11].

1.1 Spin-dependent transport in multilayered systems

Based on the synergy between industry and basic research, the birth of spintronics took place at the end of the last century through the implementation of high resolution magnetoresistive (MR) heads to interpret the digital information encoded in the ferromagnetic (FM) domains of mechanical non-volatile random-access hard-disk drives (HDD) [12–14]. Coupled inductive read-and-write paths had previously been substituted by the implementation of scanning heads based on the anisotropic magnetoresistance (AMR) effect, where the relative orientation between the applied charge current and the magnetization gives rise to a resistance-dependent signal [15–17], as it is represented in Fig. 1.1 (a). With the advent of sophisticated deposition techniques [18–20], it was possible to exploit the spin-dependent electron transport through nanometric multilayered systems, which allowed a significant increase in the stored information density due to the enormous increase in the reading sensitivity [21]. The first reproducible experimental phenomenon in the field of spintronics was the giant magnetoresistance (GMR) effect, which allows switching between two

different resistive states based on the quantum-based spin-dependent scattering of the conduction electrons passing through a system composed of two FM layers separated by a non-magnetic (NM) spacer, a structure known as spin valve (SV) [22–24], which it is depicted in Fig. 1.1 (b). Less than a decade later, it was possible to implement the tunnel magnetoresistance (TMR) effect at room temperature, based on the spin-dependent quantum tunneling of electrons through thin insulating barrier separating two FM layers, a structure known as magnetic tunnel junction (MTJ), being the process represented in Fig. 1.2 (a), which allowed to obtain a resistive signal two orders of magnitude greater than the one observed in devices based on the GMR effect [25–27]. In both types of structures, SV and MTJ, both FM sheets are coupled through a moderate NM spacer-governed Ruderman-Kittel-Kasuya-Yosida (RRKY) interaction, which dictates their relative magnetization orientation [28–32]. Moreover, one of the FM layers is usually in direct contact with an extra antiferromagnetic (AFM) sheet, pinning its magnetization direction through the so-called assistive exchange bias effect [33, 34]. However, the continuous effort to store more information in a smaller space entails certain limitations, since to ensure the prevalence of the information, the anisotropy has to be increased to ensure their thermodinamic stability, hindering at the same time the magnetic field-based information writability, problems which lie at the heart of the magnetic recording trilemma [35, 36].

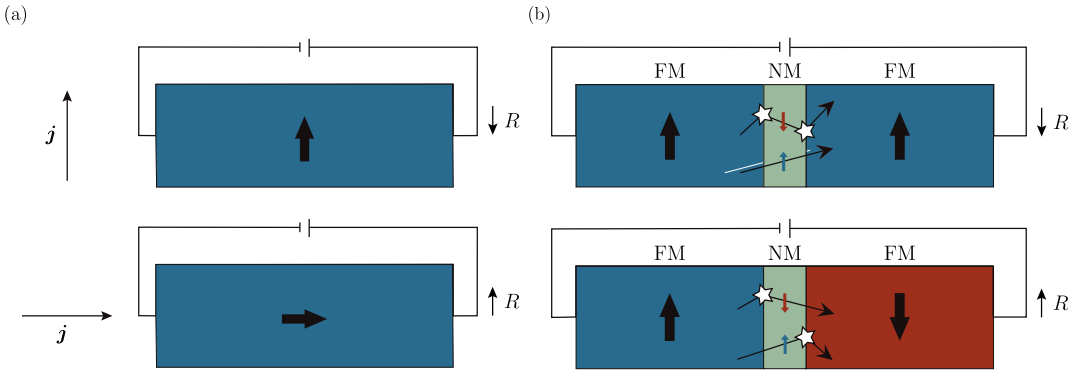

Figure 1.1: (a) In the AMR effect framework in FM materials, when the application direction of the non-polarized charge current, j, is parallel to the magnetization of the medium, a low resistance, R, state takes place , while when the injected current is perpendicular to the system polarization, a high R scenario will occur. (b) Schematic representation of the spin-dependent electron scattering involving the FM-based GMR effect. When the magnetization of both FM is arranged in a parallel fashion, the electrons will suffer fewer scatting events after crossing the NM material (low resistance, R, state) than when both FM are antiparallel polarized (high R scenario). Adapted from [37].

1.2 Current-induced magnetoelectric effects

The limitations of the HDD-based magnetic recording, such as the superparamagnetic limit and a millisecond-constrained information access speed [38, 39], motivated the search for magnetic solid-state memories with higher on-chip integrability. It was in this context that MR random-access memories (MRAM) arose, usually composed of several MTJ acting as bits of information [6, 40]. The first magnetic field-assisted prototypes employed complicated architectures where simultaneous

stimuli along the orthogonal word and bit lines caused the switching of the different storage units [41]. Due to the energy inefficiency of this intrincate arrangement, some alternatives were proposed such as adopting a thermal-assisted scheme where a Joule heating-based switching field reduction was induced by coupling the free layer with an AFM with a blocking temperature different from that of the pinned sheet [42, 43], but most of the efforts were focused on obtaining a magnetic field-free approach to the problem. In this sense, it was proposed to base the writing mechanism on the current-induced spin-transfer torque (STT) phenomena, in which a current injected into a pinned FM layer becomes spin-polarized, resulting in an angular momentum transfer from the conduction electrons to the free FM sheet [44, 45], leading to the precession and/or switching of its magnetization [46–49], as it can be seen in Fig. 1.2 (b). The STT-based MTJ technological interest transcends the information storage field, since they can also be used as tuneable low-power microwave nano-oscillators with great applicability in wireless devices [50, 51]. This is because the STT can act as an antidamping-like torque, leading to steady-state coherent precession regimes [52, 53]. Interestingly, compact nano-oscillators-based arrays are very sensitive to their neighbours dynamics, but this approach is still far from the brain-like energy efficiency and requires online training algorithms [54–56]. Despite the advantageous STT-based nanosecond writing process, the need to employ large current densities to increase the switching velocity can lead to the dielectric breakdown of the thin oxide barriers of a MTJ [57].

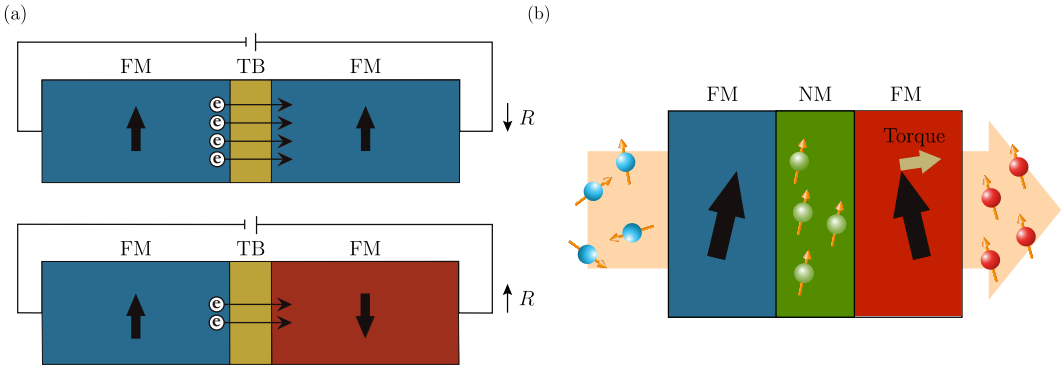

Figure 1.2: (a) Scheme of the mechanism of the TMR effect in FM-based systems. When the magnetization of both FM is arranged in a parallel fashion, the tunneling probability of the electrons through the insulating tunnel barrier (TB) is greater (low resistance, R, state) than when both FM are polarized antiparallel, situation in which the probability is lower (high R scenario). Adapted from [58]. (b) Graphic depiction of the STT in FM-based systems. The electrons that make up the charge current applied to a FM are polarized in the same direction as the underlying magnetization, producing a transfer of angular momentum between these electrons and the second FM after crossing the spacer between them, inducing a torque in its magnetization. Adapted from [59].

In this context, the use of materials with sizable spin-orbit coupling (SOC) can mitigate some of the disadvantages of STT-based excitation schemes, since the emergent effective field is based on the relative orientation of the injected current with respect to the crystallographic structure of the system, being independent of a reference magnetic configuration layer [60]. The first mechanism that can be mentioned in this regard is the spin Hall effect (SHE), in which an unpolarized charge current

produces a transverse pure spin current [61–64], being represented in Fig. 1.3 (a). On the other hand, the Edelstein effect (EE) is based on the production of a non-equilibrium bulk spin polarization perpendicular to an externally applied electric field [65–68], which it is exposed in Fig. 1.3 (b). It should be noted that, in contrast to the case of the SHE, the EE requires the simultaneous presence of the SOC with a broken inversion symmetry [69]. Although these phenomena can be achieved in single FM layers, they are usually combined with NM heavy metals (HM) due to their stronger SOC, which allows to generate a magnetization torque due to the induced interfacial spin accumulation [70–72]. Even if this interfacial-induced symmetry breaking scheme allows decoupling the reading and writing channels [73], perpendicularly magnetized FM require an AFM-induced assistive field to achieve a real magnetic field-free deterministic magnetization switching [74, 75]. However, devices based on the spin-orbit torque (SOT) show great advantages over its STT-governed counterpart, such as higher reliability, endurance, and sub-nanosecond switching speeds [1, 76].

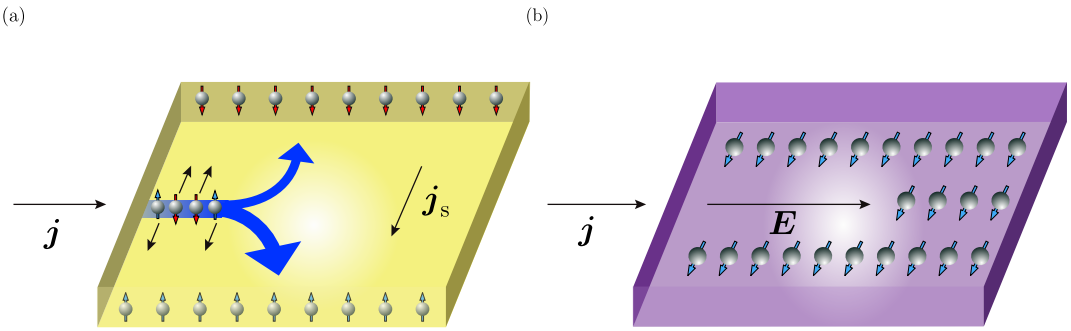

Figure 1.3: (a) Conversion of an unpolarized charge current, j, into a chargeless pure spin current, j_s, due to the SO-based SHE in a FM system. Adapted from [77]. (b) Appearance of a non-equilibrium bulk spin polarization perpendicular to an electric field, E, generated in the FM sample due to the injection of a charge current, j, through the SO-based EE. Adapted from [59].

1.3 Spin-orbit-based ferromagnetic soliton dynamics

The transition regions of multidomain structures, known as domain walls (DW), are of special interest due to their potential mobility and topologically-based stability [78–81], whose position in a sample can be used to encode information. In this sense, the non-volatile solid-state magnetic storage device known as racetrack memory stands out, where the dynamics of magnetic texture arrays in three-dimensional schemes is exploited [82]. Of special interest is the case in which the dynamics of the one-dimensional (1D) magnetic solitons is excited through current-induced spin polarization transfer-based mechanisms, since in this case the magnetic textures will move in the same direction regardless of their relative topological charges [83–85]. On the other hand, if magnetic fields were used for this purpose, adjacent magnetic textures with opposite chiralities would annihilate each other, causing a loss of information [86, 87], both processes being schematized in Fig. 1.4 (a). This type of sequential storage architecture is very promising because it is as cheap as HDD and as fast and reliable as MRAM, being its efficiency based on obtaining the maximum

stable DW velocity at reasonable current densities [82, 88]. However, it is necessary to have great control over the pinning processes to define the bit length and take into account the unwanted stray fields that can disturb the densely packed DW arrays [89, 90]. Besides this, far from the thermally-activated stochastic creep motion, in FM exist an external stimulus-based threshold for the steady-state DW dynamics, known as Walker breakdown (WB), where the soliton enters an unstable regime due to the emergent oscillatory dynamical trend of the texture [91–93].

Perpendicular magnetic anisotropy-based media can host higher information densities due to the presence of narrow DW, which can potentially move very fast [94, 95]. Interestingly, using current densities of about 10^8 A/cm^2 in this type of FM media, it is possible to obtain SHE-induced velocities of the order of 400 m/s [96, 97], speeds significantly greater than using the STT for the same electrical stimulus [88, 98]. To generate the aforementioned SOT, it is usual to put the magnetic material in contact with a HM with strong SOC, giving rise to an interfacial Dzyaloshinskii-Moriya interaction (DMI) due to the induced structural inversion asymmetry [99, 100], which it is represented in Fig. 1.4 (b). This extra interaction causes a symmetry breaking favoring a specific chirality of the texture [92, 101], prioritizing the stabilization of Néel-like DW and a consequent delay of the WB-based threshold [102, 103], not requiring in this case an assistive magnetic field [104, 105]. In the same line, it is possible to exploit the surface curvature of a cylindrical nanowire to induce a DMI-like chiral symmetry breaking that confers an extra stability to the DW against potential internal torques [106, 107]. This results in the prevention of the WB and allows the texture to reach speeds of the order 1 km/s and even enter a spin wave (SW) emission regime due to exceeding its phase velocity, which is known as the spin Cherenkov effect [108, 109].

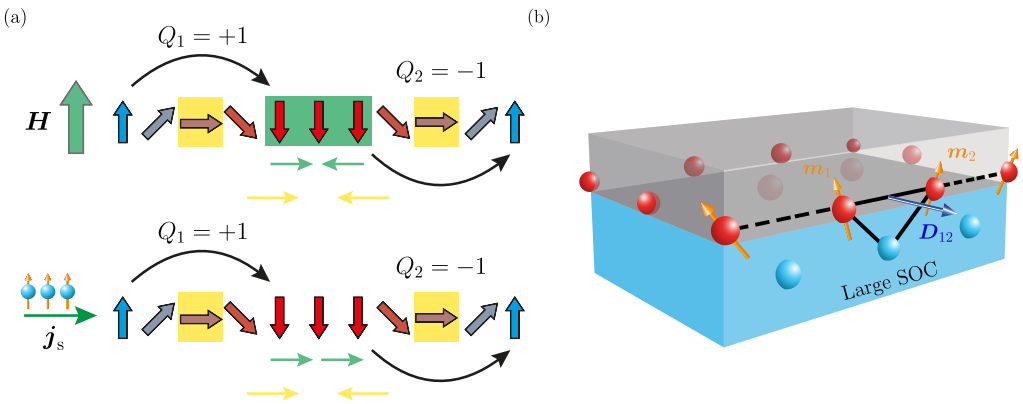

Figure 1.4: (a) Graphical representation of the different dynamic behavior of a DW pair with opposite relative topological charges, $Q_1Q_2 = -1$, under the action of a magnetic field, $\boldsymbol{H}$, and a spin polarized current, $\boldsymbol{j}_s$. The green arrows correspond to the direction of movement of each magnetic soliton, while the yellow ones exemplify the exchange-based attraction between the pair of magnetic textures. (b) Interfacial DMI at the boundary between a FM and a non-magnetic metal with strong SOC, where the DMI vector, $\boldsymbol{D}_{12}$, related to the triangle composed of two magnetic sites, $\boldsymbol{m}_1$ and $\boldsymbol{m}_2$, and an atom with strong SOC is perpendicular to the triangle plane. Adapted from [110].

Beyond the non-volatile storage envisioned through racetrack memories, it is possible to exploit the intrinsic functionalities of magnetic textures and SOC-based

phenomena to envision sensor-based information interconnectivity and all-spintronics computation architectures. On the one hand, tuneable microwave oscillators can be generated through the pulsed SOT-induced back-and-forth motion of a DW train through the time-dependent resistive response of the system [111], while soliton-based sensitive schemes can be integrated relying on the variation of the spatial properties or the number of nucleated magnetics textures in response to an external stimulus [112, 113]. On the other hand, the possibility of carrying out on-chip logic-in-memory computing has been proposed through the engineering of DW inverters, taking advantage of the domain-based chiral interaction induced through the interfacial DMI, which serves as the building block to develop Boolean operations [114]. In the same line, it has been shown that it is possible to achieve SOT-induced multilevel switching in FM/AFM heterostructures, which has great potential to implement analog plasticity-like synaptic memristors. This can be achieved either through the existence of an unequal threshold reversal stimulus of the sample caused by inhomogeneities in the exchange bias effect as well as due to a continuous change in the resistive signal of a MTJ originated by the DW displacement [74, 115, 116].

Apart from the 1D DW, there is a vast zoology of magnetic textures, among which we can highlight the topologically-protected two-dimensional (2D) skyrmions, whose stabilization is possible in FM/NM heterostructures due to the combination of a broken inversion symmetry-induced DMI interaction with a large SOC [117, 118]. These solitons, in addition to being inherently stable, have some advantages over the DW, among which its excitation through ultralow current densities stands out, potentially being as fast as its 1D counterpart [119]. However, its prevalence is overshadowed due to the fact that, experimentally, SHE-based velocities of order of 100 m/s have been reached in multilayered systems [120]. These speeds are lower than those achieved by DW, and, additionally, skyrmions present non-rectilinear propagations due to the skyrmion Hall effect [121, 122]. Despite this, due to their compact pseudoparticle behavior and low current-based depinning [123–125], they have been envisioned as robust proposals in unconventional computational approaches, because in contrast to the von Neumann paradigms they consume less energy and present nonlinear responses. In this context, it has been proposed to obtain uncorrelated output skyrmion-based bit patterns through their thermally-activated reshuffle or random laser-induced nucleation with potential applicability in the field of efficiency-optimized stochastic computing [126, 127]. On the other hand, it is possible to exploit the nonlinear resistance-based response of a pinned magnetic skyrmion reservoir to a set of time-varying voltage pulses for pattern recognition [128].

1.4 State-of-the-art antiferromagnetic spintronics

Until now, the inclusion of an AFM in MR stacks played a support role, specifically pinning a FM layer through the exchange bias effect. However, AFM used as active elements in spintronics applications have notable advantages over FM. These qualities include the non-generation of stray fringing fields [129, 130], zero-momentum resonance frequencies of the order of THz [131, 132], absence of the WB understood through the tilting of the magnetization of the DW plane at rest [133, 134], and propagation speeds of the magnetic textures of the order of tens of km/s in the special relativity framework, being only limited by the maximum magnon group velocity of the medium [135–137] or by superluminal-like regimes accessible to contracted magnetic solitons whose extent is comparable to the atomic spacing [138, 139]. This is because the antiparallel alignment is accompanied by a large magnitude of the

AFM-based intersublattice exchange interaction, tangibly greater than those provided by the DMI and FM contributions. Due to the zero net magnetization of these systems, it is difficult both to manipulate them through static magnetic fields and to measure their magnetic state due to their low magnetic susceptibility [140, 141]. However, in AFM it has been possible to reorient experimentally the DMI-induced canted Néel order parameter through a time-dependent magnetic field through an inertial-driven process [142]. Likewise, it has been proposed to induce dynamic processes by coupling spatially asymmetric magnetic fields with the spatial variation of the order parameter or, on the other hand, with the spatial gradient-based intrinsic magnetization of a DW [143, 144].

Given the difficulty of exciting AFM media, special emphasis has been placed on adapting the different current-induced phenomena that have been shown to be efficient in FM to trigger both the order parameter switching and the dynamics of magnetic textures. In this regard, what it is necessary to achieve an AFM-driven process is that the local fields generated in each sublattice are staggered with respect to those of its first antiparallel polarized neighbors [140, 141], as it is schematized in Fig. 1.5. This is satisfied in any AFM, irrespective of the symmetry of its unit cell, if the injected spin-polarized current exerts an antidamping-like torque on the magnetization [134, 145–147]. On the other hand, in a pair of metallic AFM meeting a series of stringent symmetry requirements, namely CuMnAs and Mn_2Au, there exists the AFM version of the EE, which is known as the Néel SO torque. This is due to the fact that these systems have globally centrosymmetric with locally broken inversion symmetry crystallographic structures at the same time that their lattice sites form inversion partners coinciding with their two spin sublattices, which allows to exert field-like staggered local fields dependent on the basal in-plane current injection direction [69, 148]. Interestingly, AFM show a memristive-like multilevel switching behavior, which can be tuned through the number of pulses and their duration, being possible to exploit the elusive THz band due to its demonstrated response to both current- and infrared laser-induced ultrashort stimuli [149–151]. Nevertheless, despite the absence of stray fields in AFM, the order of magnitude of the small signals obtainable through the AMR and DW MR effects in metals [152–155] and, on the other hand, through the spin Hall (SH) MR effect in insulators [156, 157], limit the miniaturization of potential devices. In principle, this fact could be patched up through the experimental verification of the AFM versions of the non-SOC-dependent GMR and TMR, which are theoretically possible in this type of materials [158–160], but which would require perfectly epitaxial samples [141]. On the other hand, the existence of the SOC-based AMR effect has been demonstrated using a current tunneling through an AFM towards a NM metal, being the signal really appreciable at low temperatures [161, 162], requiring, at room temperature, the existence of an additional FM layer with perpendicular anisotropy to induces an out-of-plane polarization of the AFM [163].

In this sense, the difficult dynamic characterization of potentially ultrafast magnetic textures hinders their potential in non-volatile racetrack memories. In fact, at the moment there are at least two proposals through thermoelectric-based effects in metals. The first one is based on the experimental detection of the magnetic soliton position through the nonzero magneto-Seebeck-based electric voltage induced by a laser-induced localized temperature gradient between AFM boundaries [164] and, the other one, in the theoretically proposed localized electronic-based heat wave that slightly lags the ultrafast current-induced spin-orbit (SO) field-based DW dynamic process and that could be tracked experimentally through scanning thermal

microscopy [165]. An alternative to be able to attest the benefits of this type of materials through experimental methods is to rely on synthetic AFM, which are composed of two antiparallel-aligned FM layers coupled through the RKKY interaction due to the presence of a NM spacer, contribution that is weaker than the intrinsic AFM one. Along this line, in perpendicularly magnetized systems with interfacial DMI, it has been proven that it is possible to induce the SHE-based dynamics of the two Néel-like DW coupled to each other in each sheet of the system, reaching speeds of the order of 750 m/s [166], notably higher than in FM and without a trace of the undesirable WB. On the other hand, the stabilization at room temperature of individual skyrmions has been demonstrated in this type of engineered systems [167], while their deflection-free dynamics will require new studies that go beyond the low speeds reported in the presence of large pinning effects and low SOT-based stimuli [168, 169]. Experimentally, it has been possible to observe multidomain structures and DW displacement-induced Néel order parameter switching [170, 171], while to nucleate skyrmions it has been demonstrated that a critical temperature must be exceeded to create topologically-protected nanoislands or to induce a printing process from an adjacent FM due to the exchange bias effect in its cooling process [172, 173]. Although at the moment only theoretical conjectures can be made beyond magnetic storage schemes in AFM, it is interesting to mention that it has been proposed that skyrmions in synthetic AFM can both emulate a synaptic-like behavior through the voltage-controlled skyrmion size and its consequent MR signal tuning as well as a neuron spiking-based process through the annihilation of these solitons [174].

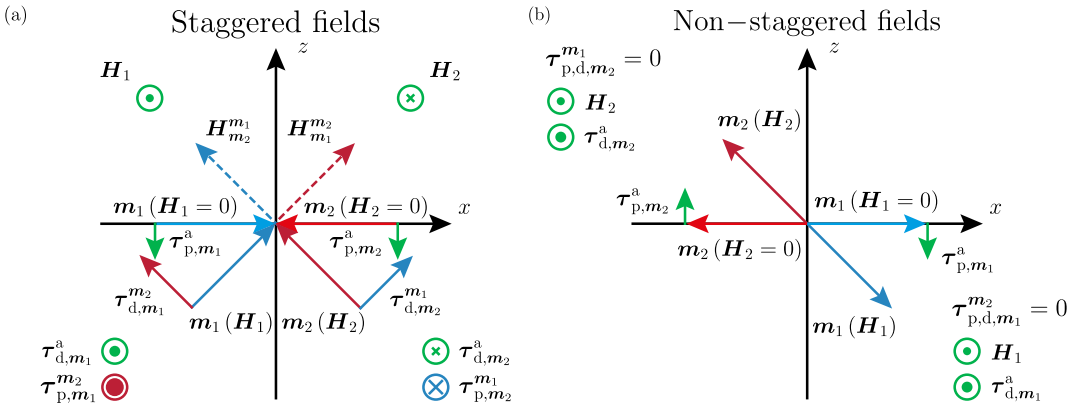

Figure 1.5: Torque-based contributions, $\boldsymbol{\tau}$, experienced by two spins, represented by their *i-th* magnetization vectors, $\boldsymbol{m}_i$, initially aligned antiparallel, in the presence of (a) staggered or (b) non-staggered fields, $\boldsymbol{H}_i$. The subscripts p and d refer, respectively, to the precessional and damping components, respectively, the superscript a indicates that it has been induced by the external stimulus, and the indices $\boldsymbol{m}_{1,2}$ allude to the exchange interaction between the two considered atomic magnetic moments that reside in the xz easy-plane of the system. The fields $\boldsymbol{H}_{\boldsymbol{m}_i}^{\boldsymbol{m}_j}$ represent the exchange-based contribution experienced by the *j-th* magnetization vector, $\boldsymbol{m}_j$, due to the presence of the *i-th* atomic moment, $\boldsymbol{m}_i$.

1.5 Framework and summary of the thesis

The objective of the preceding sections has been to provide a brief overview, from my point of view, of the current state of research of a certain part of the spintronics community, with special emphasis on the potential advantages of SO field-based

excitation methodologies, topologically-protected magnetic textures, and AFM materials. In this context, the research works exposed in this thesis in the next chapters will be focused, especially, in the relativistic signatures experienced by DW during their dynamic evolutions as well as in topologically-mediated processes involving the creation or annihilation of magnetic solitons in spin space. For this, we will use atomistic spin dynamics simulations (ASDS), carried out through a private software from Hitachi Cambridge Laboratories, as well as analytical methods mainly based on the absence of sizable deformations of the magnetic textures during their propagation processes. The structure of this manuscript will be as follows:

- In Chap. 2 it has been introduced how to characterize the dissipative dynamic processes in spin space based on the different magnetic contributions of the system, as well as the conditions under which solitonic solutions exist in long-range magnetically-ordered media whose energetically-induced stabilities can be characterized through topological notions.

- In Chap. 3 the crucial features that dictate the stability of dynamic DW in both FM and AFM have been discussed, as well as the impact of topology on the propagation of magnetic textures and what kind of computational and experimental approaches exist to characterize these soliton solutions.

- In Chap. 4 we have addressed the reduction of the dynamic DW description in a biaxial FM to a sine-Gordon (SG) expression, a situation which is physically consistent in the Walker-type of solutions framework in the presence of a very large hard-axis anisotropy that constrains the magnetization in the plane at rest of the magnetic soliton, which is validated by the relativistic traces found through ASDS.

- In Chap. 5 we have analytically replicated the inertial signatures appearing between concatenated quasistatic DW dynamic regimes obtained through ASDS for the AFM Mn_2Au in the framework of an effective version of the nonlinear σ-model, based on its multisublattice structure with different exchange-oriented contributions, as well as its after-pulse displacement through the knowledge of its steady-state relativistic mass.

- In Chap. 6 we have obtained, through ASDS, that a primal DW excited by sufficiently large SO field-based stimuli in the AFM Mn_2Au can act as a seed for the appearance of a pair of magnetic textures preserving the overall topological charge of the system, subsequently giving rise to one of the nucleated magnetic solitons transiently propagating at supermagnonic velocities.

- In Chap. 7 we have studied through ASDS the partial or total release of the exchange-based self-energies dynamically accumulated by two DW through their topologically-mediated collision in the AFM Mn_2Au, being possible to distinguish the outcome of the impact through the energy redistribution to the electron and phonon reservoirs described by the two temperature model.

Chapter 2

Energetically-induced magnetic texture stability in spin space

2.1 Quantum-based nature of the isolated atomic magnetic moment

2.1.1 Discretized spectrum of the electron angular momentum eigenvalues

Magnetism on the atomic scale is primarily dominated by the net electronic contribution, which is about three orders of magnitude greater than the nuclear one due to their associated masses [175]. Electrons are massive charged point-like particles which have a two sources-based magnetic moment: one linked to its orbital motion around the positively-charged core of the atom and the other due to its intrinsic spin. When an electron revolves around the nucleus under the influence of the Coulomb interaction, having an associated orbital angular momentum, it constitutes a current loop to which can be related a magnetic dipole moment [176]. While this orbital contribution can be understood classically, the spin one cannot be interpreted in this context, since it arises naturally in the relativistic quantum-based Dirac equation and does not have an accurate macroscopic analog [177, 178]. The fact that a magnetic moment can be associated with this intrinsic property, as in the orbital case, is due to the fact that its existence is necessary to explain real experiments for, for example, atoms with valence electrons in the s orbital, for which the orbital contribution is zero [179, 180], and due to the precise theoretical predictions obtained by quantum electrodynamics [181–184]. The total electronic magnetic moment operator, $\hat{\boldsymbol{\mu}}_J$, given by the sum of its orbital and spin contributions, can be associated with the total electronic angular momentum operator, $\hat{\boldsymbol{J}}$, being expressed as

$$\hat{\boldsymbol{\mu}}_J = -\gamma g_J \hat{\boldsymbol{J}}, \tag{2.1}$$

where g_J represents the dimensionless g-factor associated to the total angular momentum while γ expresses the gyromagnetic ratio [185]. In quantum mechanics, both components of the electronic angular momentum are subject to the discretization of their eigenvalues, not being possible to accurately characterize more than one angular momentum component of the electron simultaneously due to the Heisenberg uncertainty principle [186]. This non-continuous nature of the eigenvalues can

be clearly seen through the characterization of its projection along a particular direction, for example, the *z-th* axis, as well as its module, which will be given, respectively, by

$$\hat{\mu}_J^z = -g_J \mu_B m_J, \qquad \left|\hat{\boldsymbol{\mu}}_J\right| = -g_J \mu_B \sqrt{J\left(J+1\right)}, \tag{2.2}$$

where m_J and J codify the quantum numbers associated to the total electronic angular momentum and μ_B characterizes the Bohr magneton [187]. In this context, it is possible to get an idea of what the discretized spectrum of the electronic magnetic moments, $\left|\hat{\boldsymbol{\mu}}_J\right|$ and $\hat{\mu}_J^z$, looks like for the case in which the quantum number of the modulus of the vector operator takes an arbitrary value $J = 2$, which constrains the associated *z-th*-based parameter, m_J, to the interval $m_J \in [-2, -1, 0, 1, 2]$. As it is shown in Fig. 2.1 (a), the arrows are supposed to represent the hypothetical modulus of the total magnetic moment of the electron, but it should be noted that the radius of the sphere is greater than the value of its *z-th* component, which is misleading because there are, in fact, no other possible projections of the operator vector along other spatial directions, since a particle cannot have a determinate angular momentum vector [186].

2.1.2 Dynamic and classical-like picture of the atomic spin angular momentum

Typically, an atom is not made up of a single electron, but of many of them. Only those cases in which the valence shells are partly filled will have a non-zero net atomic magnetic moment, $\hat{\boldsymbol{\mu}}$, being its ground state governed by the combination of its orbital and spin components. In its calculation, the Pauli exclusion principle must be respected and, at the same time, the associated electrostatic Coulomb energy has to be minimized, being important to take into account, in addition, the energy hierarchy of the spin-spin, orbit-orbit, and SO interactions [176]. It must be noted, however, that there are cases in which the orbital contribution is zero, either because the unpaired electrons live in the s shell or due to its quenching, as it occurs for 3d ions [188], being possible to approximate the atomic angular momentum to the spin one, $\hat{\mathbf{S}}$. In this context, the time-dependent behavior of the spin angular momentum due to the influence of its atomic environment or an external stimulus, which will be encoded in the Hamiltonian operator, $\hat{H}\left\{\hat{\mathbf{S}}\right\}$, can be explored. To do this, it is possible to use the quantum-based equation of motion, in the Heisenberg picture [185], for the expectation value for the *i-th* component of the spin operator, $\left\langle \hat{S}_i \right\rangle$, which can be expressed as

$$\partial_t \left\langle \hat{S}_i \right\rangle = \frac{1}{\mathrm{i}\hbar}\left[\hat{S}_i, \hat{H}\left\{\hat{\mathbf{S}}\right\}\right] = \frac{1}{\mathrm{i}\hbar}\left[\left[\hat{S}_i, \hat{S}_j\right]\frac{\partial \hat{H}\left\{\hat{\mathbf{S}}\right\}}{\partial \hat{S}_j} + \cdots\right], \tag{2.3}$$

where potential higher order terms in the spin operator coming from the Taylor series expansion of the associated Hamiltonian, governed by the commutation relations between different angular momentum components [186], are given by

$$\left[\hat{S}_i, \hat{S}_j\right] = \mathrm{i}\hbar\varepsilon_{ijk}\hat{S}_k, \tag{2.4}$$

have not been explicitly included with the aim of working in the leading order in energy. Combining Eqs. (2.3) and (2.4), it is possible to obtain, in vector form [189],

that

$$\partial_t \left\langle \hat{\boldsymbol{S}} \right\rangle = -\hat{\boldsymbol{S}} \times \frac{\partial \hat{H}\left\{\hat{\boldsymbol{S}}\right\}}{\partial \hat{\boldsymbol{S}}} + \cdots \tag{2.5}$$

In the above expression, the length of the expectation value of the atomic spin angular momentum operator is subject to discretization, as expected in the quantum mechanics framework, and its value is not constant, verifying that $\left|\left\langle \hat{\boldsymbol{S}} \right\rangle\right| \leq \hbar \max \sqrt{S\left(S+1\right)}$, where S represents the spin quantum number [190]. However, there are some conditions under which one can transition from a quantum operator-based description of the spin to a classical picture in which its associated angular momentum can be considered as a continuous vector of constant magnitude rotating in Euclidean space. First, when the magnitude of the atomic spin angular momentum is large enough, such that $\left|\hat{\boldsymbol{S}}\right| \to \infty$, the associated uncertainty will be small due to the strong localization [191, 192]. On the other hand, when the reduced Planck constant approaches zero, $\hbar \to 0$, the graininess of the energy levels blurs, and the contributions beyond the leading one in Eqs. (2.3) and (2.5) become negligible, giving place to the classical dynamical Liouville equation [193, 194]. In this context, the atomic magnetic moment can be considered as a macrospin interacting with its surroundings, ignoring quantum effects such as entanglement in multielectron systems [190], which is a good approximation for systems in which the main contribution comes from localized electrons in 4f orbitals and for high temperatures [195, 196]. Because of this, it is legitimate to evaluate the evolution of the atomic magnetic moment semiclassically in Euclidean space through the angular part of the spherical coordinates representation of a unit atomic magnetization vector, $\boldsymbol{m}_i$, which would be given by $\boldsymbol{m}_i = \boldsymbol{\mu}_i / |\boldsymbol{\mu}_i|$, as it is depicted in Fig. 2.1 (b).

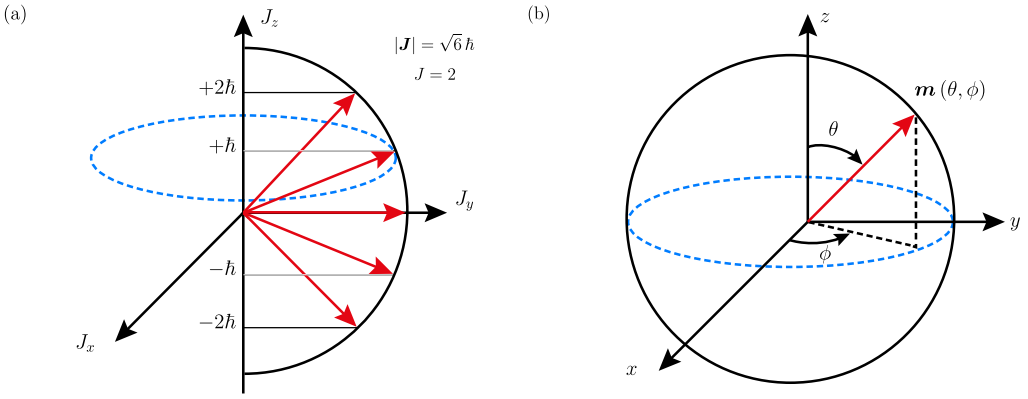

Figure 2.1: (a) Graphical representation of the supposed spectrum of eigenvalues of the modulus of the total electronic magnetic moment operator, $\left|\hat{\boldsymbol{\mu}}_J\right|$, and its projection along the z-*th* axis, $\hat{\mu}_J^z$, for the case in which the quantum number associated to the vector is given by $J = 2$. Adapted from [186]. (b) Definition of the unit magnetization vector, $\boldsymbol{m}$, in terms of the polar, θ, and azimuthal, ϕ, angular variables relative to the Cartesian coordinate system in Euclidean space at the atomic length scale far from the one dictated by the Planck constant, $\hbar$.

2.2 Magnetic interactions and collective phenomena in solids

Elucidating the arrangement of the atomic magnetic moments in a solid constitutes a multibody problem in which different causes of various kinds are involved. On

the one hand, the electric charge distribution associated with each atom and its interaction with its surroundings is known as the crystal field. However, macroscopically, magnetism cannot be explained through a static approach alone, but rather needs to take into account the relativistic motion of the electrons around the atomic nuclei and their associated emergent magnetic field in accordance with Maxwell's equations. On the other hand, the spatial atomic scale involved must be taken into account, where a classical description may not be sufficient, having to take into account the precepts of quantum mechanics such as the Pauli exclusion principle. This has the consequence that there will be contributions to the magnetic macroscopic ordering of a sample with a different range and magnitude of influence with its neighbors, which also depends on the potential delocalization of the electrons involved depending on the conductivity of the system and symmetry of its unit cell.

2.2.1 Long-range classic dipole-dipole interaction

Due to the point-like nature of the electrons that contribute to the atomic magnetic moment, they can be modeled as infinitesimally small current loops and thus be interpreted as magnetic dipoles. In order to extrapolate this approximation to the atomistic case and estimate the interaction energy associated to the Biot-Savart's law-based field created by them at every point in space, it is essential that the interatomic distance is as large as possible compared to the electronic scale [197]. For two atomic-scale magnetic dipoles with associated magnetization vectors $\boldsymbol{m}_i$ and $\boldsymbol{m}_j$, separated by a distance $\left|\boldsymbol{r}_{ij}\right|$, this non-local energy would be given by

$$E_{\text{dip}} = -\frac{\mu_0 \mu_{\text{s}}^2}{4\pi \left|\boldsymbol{r}_{ij}\right|^3} \left[3\left(\boldsymbol{m}_i \cdot \hat{\boldsymbol{r}}_{ij}\right)\left(\boldsymbol{m}_j \cdot \hat{\boldsymbol{r}}_{ij}\right) - \left(\boldsymbol{m}_i \cdot \boldsymbol{m}_j\right)\right], \tag{2.6}$$

where $\hat{\boldsymbol{r}}_{ij}$ represents a unit vector joining their centers and where μ_0 and μ_{s} express the vacuum magnetic permeability and atomic magnetic moment, respectively [198]. Even being Eq. (2.6) a valid and sufficient expression in the classical physics framework, formally on its right-hand side there should be a contribution that realizes that two different current distributions cannot occupy the same position in space [199]. In accordance with Maxwell's equations that guarantee that the magnetic field induced from the magnetization of a sample must not diverge, the flux lines arising from each dipole of the considered system must be closed loops in such a way that the net contribution of surface magnetic poles is minimized [200]. This associated field depends on the size, mutual alignment, shape, and separation between atomic magnetic moments, for which it takes into account the sum of the interaction between all the dipoles of the system [201]. Its contribution is small, but not negligible, and it is not enough to explain the existence of long-range magnetic ordering in real materials due to the transition temperature to these type of phases [202].

2.2.2 Short-range quantum-based exchange contribution

The interaction between two electrons, which must verify the Pauli exclusion principle due to their fermionic character, imposes that the total wavefunction product of their overlapping must be antisymmetric under the exchange of both particles. This can be verified if, simultaneously, both the radial part is symmetric and the spin one antisymmetric (which is known as singlet state) and also if the roles are reversed (in which case it will be known as triplet state). Due to the electrostatic repulsion between both electrons, in the intra-atomic scenario, the triplet state is energetically

favored because the antisymmetry of the radial part leads to the cancellation of the wavefunction for the virtual case in which both particles occupy the same position in the space [175]. In this circumstance, the total spin of the two electron system will be non-zero, lining up parallel to each other. Although the Coulomb interaction, which mediates the crosstalking between the fermions, is of a short-range nature, it equally affects two electrons in nearest neighboring atoms. However, in this case, it must be taken into account that it is possible to minimize the kinetic energy associated with an electron if it is allowed to be delocalized and not constrained in a single atom, which gives rise to the formation of molecular-like bonding between the two considered fermions [202, 203]. This results in the singlet state being energetically favored in principle, since an antisymmetric radial part leads to a larger orbit with a higher associated kinetic energy [176]. In this case, the electron spins will tend to group antiparallel, giving rise to a compensated joint state concerning their spin-based quantum numbers.

In most cases it is possible to characterize the correlation between two atomic magnetic moments due to the overlapping of their wavefunctions through the simple functional form of the quantum-based Heisenberg model [204], which is given by

$$E_{\text{exc}} = -\sum_{ij} \mathcal{J}_{ij} \left(\boldsymbol{m}_i \cdot \boldsymbol{m}_j \right), \tag{2.7}$$

where $\mathcal{J}_{ij}$ is known as exchange constant which accounts for the difference between the energy of the triplet and the singlet states, such that when the spins of both electrons are parallel it will have to be positive, $\mathcal{J}_{ij} > 0$, while when they are antiparallel it will be negative, $\mathcal{J}_{ij} < 0$. This isotropic contribution is the predominant one in most magnetic materials, being approximately seven orders of magnitude greater than the dipole-dipole interaction, and is usually the main cause of the existence of long-range magnetic ordering, governing the transition temperature between this ordered state and a randomly-oriented paramagnetic one [202]. However, this type of direct exchange is not enough to explain the magnetic properties observed in real materials due to insufficient overlap between orbitals of neighboring atoms. This is appreciable both in rare earths and in transition metals due to the location of their valence electrons, cases in which it is important to also take into account the role of the conduction electrons closest to the nucleus [176]. Real magnetic systems are more complicated than what has been exposed so far, since they involve many atoms composed of multiple electrons living in different orbitals interacting with each other, a problem which is unsolvable exactly.

2.2.3 Antisymmetric exchange Dzyaloshinskii-Moriya interaction

Beyond the symmetric part of the exchange interaction introduced in Sec. 2.2.3, it is also possible to find an antisymmetric contribution due to a potential low symmetry of the atomic local environment. Based on the SOC in a medium with broken inversion symmetry, which links the lattice with the spin space disposition, the crystal field energy can be minimized through the creation of a non-collinear state. In this way, this contribution favors a perpendicular arrangement between atomic moments, which has to compete with the predominant symmetric exchange one, giving rise to a slightly canted arrangement with respect to the (anti)parallel distribution between neighboring spins [175]. Analytically, this term can be modeled through the expression

$$E_{\text{DM}} = \sum_{i,j} \boldsymbol{D}_{ij} \cdot \left(\boldsymbol{m}_i \times \boldsymbol{m}_j \right), \tag{2.8}$$

being $\boldsymbol{D}_{ij}$ the Dzyaloshinskii vector [176]. This type of situation may be due also to interfacial effects, such as when a FM layer is coupled with a HM-based sheet with large SOC [205].

2.2.4 Anisotropy-induced preferential magnetization axes

In long-range magnetically-ordered media, the isotropic exchange interaction is not able to account for the magnetization distribution in real samples. For this, there must be some term that accounts for the preference of the atomic magnetic moments to be oriented along certain directions of the crystal lattice or to be constrained in some plane of the system. The fundamental contribution to this phenomenon is known as intrinsic magnetocrystalline anisotropy, whose main source is based on the single-ion term coming from the unquenched orbitals mediated by the SOC in its competition with the crystal electric field created by neighboring atoms, depending on the local symmetry of the crystal [203]. In other cases, this scenario may be due to the interatomic dipole-dipole or anisotropy exchange interactions, having a two-ion origin [175]. There are, however, other types of anisotropies of extrinsic origin which are based on deviations from the ideal crystal symmetry through, for example, defects or partial order effects [206]. The most simplistic functional form to model this phenomenology corresponds to the case of a second-order uniaxial anisotropy term [207], which would be given by

$$E_{\text{ani}} = -K \sum_i (\boldsymbol{m}_i \cdot \hat{\boldsymbol{e}})^2, \tag{2.9}$$

where $\hat{\boldsymbol{e}}$ denotes the unit vector along a low symmetry direction, while K accounts for the anisotropy constant, which can be positive ($K > 0$), favoring the alignment of the atomic magnetic moments of the sample along the easy-axis $\hat{\boldsymbol{e}}$, or negative ($K < 0$), preferring that the magnetization lives in the plane perpendicular to the hard-axis $\hat{\boldsymbol{e}}$.

2.2.5 Externally-induced equilibrium breaking Zeeman-like term

The application of a magnetic field along a certain direction causes the breaking of the intrinsic symmetry of the medium, encouraging the externally-induced reorientation of their magnetic moments. This type of contribution potentially competes with the intrinsic anisotropy terms of the system, in such a way that their relative magnitudes will define the direction along which the energy of the medium is to be minimized [175, 176]. In this context, a Zeeman-like field, $\boldsymbol{H}$, along the arbitrary $\hat{\boldsymbol{e}}$-*th* spatial direction, so that $\boldsymbol{H} = H\,\hat{\boldsymbol{e}}$, the associated energy term can be written as

$$E_{\text{Zee}} = -\mu_0 \mu_{\text{s}} \sum_i (\boldsymbol{m}_i \cdot \boldsymbol{H})\,. \tag{2.10}$$

2.3 Magnetization dynamics-governed Landau-Lifshitz-Gilbert equation

2.3.1 Phenomenological inclusion of transverse relaxation processes

The time-dependent magnetization dynamics under the action of the intrinsic phenomena of the system or an external stimuli can be modeled through the Landau-Lifshitz-Gilbert (LLG) equation. This expression can be obtained as a semiclassical

version of the non-dissipative quantum-based Eq. (2.5) if the dissipation processes inherent to any real system are included. Thus, in addition to a term that accounts for the conservative uniform precession of magnetization around an effective magnetic field, scenario that is reflected in Fig. 2.2 (a), it is necessary to include a contribution that models the decrease in its gyration radius until the local magnetic moment aligns with the direction that minimizes the energy of the system [208]. This is consistent with the fact that in FM materials the macrospin tends to saturate in a hysteresis loop as the external field increases and because dissipative mechanisms are necessary to explain the absorption lines in resonance experiments [209, 210]. To model this contribution, the most usual approach is through the phenomenological inclusion of a term perpendicular to the precession torque, known as the Landau-Lifshitz (LL) form [79], which can be written as

$$\dot{\boldsymbol{m}} = -\gamma \left(\boldsymbol{m} \times \boldsymbol{H}^{\text{eff}} \right) - \alpha\gamma \boldsymbol{m} \times \left(\boldsymbol{m} \times \boldsymbol{H}^{\text{eff}} \right), \tag{2.11}$$

which describes the precession of a local unit magnetic moment in a system, that exchange energy with its surroundings, around the direction dictated by the effective magnetic field, $\boldsymbol{H}^{\text{eff}}$, which is depicted in Fig. 2.2 (b), being characterized by

$$\boldsymbol{H}^{\text{eff}} = -\frac{1}{\mu_0 \mu_{\text{s}}} \frac{\delta E}{\delta \boldsymbol{m}}, \tag{2.12}$$

where some of the most important potential energy contributions have been introduced in Sec. 2.2. The rate of energy dissipation is governed by the phenomenological Gilbert damping parameter, α, which is mainly governed by the interaction of the spin subsystem with the heat bath [211]. In this sense, its origin may be intrinsic, due to its interaction with external degrees of freedom such as phonons or other electrons or, at the same time, by SO interaction or magnetostatic fields that cause a misalignment between atomic magnetic moments, increasing the magnetic energy of other spins in the system, or extrinsic, due to the presence of impurities in the system, the hierarchy of mechanisms depending entirely on the considered material [201, 203].

2.3.2 Rayleigh-governed description of the dissipation phenomena

Interestingly, apart from the description of the relaxation processes intrinsic to the magnetization dynamics in long-range magnetically-ordered media given by the LLG equation in its LL form, which are encapsulated in the second term of the right-hand side of Eq. (2.11), there is another functional form of this expression that can be used for the same purpose. This alternative version, which is known as the Gilbert version of the LLG equation, can be described by

$$\dot{\boldsymbol{m}} = -\gamma \left(\boldsymbol{m} \times \boldsymbol{H}^{\text{eff}} \right) + \alpha \left(\boldsymbol{m} \times \dot{\boldsymbol{m}} \right), \tag{2.13}$$

which, if it is multiplied vectorially by $\boldsymbol{m}$ and it is considered that the magnetization vector has a fixed length, it can be rewritten as

$$\dot{\boldsymbol{m}} = -\frac{\gamma}{1+\alpha^2} \left[\boldsymbol{m} \times \boldsymbol{H}^{\text{eff}} + \alpha\, \boldsymbol{m} \times \left(\boldsymbol{m} \times \boldsymbol{H}^{\text{eff}} \right) \right], \tag{2.14}$$

expression which approaches Eq. (2.11) in the limit $\alpha \ll 1$, differing substantially for larger values of the damping parameter, the last referred equation being less

realistic due to its inability to predict the existence of a minimum switching time [201]. The more physical character of Eq. (2.13) can be glimpsed because it can be derived through a Lagrangian formalism that takes into account that the force acting on a moving particle in a viscous medium is proportional and antiparallel, to a first approximation, to its velocity, which is encapsulated in what is known as the Rayleigh dissipation function, R [212, 213]. To show this, it is possible to note that the energy dissipation rate can be expressed, taking into account Eq. (2.12), as

$$R = -\frac{1}{2}\frac{\mathrm{d}E}{\mathrm{d}t} = -\frac{1}{2}\frac{\delta E}{\delta \boldsymbol{m}}\dot{\boldsymbol{m}} = \frac{\mu_0 \mu_\mathrm{s}}{2}\left(\boldsymbol{H}^\mathrm{eff}\cdot\dot{\boldsymbol{m}}\right), \tag{2.15}$$

expression which has a term resembling what can be found in the functional forms of the LLG equation. At this point, if one scalarly multiplies Eq. (2.13) by $\boldsymbol{H}^\mathrm{eff}$

$$\boldsymbol{H}^\mathrm{eff}\cdot\dot{\boldsymbol{m}} = \alpha\,\boldsymbol{H}^\mathrm{eff}\cdot\left(\boldsymbol{m}\times\dot{\boldsymbol{m}}\right), \tag{2.16}$$

and, on the other hand, by $\dot{\boldsymbol{m}}$

$$\dot{\boldsymbol{m}}^2 = -\gamma\,\dot{\boldsymbol{m}}\cdot\left(\boldsymbol{m}\times\boldsymbol{H}^\mathrm{eff}\right), \tag{2.17}$$

it is possible to obtain two equations that allow to rewrite Eq. (2.15) in the desired way [205]. By doing so, combining both expressions [214, 215], one arrives at

$$R = \frac{\alpha\mu_0\mu_\mathrm{s}}{2\gamma}\,\dot{\boldsymbol{m}}^2. \tag{2.18}$$

2.3.3 Longitudinal relaxation effects and temperature-dependent magnetization response

The LLG equation describes the time evolution of the unit magnetization vector, given by Eqs. (2.11) and (2.13), being a nonlinear expression that, in general, is highly complex and non-integrable [209]. Moreover, it only takes into account potential transversal relaxation processes of the atomic magnetic moment with respect to the direction of the local effective magnetic field [216]. Despite its generalizable use for temperature-independent processes, there are situations where this scenario is not completely satisfactory, such as in laser-induced ultrafast magnetization dynamics, where it has been observed that the modulus of the order parameter decreases due to longitudinal relaxation [217, 218]. To account for this type of situation, a generalization of the LLG equation, known as the LL-Bloch equation [219, 220], was proposed, where the main contribution to the longitudinal damping comes from high-frequency SW [221], this being a faster process than the transverse one, becoming, however, slower as the magnitude of the thermal effects increases [216]. To take into account the potential non-deterministic thermal fluctuations that result in deviations from the average trajectory, it is possible to add a stochastic contribution to the definition of the effective magnetic field, expressed by Eq. (2.12), in the Langevin framework [222, 223]. Its most common functional form, suitable for the case in which the timescale response of the thermal bath is faster than that of the spin system, is through Gaussian white noise, in which both space and time are uncorrelated, enabling the construction of a Fokker-Planck equation [219, 224]. Additionally, it is possible to model through the LLG equation the response of the system for a specific temperature through the knowledge of the value of the intrinsic parameters of the system according to power scaling laws of the magnetization vector modulus [225, 226].

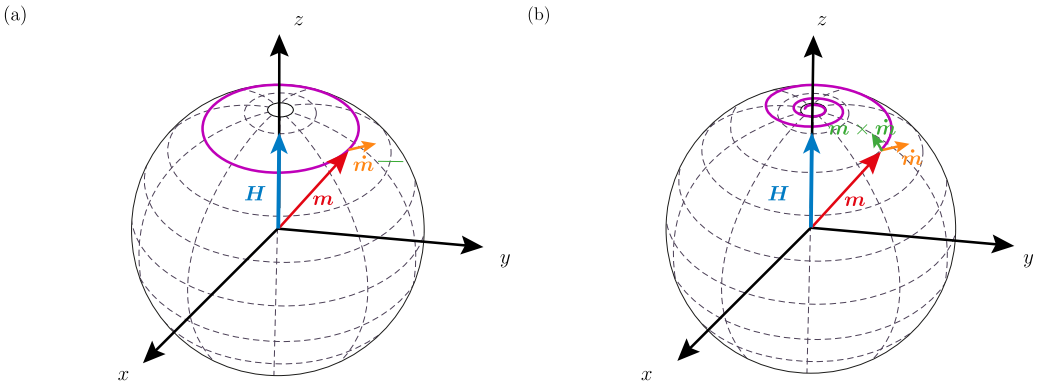

Figure 2.2: Time evolution of a single unit magnetic moment, $\boldsymbol{m}$, as described by the LLG equation in its LL form given by Eq. (2.11). (a) The magnetization vector precesses around an effective field, $\boldsymbol{H}^{\text{eff}}$, expressed by Eq. (2.12), with a constant polar angle in the absence of dissipative effects. (b) The atomic magnetic moment, in the presence of relaxation processes, tends to align with the effective field through a spiraling trajectory. Adapted from [209].

2.4 One-dimensional magnetic solitons in long-range magnetically-ordered media

2.4.1 Non-decaying localized solutions to nonlinear field theories

Interestingly, unlike in the case of wave-like solutions to linear dispersive equations, which spread out over time, in nonlinear-governed theories as in the case of the LLG expression that governs the magnetization dynamics in the presence of relaxation processes, which is given irrespectively by Eqs. (2.11) and (2.13), there can be stable solutions that can potentially persist indefinitely. In particular, those non-trivial classical solutions to nonlinear field equations that (i) are undistorted spatially localized and that move at constant velocity and (ii) that after a collision process emerge with their initial shapes and speeds, except for possible phase changes, can be referred to as solitons [227, 228]. However, it must be taken into account that there is no universal definition for this term, and that even non-dispersive wave packets moving uniformly, which do not verify condition (ii), are also known as solitons while, strictly speaking, they should be called solitary waves. However, both types of entities have in common that, to meet the dissipationless condition (i), a balance must be found between the dispersive and nonlinear terms [229]. Clearly, the concept of soliton requires more stringent conditions than for solitary waves, since to corroborate that these reemerges unscattered, it is necessary to find time-dependent propagating solutions involving several of these entities, while a solitary wave can itself be a static localized solution [230].

2.4.2 Domain wall characterization in ferromagnetic one-dimensional spin chains

2.4.2.1 Energy balance-governed inhomogeneous spin-based transition

For the case of a real non-infinite FM sample, a homogeneous state in which all the atomic spins point in the same direction entails a very large magnetic field with its

consequent magnetostatic energy. In order to reduce the self-energy of the medium, well below the critical temperature of the system, the spontaneous creation of domains, within which the magnetic moments are parallel oriented, whose size is, in general, microscopic, is favourable [80, 176]. Under the premise that the magnetization must be directed in such a way as to minimize the magnetic anisotropy energy of the system, the short-range exchange interaction will want the magnetization transition between neighboring domains to be as smooth as possible [206]. These types of soliton solutions that interpolate between two minima of the anisotropy-based vacuum manifold, separated in this case by an angular variation of 180° of the spin-based order parameter, are known as DW. For the specific case of an infinite crystal in which there exists a uniaxial second-order easy-axis anisotropy contribution along the *z-th* spatial direction, the magnetization can rotate between its two antiparalel polarization states through any plane containing the *z-th* axis. However, since, for convenience, it is possible to assume that the magnetic order parameter can only vary along the *x-th* spatial direction, the atomic magnetic moment has to rotate in the yz plane, always being $m_x = 0$, to avoid the creation of volumetric charges (since $\boldsymbol{\nabla} \cdot \boldsymbol{m} = \partial_x m_x = 0$). For this type of magnetic texture, known as Bloch-like DW, which it is represented in Fig. 2.3 (a), there are potential surface charges at the boundary of the sample, but their influence can be ignored because the considered system is infinite. Thus, in this configuration the contribution of the magnetostatic energy to the calculation of the magnetic texture profile is negligible, being entirely governed by the anisotropy and exchange terms [205].

2.4.2.2 Analytically-based spatially-localized magnetic texture features

To address the analytical characterization of the static profile of the involved magnetic soliton in the absence of external stimuli, it is necessary to take, as a reference, the number of nearest neighbors exchange-based bonds existing along the *x-th* transition direction of an atom located at an arbitrary position x_i, being its magnetization vector given by $\boldsymbol{m}(x_i)$. In this case, the atom in the aforementioned position has two first neighbors mediated by the FM exchange interaction encoded by the $\mathcal{J}$ parameter, at a distance given by the atomic spacing a_0, which can be represented as $\boldsymbol{m}(x_{i\pm1})$. Therefore, the discretized version of the FM exchange contribution, E_{exc}, can be expressed as

$$E_{\text{exc}} = -\mathcal{J}\boldsymbol{m}(x_i) \cdot [\boldsymbol{m}(x_{i-1}) + \boldsymbol{m}(x_{i+1})], \tag{2.19}$$

where possible contributions from neighbors along the *y-th* spatial direction have not been taken into account because they do not impose any type of exchange penalty that affects the static properties of the magnetic texture. A continuum version of this expression can be found assuming that the spin-based transition is smooth enough by performing a 1D Taylor series decomposition up to second order along the *x-th* axis with respect to the position x_i of the reference atom, giving rise to

$$E_{\text{exc}} = -2\mathcal{J}\boldsymbol{m}(x_i) \cdot \left[\boldsymbol{m}(x_i) + \frac{a_0^2}{2}\left(\partial_x^2 \boldsymbol{m}(x_i)\right)\right], \tag{2.20}$$

where it can be seen that the first term of the right-hand side provides a constant contribution that can be neglected. Taking into account that the magnetization order parameter is a vector of fixed length, it is possible to rewrite the second term, neglecting spatial indices, through the expression $\boldsymbol{m} \cdot \left(\partial_x^2 \boldsymbol{m}\right) = -(\partial_x \boldsymbol{m})^2$. In this

scenario, the energy of the system, E, can be written taking into account the FM exchange, E_{exc}, given by Eq. (2.20), and anisotropy, E_{ani}, contributions, which will be given by

$$E = \mathcal{J} a_0^2 \left(\partial_x \boldsymbol{m}\right)^2 + E_{\text{ani}}\left(\boldsymbol{m}\right), \tag{2.21}$$

where $E_{\text{ani}}\left(\boldsymbol{m}\right) = -K_z \left(\boldsymbol{m} \cdot \hat{\boldsymbol{z}}\right)^2$, being K_z the second-order uniaxial easy-axis anisotropy constant. In this context, it is convenient to abandon the vectorial description of the system in favor of an angular-based formalism, such that the magnetization vector, $\boldsymbol{m}$, can be reexpressed, in spherical coordinates, as

$$\boldsymbol{m} = \left(\sin\phi\, \sin\theta, \cos\phi\, \sin\theta, \cos\theta\right), \tag{2.22}$$

so that the configurational energy, E, given by Eq. (2.21), will take the functional form given by

$$E = \mathcal{J} a_0^2 \left(\partial_x \theta\right)^2 + E_{\text{ani}}\left(\theta\right), \tag{2.23}$$

being the anisotropy-based contribution, in the spherical representation, expressed as $E_{\text{ani}}\left(\theta\right) = K_z \sin^2\theta$ [207].

To explore the stationary soliton-like solutions of the system described by the exchange- and anisotropy-based configurational energy, E, given by Eq. (2.23) in its angular description, it is possible to use the Euler-Lagrange (EL) formalism to find the associated wave-like equation of motion, which will be given by

$$2\mathcal{J} a_0^2 \left(\partial_x^2 \theta\right) = \frac{\partial E_{\text{ani}}\left(\theta\right)}{\partial \theta}, \tag{2.24}$$

expression which is reminiscent of the case of the Newton-dynamic description of a classical particle in a potential lanscape given by the anisotropy-based nonlinear contribution, E_{ani} [231, 232]. To facilitate the manipulation of the previous expression, it is convenient to multiply it by $\left(\partial_x \theta\right)$ and take into account that

$$2\left(\partial_x \theta\right)\left(\partial_x^2 \theta\right) = \partial_x \left[\left(\partial_x \theta\right)^2\right], \quad \sin 2\theta \left(\partial_x \theta\right) = -\partial_x \left(\cos^2\theta\right), \tag{2.25}$$

which allows to rewrite Eq. (2.24), after its spatial integration, as

$$\mathcal{J} a_0^2 \left(\partial_x \theta\right)^2 + K \cos^2\theta = \mathrm{C}, \tag{2.26}$$

where C is an integration constant that can be characterized through the anisotropy-governed boundary conditions given by the magnetization orientation at the DW boundaries at spatial infinity. At this point, to obtain a soliton-like solution it is necessary that it has a finite associated energy, E, which is possible, in view of Eq. (2.24), when the polar angle, θ, verifies that

$$|x| \to \infty \Rightarrow \begin{cases} \left(\partial_x \theta\right) = 0, \\ E_{\text{ani}}\left(\theta\right) = 0, \end{cases} \tag{2.27}$$

which is equivalent to saying that the order parameter needs to belong to the vacuum manifold at spatial infinity, which, in the case of the considered uniaxial second-order uniaxial anisotropy, $E_{\text{ani}}\left(\theta\right) = K_z \sin^2\theta$, happens when $\theta = n\pi$, where $n \in \mathbb{Z}$ [233], as it is shown in Fig. 2.3 (b). In this scenario, because $\left(\partial_x \theta\right)|_{x \to \pm\infty} = 0$ and $\theta\left(x \to \pm\infty\right) = \left(\pi, 0\right)$, the integration constant in Eq. (2.26), C, will be given by

$C = K_z$, due to which the aforementioned expression can be reexpressed as

$$\mathcal{J} a_0^2 \left(\partial_x \theta\right)^2 = K_z \sin^2 \theta, \tag{2.28}$$

which shows that the exchange-based dissipation and anisotropy-based nonlinear energy terms are compensated at any point in the system. This first-order differential expression is usually known as Bogomolny equation or first integral of the system (or, in the classical particle picture, as the virial theorem, relating its kinetic and potential energies) [234, 235], which, if it is spatially integrated, can be rewritten as

$$\int_{\pi/2}^{\theta(x)} \frac{\mathrm{d}\theta}{\sin\theta} = \pm \frac{1}{a_0} \sqrt{\frac{K_z}{\mathcal{J}}} \int_X^x \mathrm{d}x, \tag{2.29}$$

where it has been taken into account that, at the DW center position, given by X, the polar angle takes the value $\theta\left(x = X\right) = \pi/2$. It should be noted that the $\pm$ sign on the right-hand side of Eq. (2.29) is due to the symmetry of Eq. (2.23) under the transformation $\theta \to \theta + \pi$. Since throughout the magnetic texture transition the polar angle is constrained to the range of values given by $\theta \in (0, \pi)$, the involved trigonometric function will always be positive in the aforementioned expression, being the sign duality entirely governed by the spatial derivative of the angle θ, that is, by the sense of rotation between its two defining extremes. This freedom is what is known as the topological charge, Q, of the DW. Interestingly, the charge nomenclature can be interpreted in line with the behavior of the magnetic soliton under the action of an applied magnetic field along the $\pm$ *z-th* semiaxis, governing whether it moves to the left or to the right along the *x-th* spatial direction [81, 236].

From Eq. (2.29) it can be obtained, after the integration process, the functional form of the magnetic texture profile along the *x-th* spatial direction through its polar angle, θ, representation, which can be expressed as

$$\theta\left(x\right) = 2 \arctan \exp\left[\frac{Q\left(x - X\right)}{\Delta_0}\right], \tag{2.30}$$

where Δ_0 represents the DW width at rest, which is given by $\Delta_0 = a_0 \sqrt{\mathcal{J}/K}$ [80, 237]. In this expression it is possible to distinguish the effect of the different energy contributions in the spatial extension of the magnetic texture, where the anisotropy term advocates for an extremely narrow localized solution, without spins not aligned with the dictated easy-axis, while the FM exchange interaction favors the opposite, seeking the angle between neighboring spins withing the magnetic soliton transition to be as small as possible, thus favoring a wider soliton configuration [238]. Additionally, taking into account the Bogomolny expression depicted in Eq. (2.28), which reflects the energy balance between the dispersive exchange-based interaction and the nonlinear anisotropy-governed term, it is possible to rewrite the angular description of the configurational energy, E, given by Eq. (2.23), to find that this type of soliton solution has, in fact, a localized energy profile, given by

$$E = 2K_z \operatorname{sech}^2 \frac{x - X}{\Delta_0}, \tag{2.31}$$

which is independent of the involved topological charge, Q, due to the even trigonometric function involved, and that, if it is spatially integrated, gives rise to a finite energy associated with the magnetic texture. As it can be seen in Eq. (2.30), there

are two different types of DW due to the intrinsic inversion symmetries of the configurational energy, E, of the system, given by Eq. (2.23), both in the polar order parameter, $\theta \rightarrow -\theta$, and in the spatial coordinate, $x \rightarrow -x$, which are known as kink ($Q = +1$) and antikink ($Q = -1$) solutions, which have the same associated energies but different anisotropy-based boundary conditions at spatial infinity, which it can be seen in Fig. 2.4 (a).

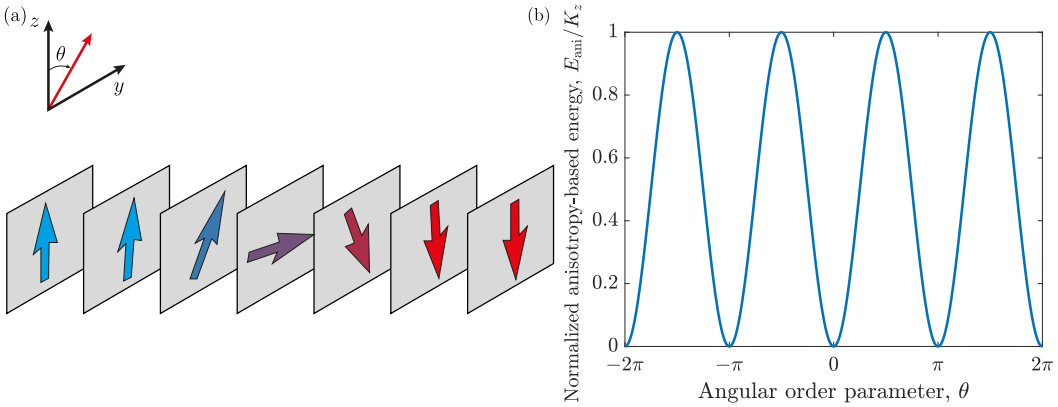

Figure 2.3: (a) Spin distribution of a Bloch DW in an infinite FM medium, in which the magnetization rotates between two anisotropy-governed domains aligned in an antiparallel fashion through the plane perpendicular to the *x-th* spatial direction along which the magnetic moment changes. Adapted from [205]. (b) Representation of the normalized uniaxial second-order easy-axis anisotropy distribution, E_{ani}/K_z, being K_z the parameter that governs its magnitude, as a function of the angular order parameter, θ.

2.4.3 Order parameter-based description of antiferromagnetic inhomogeneous spin transitions

Both the functional form of the 180° DW profile encoded in the spatial behavior of the angular order parameter, θ, which is characterized by Eq. (2.30), as well as its localized energy distribution, E, which it is represented by Eq. (2.31), are equally valid for the case of AFM media. Taking as reference the case of a 1D AFM spin chain in which its antiparallel aligned sublattices are coupled through the exchange parameter $\mathcal{J}$, it is possible to consider, again, as it was done in the developed FM scenario in Sec. 2.4.2.2, the existence of a uniaxial second-order easy-axis anisotropy along the *z-th* spatial direction, as the one depicted in Fig. 2.3 (b), contribution which would be characterized by the anisotropy constant K_z. To demonstrate this, it is convenient, again, to take an arbitrary magnetic atom as a reference, which can be located at the arbitrary position x_i, while its magnetization vector will be defined as $\boldsymbol{m}_1(x_i)$. To explore the AFM behavior of the system, its first two intersublattice nearest neighbors along the *x-th* spatial transition direction, located at distance a_0, must be taken into account, being characterized through the unit atomic magnetic moment vectors $\boldsymbol{m}_2(x_{i\pm1})$. In this scenario, the associated atomistic AFM exchange-based energy contribution, E_{exc}, is completely analogous to the one exposed in the FM scenario, which is described by Eq. (2.19) in its vector form, being possible to express it as

$$E_{exc} = -\mathcal{J}\boldsymbol{m}_1(x_i) \cdot [\boldsymbol{m}_2(x_{i-1}) + \boldsymbol{m}_2(x_{i+1})], \tag{2.32}$$

where the *i-th* subscripts attached to the atomic magnetization vectors, $\boldsymbol{m}_i$, express their belonging to different magnetic sublattices of the system, which are antiparallel distributed. However, because the unit atomic magnetic moment vector, $\boldsymbol{m}$, changes abruptly at the spatial scale given by the cutoff distance a_0, it is necessary to redefine the order parameter in such a way that it may be suitable for a description in the continuum limit [239, 240]. In this sense, it is possible to introduce two new vectors resulting from the linear combination of the magnetization vector of two contiguous sublattices, $\boldsymbol{m}_1$ and $\boldsymbol{m}_2$, which will be given by

$$\boldsymbol{n} = \frac{\boldsymbol{m}_1 + \boldsymbol{m}_2}{2}, \qquad \boldsymbol{l} = \frac{\boldsymbol{m}_1 - \boldsymbol{m}_2}{2}, \tag{2.33}$$

expressions which allow to rewrite the sublattice magnetization vectors as

$$\boldsymbol{n} + \boldsymbol{l} = \boldsymbol{m}_1, \qquad \boldsymbol{n} - \boldsymbol{l} = \boldsymbol{m}_2, \tag{2.34}$$

being possible to name $\boldsymbol{n}$ as the total magnetization vector and $\boldsymbol{l}$ as the staggered vector [241, 242].

In this context, performing a 1D Taylor series decomposition up to second order for the atoms belonging to sublattice 2 with respect to the position x_i of the reference atom, it can be found that

$$E_{\text{exc}} = 2|\mathcal{J}|\boldsymbol{m}_1\left(x_i\right) \cdot \left[\boldsymbol{m}_2\left(x_i\right) + \frac{a_0^2}{2}\left(\partial_x^2 \boldsymbol{m}_2\left(x_i\right)\right)\right], \tag{2.35}$$

expression which can be rewritten in terms of the AFM vectors, $\boldsymbol{n}$ and $\boldsymbol{l}$, through the use of Eq. (2.34). Taking into account that $\boldsymbol{n}^2 + \boldsymbol{l}^2 = 1$, working in the exchange limit framework, according to which $|\boldsymbol{n}|^2 \ll |\boldsymbol{l}|^2$ [144, 243], and neglecting spatial indices, it is possible to obtain

$$E_{\text{exc}} = \frac{1}{2} A\, \boldsymbol{n}^2 + \frac{1}{8} a \left(\partial_x \boldsymbol{l}\right)^2, \tag{2.36}$$

where the AFM homogeneous, $A = 8|J|$, and inhomogeneous, $a = 8|J|\, a_0^2$, exchange parameters have been introduced, taking into account, furthermore, that since the staggered order parameter, $\boldsymbol{l}$, is a vector of fixed length, it can be found that $\boldsymbol{l} \cdot \left(\partial_x^2 \boldsymbol{l}\right) = -(\partial_x \boldsymbol{l})^2$. On the other hand, regarding the uniaxial second-order easy-axis anisotropy term, encoded through the K_z parameter, it is necessary to take into consideration the contribution of two neighboring sublattices with antiparallel alignment, which are characterized through the magnetization vectors $\boldsymbol{m}_1$ and $\boldsymbol{m}_2$. In this context, it is possible to write, taking into account the definition of the AFM vectors, $\boldsymbol{n}$ and $\boldsymbol{l}$, given by Eqs. (2.34), the anisotropy energy, E_{ani}, in its vector form, as

$$E_{\text{ani}} = -K_z \left[\left(\boldsymbol{m}_1 \cdot \hat{\boldsymbol{z}}\right)^2 + \left(\boldsymbol{m}_2 \cdot \hat{\boldsymbol{z}}\right)^2\right] \simeq -2K_z \left(\boldsymbol{l} \cdot \hat{\boldsymbol{z}}\right)^2, \tag{2.37}$$

which has being derived in the exchange limit framework. As a result, the configurational energy of the system, E, taking into account Eqs. (2.36) and (2.37), can be expressed, in spherical coordinates, taking into account the representation given by Eq. (2.22), which is equally valid in this AFM-based description, as

$$E = \frac{1}{8} a \left(\partial_x \theta\right)^2 + E_{\text{ani}}\left(\theta\right), \tag{2.38}$$

where the anisotropy energy is defined as $E_{\text{ani}}\left(\theta\right) = 2K_z \sin^2\theta$, being also important to take into account that the homogeneous contribution coming from the first term

of the right-hand side of the exchange-based contribution given by Eq. (2.36) has not been taken into consideration because the objective is to evaluate the associated static DW profile. At this point, it is possible to appreciate that, compared to the FM-based scenario exposed in Eq. (2.23), the anisotropy energy contribution, $E_{\text{ani}}(\theta)$, is doubled in the AFM formalism concerning a 1D spin chain, while the exchange-governed term, E_{exc}, is fully equivalent to the previously mentioned case. Because of this, the expressions concerning the DW profile, given by Eq. (2.30), and its associated energy, expressed by Eq. (2.31), will be equally valid for the considered AFM system, except for the fact that the static spatial extent of the magnetic soliton, Δ_0, will be smaller in this case if the FM and AFM exchange parameters, $\mathcal{J}$, have the same magnitude, being given by $\Delta_0 = a_0\sqrt{|\mathcal{J}|/(2K_z)}$, which is due to the fact that the spatial distance between two atoms belonging to the same sublattice is given by $2a_0$, as it can be seen in the staggered vector-governed representation in Fig. 2.4 (b).

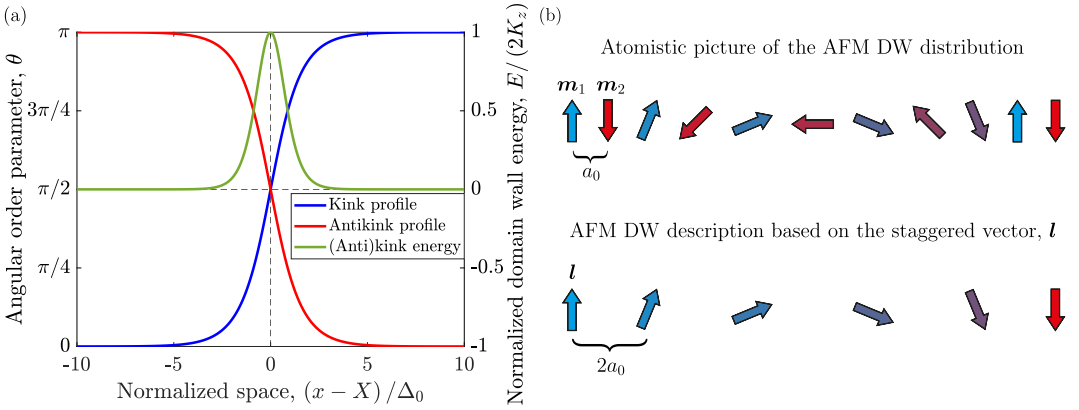

Figure 2.4: (a) Static localized kink and antikink solutions, given by Eq. (2.30), expressed through the angular order parameter, θ, and their associated normalized energies, $E/(2K_z)$, being K_z the parameter that controls the magnitude of the anisotropy-based contribution, governed by Eq. (2.31), as a function of the normalized space, $(x - X)/\Delta_0$, where X represents the DW center position and Δ_0 its spatial extent at rest. (b) Transition from an atomic magnetization vector, $\boldsymbol{m}$, description of the magnetic soliton transition in an AFM spin chain, where the separation between neighboring spins is given by the atomic spacing a_0, to a representation based on the staggered vector, $\boldsymbol{l}$, which was defined in Eq. (2.33), where the distance between magnetic moments belonging to the same sublattice is $2a_0$.

2.5 Energy-based topological protection notions

As it has been shown so far, magnetic solitons are localized smooth solutions of nonlinear field equations with an associated finite total energy. Their existence is intimately linked to the boundary conditions in spatial infinity, connecting different anisotropy-based degenerated minima of the ground state. It should be noted at this point that the magnetic texture solution exposed in Eq. (2.30) is stable because the values of the angular-based polar order parameter, θ, at their endpoints are time-independent [230, 234]. This is because the energy of non-trivial configurations has to be conserved and kept finite, and there is no way to transfer a (semi)infinite region lying on a certain ground state to another equivalent sector without applying an infinite amount of energy to the system to overcome the associated potential barrier [244, 245]. This is due to the discrete nature of the vacuum manifold, as there are

no continuous deformations that make it possible. This is the basis of their non-deformable nature, which allows classifying the different solutions by interpolating between different energy minima.

To delve into this concept, it is possible to consider the case of two consecutive anisotropy-based degenerate energy minima of the discrete vacuum manifold that enabled the stabilization of a Bloch-like DW solitonic solution, which can be denoted as θ_- and θ_+, such that they verify the condition $\theta = n\pi$, being $n \in \mathbb{Z}$. In this scenario, it is interesting to evaluate which are the four possible resulting configurations that interpolate between these two states, that is, $\theta\left(x \to \pm\infty\right) = \{\theta_-, \theta_+\}$, $\{\theta_+, \theta_-\}$, $\{\theta_-, \theta_-\}$, or $\{\theta_+, \theta_+\}$. The first two cases allow the existence of kink/antikink solutions, while the remaining ones correspond, equivalently, to the uniform ground state or to a kink-antikink pair. In this context, it is possible to take advantage of the fact that these disconnected regions cannot be distorted into each other without violating the finite energy requirement to differentiate them through topological notions [230, 233]. Contrary to the Noether's theorem framework, where there are conserved currents associated to continuous symmetries of the Lagrangian, in this context it is possible to define a time-independent topological charge linked to the symmetry of the vacuum manifold and which characterizes the non-deformability of the involved soliton-like solutions [232]. To characterize the aforementioned topological invariant, it is possible to define an associated current, j^μ, given by

$$j^\mu = \frac{1}{\pi}\,\varepsilon^{\mu\nu}\,\partial_\nu\theta, \tag{2.39}$$

where μ and ν are two dummy indices in the Einstein's summation convention, $\varepsilon^{\mu\nu}$ denotes the two-dimensional antisymmetric Levi-Civita tensor, and where the right-hand side of the previous expression has been normalized to the field-based difference between two consecutive energy minima [233, 238]. This quantity obeys a topological conservation law due to its divergenless nature due to the commutation of the mixed partial derivatives involved, and allows to define a charge, Q, locally conserved under continuous deformations of the field [246], of the form

$$Q = \frac{1}{\pi}\int_{-\infty}^{+\infty}\left(\partial_x\theta\right)\,\mathrm{d}x = \frac{1}{\pi}\left[\theta\left(x=+\infty\right) - \theta\left(x=-\infty\right)\right], \tag{2.40}$$

which depends entirely on the boundary conditions and which can only take integer values, by definition [232, 247]. Applying this equation to the case of the energy distibution governed by the uniaxial second-order easy-anisotropy contribution, it is possible to appreciate that of the four possible configurations previously exposed interpolating between the different minima of the ground state, the first two can be characterized through a non-zero topological charge, $Q = \pm 1$, while the remaining two cases have an associated trivial one, $Q = 0$. Interestingly, those field configurations that have the same topological charge can be deformed into each other as long as the necessary energy is available, and therefore they are said to be homotopic, as is the case of a kink-antikink pair and the vacuum, which reveals the additive nature of the topological charge [230]. Therefore, the importance of non-equal minima lies in the fact that, if identical, the field could be continuously deformed to a trivial constant state, while if both boundaries are different, the order parameter must be non-zero in its smooth transition between them [233, 244].

Interestingly, because the anisotropy-based potential energy term is periodic, it is possible to note that there is an infinite number of discretized minima, with which it is possible to compactify its values in $\mathbb{R}$ to a circle joining their ends, $\mathbb{S}^1$. In this

scenario, the topological charge, Q, of a given field configuration can be related to the number of times this new target space is wrapped around, which highlights the angular character of the order parameter θ, as it can be seen in Fig. 2.5 (a) for different field configurations, concept which is known as winding number [231, 248]. However, contrary to the case of ideal systems in the classical field theory framework, the anisotropy-based potential energy barrier is not infinite due to its extensive character, and, at the same time, a magnetic texture in a real finite sample can collide with the edges of the system and be annihilated. Therefore, in this context, the topologically-based protection that hinders the deformability of a magnetic texture is a concept that helps to characterize the type of soliton-like solutions and to explain why these magnetic textures do not decay in SW excitations of minimum energy of the magnetic medium, although its deep meaning differs from that existing in infinite systems in the classical field theory framework. A good way to determine, in the case of 1D DW, whether a specific magnetic soliton enjoys topological-like protection or not is to evaluate its behavior in the presence of an applied magnetic field, $\boldsymbol{H}$, as it is shown in Fig. 2.5 (b). If this external stimulus produces a null torque in the spins that live in the boundaries of the magnetic texture, which are aligned with the minimum anisotropy-based of the system, it can be said that this soliton-like solution is topologically protected, which happens, for example, for 180° DW. However, in the case of, for example, a 90° magnetic texture, it is not possible to find an application direction of the magnetic field that does not exert a torque in at least one of the homogeneously magnetized domains between which the magnetic soliton is defined, scenario in which it could be said that this type of solution is not topologically protected.

2.6 Zoology of magnetic solitons: vortices and skyrmions

2.6.1 Experimental stabilization of whirling magnetic textures

As it was previously introduced, solitons are solutions to nonlinear wave expressions which, depending on the symmetry of the vacuum manifold, can exhibit topological-like signatures that explain their potential stability. Beyond the previously introduced localized field configurations inherent to the LLG equation in the form of DW in (1+1)-dimensional spacetime, there are other classes of solitonic entities that can be accommodated in spin space. Taking into account one more spatial dimension, it is possible to highlight, in the first place, the possibility of finding stable magnetic vortex configurations, in which the magnetization curls in the film plane around a core region in which the central spin is oriented perpendicular to the easy-plane, as it is shown in Fig. 2.6 (a) [249]. Taking the case of magnetic nanodots as a reference, the magnetization field tends to line up parallel to its perimeter in order to minimize the creation of surface magnetic charges, which cannot be avoided in the central region of the system due to the out-of-plane magnetic moment created to reduce the associated exchange energy [250]. Along the same lines, it is possible to stabilize another type of topologically-protected magnetic texture known as skyrmion, mainly in bulk magnets with broken inversion symmetry and HM/FM multilayer systems [118, 251], due to, in both cases, the trade-off between the symmetric exchange and bulk or interfacial DMI [252]. For the first case, in non-centrosymmetric crystals it is possible to go from a helical spiral state to a triangular skyrmion lattice in the presence of an external magnetic field [253, 254], which prevents the implementation of this type of scheme in potential devices [255]. On the other hand, in the case of multilayered structures, it occurs when the metallic sheet presents a

large SOC, not requiring the presence of a magnetic-based external stimulus since the skyrmionic configuration is the ground state of the system [256, 257]. Other alternatives to achieve the nucleation of this type of magnetic solitons encapsulate the case of ultrathin magnetic films, based on the indirect exchange interaction of three neighboring atoms where the non-magnetic one has a large SOC [258], or on the competition between a perpendicular easy-axis anisotropy, with an applied magnetic field parallel to it, and a dipolar interaction favoring an in-plane magnetization constriction [259, 260]. A typical skyrmion spin structure consists of, for example, its central magnetic moment pointing downwards perpendicular to the film plane, rotating its magnetization distribution radially until finally pointing antiparallel to its core spin at the edge of the magnetic texture, as it is depicted in Fig. 2.6 (b) [261]. In the case of AFM, it has been possible, on the one hand, to stabilize magnetic vortices through their imprinting from a FM layer through the exchange bias effect [262, 263], and on the other hand to do it with skyrmions in layered AFM [167].

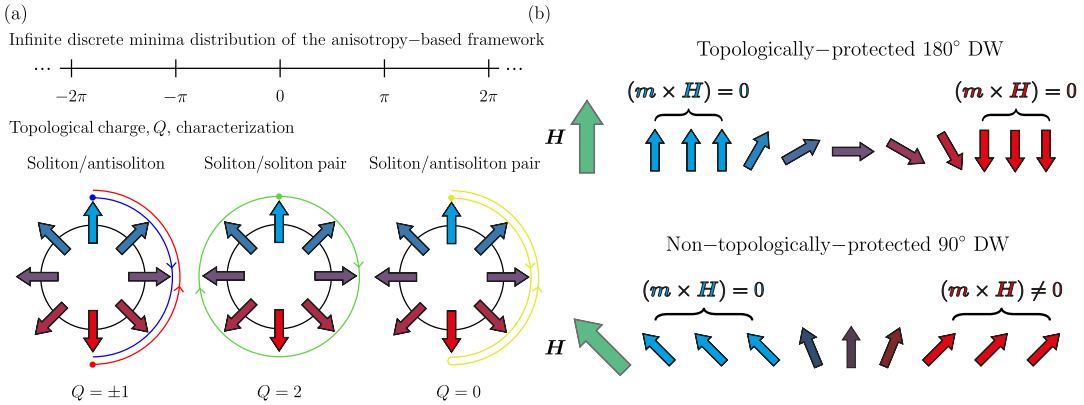

Figure 2.5: (a) Classification of different soliton-based field configurations in the anisotropy-based framework depicted in Fig. 2.3 (b), encoded by Eq. (2.23), through the notion of the number of times that the unit circle is wrapped around between energy minima to estimate the topological charge, Q, of the considered system. Adapted from [236]. (b) Precessional torque induced by an external magnetic field, $\boldsymbol{H}$, in the domains between which the magnetic textures are defined, for the cases of a topologically-protected 180° and a 90° DW whose integrity is potentially affected by the external stimulus applied parallel to one of its ends.

2.6.2 Two-dimensional topological protection-rooted characterization

To characterize the stability of these two different classes of magnetic solitons, as well as to be able to distinguish them from each other, it is possible to evaluate which is the functional form of the skyrmion topological charge, N, in the case in which the magnetization vector, $\boldsymbol{m}$, is allowed to evolve in 2D Euclidean space. Under these circumstances, this can be expressed as

$$N = \frac{1}{4\pi} \int \boldsymbol{m} \cdot \left(\frac{\partial \boldsymbol{m}}{\partial x} \times \frac{\partial \boldsymbol{m}}{\partial y} \right) \mathrm{d}x \, \mathrm{d}y, \tag{2.41}$$

which accounts for how many times the order parameter, $\boldsymbol{m}(\boldsymbol{r}) = \boldsymbol{m}(x, y)$, wraps the unit sphere S^2, being normalized to the integral of the solid angle, which guarantees that its value will be a rational number [81, 241]. To facilitate the manipulation of the previous expression, it is possible to take advantage of the radial symmetry of

the out-of-plane magnetization component along the *z-th* spatial direction to parameterize the spherical representation of the three-dimensional magnetization vector, $\boldsymbol{m}$, in terms of the polar coordinates (ρ, φ), being ρ and φ the radial and azimuthal components, respectively, so that it can be rewritten as

$$\boldsymbol{m} = \left(\cos\phi\left(\varphi\right)\,\sin\theta\left(\rho\right), \sin\phi\left(\varphi\right)\,\sin\theta\left(\rho\right), \cos\theta\left(\rho\right)\right), \tag{2.42}$$

with which the skyrmion topological charge, N, obtains a reduced functional form given by

$$N = \left[-\frac{1}{2}\,\cos\theta\left(\rho\right)\right]_{0}^{\infty}\left[\frac{1}{2\pi}\,\phi\left(\varphi\right)\right]_{0}^{2\pi} = pm, \tag{2.43}$$

where p and m represent, respectively, the polarity and vorticity of the considered 2D magnetic texture [264]. On the one hand, the polarity, p, characterizes the orientation variation of the out-of-plane magnetization component, m_z, of the considered swirling magnetic configuration between its core, $\cos\theta\left(\rho = 0\right) = \pm 1$, and its border. Interestingly, it is this parameter that accounts for the fact that the skyrmions, for which $\cos\theta\left(\rho \to \infty\right) = \pm 1$ is verified, present integer values of the topological charge , N, represented by Eq. (2.43), while the vortices, where $\cos\theta\left(\rho \to \infty\right) = 0$, have non-integer ones. On the other hand, due to the continuity of the order parameter, the azimuthal angle, φ, can only wrap the configuration space in multiples of 2π, with which the vorticity, m, can only take integer values, such that $m = 0, \pm 1, \pm 2, \ldots$ accounting for the rotation direction of the in-plane magnetization component, which allows to distinguish between different classes of vortices and skyrmions [265]. The azimuthal angles of the position vector in polar coordinates, φ, and the order parameter, ϕ, at each position are linearly related as $\phi = m\varphi + \chi$, where χ is an offset quantity which is known as helicity. Depending on the orientation of the in-plane magnetization component, the helicity, χ, can take different values, such as $\chi = 0$ when it always points in the radial direction, or $\chi = \pm 1/2$ for toroidal configurations, being a continuous parameter, unlike p and m [266]. These three parameters, polarity, p, vorticity, m, and helicity, χ, allow to categorize the different types of 2D radially symmetric magnetic solitons.

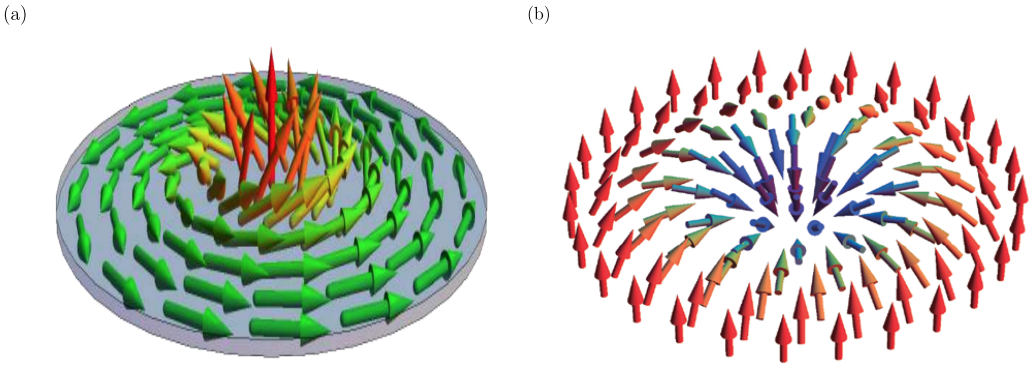

Figure 2.6: (a) Magnetic vortex distribution in which the magnetization curls parallel to the perimeter of the cylindrical structure around a core region where the central spin is oriented perpendicular to the dot plane. Extracted from [267]. (b) Skyrmion structure in which the magnetization rotates radially from its core spin, which is polarized perpendicular to the film plane, to its magnetic-based periphery. Extracted from [268].

Chapter 3

Magnetic ordering-dependent magnetic soliton dynamic behavior

3.1 Berry phase geometrical factor: a coherent states approach

3.1.1 Semiclassical treatment of the quantum-based spin eigenstates

In view of the functional form of the LLG equation, given by Eqs. (2.11) and (2.13), taking into account only its precessional character, that is, only the first term of the right-hand side of the aforementioned expressions, without the dissipative contribution, it is worth questioning which type of Lagrangian, L, would be necessary to replicate it. The path from the Hamiltonian formalism to the Lagrangian one in classical mechanics is to first identify the canonical coordinate pair of the system (given, for example, by the position, r_i, and linear momentum, p_i, of a particle) and then using the Legendre transformation, expressed as

$$L\left(r_i, \dot{r}_i\right) = p_i \dot{r}_i - H\left(r_i, p_i\right), \tag{3.1}$$

where $H\left(r_i, p_i\right)$ represents the Hamiltonian of the system, being the conjugate variables $\left(r_i, p_i\right)$ related through the Hamilton's equations of motion given by

$$\dot{r}_i = \frac{\partial H\left(r_i, p_i\right)}{\partial p_i}, \qquad p_i = -\frac{\partial H\left(r_i, p_i\right)}{\partial r_i}, \tag{3.2}$$

which allow to reexpress Eq. (3.1) solely in terms of the position, r_i, and velocity, $\dot{r}_i$, of the particle [269, 270]. However, this relationship is not straightforward for the case in which the atomic moments have been modeled as unit vectors in the description of the energetic contributions of the magnetic medium, which have been exposed in Sec. 2.2, since the associated Hamiltonian depends on the angular-based characterization of the spin orientation, given by the polar, θ, and azimuthal, ϕ, angles, which must be correlated, but it is not obvious how. To circumvent this problem, it is necessary to take into account the quantum-based nature of the spin, which can be done through the construction of states, known as spin coherent states, which result from the arbitrary rotation of the eigenstate that maximizes the projection of the expectation value of the spin angular momentum along a quantized axis until it lines up with the $\boldsymbol{m}$ direction [202]. To do this, taking the *z-th* spatial direction as the reference axis and being S and M_S the spin projection and magnetic quantum numbers, verifying that $M_S = \{-S, -S+1, \cdots, S-1, S\}$, the starting eigenstate

that will act as ground state will be given by $|S, M_S = S\rangle$, which fixes a spin component, namely $S_z |S, S\rangle = \hbar S |S, S\rangle$, the rest being given by the commutation relations exposed in Eq. (2.4) [271]. In this context, the higher the magnitude of S, the lower the associated uncertainty principle due to its strong localization, accessing a semiclassical scenario where the quantum-mechanical average of the spin operator resembles a continuously varying vector even when the three components of the spin operator cannot have the same eigenstate in common [191, 192]. The target direction of rotation on the unit sphere will be characterized by a unit vector, such that $\boldsymbol{m} = (\sin\theta\,\cos\phi, \sin\theta\,\sin\phi, \cos\theta)$, represented in Fig. 3.1 (a), whose eigenstate may be defined in terms of Euler angles, which is the usual way of parameterizing rotations in space, such that

$$|\boldsymbol{m}\rangle = e^{-\mathrm{i}S_z\theta} e^{-\mathrm{i}S_y\phi} e^{-\mathrm{i}S_z\chi} |S, S\rangle\,, \tag{3.3}$$

where θ and ϕ represent the latitude and longitude rotation angles on the unit sphere, being defined as $\theta \in [0, \pi]$ and $\phi \in [0, 2\pi]$, respectively, while the exponential term that carries the variable χ acts only as a gauge term [272, 273]. Conveniently, it is possible to rewrite the previous equation, up to a phase factor, as

$$|\boldsymbol{m}\rangle = \sum_{M_S=-S}^{M_S=+S} \binom{2S}{S+M_S}^{\frac{1}{2}} e^{-\mathrm{i}(M_S-S)\phi} \left(\cos\frac{\theta}{2}\right)^{S+M_S} \left(\sin\frac{\theta}{2}\right)^{S-M_S} |S, M_S\rangle\,, \tag{3.4}$$

which is known as Wigner's formula [185]. To corroborate that the average spin orientation is defined along the arbitrary direction given by the vector $\boldsymbol{m}$ in the unit sphere, it is enough that the expectation value associated with this state fulfills that [274, 275]

$$\langle \boldsymbol{m}|\, \boldsymbol{S}\, |\boldsymbol{m}\rangle = \hbar S\, \boldsymbol{m}, \tag{3.5}$$

$|\boldsymbol{m}\rangle$ not being an eigenstate of $\boldsymbol{S}$ [276].

On the other hand, the internal product of two such states results in

$$\langle \boldsymbol{m}'|\boldsymbol{m}\rangle = \left(\cos\frac{\theta}{2}\,\cos\frac{\theta'}{2} + \sin\frac{\theta}{2}\,\sin\frac{\theta'}{2}\,e^{\mathrm{i}(\phi-\phi')}\right)^{2S}, \tag{3.6}$$

which reveals the general non-orthogonality of these coherent states due to the commutation relations given by Eq. (2.4) between the spin components [277, 278]. From this expression, it is possible to see that when the unit vectors $\boldsymbol{m}$, $\boldsymbol{m}'$ denoting infinitesimally close eigenstates in imaginary time are antiparallel, the overlapping will be zero, reducing the quantum-based nature of the problem [239]. Moreover, it is possible to appreciate that, when $S \to \infty$, large deviations from adjacent coherent states are exponentially suppressed, which causes trajectories in imaginary time to become smooth [272, 275]. On the other hand, the previous equation can be rewritten, in the north pole parametrization for infinitesimally separated angles and $S = 1/2$, as

$$\langle \boldsymbol{m}'|\boldsymbol{m}\rangle = 1 + \mathrm{i}S\delta\phi\,(\cos\theta - 1)\,, \tag{3.7}$$

where $\delta\phi = \phi' - \phi$ [272]. Moreover, these coherent states form an overcomplete set, which can be seen through the closure relation given by

$$\int \mathrm{d}\mu\,(\boldsymbol{m})\,|\boldsymbol{m}\rangle\,\langle\boldsymbol{m}| = \mathbb{1}, \text{ being } \mathrm{d}\mu\,(\boldsymbol{m}) = \left(\frac{2S+1}{4\pi}\right)\mathrm{d}\boldsymbol{m}\;\delta\left(\boldsymbol{m}^2 - 1\right), \tag{3.8}$$

where $d\boldsymbol{m} = d(\cos\theta)\, d\phi$, being this ingredient crucial in the path integral formulation since it allows its insertion at every intermediate time interval [239, 279].

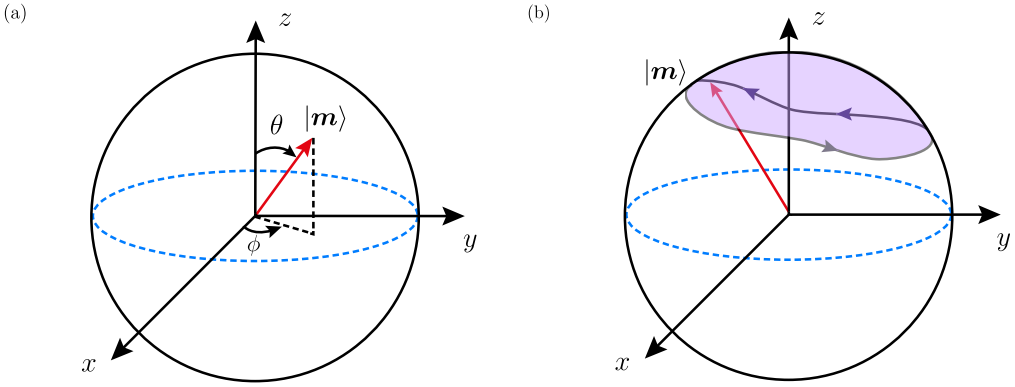

Figure 3.1: (a) Representation of a spin coherent state, $|\boldsymbol{m}\rangle$, obtainable from rotating the highest-weighted S_z eigenstate until it points in the direction dictated by the unit vector, $\boldsymbol{m}$, on the Bloch sphere definable through the polar, θ, and azimuthal, ϕ, angles. Adapted from [280]. (b) Geometric phase acquired by a single spin, characterized by the spin coherent state $|\boldsymbol{m}\rangle$, in its process of aligning adiabatically, at each time step τ_j, with an external magnetic field that evolves adiabatically until forming a closed path on the unit sphere. Adapted from [281].

3.1.2 Path integral formalism of smooth-varying spin vectors

In the Feynman's path integral formalism, the quantum mechanical amplitude can be reformulated as an equally weighted sum of all possible trajectories, where the classical action, $\mathcal{S}$, acts as the phase associated with the path [271]. Interestingly, in the classical limit this integral is dominated by the trajectories of stationary phase which minimizes the action, as expected [238]. In the spin-based case, the construction of the spin coherent states guarantees the smooth variation of their eigenstates between intermediate steps in the possible paths due to their continuous vector character [185, 282]. In statistical mechanics, the equilibrium properties of the system can be characterized through the canonical partition function, Z, which can provide information about its evolution since it can be associated with the trace of the amplitude transition between the initial and final states, which characterizes the sum over all the possible paths between them [240, 283]. In this context, it is possible to write that

$$Z = \mathrm{Tr}\left[e^{-\beta_T H[\hat{\mathcal{S}}]}\right] = \int d\mu(\boldsymbol{m}) \left\langle \boldsymbol{m}(\tau_f)\right| e^{-\beta_T H[\hat{\mathcal{S}}]} \left|\boldsymbol{m}(\tau_i)\right\rangle, \tag{3.9}$$

where β_T represents the inverse of the thermal energy, given by $\beta_T = 1/(k_B T)$, denoting k_B the Boltzmann constant and T the absolute temperature [271]. In this case, the exponential can be interpreted as an evolution operator where the inverse of T plays the role of the imaginary time, ranging from $\tau = 0$ to $\tau = \hbar\beta_T$ [274]. The partition function is defined in Euclidean space-time as a result of the Wick rotation that gives rise to sign homogeneity in the Minkowski metric and, furthermore, has as a result that Z represents the sum over amplitudes over closed path, acting as periodic boundary conditions [238, 271]. To deal with the internal product in Eq. (3.9), it is possible to divide the imaginary time interval into N slices, where the infinitesimal step is given by $\Delta\tau = \hbar\beta_T/N$. Thus, when $N \to \infty$, the exponentiated operators on consecutive time steps become commutative [278], and it is possible to

introduce the identity relation exposed in Eq. (3.8) between every intermediate time step. Using the Trotter formula [239], Eq. (3.9) can be rewritten as

$$Z = \lim_{N\to\infty} \left(\prod_{j=0}^{N-1} \int \mathrm{d}\mu \left(\boldsymbol{m}_j \right) \right) \left(\prod_{j=0}^{N-1} \left\langle \boldsymbol{m} \left(\tau_j \right) \right| e^{-\Delta\tau H\left[\hat{\boldsymbol{S}} \right]/\hbar} \left| \boldsymbol{m} \left(\tau_{j+1} \right) \right\rangle \right). \tag{3.10}$$

Taking advantage of the fact that $\Delta\tau$ is small by definition, it is possible to perform a time-based Taylor series expansion up to first order due to the smooth time-dependent variation of the spin's trajectory, obtaining a more manageable expression given by

$$Z \simeq \lim_{N\to\infty} \left(\prod_{j=0}^{N-1} \int \mathrm{d}\mu \left(\boldsymbol{m}_j \right) \right) \left(\prod_{j=0}^{N-1} \left\langle \boldsymbol{m} \left(\tau_j \right) \right| \left(1 - \Delta\tau H \left[\hat{\boldsymbol{S}} \right] / \hbar \right) \left| \boldsymbol{m} \left(\tau_{j+1} \right) \right\rangle \right), \tag{3.11}$$

where the inner products of different operators of the originally exponential function are involved. To deal with this, it is possible to realize that, according to the variational theorem, the "classical" Hamiltonian can be characterized, in accordance with Eq. (3.5) [202], as

$$\frac{\left\langle \boldsymbol{m} \left(\tau_{j+1} \right) \right| H \left[\hat{\boldsymbol{S}} \right] \left| \boldsymbol{m} \left(\tau_j \right) \right\rangle}{\left\langle \boldsymbol{m} \left(\tau_{j+1} \right) \middle| \boldsymbol{m} \left(\tau_j \right) \right\rangle} \simeq H \left[\hbar S \, \boldsymbol{m} \left(\tau_j \right) \right] + \mathcal{O} \left(\Delta\tau \right), \tag{3.12}$$

where terms proportional to the time difference given by $\Delta\tau$ have not been made explicit to work up to first order in the original exponential expansion. With these ingredients, it is possible to rewrite Eq. (3.11) as [202, 271, 274]

$$Z = \oint_{\boldsymbol{m}(0)=\boldsymbol{m}(\hbar\beta_T)} \mathcal{D}\,\boldsymbol{m} \; e^{-\mathcal{S}_{\mathrm{E}}[\boldsymbol{m}]/\hbar}, \tag{3.13}$$

where the measure, $\mathcal{D}\,\boldsymbol{m}$, for paths on a unit sphere [239], has been defined as

$$\mathcal{D}\,\boldsymbol{m} = \lim_{N\to\infty} \prod_{j=0}^{N-1} \mathrm{d}\mu \left(\boldsymbol{m} \right), \tag{3.14}$$

and the Euclidean action, $\mathcal{S}_{\mathrm{E}}\left[\boldsymbol{m} \right]$, is given by

$$\mathcal{S}_{\mathrm{E}}\left[\boldsymbol{m} \right] = \int_0^{\hbar\beta_T} \mathrm{d}\tau \left\{ \mathrm{i}\hbar S \left(\partial_\tau \phi \right) \left(1 - \cos\theta \left(\tau \right) \right) + H \left[\hbar S \boldsymbol{m} \left(\tau \right) \right] \right\}, \tag{3.15}$$

where the first term is known as Wess-Zumino or Berry phase [284], which is imaginary regardless of whether it is considered in Euclidean or Minkowski space-time, this being a quality of a topological term [273], while the second one represents the usual potential energy contributions, as those collected in Sec. 2.2. The kinetic contribution, which is the result of the non-orthogonality between adjacent eigenstates, describes the phase acquired by a spin in its process of aligning itself adiabatically with a rotating magnetic field parallel to $\boldsymbol{m}\left(\tau_j \right)$ at each time step [202], represented in Fig. 3.1 (b) in the case of a closed path on the unit sphere. Moreover, its origin is geometric, since it depends on the traced path on the unit sphere, representing the area enclosed in its trajectory, being independent of an hypothetical explicit time dependency [274]. In this framework, in line with Eq. (3.1), it is possible to see from Eq. (3.15) that the angular coordinate ϕ has a corresponding canonical momentum, p_ϕ, given by $p_\phi = \hbar S \left(1 - \cos\theta \right)$, which makes it possible to replicate the LLG equation,

given by Eqs. (2.11) and (2.13), without the dissipative term of its right-hand sides [285]. Performing a Wick rotation that allows one to return to the real-valued time formalism, t, through the expression $t = -\mathrm{i}\tau$, the Minkowskian action, S_{M}, will be given by $\mathrm{i}\mathcal{S}_{\mathrm{M}} = -\mathcal{S}_{\mathrm{E}}$, which implies that the Lagrangian of the system, L, will be given by

$$L = \frac{\mu_0 \mu_{\mathrm{s}}}{\gamma} \left(\cos\theta - 1\right) \dot{\phi} + E, \tag{3.16}$$

where it has been taken into account that, for $S = 1/2$, it is possible to find that $S\hbar = \mu_0 \mu_{\mathrm{s}}/\gamma$, given the atomic magnetic moment, μ_{s}, in this case, by $\mu_{\mathrm{s}} = \mu_{\mathrm{B}}$.

3.2 Walker breakdown for propagating ferromagnetic domain walls

3.2.1 Steady-state magnetic texture translation below critical stimulus

3.2.1.1 Lagrangian dissipative formalism for biaxial ferromagnets

As a natural extension of the static DW scenario exposed for the case of a FM spin chain in Secs. 2.4.2.1 and 2.4.2.2, it is possible to explore the dynamic behavior of the magnetic texture in the presence of an external magnetic field, $\boldsymbol{H}$. Previously, in Eqs. (2.21) and (2.23), only the FM exchange-based interaction between neighboring spins along the *x-th* axis, characterized by the parameter $\mathcal{J}$, and the uniaxial second-order easy-axis anisotropy contribution along the *z-th* spatial direction, encoded by the constant K_z, were considered. Additionally, the existence of an additional uniaxial second-order hard-axis anisotropy term along the *x-th* axis, represented by the K_x parameter, can be taken into account. This will guarantee the constriction of the magnetization in the yz plane, supporting the assumption made in Sec. 2.4.2.1 to minimize the impact of magnetostatic contribution, which causes the redefinition of the anisotropy energy, E_{ani}, such that $E_{\mathrm{ani}} = -K_z \left(\boldsymbol{m} \cdot \hat{\boldsymbol{z}}\right)^2 + |K_x| \left(\boldsymbol{m} \cdot \hat{\boldsymbol{x}}\right)^2$. It is important to note that this anisotropy-based addition to the energy of the system, E, has no impact on the plane where the magnetization rotates between the two consecutive energy minima, so it will not affect the static properties of the magnetic texture. Therefore, the functional form of the DW profile, given by the angular order parameter, θ, through Eq. (2.30), as well as its width at rest, Δ_0, remain unchanged. On the other hand, if the external magnetic field, $\boldsymbol{H}$, is assumed to be applied along the *z-th* spatial direction, $\boldsymbol{H} = H\,\hat{\boldsymbol{z}}$, it will not exert any type of torque on the spins that make up the domain boundaries of the magnetic soliton, as it can be seen in Fig. 2.5 (b), but it will cause potential tiltings of the inhomogeneous magnetization transition from the yz plane, described by the azimuthal angle, ϕ. In this scenario, the Lagrangian, L, of the system can be expressed, taking into account the parameterization of the magnetization vector, $\boldsymbol{m}$, in spherical coordinates [215, 286], given by Eq. (2.22), and the Zeeman-like representation of the external stimulus-based energy, E_{Zee}, encoded by Eq. (2.10), as

$$L = \frac{\mu_0 \mu_{\mathrm{s}}}{\gamma} \cos\theta\, \dot{\phi} + \mathcal{J} a_0^2 \left(\partial_x^2 \theta\right) + \left(K_z + |K_x| \sin^2\phi\right) \sin^2\theta - \mu_0 \mu_{\mathrm{s}} H \cos\theta, \tag{3.17}$$

in accordance with what was stated in Eq. (3.16), where it must be taken into account that, unlike the parameterization in spherical coordinates used in Sec. 3.1 for the unit magnetic moment, $\boldsymbol{m}$, the more physical one given by Eq. (2.22) has been used in this case. Furthermore, to characterize the dynamic evolution of a magnetic

texture propagating in a dissipative medium, it is necessary to take into account the associated friction-based energy losses in the magnetic medium. With this objective in mind, it is possible to take into account the representation in spherical coordinates of the Rayleigh dissipation function, R, given by Eq. (2.18) in its vector form [212, 213], obtained through the parameterization of the magnetization encoded by Eq. (2.22), which results in

$$R = \frac{\alpha \mu_0 \mu_s}{2\gamma} \left(\dot{\theta}^2 + \sin^2 \theta \, \dot{\phi}^2 \right). \tag{3.18}$$

3.2.1.2 Rigid profile-based collective coordinates formulation

To facilitate the analytical treatment of the dynamic DW behavior, it is convenient to work on the collective coordinates framework, in which the center position, X, of the magnetic soliton and the tilting azimuthal-based angle, ϕ, play the role of the generalized coordinates of the system [287, 288]. To this end, it is possible to extrapolate the static Walker-like rigid profile of the magnetic texture, characterized by the angular order parameter, θ, through Eq. (2.30), to a time-dependent scenario in which the aforementioned coordinates, $(X(t), \phi(t))$, are far from their values at rest. In this line, substituting the dynamically-based Eq. (2.30) in the different polar angle-dependent terms of Eqs. (3.17) and (3.18), it is possible to find that

$$\cos\theta = -\tanh \frac{x - X}{\Delta}, \qquad \sin\theta = \operatorname{sech} \frac{x - X}{\Delta}, \tag{3.19}$$

$$(\partial_x \theta) = \frac{1}{\Delta} \operatorname{sech} \frac{x - X}{\Delta}, \qquad \dot{\theta} = -\frac{(x - X)\dot{\Delta} + \Delta \dot{X}}{\Delta^2} \operatorname{sech} \frac{x - X}{\Delta}, \tag{3.20}$$

expressions which allow one to rewrite the Lagrangian, L, and Rayleigh dissipation function, R, as a function of the new pair of generalized terms, giving rise to

$$L = \frac{\mu_0 \mu_s}{\gamma} (\gamma H - \dot{\phi}) \tanh \frac{x - X}{\Delta} + \left(\frac{\mathcal{J} a_0^2}{\Delta^2} + K_z + |K_x| \sin^2 \phi \right) \operatorname{sech}^2 \frac{x - X}{\Delta}, \tag{3.21}$$

$$R = \frac{\alpha \mu_0 \mu_s}{2\gamma} \left[\left(\frac{(x - X)\dot{\Delta} + \Delta \dot{X}}{\Delta^2} \right)^2 + \dot{\phi}^2 \right] \operatorname{sech}^2 \frac{x - X}{\Delta}, \tag{3.22}$$

which are given in terms of trigonometric functions. In order to obtain a manageable set of coupled first-order differential equations, it is convenient to obtain the net contribution of the preceding expressions through their spatial integration along the x-*th* spatial direction of the 1D spin chain. In this sense, it is possible to find, in the first instance, that [289]

$$\int_{-\infty}^{+\infty} \operatorname{sech}^2 \frac{x - X}{\Delta} \, dx = 2\Delta, \qquad \int_{-\infty}^{+\infty} \tanh \frac{x - X}{\Delta} \, dx = 2X, \tag{3.23}$$

$$\int_{-\infty}^{+\infty} \frac{x - X}{\Delta} \operatorname{sech}^2 \frac{x - X}{\Delta} \, dx = 0, \quad \int_{-\infty}^{+\infty} \left(\frac{x - X}{\Delta} \right)^2 \operatorname{sech}^2 \frac{x - X}{\Delta} \, dx = \frac{\pi^2 \Delta}{6}, \tag{3.24}$$

from which the spatially-integrated Lagrangian, $\mathcal{L}$, and Rayleigh dissipation function, $\mathcal{R}$, can be obtained through Eqs. (3.21) and (3.22) [205, 215], being given by

$$\mathcal{L} = \frac{2\mu_0\mu_s X}{\gamma}\left(\gamma H - \dot{\phi}\right) + 2\left[\frac{\mathcal{J}a_0^2}{\Delta} + \Delta\left(K_z + |K_x|\sin^2\phi\right)\right], \tag{3.25}$$

$$\mathcal{R} = \frac{\alpha\mu_0\mu_s}{\gamma}\left(\frac{\pi^2\dot{\Delta}^2}{12\Delta} + \frac{\dot{X}^2}{\Delta} + \Delta\dot{\phi}^2\right). \tag{3.26}$$

Through the variational principle in the context of the EL formalism, in combination with the friction-like processes characterized by the Rayleigh dissipation function, $\mathcal{R}$, defined as

$$\frac{\partial\mathcal{L}}{\partial\xi} - \frac{\mathrm{d}}{\mathrm{d}t}\left(\frac{\partial\mathcal{L}}{\partial\dot{\xi}}\right) = -\frac{\partial\mathcal{R}}{\partial\dot{\xi}}, \tag{3.27}$$

it is possible to find the equations of motion of the system taking into account Eqs. (3.25) and (3.26), which will be given by

$$\frac{\dot{X}}{\Delta} - \alpha\dot{\phi} = \frac{\gamma H_K}{2}\sin 2\phi, \tag{3.28}$$

$$\frac{\alpha\dot{X}}{\Delta} + \dot{\phi} = \gamma H, \tag{3.29}$$

$$\dot{\Delta} = \frac{12\gamma}{\alpha\mu_0\mu_s\pi^2}\left[\frac{\mathcal{J}a_0^2}{\Delta} - \left(K_z + |K_x|\sin^2\phi\right)\Delta\right], \tag{3.30}$$

where the hard-axis-based anisotropy field, $H_K = 2|K_x|/\left(\mu_0\mu_s\right)$, has been introduced [290, 291]. It should be noted that, in the static scenario, in which there are no potential tiltings the from easy-plane in the absence of an applied magnetic field, H, the hard-axis anisotropy contribution, encoded by the $|K_x|$, has no impact on the first-order differential equations concerning the DW center position, X, and width, Δ, as it might be expected. On the other hand, it is plausible to rewrite these two expressions, given by Eqs. (3.28) and (3.29), as

$$\dot{X} = \frac{\gamma\Delta}{(1+\alpha^2)}\left(\alpha H + \frac{H_K}{2}\sin 2\phi\right), \tag{3.31}$$

$$\dot{\phi} = \frac{\gamma}{(1+\alpha^2)}\left(H - \frac{\alpha H_K}{2}\sin 2\phi\right), \tag{3.32}$$

which can be decoupled for quasistatic dynamic scenarios in which there are negligible deviations from the DW yz-based plane at rest, characterized by the azimuthal angle, ϕ, which would be accompanied by small variations of the spatial extension of the magnetic soliton, Δ, with respect to its value at rest, Δ_0. In this context, for low magnitudes of the applied magnetic field, H, it is possible to linearize the involved trigonometric functions in Eqs. (3.31) and (3.32) to obtain a Newton-like second-order differential equation for the center position, X, of the magnetic texture, given by

$$\ddot{X} + \frac{\alpha\gamma H_K}{1+\alpha^2}\dot{X} - \frac{\gamma^2\Delta_0 H_K H}{1+\alpha^2} = 0, \tag{3.33}$$

that reveals the inherent inertial signatures experienced by a dynamic DW in a FM medium, highlighting, at the same time, its pseudoparticle behavior [215, 292]. Similarly, the same can be done with the remaining generalized coordinate, given by the azimuthal angle, ϕ, being possible to find that its associated dynamic magnetic soliton mass is greater than the one existing in the previous expression for its center

position, X. This is the reason why a formalism based on Eq. (3.33) is appropriate to describe a system with weak pinning effects, being necessary to transition to an azimuthal angle-based formalism if these contributions become stronger [293].

Concerning the dynamic evolution of the spatial extension of the magnetic texture, Δ, given by Eq. (3.30), it is possible to appreciate that this parameter relaxes, in a precession-free regime governed by the azimuthal angle, ϕ, towards an equilibrium value, Δ^*, given by

$$\Delta^*(\phi) = \frac{\Delta_0}{\sqrt{1+\lambda \sin^2 \phi}}, \tag{3.34}$$

where it can be seen that the DW width, Δ^*, is a time-dependent parameter due to its dependence on the azimuthal angle, $\phi(t)$, where λ is a dimensionless constant given by the hard-axis to easy-axis anisotropy ratio $\lambda = |K_x|/K_z$ [91, 294]. In the dynamic scenario in which there are no sizable azimuthal angle-dominated tiltings from the easy-plane at rest of the magnetic soliton, the magnetic texture will propagate in a precession-free steady-state regime, as it is depicted in Fig. 3.2 (a), according to Eq. (3.31), where the velocity, $\dot{X} = v$, is characterized by

$$v = \frac{\gamma \Delta}{1+\alpha^2}\left(\alpha H + \frac{H_K}{2}\sin 2\phi^*\right), \tag{3.35}$$

where it is verified that $\dot{\phi} = 0$. This situation is verified as long as the anisotropy field-based contribution, governed by H_K, is capable of compensating the action of the external stimulus, H, a condition which is characterized as

$$\sin 2\phi^* = \frac{H}{H_W}, \tag{3.36}$$

which is fulfilled whenever $|H| \leq H_W$, where H_W represents the so-called Walker field, which is defined as $H_W = \alpha H_K/2$, being given the limiting azimuthal angle-based tilting from the DW plane at rest allowed to remain in the steady-state regime by $\phi = \pi/4$ [91, 215]. Interestingly, the velocity, v, of the magnetic soliton in the aforementioned low field-governed translational stationary tendency can be rewritten through the combination of Eqs. (3.35) and (3.36), being possible to express it through

$$v = \frac{\gamma \Delta^*(\phi^*) H}{\alpha}, \tag{3.37}$$

functional form in which it can be interpreted that during the uniform magnetic texture motion, for a certain applied magnetic field, H, there is a constant energy dissipation rate of the Zeeman-like contribution governed by the Gilbert damping parameter, α [205, 295, 296]. Since the speed, v, is inversely proportional to α, it can be deduced that the smaller the damping parameter, the larger the deviation azimuthal angle, ϕ, from the static DW plane at rest has to be for a given magnitude of the external stimulus, H, according to Eq. (3.36), to compensate its effect to remain in the steady-state regimen [237].

3.2.1.3 Hard-axis anisotropy-enabled maximum stationary velocity

Interestingly, if the expression for the equilibrium DW width, Δ^*, in the stationary dynamic regime, given by Eq. (3.34), is substituted into the steady-state velocity

equation, v, denoted by Eq. (3.37), it is possible to find that

$$v = \frac{\gamma \Delta_0 H_W h}{\alpha \sqrt{1 + \lambda \left(1 - \sqrt{1 - h^2}\right)/2}}, \tag{3.38}$$

where the normalized applied magnetic field is denoted as $h = H/H_W$, and where the functional form of the azimuthal angle in the rigid regime, ϕ^*, given by Eq. (3.36), has been used. It should be noted that, in this case, the relationship between the speed, v, of the magnetic texture and the external stimulus, H, is now strongly nonlinear due to the nature of Eq. (3.36). To find the maximum velocity, v_{max}, that the DW can reach below the Walker field [297], it is necessary to find the associated reduced field, h_{max}, for which the previous expression reaches a stationary point through its derivative with respect to h, which gives rise to

$$h_{max} = \frac{2(1+\lambda)^{1/4}\left(\sqrt{1+\lambda} - 1\right)}{\lambda}, \tag{3.39}$$

equation which allows to obtain

$$v_{max} = \frac{\gamma \Delta_0 H_K \left(\sqrt{1+\lambda} - 1\right)}{\lambda}, \tag{3.40}$$

from which it can be inferred that, the greater the dimensionless anisotropy-based parameter λ, the smaller the needed magnitude of the external stimulus, H, to reach the maximum velocity obtainable in the rigid dynamic regime, as it can be seen in Fig. 3.2 (a). For the case in which the applied magnetic field reaches the Walker field value, $H = H_W$, it is possible to find that Eq. (3.37) can be reexpressed to obtain the so-called Walker velocity, v_W, which is given by

$$v_W = \frac{\gamma \Delta_0 H_K}{\sqrt{2(2+\lambda)}}, \tag{3.41}$$

equation which is independent of the Gilbert damping parameter, α [91, 241]. It is remarkable to note that, if this expression is compared with the maximum attainable DW speed, v_{max}, given by Eq. (3.40), giving rise to

$$\frac{v_{max}}{v_W} = \frac{\left(\sqrt{1+\lambda} - 1\right)\sqrt{2(2+\lambda)}}{\lambda}. \tag{3.42}$$

3.2.2 Abrupt transition to an unstable magnetic soliton propagation trend

3.2.2.1 External stimulus-induced oscillatory to steady kinematics transition

If the applied magnetic field, H, exceeds the Walker field, H_W, the dissipation mechanism governed by the Gilbert damping constant, α, is no longer capable of compensating for the torque exerted by the external stimulus to keep the tilting from the DW plane at rest below the azimuthal angle-based critical value given by $\phi = \pi/4$, as dictated by Eq. (3.36). In this scenario, the system enters a new dynamic regime in which the magnetization, $\boldsymbol{m}$, will undertake a time-dependent precession process, which is nonlinear due to the anisotropy-based contribution governed by the uniaxial easy-axis parameter K_z in Eq. (3.32) [205, 237]. This has as a consequence that

both, the time evolution of the center position, X, of the magnetic soliton and the azimuthal angle, ϕ, given, respectively, by Eqs. (3.31) and (3.32), must be taken into consideration to describe the dynamic behavior of the magnetic texture, contrary to the case exposed in the rigid translational mechanism described by Eq. (3.37). In this new propagation regime, where the stable DW dynamics are abruptly interrupted, which is known as WB, a sharp decrease in the speed, v, of the magnetic soliton takes place, as it is shown in Fig. 3.2 (a), while its spatial extension, Δ, which in the steady-state process decreased as the applied magnetic field, H, increased, it will now begin to periodically expand and contract [298, 299], being its mean value depicted in Fig. 3.2 (b). Interestingly, the precession period, T, of the magnetization can be obtained through the dynamic equation for the azimuthal angle, ϕ, given by Eq. (3.32), which will be characterized as

$$T = \frac{\pi\left(1+\alpha^2\right)}{\gamma H_{\mathrm{W}}\sqrt{h^2-1}}, \tag{3.43}$$

where it must be taken into account that tangent trigonometric function that appears during the time integration process of Eq. (3.32) has period π. The averaged velocity of the magnetic texture over an oscillation period, T, can be obtained from Eq. (3.29) taking into account that, in this case, the DW width, Δ, is not constant, which results in

$$\left\langle \frac{\dot{q}}{\Delta} \right\rangle = \frac{\gamma H_{\mathrm{W}}}{\alpha\left(1+\alpha^2\right)}\left[h\left(1+\alpha^2\right)-\sqrt{h^2-1}\right], \tag{3.44}$$

expression that implicitly contains the variation of the spatial extension of the magnetic soliton [215, 300]. On the other hand, in the limit $H \gg H_{\mathrm{W}}$, the averaged DW velocity again becomes linearly dependent on the applied magnetic field, H, as in Eq. (3.37), because in the dynamic expression for the azimuthal angle, ϕ, given by Eq. (3.32) the periodic torque term present in the second term of its right-hand side becomes negligible. Under these circumstances, the dominant contribution to the net speed, v, of the magnetic soliton, which is described by Eq. (3.31), will be the torque related to the damping parameter, α, which corresponds to the first term of its right-hand side, with which it can be asserted that

$$v = \frac{\alpha\gamma\Delta H}{1+\alpha^2}, \tag{3.45}$$

whereupon a steady-state regime is recovered in this limiting case [91, 215].

3.2.2.2 Field- and anisotropy-governed torque competition in the precessional regime

To achieve a deeper insight into the different dynamical regimes experienced by a DW in a biaxial FM under the action of an applied magnetic field, $\boldsymbol{H}$, along the *z-th* spatial direction, $\boldsymbol{H} = H\,\hat{\boldsymbol{z}}$, it is possible to perform a torque-based analysis based on the LLG equation governed by Eq. (2.11), which it is developed in Fig. 3.3 (a). Initially, all the spins that make up the inhomogeneous transition of the magnetic soliton between its two domain boundaries aligned along the *z-th* axis will experience a precessional, $\boldsymbol{\tau}_{\mathrm{p}}^{\mathrm{a}}$, torque characterized by $\boldsymbol{\tau}_{\mathrm{p}}^{\mathrm{a}} = \gamma H \sin\theta\,\hat{\boldsymbol{\phi}}$, where it has been taken into account that $\boldsymbol{m} = \hat{\boldsymbol{r}}$, being defined by Eq. (2.22). This contribution, which will predominate over the damping one, given by $\boldsymbol{\tau}_{\mathrm{d}}^{\mathrm{a}} = -\alpha\gamma H \sin\theta\,\hat{\boldsymbol{\theta}}$, due to the order of magnitude of the Gilbert damping parameter, α, causes an azimuthal precession around the direction of application of the external stimulus, $\boldsymbol{H}$ [237]. Referring from now on to the case of the central spin of the magnetic texture, which is initially

aligned along the *y-th* spatial direction, $\boldsymbol{m} = \hat{\boldsymbol{y}}$, as it is illustrated in Fig. 2.2 (a), the applied magnetic field will cause its related torques to be given by $\boldsymbol{\tau}_{\mathrm{p}}^{\mathrm{a}} = -\gamma H\, \hat{\boldsymbol{x}}$ and $\boldsymbol{\tau}_{\mathrm{d}}^{\mathrm{a}} = -\alpha\gamma H\, \hat{\boldsymbol{z}}$. Due to the magnetization tilting caused by the external stimulus from the DW plane at rest, characterized by a non-null azimuthal angle, ϕ, in an evolving counter-clockwise fashion, the appearance of a volumetric magnetic charge-based contribution will take place, which the system will want to minimize by realigning the referenced central spin again along the *y-th* axis. In the same line, the uniaxial second-order hard-axis anisotropy, encoded by the $|K_x|$ parameter, will act in the same way as the emergent demagnetizing term, whereby both effects can be reabsorbed through the anisotropy-based restoring field, $\boldsymbol{H}_K$, given by $\boldsymbol{H}_K = H_K\, \hat{\boldsymbol{x}}$, from now on. Thus, in the rigid translational regime, being now given the magnetization vector, $\boldsymbol{m}$, associated to the central spin by $\boldsymbol{m} \propto -\hat{\boldsymbol{x}} + \hat{\boldsymbol{y}}$, the torques associated with the anisotropy contribution can be characterized as $\boldsymbol{\tau}_{\mathrm{p}}^{K} \propto \gamma H_K\, \hat{\boldsymbol{z}}$ and $\boldsymbol{\tau}_{\mathrm{d}}^{K} \propto \alpha\gamma H_K\, (\hat{\boldsymbol{x}} + \hat{\boldsymbol{y}})$. On the other hand, the torque terms associated with the external stimulus, $\boldsymbol{H}$, in this tilted scenario will be denoted by $\boldsymbol{\tau}_{\mathrm{p}}^{a} \propto -\gamma H\, (\hat{\boldsymbol{x}} + \hat{\boldsymbol{y}})$ and $\boldsymbol{\tau}_{\mathrm{d}}^{a} \propto 2\alpha\gamma H\, \hat{\boldsymbol{z}}$.

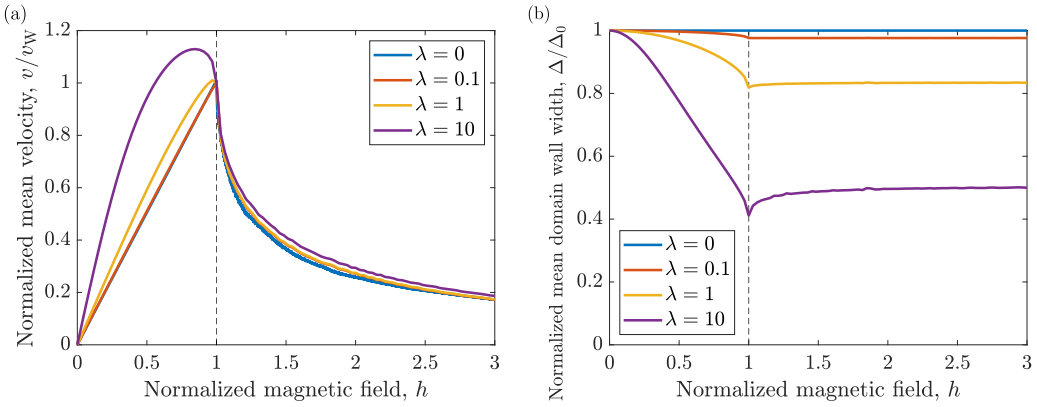

Figure 3.2: (a) Numerically-obtained mean speed, v, of a FM magnetic texture, normalized to the Walker velocity, v_{W}, defined by Eq. (3.41), as a function of the normalized magnetic field, h, for different values of the dimensionless anisotropy-based parameter, λ, obtained through the simultaneous resolution of Eqs. (3.28), (3.29), and (3.30). (b) Numerically-calculated mean DW width, Δ, normalized to its rest value, Δ_0, as a function of the speed, v, of the FM magnetic soliton divided by the Walker velocity, v_{W}, defined by Eq. (3.41), for different values of the dimensionless anisotropy-based parameter, λ, obtained through the simultaneous resolution of Eqs. (3.28), (3.29), and (3.30).

As it can be seen, there is a competition between the applied magnetic field-induced precessional, $\boldsymbol{\tau}_{\mathrm{p}}^{\mathrm{a}}$, and the hard-axis anisotropy-based damping, $\boldsymbol{\tau}_{\mathrm{d}}^{K}$, torques which can be glimpsed in the presence of the two terms, of opposite sign, in the right-hand side of Eq. (3.32) [205]. In fact, if the precessional and damping terms are made explicit all together in the LLG equation, given by Eq. (2.11), for the central DW spin characterized by a polar angle given by $\theta = \pi/2$, it can be found that

$$\dot{\boldsymbol{m}} = \gamma \left(\alpha H + \frac{H_K}{2} \sin 2\phi \right) \hat{\boldsymbol{z}} + \gamma \left(H - \frac{\alpha H_K}{2} \sin 2\phi \right) \hat{\boldsymbol{\phi}}, \tag{3.46}$$

where the first term of the right-hand side has a functional form equivalent to that stated in Eq. (3.31), while the second contribution is reminiscent of Eq. (3.32). This

implies that the steady-state regime below the Walker field, H_{W}, is dominated by a time-dependent magnetization vector, $\dot{\boldsymbol{m}}$, with a constant azimuthal angle, ϕ, being only given by its *z-th* component [237]. If the precessional contribution related to the external stimulus, H, exceeds the maximum strength of the damping-based hard-axis anisotropy one, characterized by the Walker field, H_{W}, the system will enter a oscillatory dynamic regime known as WB. This propagation trend of the magnetic soliton is non-uniform because the torque terms that control the motion of the magnetic texture, $\boldsymbol{\tau}_{\mathrm{p}}^{\mathrm{a}}$ and $\boldsymbol{\tau}_{\mathrm{d}}^{K}$, which are implicitly included in the *z-th* component of the magnetization variation, $\dot{\boldsymbol{m}}$, characterized by Eq. (3.46), see how their contributions vary their relative collinear arrangement in the different quadrants of the xy plane, which is due to the involved sine trigonometric function. Because of this, the azimuthal angle-based precession rate, $\dot{\phi}$, is not constant over time, and the DW rotation is slower in quadrants I and II, where the hard-axis anisotropy-governed damping torque, $\boldsymbol{\tau}_{\mathrm{d}}^{K}$, is opposed to the applied magnetic field-induced precessional torque, $\boldsymbol{\tau}_{\mathrm{p}}^{\mathrm{a}}$ [205].

3.3 Stable relativistic antiferromagnetic domain walls dynamics

3.3.1 Configurational energy in two sublattice antiferromagnetic spin chains

In the same way that it was done with the case of the 1D FM spin chain in Sec. 3.2, it is plausible to analyze the dynamic behavior of an AFM DW in the presence of an external magnetic field, $\boldsymbol{H}$, using, for this, the static scenario exposed in Sec. 2.4.3 for the case of a 1D spin chain. Previously, in Eq. (2.37), it was considered the situation in which there was only a uniaxial second-order easy-axis anisotropy contribution, encoded by the parameter K_z, along the *z-th* spatial direction. In this case, in accordance with what was stated for biaxial FM in Sec. 3.2, the existence of an additional anisotropic term will be taken into account, which consists of a uniaxial second-order hard-axis anisotropy defined along the *x-th* axis, being characterized by the constant $|K_x|$. In this way, the anisotropy-based energy contribution, E_{ani}, will be given, through an extrapolation of Eq. (2.37), by $E_{\mathrm{ani}} = -2K_z\left(\boldsymbol{l}\cdot\hat{\boldsymbol{z}}\right)^2 + 2|K_x|\left(\boldsymbol{l}\cdot\hat{\boldsymbol{x}}\right)^2$, in the exchange limit framework [144, 243]. As a result of this, the magnetization, $\boldsymbol{m}$, will be constrained in the yz plane, although in this case, as opposed to its FM counterpart, potential deviations of the unit atomic magnetic moment from the plane at rest of the magnetic soliton do not result in the appearance of sizable unwanted magnetostatic contributions. This is due to the antiparallel arrangement of neighboring spins promoted by the AFM exchange interaction, being encoded through the parameter $|\mathcal{J}|$, which represents the dominant term in the system. If the 1D AFM spin chain is subjected to the action of a non-staggered magnetic field, $\boldsymbol{H}$, applied along the *z-th* spatial direction, $\boldsymbol{H} = H\,\hat{\boldsymbol{z}}$, not only its torque associated with the spins that make up the boundaries of the DW, which are collinear to the external stimuli, will be zero, but its effect will be almost negligible for moderate magnitudes in the inhomogeneous magnetization transition due to the effect of mutual partial cancellation between neighboring spins. To characterize the related Zeeman-like energy contribution, E_{Zee}, through the sum of its impact on each magnetic sublattice, according to Eq. (2.10), it is necessary to take into account the definition of the AFM vectors, $\boldsymbol{n}$ and $\boldsymbol{l}$, given by Eqs. (2.33) and (2.34), which allows one to express this term as

$$E_{\mathrm{Zee}} = -\mu_0\mu_{\mathrm{s}}\left[\left(\boldsymbol{m}_1\cdot\boldsymbol{H}\right) + \left(\boldsymbol{m}_2\cdot\boldsymbol{H}\right)\right] = -\gamma\hbar\left(\boldsymbol{n}\cdot\boldsymbol{H}\right), \tag{3.47}$$

which depends solely on the non-staggered AFM vector, $\boldsymbol{n}$ [135, 136]. In this line, taking into account the anisotropy-based, E_{ani}, and exchange-dependent, E_{exc}, energy terms, the latter being made explicit by Eq. (2.36), it is possible to write the configurational energy, E, of the system, which will be given by

$$E = \frac{1}{2}\, A\, \boldsymbol{n}^2 + \frac{1}{8}\, a\, (\partial_x \boldsymbol{l})^2 + E_{\text{ani}}\,(\boldsymbol{l}) - \gamma\hbar\ (\boldsymbol{n}\cdot\boldsymbol{H})\,, \tag{3.48}$$

where, as it was defined in Sec. 2.4.3, the AFM homogeneous, A, and inhomogeneous, a, exchange parameters are defined, respectively, by $A = 8|J|$ and $a = 8|J|\, a_0^2$ [241].

3.3.2 Lorentz-invariant equation of motion for non-staggered fields

To characterize the dynamic response of the system under the action of the applied magnetic field, $\boldsymbol{H}$, it is pertinent to introduce the AFM version of the LLG equation, which is given by Eqs. (2.11) and (2.13) for the case of a single spin or a FM medium, to characterize the time evolution of the total magnetization, $\boldsymbol{n}$, and staggered, $\boldsymbol{l}$, vectors, which, in the exchange limit [144, 241], will look like

$$\dot{\boldsymbol{l}} = \gamma\, \boldsymbol{H}_{\boldsymbol{n}}^{\text{eff}} \times \boldsymbol{l}, \tag{3.49}$$

$$\dot{\boldsymbol{n}} = \left(\gamma\, \boldsymbol{H}_{\boldsymbol{l}}^{\text{eff}} - \alpha\, \dot{\boldsymbol{l}}\right) \times \boldsymbol{l} + \gamma\, \left(\boldsymbol{H}_{\boldsymbol{n}}^{\text{eff}} \times \boldsymbol{n}\right), \tag{3.50}$$

where $\boldsymbol{H}_{\boldsymbol{n},\boldsymbol{l}}^{\text{eff}}$ refer to the effective magnetic fields associated to the variables $\boldsymbol{n}$ and $\boldsymbol{l}$, which will be given, in this case, respectively, by $\boldsymbol{H}_{\boldsymbol{n},\boldsymbol{l}}^{\text{eff}} = -\frac{2}{\gamma\hbar}\frac{\delta E}{\delta(\boldsymbol{n},\boldsymbol{l})}$. In view of the configurational energy, E, of the system, characterized by Eq. (3.48), the associated effective magnetic fields, $\boldsymbol{H}_{\boldsymbol{n},\boldsymbol{l}}^{\text{eff}}$, will be characterized by

$$\boldsymbol{H}_{\boldsymbol{n}}^{\text{eff}} = 2\boldsymbol{H} - \frac{2A}{\gamma\hbar}\,\boldsymbol{n}, \qquad \boldsymbol{H}_{\boldsymbol{l}}^{\text{eff}} = \frac{1}{\gamma\hbar}\left[\frac{a}{2}\,\left(\partial_x^2 \boldsymbol{l}\right) - \frac{2\,\partial E_{\text{ani}}\,(\boldsymbol{l})}{\partial \boldsymbol{l}}\right], \tag{3.51}$$

which allow evaluating the dynamic evolution of the magnetic texture in the presence of the external magnetic field, $\boldsymbol{H}$, through the AFM LLG equations given by Eqs. (3.49) and (3.50). Interestingly, combining the functional form of the effective magnetic field associated with the total magnetization vector, $\boldsymbol{H}_{\boldsymbol{n}}^{\text{eff}}$, made explicit in the previous expression together with Eq. (3.49), it is possible to find that

$$\boldsymbol{n} = \frac{\hbar}{2A}\, \boldsymbol{l} \times \left[2\gamma\, (\boldsymbol{H} \times \boldsymbol{l}) - \dot{\boldsymbol{l}}\right], \tag{3.52}$$

from which it can be deduced that the non-staggered AFM vector, $\boldsymbol{n}$, is a "slave" variable whose behavior is governed not only by the external stimulus, $\boldsymbol{H}$, but also by the evolution of the Néel order parameter, $\boldsymbol{l}$, and its time derivative, $\dot{\boldsymbol{l}}$ [277, 301]. Substituting this last equation in the dynamic Eq. (3.50) along with the expression for the effective magnetic field associated with the staggered AFM vector, $\boldsymbol{H}_{\boldsymbol{l}}^{\text{eff}}$, given by Eq. (3.51), it can be obtained that

$$\boldsymbol{l} \times \left\{\left(\partial_x^2 \boldsymbol{l}\right) - \frac{1}{v_{\text{m}}^2}\,\ddot{\boldsymbol{l}} - \frac{4}{a}\,\frac{\partial E_{\text{ani}}\,(\boldsymbol{l})}{\partial \boldsymbol{l}} - \eta\dot{\boldsymbol{l}} - v_{\text{m}}^2\, \boldsymbol{h}\,(\boldsymbol{h}\cdot\boldsymbol{l}) + \partial_t\,(\boldsymbol{h}\times\boldsymbol{l})\right\} - \left(\dot{\boldsymbol{l}}\cdot\boldsymbol{h}\right)\boldsymbol{l} = 0, \tag{3.53}$$

where v_{m} represents the maximum magnon group velocity of the medium, which is given by $v_{\mathrm{m}} = \sqrt{aA}/\hbar$, $\boldsymbol{h}$ encodes the reduced magnetic field characterized as $\boldsymbol{h} = 2\gamma \boldsymbol{H}/v_{\mathrm{m}}^2$, and η denotes the dissipative parameter expressed by $\eta = 2\alpha\hbar/a$. Interestingly, this expression is a Lorentz-invariant second-order differential equation in the sense that, even in the presence of external stimulus and dissipative effects, its first two terms show a wave-like functional form, which implies that the AFM system will show special relativity traces [136, 137], some of which are shown in Figs. 3.3 (b) and 3.4 (a), which will be detailed later in Secs. 5.4.1 and 7.3.3. This framework is fundamentally different from the Galilean dynamic signatures that appear naturally in FM, which can be made explicit, for the scenario exposed in Sec. 3.2, where the functional form of the configurational energy, E, of the system is given by Eq. (3.17), taking the LLG equation in its Gilbert form, which is characterized by Eq. (2.13), through

$$\dot{\boldsymbol{m}} = \boldsymbol{m} \times \left[\alpha \dot{\boldsymbol{m}} - \frac{\mathcal{J} a_0^2}{\hbar} \left(\partial_x^2 \boldsymbol{m} \right) + \frac{2}{\hbar} \frac{\partial E_{\mathrm{ani}} \left(\boldsymbol{m} \right)}{\partial \boldsymbol{m}} - \gamma \boldsymbol{H} \right], \tag{3.54}$$

where the existence of only first-order time derivatives of the magnetization vector, $\boldsymbol{m}$, as opposed to the AFM case exposed in Eq. (3.53), where second-order time derivatives of the staggered vector, $\boldsymbol{l}$, appear, can be clearly seen. It is worth mentioning that, as it can be seen in Eq. (3.53), under the influence of a time-dependent ultrashort pulse, $\partial_t \boldsymbol{H}$, it is possible to trigger the dynamics of the Néel order parameter, $\boldsymbol{l}$, a circumstance which allows exploiting the explicit inertial character of the aforementioned expression to complete potential switching processes in AFM [142, 302].

To find the Lagrangian, L, of the system, as it was done in the FM case, embodied in Eq. (3.21), it is necessary to take into account the quantum-based Berry phase contribution, which for the case of a single spin or a FM medium is encoded in Eq. (3.16). On the other hand, the AFM kinetic energy term, L_{kin}, can be expressed, in the exchange limit, in this case, through the expression given by

$$L_{\mathrm{kin}} = \frac{\hbar}{2} \boldsymbol{n} \cdot \left(\dot{\boldsymbol{l}} \times \boldsymbol{l} \right), \tag{3.55}$$

which depends simultaneously on the total magnetization, $\boldsymbol{n}$, and Néel order, $\boldsymbol{l}$, parameters, which make up a set of orthonormal vectors [144, 192, 239]. Taking advantage of the "slave"-like functional form of the non-staggered vector, $\boldsymbol{n}$, represented by Eq. (3.52), it is possible to rewrite the previous equation such that

$$L_{\mathrm{kin}} = \frac{\hbar^2}{4A} \left[\dot{\boldsymbol{l}}^2 + 2\gamma \boldsymbol{H} \cdot \left(\dot{\boldsymbol{l}} \times \boldsymbol{l} \right) \right], \tag{3.56}$$

where the second term of the right-hand side appears due to the coupling of the applied magnetic field, $\boldsymbol{H}$, with the small total magnetization vector, $\boldsymbol{n}$, of the system [303, 304]. Similarly, it is possible to rewrite the configurational energy, E, of the system, given by Eq. (3.48), solely in terms of the AFM staggered vector, $\boldsymbol{l}$, using Eq. (3.52), which results in

$$E = \frac{\hbar^2}{8A} \dot{\boldsymbol{l}}^2 + \frac{1}{8} a \left(\partial_x \boldsymbol{l} \right)^2 + E_{\mathrm{ani}} \left(\boldsymbol{l} \right) + \frac{\gamma^2 \hbar^2}{2A} \left(\boldsymbol{l} \cdot \boldsymbol{H} \right)^2, \tag{3.57}$$

where a constant quadratic term in the external stimulus, $\boldsymbol{H}$, not coupled to the Néel order parameter, $\boldsymbol{l}$, has been ignored, which would have no impact on the equations

of motion [136]. It is worth noting that the quadratic magnetic field-based contribution, given by the last term on the right-hand side of the previous expression, is weakened by being divided by the strong AFM homogeneous exchange parameter, A [133]. Interestingly, the magnetic field-governed last term of the right-hand side of the previous expression acts as a kind of induced uniaxial easy-axis anisotropy, as it can be seen from its resemblance to a contribution of the type given by Eq. (2.9).

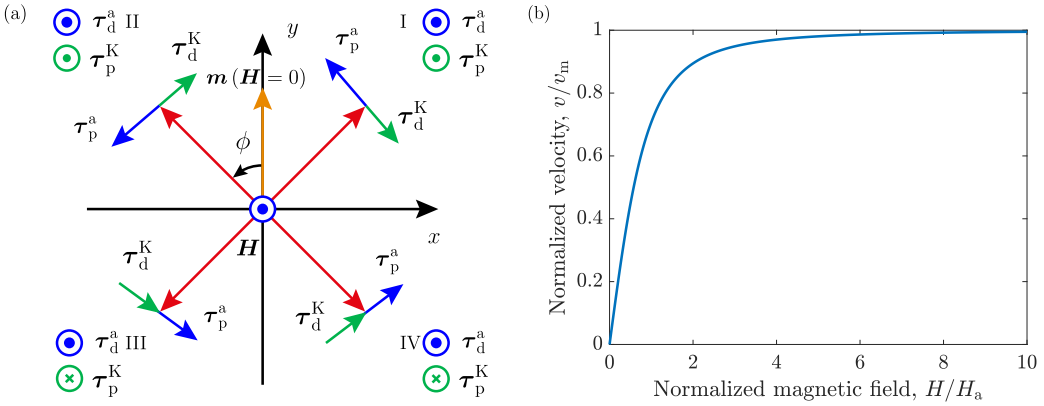

Figure 3.3: (a) Torque-based contributions, $\boldsymbol{\tau}$, dependent on the quadrant of the xy plane in which the central spin of the FM DW, $\boldsymbol{m}$, which starts out aligned along the $+y$-*th* semiaxis, resides in the different dynamic stages of the system under the action of a magnetic field, $\boldsymbol{H}$, along the z-*th* spatial direction. The subscripts p and d refer, respectively, to the precessional and damping components that appear on the right-hand side of Eq. (2.11), respectively, while the superscripts a and K indicate whether they are induced by the external stimulus or by the magnetostatic/anisotropy term, correspondingly. Adapted from [205]. (b) Saturation of the speed, v, of an AFM magnetic soliton during its quasistatic relativistic dynamic trend to the limiting maximum magnon group velocity, v_m, of the medium as the externally-applied normalized magnetic field, H/H_a, increases.

3.3.3 Decoupled generalized coordinates-based excitation modes in antiferromagnets

Combining the kinetic, L_kin, and "potential", E, energy terms, given, respectively, by Eqs. (3.56) and (3.57), it can be found that the Lagrangian, L, of the system can be expressed as

$$L = \frac{a}{8}\left[\frac{1}{v_\mathrm{m}^2}\,\dot{\boldsymbol{l}}^2 - \left(\partial_x \boldsymbol{l}\right)^2\right] - E_\mathrm{ani}\left(\boldsymbol{l}\right) + \frac{a}{4}\,\boldsymbol{h}\cdot\left(\dot{\boldsymbol{l}}\times\boldsymbol{l}\right) - \frac{\hbar^2 v_\mathrm{m}^4}{8A}\left(\boldsymbol{l}\cdot\boldsymbol{h}\right)^2, \tag{3.58}$$

where it can be seen that the first two contributions of the right-hand side are the ones that confer the relativistic functional form to the AFM dynamic equation given by Eq. (3.53) [303]. However, it should be noted that the presence of the fourth magnetic field-governed gyroscopic term of the right-hand side of Eq. (3.48) can break the aforementioned Lorentz-invariant-like symmetry of the system, something that could also be induced by a DMI [304]. Using the spherical coordinates-based parameterization of the order parameter, $\boldsymbol{l}$, of the system, which is given by Eq. (2.22), it is

possible to rewrite the AFM Lagrangian, L, such that

$$L = \frac{a}{8}\left\{\frac{1}{v_{\mathrm{m}}^2}\left[\dot{\theta}^2 + \sin^2\theta\,\dot{\phi}^2\right] - \left(\partial_x\theta\right)^2\right\} + 2\left(K_z + |K_x|\,\sin^2\phi\right)\sin^2\theta + \frac{h}{4}\left(a\dot{\phi} + \frac{h\hbar^2 v_{\mathrm{m}}^4}{2A}\right)\sin^2\theta, \tag{3.59}$$

where it is possible to appreciate that, compared to Eq. (3.17), in this expression there is a squared first-order time derivative of the staggered vector, $\boldsymbol{l}$, which is absent in its FM counterpart. On the other hand, the dissipation processes inherent to the magnetic medium, characterized by the Gilbert damping parameter, α, can be encapsulated through the Rayleigh dissipation function, R, given by Eq. (2.18), expression which can be extrapolated to the AFM formalism giving rise to

$$R = \frac{\alpha\hbar}{4}\left(\dot{\boldsymbol{m}}_1^2 + \dot{\boldsymbol{m}}_2^2\right) \simeq \frac{\alpha\hbar}{2}\,\dot{\boldsymbol{l}}^2, \tag{3.60}$$

where the relationship between the AFM vectors, $\boldsymbol{n}$ and $\boldsymbol{l}$, and the unit atomic magnetic moment, $\boldsymbol{m}$, encapsulated by Eqs. (2.33) and (2.34), has been used. In this case, potential cross-sublattice terms have not been taken into account and, in addition, the related derivation has been made in the exchange limit framework, $|\boldsymbol{n}|^2 \ll |\boldsymbol{l}|^2$ [145, 305, 306]. From the parameterization in spherical coordinates of the AFM staggered vector, $\boldsymbol{l}$, given by Eq. (2.22), it is possible to rewrite the Rayleigh dissipation function, R, as

$$R = \frac{\alpha\hbar}{2}\left(\dot{\theta}^2 + \sin^2\theta\,\dot{\phi}^2\right). \tag{3.61}$$

At this point, it is convenient, as it was done in Sec. 3.2, to work on the collective coordinates framework, for which it is necessary to take into account the Walker-like DW rigid profile, given by Eq. (2.30), characterized by the polar angle, θ, taking into consideration the AFM peculiarities exposed in Sec. 2.4.3, to simplify the problem [91, 137]. As a result, the Lagrangian, L, of the system, represented by Eq. (3.59), and the Rayleigh dissipation function, R, defined by Eq. (3.61), can be reexpressed as

$$L = \left\{\frac{a}{8\Delta^2}\left[\frac{1}{v_{\mathrm{m}}^2}\left(\dot{X}^2 + \Delta^2\dot{\phi}^2\right) - 1\right] + 2\left(K_z + |K_x|\,\sin^2\phi\right) + \frac{h}{4}\left(a\dot{\phi} + \frac{h\hbar^2 v_{\mathrm{m}}^4}{2A}\right)\right\}\operatorname{sech}^2\frac{x-X}{\Delta}, \tag{3.62}$$

$$R = \frac{\alpha\hbar}{2\Delta^2}\left(\dot{X}^2 + \Delta^2\dot{\phi}^2\right)\operatorname{sech}^2\frac{x-X}{\Delta}, \tag{3.63}$$

where it can be observed, in the first of these equations, corresponding to the AFM Lagrangian, L, of the system, that, in this case, there is no coupling between the generalized coordinates given by the position, X, of the magnetic soliton and the tilting-based azimuthal angle, ϕ, contrary to the magnetic field-induced FM scenario, as it is shown in Eq. (3.21) [304]. In addition, it is important to note that Eqs. (3.19) and (3.20) have been used for the derivation of the previous expressions, but it has been assumed that the DW width, Δ, will not be taken as a generalized coordinate in the dynamic evaluation of the system. This is because its time evolution, for quasistatic processes, it is governed by the velocity, v, of the magnetic texture through the relativistic functional form given by $\Delta = \Delta_0\,\beta$, where β is the symmetric Lorentz factor, which can be expressed as $\beta = \sqrt{1 - (v/v_{\mathrm{m}})^2}$ [135, 307]. If the Lagrangian, L, and

Rayleigh dissipation function, R, contributions, given, respectively, by Eqs. (3.62) and (3.63), are spatially integrated, the appearance of an overall multiplication of the aforementioned expressions by a factor proportional to the DW width, Δ, will be produced, as it can be induced from Eq. (3.23). In this scenario, using the EL formalism in the presence of dissipative mechanisms, expressed by Eq. (3.27), it is possible to find the equations of motion of the generalized coordinates of the system, given by the center position, X, of the magnetic texture and the azimuthal angle, ϕ, which will be characterized by

$$\ddot{X} - \frac{4\alpha\hbar v_{\mathrm{m}}^2}{a}\,\dot{X} = 0, \tag{3.64}$$

$$\ddot{\phi} - \frac{4\alpha\hbar v_{\mathrm{m}}^2}{a}\,\dot{\phi} - \frac{8|K_x|v_{\mathrm{m}}^2}{a}\,\sin 2\phi = -v_{\mathrm{m}}^2\,(\partial_t h)\,, \tag{3.65}$$

where it can be seen that, contrary to what happened in the FM scenario, whose dynamic behavior is represented by Eqs. (3.28) and (3.29), the translational and oscillatory modes constitute independent degrees of freedom in the AFM case [307–309]. This avoids the appearance of the WB understood as the tilting of the azimuthal angle, ϕ, with respect to the DW plane at rest as the external stimulus approaches a threshold, from which a stable magnetic texture motion is not possible anymore due to the intrinsic instabilities that arise in the magnetic soliton [133, 134]. It is important to note that, in the exposed AFM framework, the magnetization, $\boldsymbol{m}$, dynamics can only be excited through time-dependent external stimuli, $\boldsymbol{H}$ [142, 302].

3.3.4 Uniform field-based torque compensated by the exchange contribution

To better understand why an applied moderate non-staggered static magnetic field, $\boldsymbol{H}$, does not induce dynamics in the case of an AFM spin chain, contrary to its FM counterpart, which was discussed in Sec 3.2, it is useful to perform a torque-based analysis of the underlying system. With this goal in mind, two contiguous spins of the inhomogeneous DW transition, like the one shown at the top of Fig. 2.3 (b), can be considered, whose associated AFM exchange energy, E_{exc}, will be characterized by $E_{\mathrm{exc}} = |\mathcal{J}|\,(\boldsymbol{m}_1 \cdot \boldsymbol{m}_2)$, according to Eq. (2.7). If the external stimulus is defined along the *z-th* axis, such that $\boldsymbol{H} = H\,\hat{\boldsymbol{z}}$, the induced field-like torque, $\boldsymbol{\tau}^{\mathrm{a}}_{\mathrm{p},\boldsymbol{m}_i}$, at each considered spin $\boldsymbol{m}_i$, as it is shown in Fig. 3.4 (b), will be given by $\boldsymbol{\tau}^{\mathrm{a}}_{\mathrm{p},\boldsymbol{m}_1} \propto -\gamma H\,\hat{\boldsymbol{x}}$ and $\boldsymbol{\tau}^{\mathrm{a}}_{\mathrm{p},\boldsymbol{m}_2} \propto \gamma H\,\hat{\boldsymbol{x}}$, according to the LLG expression given by Eq. (2.11). In a similar fashion, the field-induced damping torque, $\boldsymbol{\tau}^{\mathrm{a}}_{\mathrm{d},\boldsymbol{m}_i}$, in each involved magnetization vector will have a functional form such that $\boldsymbol{\tau}^{\mathrm{a}}_{\mathrm{d},\boldsymbol{m}_i} \propto \alpha\gamma H\,(-\hat{\boldsymbol{y}} + \hat{\boldsymbol{z}})$, contributions which will want to rotate the exchange- and anisotropy-governed angular position in the yz easy-plane of both spins. On the other hand, due to the AFM exchange interaction between both atomic magnetic moments, governed by the functional form of the involved exchange energy, E_{exc}, each spin will sense an exchange-based effective field, $\boldsymbol{H}^{\mathrm{eff}}_{\boldsymbol{m}_i}$, according to Eq. (2.12), induced by the presence of its neighbor due to their non-collinear arrangement. In this line, the AFM exchange-induced field-like torque, $\boldsymbol{\tau}^{\boldsymbol{m}_j}_{\mathrm{p},\boldsymbol{m}_i}$, experienced by the spin $\boldsymbol{m}_i$ due to the presence of the atomic magnetic moment $\boldsymbol{m}_j$, will be given by $\boldsymbol{\tau}^{\boldsymbol{m}_2}_{\mathrm{p},\boldsymbol{m}_1} \propto \gamma|\mathcal{J}|/\,(\mu_0\mu_{\mathrm{s}})\,\hat{\boldsymbol{x}}$ and $\boldsymbol{\tau}^{\boldsymbol{m}_1}_{\mathrm{p},\boldsymbol{m}_2} \propto -\gamma|\mathcal{J}|/\,(\mu_0\mu_{\mathrm{s}})\,\hat{\boldsymbol{x}}$, contributions which, for each considered magnetization vector, oppose the action of the magnetic field, $\boldsymbol{H}$. The same goes for the AFM-based damping torque, $\boldsymbol{\tau}^{\boldsymbol{m}_j}_{\mathrm{d},\boldsymbol{m}_i}$, which in each involved magnetic sublattice is described as $\boldsymbol{\tau}^{\boldsymbol{m}_j}_{\mathrm{d},\boldsymbol{m}_i} \propto \alpha\gamma|\mathcal{J}|/\,(\mu_0\mu_{\mathrm{s}})\,[\hat{\boldsymbol{y}} - \hat{\boldsymbol{z}}]$, as it

can be seen in Fig. 3.4 (b). Since the order of magnitude of the AFM exchange contribution, $|\mathcal{J}|$, is typically much larger than that associated with the applied magnetic field, $\boldsymbol{H}$, the effect of the non-staggered external stimulus will be completely overshadowed, prevailing the exchange- and anisotropy-based angular arrangement of the spins that make up the magnetic soliton in the yz easy-plane.

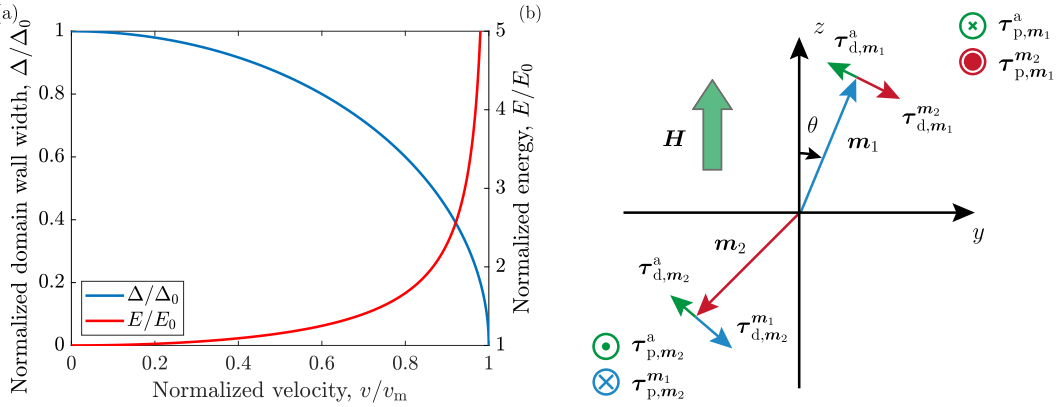

Figure 3.4: (a) Relativistic behavior of the contracting normalized width, Δ/Δ_0, and of the increasing normalized energy, E/E_0, where Δ_0 and E_0 represent their respective values at rest, of a propagating steady-state AFM DW as its normalized velocity, v/v_m, increases, being v_m the maximum magnon group velocity of the medium. (b) Torque-based contributions, $\boldsymbol{\tau}$, experienced by two contiguous spins belonging to the inhomogeneous magnetic texture transition of an AFM spin chain in the presence of a non-staggered static magnetic field, $\boldsymbol{H}$, defined along the z-*th* spatial direction, $\boldsymbol{H} = H\,\hat{\boldsymbol{z}}$. The subscripts p and d refer, respectively, to the precessional and damping components that appear on the right-hand side of Eq. (2.11), respectively, while the superscript a indicates that it has been induced by the external stimulus, and the indices $\boldsymbol{m}_{1,2}$ allude to the exchange interaction between the two considered atomic magnetic moments that reside in the yz easy-plane of the system.

3.4 Gyrotropic deformation-free propagation description of non-collinear magnetic textures

Interestingly, it is possible to simplify the dynamic description of non-collinear spin textures, expressed by the LLG expressions collected in Eqs. (2.11) and (2.13), under the assumption that the considered magnetic soliton remains rigid during its motion. This can be characterized through the traveling wave *ansatz* given by $\boldsymbol{m}(\boldsymbol{r},t) = \boldsymbol{m}(\boldsymbol{r}-\boldsymbol{X}(t))$, where $\boldsymbol{X}$ is a collective coordinate that characterizes the in-plane deviations from the initial position of the core of the magnetic texture [266]. Taking into account that, in this context, the unit atomic magnetic moment, $\boldsymbol{m}$, depends on time through the position vector $\boldsymbol{X}$, it is possible to express the time derivative of the magnetization vector as

$$\dot{m}_i = -v_j \frac{\partial m_j}{\partial X_i}, \tag{3.66}$$

where $\boldsymbol{v}$ is the steady-state velocity of the magnetic pseudoparticle. This will ultimately allow characterizing the trajectory of a magnetic soliton without the need to evaluate the LLG equation at each time step. The assumption of a propagation without appreciable deformations implies that there is a balance between the existing forces in the system, as it was shown in the case of FM DW through Eq. (3.37),

where there is a balance between the external stimulus-based driving mechanism and the dissipation processes [296]. The force experienced by the rigid magnetic texture due to the different interactions of the magnetic medium and potential external stimuli, F_i^{eff}, which is characterized by the effective magnetic field, $\boldsymbol{H}^{\text{eff}}$, embodied in Eq. (2.12), can be expressed as

$$F_i^{\text{eff}} = -\mu_0 \mu_{\text{s}} H_k^{\text{eff}} \frac{\partial m_k}{\partial X_i} = \frac{\partial E}{\partial X_i}, \tag{3.67}$$

expression which makes explicit the conservative nature of the involved force [310]. Taking the cross product of the LLG equation, given by Eq. (2.13), with the magnetization vector, $\boldsymbol{m}$, it is possible to obtain that

$$H_k^{\text{eff}} = -\frac{1}{\gamma}\left(v_j \varepsilon_{kln} m_l \frac{\partial m_n}{\partial X_j} + \alpha v_j \frac{\partial m_k}{\partial X_j}\right), \tag{3.68}$$

being possible to rewrite it, in a force-based picture, after multiplying it by $(\partial m_k / \partial X_i)$, as

$$F_i^{\text{eff}} + F_i^{\text{gyro}} + F_i^{\text{dissip}} = 0, \tag{3.69}$$

where the gyrotropic, F_i^{gyro}, and dissipative, F_i^{dissip}, forces are given by

$$F_i^{\text{gyro}} = \frac{\mu_0 \mu_{\text{s}}}{\gamma} v_j \varepsilon_{lkn} m_l \frac{\partial m_k}{\partial X_i} \frac{\partial m_n}{\partial X_j}, \tag{3.70}$$

$$F_i^{\text{dissip}} = -\frac{\alpha \mu_0 \mu_{\text{s}}}{\gamma} v_j \frac{\partial m_k}{\partial X_i} \frac{\partial m_k}{\partial X_j}, \tag{3.71}$$

which receive their name because they come from the precessional and damping terms of the LLG equation, given by Eq. (2.13), respectively [311].

If the expression given by Eq. (3.69) is spatially integrated, it is possible to obtain the massless Thiele's equation for the central position, $\boldsymbol{X}$, of the considered magnetic soliton, which will be characterized as

$$\boldsymbol{G} \times \boldsymbol{v} - \alpha \overleftrightarrow{\boldsymbol{D}}\, \boldsymbol{v} = -\int \frac{\partial E}{\partial \boldsymbol{X}}\, \mathrm{d}\boldsymbol{r}, \tag{3.72}$$

where $\boldsymbol{G}$ and $\overleftrightarrow{\boldsymbol{D}}$ represent, respectively, the gyrovector and dissipative tensor of second order, which can be expressed as

$$\boldsymbol{G} = \frac{\mu_0 M_{\text{s}}}{\gamma} \int \boldsymbol{m} \cdot \left(\frac{\partial \boldsymbol{m}}{\partial X_i} \times \frac{\partial \boldsymbol{m}}{\partial X_j}\right) \mathrm{d}\boldsymbol{r}, \tag{3.73}$$

$$\overleftrightarrow{\boldsymbol{D}} = \frac{\mu_0 M_{\text{s}}}{\gamma} \int \left(\frac{\partial \boldsymbol{m}}{\partial X_i} \cdot \frac{\partial \boldsymbol{m}}{\partial X_j}\right) \mathrm{d}\boldsymbol{r}, \tag{3.74}$$

being M_{s} the volumetric saturation magnetizaton, given by $M_{\text{s}} = \mu_{\text{s}}/V$, where V is the volume of the considered unit cell [296]. Interestingly, the first term on the left-hand side of Eq. (3.72) is usually known as Magnus force, which leads to the existence of a transverse dynamic component, and reflects the relationship between the topological skyrmion number, given by Eq. (2.41), and the existing non-trivial dynamics. This is because the gyrovector, $\boldsymbol{G}$, only has a perpendicular component proportional to the topological term, N, such that $\boldsymbol{G} = -4\pi N \hat{\boldsymbol{z}}$ [250, 312]. It should be noted that this contribution, in the case of a 1D magnetic texture like a DW, is null, giving rise to the fact that in the steady-state scenario its motion is rectilinear

and comes from the balance between the driving and the dissipative forces [313]. Additionally, the input on the right-hand side of Eq. (3.72) is a force originating from the inhomogeneous energy landscape of the system in addition to possible applied external stimuli, repulsive potential contributions from the sample edges, or pinning effects from local defects [314]. Interestingly, Thiele's equation has been shown to be efficient in predicting and characterizing the gyrotropic dynamics of magnetic vortices and skyrmions in FM cylindrical dots, as well as showing the Hall effect-based dynamic deflection of skyrmions in ultrathin films [121, 122, 249, 266], the latter having been shown in Fig. 3.5 (a). Interestingly, it is important to note that, in AFM, the skyrmion Hall effect is strongly suppressed due to the strong coupling of two skyrmion structures which present opposite topological charges and that live in different magnetic sublattices, which produces the cancellation of the potential Magnus force predicted by Eq. (3.72) on its FM counterpart [315, 316].

3.5 Discretization schemes-dependent computational spin dynamics simulations

Computational spintronics, based on solving the LL equation with dissipative torques, as the temperature-independent LLG expressions given by Eqs. (2.11) and (2.13), acts as a bridge between fundamental theories and experiments. In order to emulate nanoscale magnetic phenomena and real spintronic devices, it is necessary to decide from the beginning which type of external stimulus is applied, what the initial magnetic state is like, which type of geometry the system presents, and if there are thermal effects involved. By knowing in advance what the exchange length and the potential DW width of the medium are, it is possible to decide which type of discretization scheme can be used in the simulations [221]. Usually, for FM at low temperatures it is convenient to average the atomic magnetic properties over small volumes [317], usually of the order of a few nm^3, through the assumption that the magnetization direction varies slowly in space and time [214, 318], which it is depicted in Fig. 3.5 (b). This micromagnetic formalism is plausible when the discretized grid is small enough compared to the dynamically-governed spatial extent of the inhomogeneous transitions between domains of the medium, since otherwise the exchange interaction between neighboring averaged spins would be greatly overestimated, so there must be enough cells to validate the continuous approximation. This procedure has been widely used, especially for calculations of hysteresis cycles, reversal magnetization processes, and dynamics in magnetic nanostructures such as magnetic thin films, dots, or stripes [319]. Although using this modeling scheme, large systems can be implemented with an inherent saving in computational time, this is not recommended when the magnetization direction changes strongly on the atomic scale, which happens in AFM, ferrimagnets, and complicated heterostructures as well as in presence of high temperatures that originate disorder [318, 320]. Due to the related discretization process of the spin space, a cutting of the high-frequency modes of the SW spectra is produced, which are necessary to take into account longitudinal magnetization fluctuations in the system [221]. This has as a consequence that micromagnetic simulations are not adequate to characterize ps-based switching events in FM produced by the energy redistribution from laser-excited conduction electrons to the spin reservoir, producing, in addition, an overestimation of the critical temperature of the medium in this framework [217, 321, 322]. In this context, it is necessary to consider an atomistic approach that not only accounts for realistic lattice structures and interactions of the system but also for defects and interfaces

where the magnetization changes significantly at the atomic level. However, this approach does not allow simulating large systems, being restricted to approximately 10^7 spins, which means that samples are limited to volumes of a few tens of nm^3 at the moment due to the large number of differential equations that must be numerically integrated [323]. In both cases, the most challenging part consists of calculating the effective magnetic fields associated with the different energy contributions of the system, among which we can find both local and collective terms involving a certain number of neighbors or all the spins of the system, such as anisotropy, on the one hand, and exchange or magnetostic interactions, on the other, respectively, which have been summarized in Sec. 2.2. Even though there are methods to lighten the numerical process, it is precisely the calculation of the long-range stray fields that is more time consuming to characterize, since for each time step it is necessary to evaluate, for each discretized element, the contribution of the rest of the elements in the medium [324].

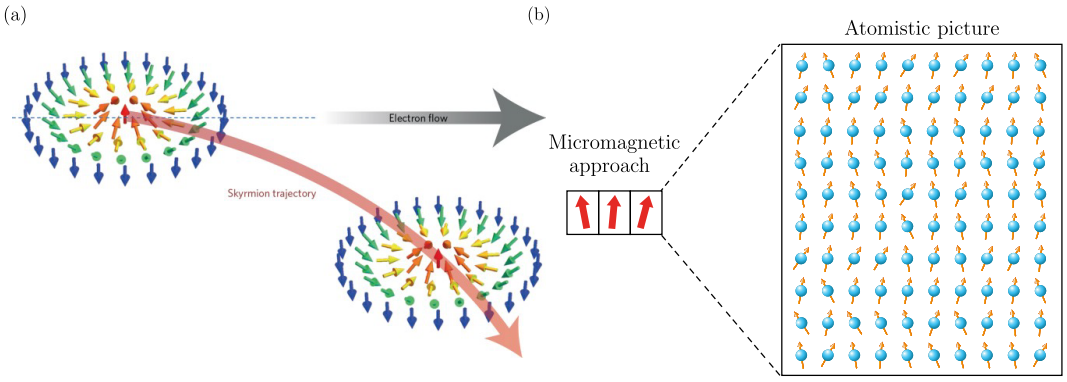

Figure 3.5: (a) Schematic representation of the skyrmion Hall effect in FM, in which the considered magnetic soliton does not move along the direction dictated by the applied electron flow but instead shows a transverse dynamic component governed by the gyrotropic component existing in the massless Thiele expression given by Eq. (3.72). Extracted from [325]. (b) Illustration of the relationship between the atomistic model and the micromagnetic approach, the latter being based on averaging the atomic magnetic properties over small volumes of the order of a few nm^3, which is convenient when the magnetization direction between neighboring spins varies smoothly. Adapted from [221].

3.6 Experimental antiferromagnetic response characterization

While the advent of high-resolution imaging techniques such as the magneto-optical Kerr [93], magnetic force [326], scanning electron [327], and x-ray photoemission electron microscopies [328] has made it possible to systematically characterize the magnetic domains on the surfaces of FM and ferrimagnets at the nanoscale [329], its experimental extrapolation to the AFM case is relatively new and is in full swing [330]. This is because, although there are many types of AFM ordering, most AFM metals exhibit collinear alignment with an associated lack of net magnetization, which means that they do not generate stray fringing fields and are robust against external magnetic fields [331]. However, there are certain classes of AFM that present a weak magnetization which originates due to the DMI, which allows characterizing the magnetic state of the system due to the coupling between the parasitic magnetic

moment and the Néel order parameter [332]. On the other hand, it is also possible to take advantage of FM/AFM heterostructures, where both magnetic materials are strongly connected through exchange interaction, to employ the usual FM readout techniques to characterize the domain pattern imprinted on it from the AFM [333, 334].

3.6.1 Real space imaging magnetic morphology reconstruction

The first static domain characterizations in AFM materials were performed through neutron tomography and optical microscopy techniques on insulating materials as alternative measures due to the absence of measurable stray fields [335–337]. However, using photoemission electron microscopy, with contrast enabled by x-ray magnetic linear dichroism [338], its visualization could be extended to metals, providing information on the microscopic magnetic properties of the system with better resolution than 100 nm [339, 340]. The emitted photons generated through radially-accelerated electrons in the presence of magnetic fields in synchrotron-based facilities interact with the electronic distribution of the system promoting electrons from different core levels to the Fermi level depending on the x-ray incident energy [341]. In this coherent absorption process, the decay of the created holes generates secondary electrons which allow to measure the absorption spectrum at different radiation energies [342, 343], as it is schematized in Fig. 3.6 (a). To obtain complementary magnetic-based information, it is possible to exploit the asymmetric degree of absorption depending on the relative orientation of the Néel order parameter and the linear polarization vector of the incident light, which makes it possible to obtain information about the domain structure after switching processes [344, 345], where two different resistive states dependent on the relative orientation of the electric field-based linear polarization of the incident radiation and the Néel order parameter are shown in Fig. 3.6 (b). If, on the other hand, circularly polarized light were used to try to characterize the morphology domain in AFM, this would not be efficient due to the non-existence of an asymmetric density of spin up and down states at the Fermi level, which does happen in FM due to its measurable net magnetization [346]. The convenience of this detection scheme is due to the fact that it is a linear optical technique, consisting of coherent processes that change the amplitude or polarization of light in its interaction with a material, leaving the frequency of the wave undisturbed, based on quadratic magneto-optical effect which are, however, generally weaker than their linear counterparts [330]. The linear magneto-optical Kerr effect, which is based on a rotation of the plane of polarization of linearly polarized light when it is reflected by a magnetized surface, which it is depicted in Fig. 3.7 (a), is proportional to the magnetization of the medium, which makes it difficult to use it in AFM [331]. However, symmetry-based considerations have revealed that the existence of a finite Berry curvature in momentum space due to macroscopic time-reversal symmetry breaking can give rise to off-diagonal components of the dielectric tensor even in collinear AFM [347]. In a similar fashion, the second-harmonic generation nonlinear optical technique, based on the simultaneous absorption of two photons from the incident excitation followed by the emission of a frequency-doubled light wave, as it is illustrated in Fig. 3.7 (b), depends on the symmetry of the material under study rather than on its magnetization [348, 349]. This process is very unlikely to occur, requiring, in addition, the use of high electromagnetic field strengths such as those provided by high-power pulsed lasers [331], but it is especially suitable for the case of AFM materials with broken inversion symmetry [330, 350, 351]. The problem with these non-destructive sampling techniques is

that they require large-scale synchrotron-based experimental facilities. As an alternative, the high spatial resolution scanning nitrogen-vacancy center magnetometry can be used to investigate the magnetic stray field emanating from AFM domain textures, where a diamond probe containing a single center at the apex is scanned at constant height above the sample surface [352]. At every location the shift in the nitrogen vacancy center's spin resonance is mearured using optical readout, which is directly proportional to the magnetic stray field at that location [353]. Using the known orientation of the vacancy center, the full magnetic vector field at the apex position can be reconstructed, allowing to study the domain morphology [354, 355], as it is schematized in Fig. 3.8 (a).

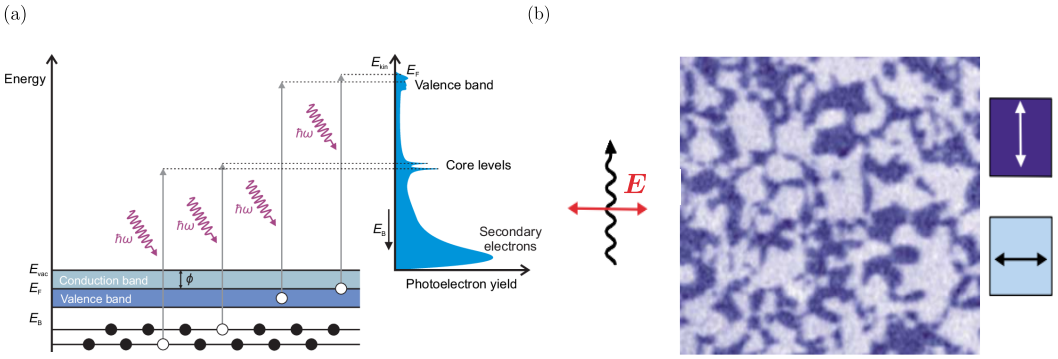

Figure 3.6: (a) Schematic representation of linear photoemission processes in a solid. Those electrons with sufficient kinetic energy, E_{kin}, obtained through the absorption of photons with energy $\hbar\omega$, where ω is their related frequency, are able to leave the valence bands and core levels of the material, promoting to vacuum if the related electronic energy is greater than the work function, ϕ, and the associated binding energy, E_{B}. Extracted from [356]. (b) Through x-ray magnetic linear dichroism spectroscopy, it is possible to find well-differentiated domain contrast dependent on the relative orientation of the electric field-based linear polarization of the incident light and the directionality of the staggered vector of the AFM system due to the different degrees of absorption that will suffer the applied radiation. Extracted from [357].

3.6.2 Magnetoresistive-based static domain configuration

AFM materials have a great robustness against external magnetic fields, due to which it is highly desirable to use electrical read-out methods to characterize the magnetization configuration of the system. In this context, for metals, even though it would be desirable to use phenomena widely used in FM such as GMR or TMR, which are shown, respectively, in Figs. 1.1 (b) and 1.2 (a), the scattering processes involved in SV and the low signal obtained experimentally in MTJ mean that these methods are not completely suitable at the moment [358, 359]. As an alternative, AMR, which is based on the relative orientation of an applied charge current and the in-plane magnetization, which has been introduced for the FM case in Fig. 1.1 (a), has been shown to be an efficient method in AFM to characterize the evolution of the number of electrically switched domains along a certain direction [149, 154]. In addition to being a bulk phenomenon, not requiring complex multilayer structures, its existence in AFM is due to the fact that it is even in magnetization, being invariant against reversal magnetization processes [301]. Because the signal associated with AMR is usually small, it is possible to greatly amplify it through the inclusion of a

TB, which has been proven at low temperatures [162, 360]. On the other hand, in metals there is also the DW MR, which takes into account how the electrons that make up a charge current are scattered by a DW, whose existence and signal variation can be appreciated through the reconfiguration of domains under magnetic fields, which can vary in number and width [155, 361], being schematized in Fig. 3.8 (b) for the case of a layered AFM. On the other hand, it is possible to take advantage of the spin current generated through the SHE in a HM with strong SOC due to the injection of an electrical current to obtain information on the domain morphology of an AFM insulator in contact with it [156, 157]. Due to the exchange of angular spin momentum, it is possible to characterize changes in metal resistivity due to the relative angle between the polarization of the spin accumulation at the interface and the magnetization direction in the magnetic material, phenomenon which is known as SH MR [362], which it is represented in Fig. 3.9 (a). It should be noted, however, that it has recently been suggested that the electrically-induced AMR/SH MR readout signals may actually be thermal or electromigration artifacts caused by the high current densities needed to switch the magnetic state of the system [363–366].

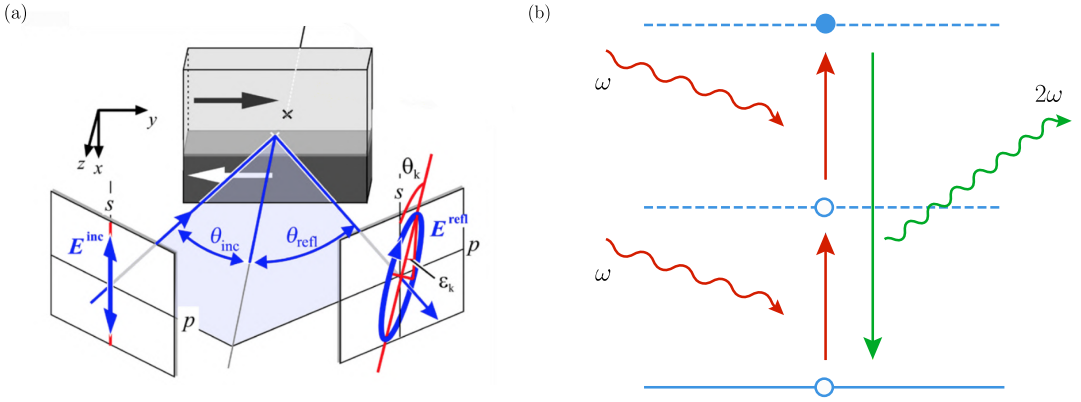

Figure 3.7: (a) The linear magneto-optical Kerr effect is based on the rotation of the polarization plane of light after its reflection process induced by its interaction with the magnetized medium, passing from a linearly polarized state to an elliptical one. Extracted from [367]. (b) Simplified picture of the second-harmonic generation nonlinear optical technique, in which two photons of frequency ω excite an electron of the system, which causes the emission of a quantum of light in the process of electronic relaxation to the initial ground state with twice the frequency that the one treasured by the incident waves. Adapted from [368].

3.6.3 Thermoelectric-dependent magnetic soliton dynamics proposals

Additionally, there are two alternatives through thermoelectric-based effects in AFM metals. In the first one, local heat gradients are generated through scanning far- or near-field techniques and, subsequently, the laser-induced voltage at the two ends of the device is tracked, which it is schematized in Fig. 3.9 (b). Interestingly, when the temperature gradient crosses a domain boundary, a non-zero value is detected, which is because the reorientation of the Néel order parameter implies a change in the sign of the involved magneto-Seebeck coefficients [164]. This technique allows both the detection of the position of a DW and obtaining information on the 180° switching of the staggered vector. On the other hand, it is theoretically possible to

track the electric current-induced DW dynamics by taking advantage of the accompanying electronic-based localized heat wave generated through the spin Peltier effect (SPE), which it is represented in Fig. 7.3 (a) and will be discussed in detail in Sec. 7.3.2, which could be characterized through scanning thermal microscopy. This situation is especially advantageous in AFM due to the high speeds that can be achieved and the special relativity-governed contraction of the width of the texture [165].

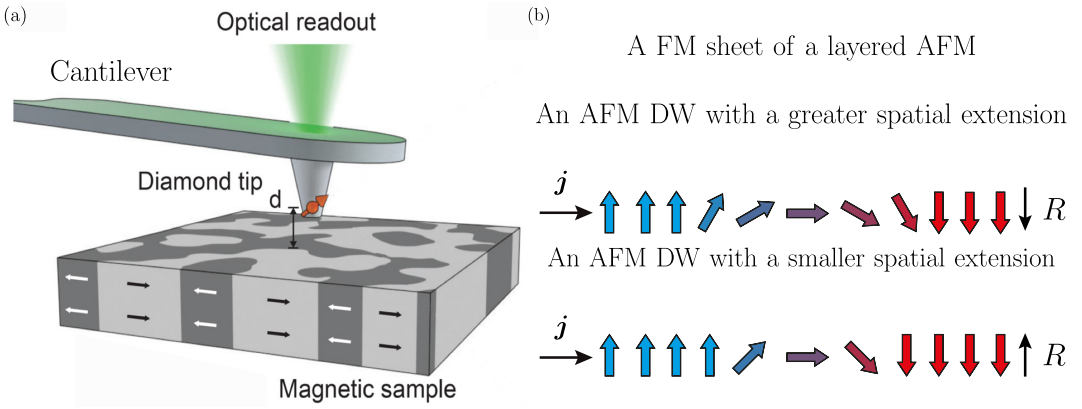

Figure 3.8: (a) The scanning nitrogen-vacancy center magnetometry is based on the shift of the spin resonance of the atom located at the apex of the probe induced by the stray magnetic field emanating at each spatial location due to the domain configuration of the system. Extracted from [369]. (b) Scheme of the DW MR for a layered metallic AFM, where different resistive states can be obtained depending on the scattering ratios experienced by the electrons that make up a charge current that crosses the inhomogeneous transition of a magnetic soliton, the measured resistance, R, being greater the narrower the spatial extent of the considered spin texture.

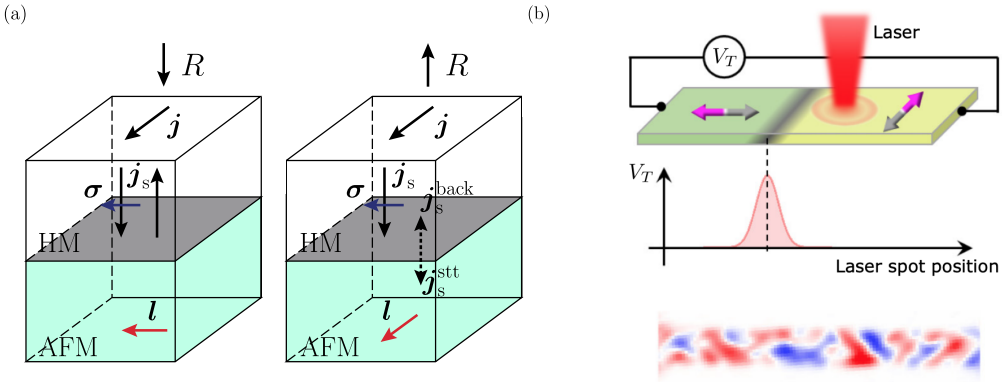

Figure 3.9: (a) The SH MR in AFM insulators is based on the different resistive, R, states obtainable depending on the relative polarization orientation, σ, of the SHE-induced spin accumulation at the interface between the HM and the magnetized medium and the directionality of the magnetic order parameter, $\boldsymbol{l}$. Adapted from [156]. (b) The magneto-Seebeck effect allows to detect the position of DW in AFM through the sign change of the involved thermoelectric-based coefficients of the system when a local heat gradient generated through scanning field techniques crosses a domain boundary. Extracted from [164].

Chapter 4

Relativistic-like domain wall dynamics in biaxial ferromagnets

4.1 Walker breakdown delay through antiferromagnetic-like traces

As it was introduced in Sec. 3.2, the stable FM DW dynamics under the action of an external stimulus is limited by a phenomenon known as WB, in which a sharp decrease in speed occurs at the same time that it enters in a regime in which its internal structure changes periodically [91–93]. This fact is unfortunate from an application point of view, since many spintronics devices are typically based on a switching process mediated by the displacement and nucleation of an inhomogeneous magnetization reversal mode, being desirable that this process is as ultrafast and deterministic as possible. In this sense, it is possible to delay or even eradicate the appearance of intrinsic instabilities in the propagating magnetic texture, such as through the DMI, either in curved nanowires or in ultrathin magnetic fields, which energetically favors one of the possible chiralities of the magnetic soliton and, therefore, the system becomes more stable [102, 108]. Under these conditions, the new dynamic threshold will be set by the minimum phase velocity of the lowest energy excitations of the spin space, producing, if this limit is exceeded, the appearance of the spin Cherenkov effect, in which the DW begins to emit SW [109, 370]. However, this methodology to transfer stiffness to the magnetic soliton represents a challenge in terms of its experimental implementation, so it is reasonable to look for alternatives that intrinsically present the desired aforementioned features. AFM materials have some advantages over their FM counterparts, such as a THz-based SW resonance frequency [131, 132], a weak motion-induced deformation tendency [371], magnetic texture velocities up to tens of km/s [133, 134], being only limited by the maximum magnon group velocity unless its spatial extent approaches the atomic spacing, giving rise to superluminal processes [138, 139], and absence of the WB mediated by the magnetization tilting from the DW plane at rest [308, 309]. Moreover, due to the different unit cells necessary to describe FM and AFM that share the same crystallographic structure, which gives rise to different definitions of the order parameter [372], even when the AFM and FM DW dynamics are qualitatively equivalent for weak fields, for AFM it is described in the nonlinear σ-model framework, due to which it will obey the special relativity precepts, while in the case of FM it is governed by the conventional Galilean dynamics, as it was shown in Secs. 3.2 and 3.3, respectively [239, 273]. Due to the fact that, at the moment, it is not possible to experimentally track the AFM DW motion, it would be desirable to transfer some

of the benefits of these type of materials to the case of FM through the reduction of the dynamic magnetic texture description to a Lorentz-invariant SG-like equation, being possible to take advantage of their well-established detection techniques.

4.2 General dynamic framework in biaxial ferromagnets

When mapping the LL equation, which was introduced in Sec. 2.3, to a SG-like expression for the case of a FM, there is both the possibility of considering a system with a hard-axis anisotropy whose induced symmetry is broken by the application of an in-plane magnetic field, giving rise to a kink solution not compatible with a DW, or through a system with biaxial anisotropy. In the latter case, it is considered that there are uniaxial second-order hard-axis and easy-axis anisotropies, which define the plane at rest of the magnetic soliton and its topological nature. In this context, we will consider a bulk FM containing a 180° Bloch-type DW that lives, in the absence of external disturbances, on the yz plane, defining its easy-axis along the z-*th* axis, as depicted in Fig. 4.1 (a), moving along the x-*th* spatial direction, as exposed in Fig. 4.1 (b). The total magnetic energy per unit area, $E[\boldsymbol{m}]$, is given by $E[\boldsymbol{m}] = \int \mathrm{d}x\, e(\boldsymbol{m})$, where e represents the energy density which, in continuum approximation, can be written as $e(\boldsymbol{m}) = A(\partial_x \boldsymbol{m})^2 + e_\mathrm{a}(\boldsymbol{m}) + e_\mathrm{m}(\boldsymbol{m})$, where A represents the FM exchange stiffness constant, while e_a and e_m denote the anisotropy and magnetostatic energy densities, respectively. As stated above, we will consider a quadratic functional form of the anisotropy such that it is given by $e_\mathrm{a}(\boldsymbol{m}) = |K_x| m_x^2 - K_z m_z^2$, whose spatial distribution, for the case in which the anisotropy energy is defined in units of $2K_z$ and the parameter $\lambda = |K_x|/K_z$ is introduced, for the particular case of $\lambda = 10$, in Fig. 4.2 (a). On the other hand, the magnetostatic energy density for the case of a bulk FM in which the magnetization varies along the x-*th* axis, gives rise to a contribution of the form $e_\mathrm{m}(\boldsymbol{m}) = 2\pi M_\mathrm{s}^2 m_x^2$, being M_s the micromagnetic saturation magnetization, which gives result in the renormalization of the anisotropy constant K_x.

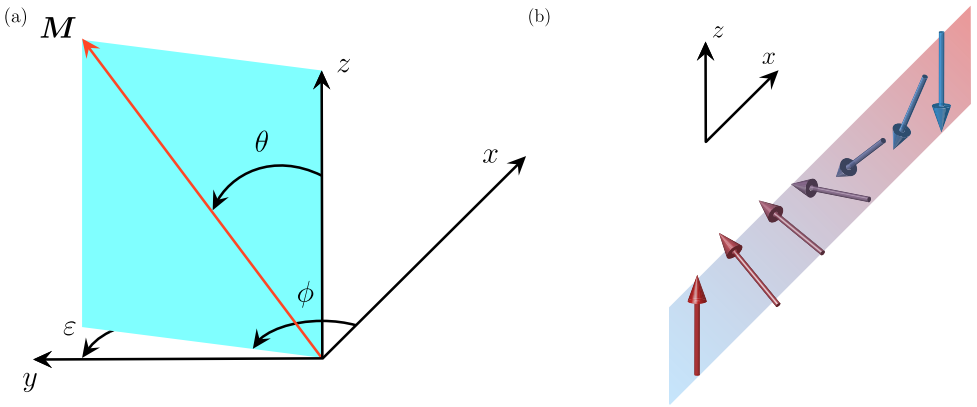

Figure 4.1: (a) Definition of the magnetization vector, $\boldsymbol{M}$, in terms of the polar, θ, and azimuthal, ϕ, angles relative to the Cartesian coordinate system. The angle $\varepsilon = \pi/2 - \phi$ accounts for magnetization deviations from the static yz DW plane. (b) Sketch of the magnetic soliton magnetization configuration along the x-*th* direction of motion.

Taking advantage of the fact that the unit magnetization vector can be expressed in terms of the spherical coordinates, such that $\boldsymbol{m} = \boldsymbol{m}(\theta, \phi)$, where the aforementioned angles are function of space, x, and of time, t, being expressed as $\theta(x,t)$ and

$\phi(x,t)$, the total energy density can be restated accordingly. By redefining the energy density in units of $2K_z$ and the lengths in units of the static DW width, given by $\Delta_0 = \sqrt{A/K_z}$, the energy can be rewritten as

$$e(\theta,\phi) = \frac{1}{2}\left[(\partial_x\theta)^2 + \left(1 + \lambda\cos^2\phi + (\partial_x\phi)^2\right)\sin^2\theta\right], \tag{4.1}$$

expression which only depends on the anisotropy-based dimensionless parameter λ. Accordingly, the corresponding Lagrangian density will be defined as $\mathcal{L}(\theta,\phi) = \cos\theta\,\dot{\phi} + e(\theta,\phi)$ [274, 286], as it is stated in Eq. (3.16), being the time expressed in units of the parameter $t_0 = 1/(\gamma H_a)$, where the anisotropy field is given by $H_a = 2K_z/M_s$. Taking into account the functional form in spherical coordinates of the LL equation

$$\sin\theta\,\dot{\theta} = -\frac{\delta e}{\delta\phi}, \qquad \sin\theta\,\dot{\phi} = \frac{\delta e}{\delta\theta}, \tag{4.2}$$

it is possible to find, from the energy density expression given by Eq. (4.1), which are the dynamic equations of the system in the absence of dissipation, which are given by

$$\sin\theta\,\dot{\theta} = \left[\lambda\,\cos\phi\,\sin\phi + \left(\partial_x^2\phi\right)\right]\sin^2\theta + \sin 2\theta\,\left(\partial_x\theta\right)\left(\partial_x\phi\right), \tag{4.3}$$

$$\sin\theta\,\dot{\phi} = \left[1 + \lambda\,\cos^2\phi + (\partial_x\phi)^2\right]\cos\theta\,\sin\theta - \left(\partial_x^2\theta\right). \tag{4.4}$$

The previous system of equations has been intensively explored in conjunction with its integrals of motion, which, in the context of characterizing the DW motion, are usually characterized in the steady-state Walker-like framework where $(\partial_x\phi) = 0$ [91], as it was exposed in Sec. 3.2. In our case, we will focus on general solutions ascribed to what is known as traveling wave *ansatz*, a premise under which the solutions of Eqs. (4.3) and (4.4) can be modeled as $\theta = \theta(\xi)$ and $\phi = \tilde{\omega}t + \phi_0(\xi)$, where $\xi = x - vt$, being v the magnetic soliton speed and $\tilde{\omega}$ the precession frequency in the DW moving frame [241]. In this context, where it is possible to interpret the moving magnetic texture as a bounded state of SW, the parameter v represents the group velocity, v_g, of the wave packet, that is, $v = v_g$. On the other hand, the frequencies in the laboratory frame, ω, and the moving frame, $\tilde{\omega}$, can be related via $\tilde{\omega} = \omega - \boldsymbol{k}\cdot\boldsymbol{v}_g$, where $\boldsymbol{v}_g = \partial\omega/\partial\boldsymbol{k}$ denotes the group velocity of the linear SW of the medium, while $\boldsymbol{k} = k\,\hat{\boldsymbol{x}}$ represents the related 1D wavevector and k refers to the associated wavenumber [241].

4.3 Small amplitude excitations-based magnetization texture characterization

4.3.1 Linear spin wave spectra description far from the magnetic soliton

Due to the anisotropy distribution of the medium, outside of the inhomogeneous transition that defines the magnetic soliton, the spin direction that minimizes the associated energy is defined along the *z-th* axis. In these uniform regions on both sides of the DW, which can be denoted as its tails, it is possible to assume the potential existence of small amplitude magnetic moment fluctuations. In this context, it is appropriate to rewrite the magnetization as a linear combination of a static, $\boldsymbol{m}_0$, and a dynamic, $\delta\boldsymbol{m}$, part, being possible to assume that the latter has all the space and time

dependency of the aforementioned vector, so that

$$\boldsymbol{m}\left(x,t\right)=\boldsymbol{m}_0+\delta\boldsymbol{m}\left(x,t\right), \tag{4.5}$$

where $\boldsymbol{m}_0=\hat{\boldsymbol{z}}$ and $\delta\boldsymbol{m}\left(x,t\right)=m_x\left(x,t\right)\,\hat{\boldsymbol{x}}+m_y\left(x,t\right)\,\hat{\boldsymbol{y}}$. In a similar way, the effective field can be decomposed as

$$\boldsymbol{H}_{\text{eff}}\left(x,t\right)=\boldsymbol{H}_{\text{eff}}^{0}+\boldsymbol{h}_{\text{eff}}\left(x,t\right), \tag{4.6}$$

where $\boldsymbol{H}_{\text{eff}}^{0}$ encapsulates those terms that depend on the static part of the magnetization, denoted by $\boldsymbol{m}_0$, while $\boldsymbol{h}_{\text{eff}}$ accounts for its dynamic contribution characterized by $\delta\boldsymbol{m}$. In this context, the LL equation, taking into account Eqs. (4.5) and (4.6), can be expressed as

$$\delta\dot{\boldsymbol{m}}=-\left[\left(\delta\boldsymbol{m}\times\boldsymbol{H}_{\text{eff}}^{0}\right)+\left(\boldsymbol{m}_0\times\boldsymbol{h}_{\text{eff}}\right)\right], \tag{4.7}$$

expression which admits plane wave solutions taking a functional form for the dynamic part of the magnetization such that

$$\delta m_{x,y}\left(x,t\right)=m_{x,y}^{0}\,e^{\mathrm{i}(kx-\omega t)}, \tag{4.8}$$

where $m_{x,y}^{0}$ represents the amplitude of the space- and time-dependent two magnetic moment components. Taking into account the energy density of the system, given by Eq. (4.1), in its vector form, it can be found that

$$-\mathrm{i}\omega\,\delta\boldsymbol{m}=\left(1+k^2\right)m_y\,\hat{\boldsymbol{x}}-\left(1+\lambda+k^2\right)m_x\,\hat{\boldsymbol{y}}, \tag{4.9}$$

which, in matrix notation, can be rewritten as

$$\begin{pmatrix}\mathrm{i}\omega & \omega_{k,x}\\ -\omega_{k,y} & \mathrm{i}\omega\end{pmatrix}\begin{pmatrix}m_x\\ m_y\end{pmatrix}=0, \tag{4.10}$$

where two frequencies have been introduced, being their functional forms given by $\omega_{k,x}=\left(1+k^2\right)$ and $\omega_{k,y}=\left(1+\lambda+k^2\right)$ [241]. To find non-trivial solutions to this set of equations, it is necessary that the involved determinant is zero, a premise under which it is possible to find that, in this case, the linear SW spectra will be given by

$$\omega^2=\left(1+k^2\right)\left(1+\lambda+k^2\right). \tag{4.11}$$

4.3.2 Critical velocities through complex small amplitude excitations

Interestingly, it is possible to exploit the small amplitude SW dispersion relation in the saturated FM region far from the DW center, as it is illustrated in Fig. 4.2 (b), to characterize the magnetic texture as long as its magnetization configuration does not change, contrary to what happens in the WB. This type of characterization requires that Eq. (4.11) is considered in the case of complex wavenumber, K, and frequency, Ω, circumstance under which it is obtained that

$$\Omega^2=\left(1+K^2\right)\left(1+\lambda+K^2\right), \tag{4.12}$$

where $\Omega=\omega+\mathrm{i}\kappa v$ and $K=k+\mathrm{i}\kappa$, denoting κ the associated scalar imaginary wavevector [373]. From now on, we will consider the case of stationary magnetic solitons, premise under which the precessional frequency in the comoving magnetic texture frame will be $\tilde{\omega}=0$, leading to a scenario in which the frequency in the laboratory frame, consistent with Sec. 4.2, can be denoted as $\omega=kv$, which also

implies that $\Omega = vK$. Calculating the squared complex phase velocity, v^2, through $v = \Omega/K$, it is possible to obtain, through Eq. (4.12), that

$$v^2 = \frac{1+\lambda}{K^2} + 2 + \lambda + K^2, \tag{4.13}$$

expression which, as shown in Fig. 4.3 (a), denotes the existence of two disconnected regions from each other in which the phase velocity is real, being given the speed in units of $\Delta_0/t_0 = 2\gamma\sqrt{AK_z}/M_s$. In the first one, which corresponds to the case of an imaginary wavenumber, $K = i\kappa$, and frequency, $\Omega = i\kappa v$, the speed will be real in the limited interval $-(1+\lambda) < K^2 < -1$, while for the second case, in which both the wavenumber and the frequency are real, such that $K = k$ and $\Omega = \omega$, it will be constrained in the scalar wavevector-based range $0 < K^2 < \infty$. Based on these aforementioned cases, it is possible to find, through Eq. (4.13), the functional form of the squared complex wavenumber, K^2, which is given by

$$K^2 = \frac{1}{2}\left(v^2 - \lambda\right) - 1 \pm \frac{1}{2}\sqrt{\left(v^2 - v_-^2\right)\left(v^2 - v_+^2\right)}, \tag{4.14}$$

from which the maximum and minimum squared scalar wavevector values in these regions can be expressed as $K_\pm^2 = \pm\sqrt{1+\lambda}$, which give rise to two limiting velocities denoted as $v_\pm = \sqrt{1+\lambda} \pm 1$, which governs the definition domain of the two intervals in which the phase velocity will be real, given by $[0, v_-]$ and $[v_+, \infty)$, respectively [373, 374].

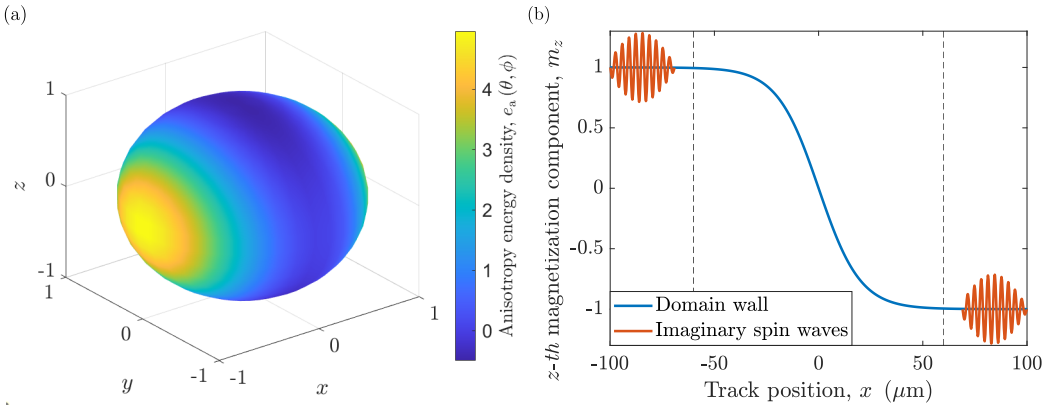

Figure 4.2: (a) Spatial distribution of the anisotropy energy density, $e_a(\theta,\phi)$, for the dimensionless anisotropy-based parameter being given by $\lambda = 10$. (b) Schematic of the linear SW of imaginary frequency, κv, and wavenumber, κ, which are given, respectively, by Eqs. (4.12) and (4.14), located in the DW tails that will allow to describe its dynamics as long as the magnetization configuration does not change.

4.3.3 Velocity-dependent exact stationary domain wall characterization

Interestingly, the critical velocity v_- plays the role of the maximum attainable DW speed in the case of a steady-state motion regime, and, therefore, it is greater than the Walker velocity, v_W, given by Eq. (3.41), as it is shown in Eq. (3.42), in the case in which the dynamics have been excited through the application of an external magnetic field or a spin-polarized current. In our case, in the absence of external stimuli that could create a potential tilting of the magnetization from the magnetic texture plane at rest, the azimuthal angle remains constant during the translational

process, such that $\phi(\xi) = \text{cte}$, value which varies depending on whether it has been considered a Bloch ($\phi = \pm\pi/2$), a Néel ($\phi = 0, \pi$), or a hybrid DW (other values of ϕ). Focusing on the case of a Bloch-like magnetic texture, which is the configuration compatible with the energy functional given by Eq. (4.1), it is possible to extract the first integral of the system, which can be written as

$$(\partial_x\theta)^2 + \sin^2\theta\,(\partial_x\phi)^2 = \left(1 + \lambda\cos^2\phi\right)\sin^2\theta, \tag{4.15}$$

expression which allows calculating the energy of the magnetic soliton as twice the exchange energy of the system [375]. In the Walker-type of solutions framework, where $\phi = \text{cte}$, it is possible to find that the linear DW energy density, E_{DW}, which is given in units of $2K_z\Delta_0$, and the spatial extent of the magnetic texture, Δ, can be expressed as

$$E_{\text{DW}}(v) = E_0\,\kappa(v), \qquad \Delta(v) = \frac{1}{\kappa(v)}, \tag{4.16}$$

where $E_0 = 2$ corresponds to the static case. Accordingly, it can be noticed that the magnetic soliton energy increases with the velocity and that, at the same time, the DW width dynamically contracts up to some limit values given, respectively, by

$$E_{\text{DW}}(v_-) = E_0\,(1+\lambda)^{1/4}, \qquad \Delta(v_-) = (1+\lambda)^{-1/4}, \tag{4.17}$$

which depend entirely on the dimensionless anisotropy-based parameter λ. Additionally, if the azimuthal angle is allowed to vary during the dynamic process, it is possible to verify that the DW plane orientation angle, ϕ, increases from $\pi/2$ to $\phi(v_-) = \arccos\sqrt{v_-/\lambda}$ as the magnetic soliton velocity increases over the range of values allowed by the $[0, v_-]$ interval.

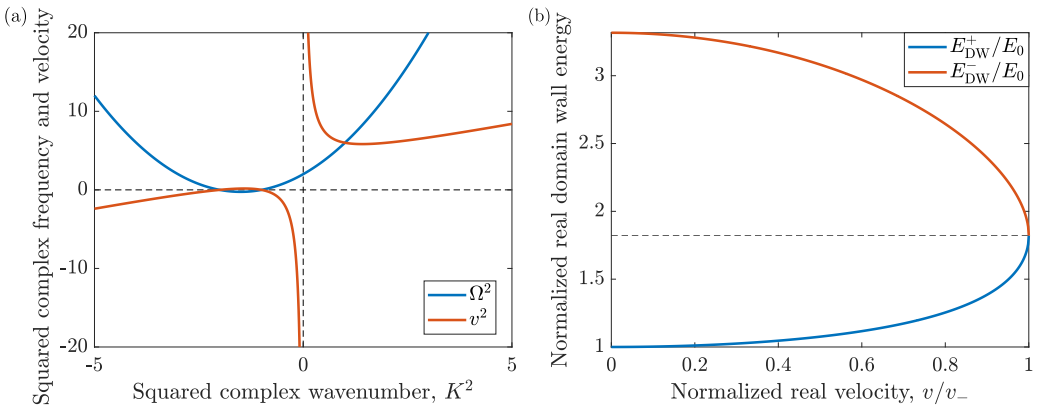

Figure 4.3: (a) Squared complex frequency, Ω^2, and velocity, v^2, in terms of the squared complex wavenumber, K^2, whose expressions are given, respectively, by Eqs. (4.12) and (4.13), for the case in which the dimensionless anisotropy-based parameter is given by $\lambda = 1$. Two regions disconnected from each other can be differentiated in which the speed is real. (b) Representation of the evolution of the normalized DW energy, $E^{\pm}_{\text{DW}}/E_0$, in the velocity-based interval $[0, v_-]$, for $\lambda = 10$, according to Eq. (4.16), for the two sign-dependent branches of the squared imaginary wavenumber, κ, according to Eq. (4.14), up to the limiting speed v_-.

Interestingly, from Eq. (4.14), for $v < v_-$, the positive sign on the right-hand side corresponds to the case of a stable solution of the system, given in this case by a Bloch DW, while the negative sign case results in an unstable Néel-like DW situation

[376]. This is because when the sign of the right-hand side of the previously mentioned expression is positive, the energy, E_{DW}^{+}/E_0, of the magnetic texture increases as its speed, v, increases, as it can be seen in Fig. 4.3 (b), at the same time as its spatial extension, Δ_+/Δ_0, contracts, which is represented in Fig. 4.4 (a), which is physically expected, obtaining an opposite situation when the sign is negative, which is encapsulated in the parameters E_{DW}^{-}/E_0 and Δ_-/Δ_0. Additionally, for the first of these cases, it is possible to perform a decomposition of the magnetic soliton energy, E_{DW}, in series of small velocities ($v \ll v_-$), which gives rise to

$$E_{\mathrm{DW}} = E_0\,\kappa_+ = \frac{E_0}{\sqrt{2}}\sqrt{(\lambda - v^2) + 2 - \sqrt{\left(v^2 - v_-^2\right)\left(v^2 - v_+^2\right)}} \simeq E_0 + \frac{E_0 v^2}{\lambda}, \quad (4.18)$$

from where it is possible to obtain that the DW Döring mass, m_{DW}, in absolute units, will be given by $m_{\mathrm{DW}} = 1/\left(2\pi\gamma^2\Delta_0\right)$ [80, 286]. Because of this, Eqs. (4.12) and (4.14), based on the interpretation that the magnetic soliton can be characterized by linear SW, with complex wavenumber and frequency, living in its tails, far from its center, give the correct result for relatively low velocities of the low-energy excitations of the medium for the interval given by $[0, v_-]$. On the other hand, it has been reported in literature that the unstable solution, encapsulated in Eq. (4.14), gives rise to a negative Döring mass, in which case instabilities emerge with respect to the inhomogeneous perturbation localized at the DW plane, which is known as the corrugation mode [376, 377].

4.3.4 Qualitative velocity-restricted magnetic configurations description

According to what is reported in the literature [241], the critical velocities $v_\pm$ separate regions that host different types of moving magnetic textures. Using a generalization of Eq. (4.14), which was based, as explained in Sec. 4.3.2, on a linear SW-based approximation, we will investigate if it is possible, at least, to account for some of the qualitative characteristics of the different magnetic configurations that reside in each dynamic regime, which has been shown in Fig. 4.4 (b). In the case of the $[0, v_-]$ sector, which corresponds to the case in which the wavenumber and the frequency are purely imaginary, that is, $K = \mathrm{i}\kappa$ and $\Omega = \mathrm{i}\kappa v$, respectively, the spatial location of the magnetization waves gives rise to the presence of DW. As it has been exposed in Sec. 4.3.3, in this case the magnetic soliton remains unchanged during its motion as its spatial extent contracts, conserving its topological charge (due to its time-independent boundary conditions given by $\theta(\pm\infty) = 0, \pi$), at least until the speed limit v_- is reached. On the other hand, in the interval (v_-, v_+), since both K and Ω are complex, there is coexistence of the imaginary and real components of the wavenumber, giving as a result that the former one decreases as the system speed approaches v_+, while the real component increases. In principle, in this case what exists is a non-topological soliton (which has boundary conditions that dictate that $\theta(\pm\infty) = 0$), which has a localized envelope governed by a confinement proportional to $1/\kappa$ at the same time that there are periodic pattern wavelength modulation of approximately $1/k$ on its envelope in the form of SW oscillations. The fact that this type of magnetic texture is not topologically protected can be ascribed, in contrast to the case of the DW in the interval $[0, v_-]$, to the appearance of a non-zero real component of the scalar wavevector. Finally, in the last section, given by $[v_+, \infty)$, only the presence of nonlinear SW is expected, which is outside of our main approximation, but yielding the logical analog nonetheless in our case reflected in Fig. 4.4 (b).

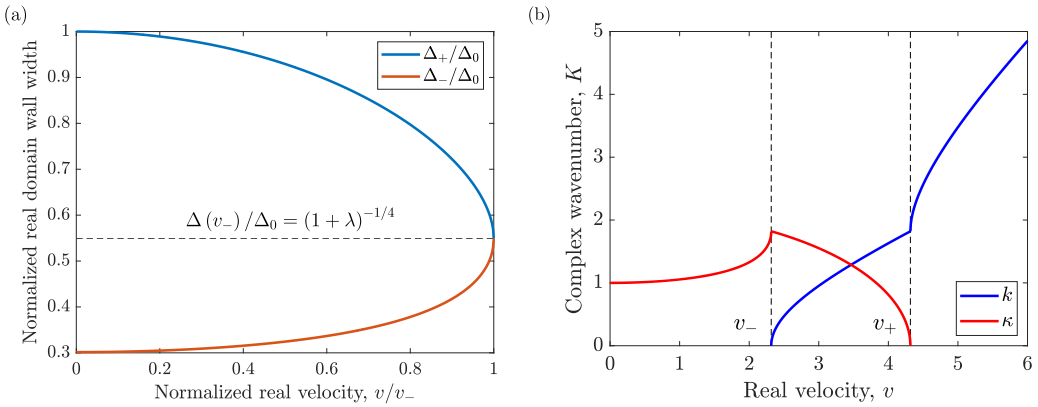

Figure 4.4: (a) Representation of the evolution of the normalized DW width, $\Delta_\pm/\Delta_0$, in the velocity-based interval $[0, v_-]$, for $\lambda = 10$, according to Eq. (4.16), for the two sign-dependent branches of the squared imaginary wavenumber, κ, according to Eq. (4.14), up to the limiting speed v_-. (b) Real, k, and imaginary, κ, wavenumber components obtained through the generalization of the linear SW dispersion as a function of the magnetic soliton velocity, v, according to Eq. (4.14), for $\lambda = 10$.

4.4 Mapping to a sine-Gordon equation in ferromagnets

4.4.1 Anisotropy parameter-independent general approach

Taking into account the parameterization of the space and time coordinates made in Sec. 4.2 in the context of the traveling wave *ansatz*, where $\xi = x - vt$, it is possible to rewrite Eqs. (4.3) and (4.4) through the reparametrization of the azimuthal angle variable, θ, through $\tan\theta/2 = \exp(-\eta)$ [241], in such a way that it can be obtained that

$$v\left(\partial_\xi \eta\right) = \lambda \cos\phi \sin\phi + \left(\partial_\xi^2 \phi\right) - 2\left(\partial_\xi \phi\right)\left(\partial_\xi \eta\right)\tanh\eta, \tag{4.19}$$

$$-v\left(\partial_\xi \phi\right) = \left(\partial_\xi^2 \eta\right) + \left[1 + \lambda\cos^2\phi + \left(\partial_\xi \phi\right)^2 - \left(\partial_\xi \eta\right)^2\right]\tanh\eta, \tag{4.20}$$

where it has been considered that it is possible to restate the time derivatives in such a way that $\partial_t = -v\partial_\xi$. In the steady-state Walker-type of solutions framework, where $\left(\partial_\xi \phi\right) = 0$, being the azimuthal angle constant, such that $\phi(\xi) = \phi_0$ [91], it is possible to reduce the above system of equations to

$$v\left(\partial_\xi \eta\right) = \lambda \cos\phi_0 \sin\phi_0, \qquad 1 + \lambda\cos^2\phi_0 = \left(\partial_\xi \eta\right)^2, \tag{4.21}$$

case for which there is a stable solution of the form $\eta(\xi) = \xi/\Delta(v)$ as long as the DW velocity does not exceed the critical speed v_-. This functional form of $\eta(\xi)$ allows us to obtain an expression of the form

$$\left(\partial_\xi^2 \theta\right) = \frac{1}{2\Delta^2}\sin 2\theta, \tag{4.22}$$

which is analogous to the static case, except for the velocity-dependence of the DW width, $\Delta = 1/\kappa(v)$. Interestingly, it is possible to rewrite the dynamical expression for the polar angle, θ, into a SG-like equation in the context of Walker-like solutions, not needing to make any assumptions about the dimensionless anisotropy-based

parameter λ, which results in

$$\left(\partial_x^2\theta\right) - \frac{1}{v_-^2}\,\ddot{\theta} = \frac{1}{2\Delta_e^2}\,\sin 2\theta, \tag{4.23}$$

where the DW width $\Delta_e = \Delta/\sqrt{1-(v/v_-)^2}$ can be expressed in a relativistic form, playing, in this case, v_- the role of the maximum attainable DW velocity. However, even though the solution obtained in the Walker-based framework is stable, it is not possible to obtain this expression through an effective relativistic Lagrangian, because the kinetic part of the Lagrangian density in FM, which has a functional form $\mathcal{L}_{\text{kin}} = \cos\theta\,\dot{\phi}$, or, equivalently, $\mathcal{L}_{\text{kin}} = -\phi\,\sin\theta\,\dot{\theta}$, does not provide the required terms in the dynamic equations. For this reason, this approach to find relativistic signatures in FM systems is not rigorous.

4.4.2 Negligible out-of-easy-plane angle-based variational approach

4.4.2.1 Anisotropy-based strong magnetization constriction in the domain wall plane at rest

It is possible to take advantage of the presence in the functional form of the configurational energy density, exposed in Eq. (4.1), of the anisotropy-based parameter λ to try to emulate the real scenario that occurs in AFM [272]. In this type of system, due to the order of magnitude of the exchange interaction, the magnetization is strongly constrained in the DW plane at rest, which prevents the appearance of appreciable tiltings from it, as a result of what it is stated in Sec. 3.3, which would lead to the potential appearance of WB. In this case, in the limit $\lambda \gg 1$, which can occur in soft magnetic materials like permalloy with an induced-uniaxial magnetic anisotropy K_z, where $\lambda = 2\pi M_s^2/K_z \gg 1$, with $K_x = 0$, having reported ratios of up to $\lambda = 21$ [91], the closer it will be to replicating the aforementioned behavior. In our case, we will work taking into account that the *x-th* magnetization component, m_x, perpendicular to the easy-plane, has to be small, that is is, $m_x \ll 1$, in the aforementioned anisotropy-based limiting case, which will allow performing perturbation theory with respect to it. To do this, it is possible to rewrite the remaining components of the magnetic moment as a function of a new scalar field, $\psi\,(x,t)$, in such a way that

$$m_y = \sqrt{1-m_x^2}\,\sin\psi, \qquad\qquad m_z = \sqrt{1-m_x^2}\,\cos\psi, \tag{4.24}$$

definitions which are consistent with the requirement that the magnetization vector, $\boldsymbol{m}$, has to be unitary. Additionally, within the different possibilities to parameterize m_x, it has been chosen that it will be given by $m_x = \varepsilon\,\sin\psi$, where ε represents the angular variable that accounts for the potential deviations from the DW plane at rest, such that $\varepsilon = \pi/2 - \phi$, as stated in Fig. 4.1 (a), where it will be assumed that, for $\lambda \gg 1$, $\varepsilon\,(\lambda) \to 0$. Taking into account the initial spherical coordinate parameterizations (θ,ϕ) through the components of the magnetization vector $\boldsymbol{m}$, it is possible to find how they relate to the new set of parameters (ψ,ε), which will be given by

$$\cos\theta = \sqrt{1-\varepsilon^2\sin^2\psi}\,\cos\psi, \qquad\qquad \cos\phi = \frac{\varepsilon}{\sqrt{1+\varepsilon^2\cos^2\psi}}. \tag{4.25}$$

Interestingly, it is possible to find, through the second equation encapsulated in Eq. (4.25), in the limit $\varepsilon \to 0$, that it can be obtained that $\cos\phi = \varepsilon + \mathcal{O}\left(\varepsilon^3\right)$ and $\sin\phi = 1 + \mathcal{O}\left(\varepsilon^2\right)$. Substituting these Taylor series expansions into the trigonometric functions containing the azimuthal angle, ϕ, into the dynamic expressions given in Eq. (4.21), which assume that $\varepsilon\left(\xi\right) = \text{cte}$, it is possible to find that

$$v\left(\partial_{\tilde{\xi}}\eta\right) = \lambda\varepsilon, \qquad \left(\partial^2_{\tilde{\xi}}\eta\right) = 0, \qquad 1 + \lambda\varepsilon^2 = \left(\frac{\lambda\varepsilon}{v}\right)^2, \tag{4.26}$$

where the last of these equations has a solution given by $\varepsilon\left(\lambda, v\right) = v/\left(\lambda\sqrt{1 - v^2/\lambda}\right)$. Accordingly, a new critical velocity, $c = \sqrt{\lambda}$, can be introduced, which verifies that, for $\lambda \gg 1$, $c = v_-$. In the same line, the originally introduced angular variable $\theta\left(x,t\right)$ will match the new variable $\psi\left(x,t\right)$ for very low values of the parameter ε, since

$$\cos\theta = \sqrt{1 - \varepsilon^2\sin^2\psi}\,\cos\psi \simeq \left(1 - \frac{\varepsilon^2\sin^2\psi}{2}\right)\cos\psi \simeq \cos\psi, \tag{4.27}$$

if the terms of order $\mathcal{O}\left(\varepsilon^2\right)$ are neglected. In this context, taking advantage of the previously discussed approximate solution for Eq. (4.26), given by

$$\eta\left(\xi\right) = \frac{\xi}{\Delta'\left(v\right)} = \frac{\xi}{\sqrt{1 - \left(v/c\right)^2}}, \tag{4.28}$$

a SG-like expression for the DW profile angle, $\theta\left(x,t\right) = 2\arctan\exp\left[-\eta\left(\xi\right)\right]$, can be deduced, such that

$$\left(\partial^2_x\theta\right) - \frac{1}{c^2}\,\ddot{\theta} = \frac{1}{2}\,\sin 2\theta, \tag{4.29}$$

which constitutes a particular case of Eq. (4.23) in which $\Delta = \Delta'$ and $v_- = c$. This last equation is valid not only for the case of the Bloch-type DW allowed in our system in accordance with Eq. (4.1), which propagates in the direction perpendicular to the easy-plane, but also, for example, for the case of a Néel DW that moves parallel to the direction that defines the potential easy-axis symmetry-breaking anisotropy in the medium [378].

In agreement with Eq. (4.29), in the limit $\lambda \gg 1$, its Lorentz-invariant form can be exploited to write the DW energy, E'_{DW}, and width, Δ', as

$$E'_{\text{DW}}\left(v\right) = \frac{E_0}{\sqrt{1 - \left(v/c\right)^2}}, \qquad \Delta'\left(v\right) = \sqrt{1 - \left(v/c\right)^2}, \tag{4.30}$$

expressions which show a quantitative behavior far from that expected from a system that legitimately shows relativistic-signatures for finite values of the dimensionless parameter λ, as it can be seen in Fig. 4.5, matching when this constant is infinitely large. As it was done for the energy of the exact DW solution in Eq. (4.18), it is possible to decompose, for low speeds ($v^2/c^2 \ll 1$), the energy given by Eq. (4.30), situation in which it is obtained that

$$E'_{\text{DW}} \simeq E_0 + \frac{E_0 v^2}{2c^2}, \tag{4.31}$$

whose associated Döring mass, $m_{\text{DW}} = E_0/c^2$, matches the one obtained in Sec. 4.3.3. However, in the limit $v \to c$, according to Eq. (4.29), the energy is singular,

$E'_{\mathrm{DW}}(v) \to \infty$, and the spatial extent of the magnetic soliton matches the extreme case of a relativistic theory, $\Delta'(v) \to 0$, results which are non-physical since, at the same time, the parameter $\varepsilon(\lambda, v) = v/\left(\lambda\sqrt{1 - v^2/\lambda}\right)$, diverges, and cannot be considered small anymore. To match the case of the exact solution to the system given by Eqs. (4.3) and (4.4), the returned result should have a finite energy and DW width in the limiting case $v \to v_-$, as the one exposed in Eq. (4.17). Therefore, although one can write a SG-like equation like the one exposed in Eq. (4.29) and the relativistic expressions in Eq. (4.30), these are only valid in the limit of small DW velocities, $v^2/c^2 \ll 1$, being a great approximation in this case. As a conclusion, the approximate solutions, coded through Eq. (4.30), are asymptotically exact for $\lambda \gg 1$, provided that $v^2/c^2 \ll 1$, a situation in which they are far from the singularities they treasure, being virtually indistinguishable from the exact solutions for a biaxial FM obtained through Eq. (4.14).

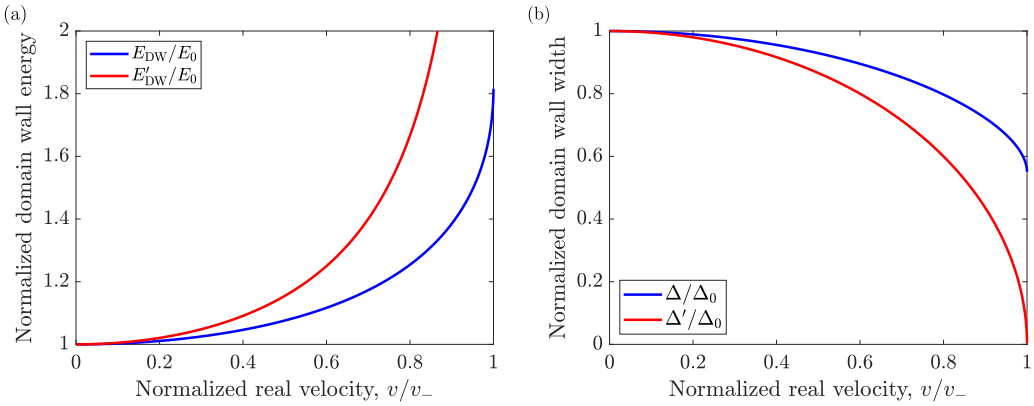

Figure 4.5: (a) Comparison between the normalized energy of a moving DW, E_{DW}/E_0, given by Eq. (4.16), for $\lambda = 10$, and the one obtainable through a relativistic Lorentz-like expression, E'_{DW}/E_0, like the one exposed in Eq. (4.30), where the limiting speed is given by the maximum SW phase velocity v_-. (b) Comparison between the normalized DW width, Δ/Δ_0, given by Eq. (4.16), for $\lambda = 10$, and the one obtainable through a relativistic Lorentz-like expression, Δ'/Δ_0, like the one exposed in Eq. (4.30), where the limiting speed is given by the maximum SW phase velocity v_-.

4.4.2.2 Solutions under conditions incompatible with real domain wall

Along the same lines as in the previous section, in the context of steady-state Walker-like solutions, in the limit $\lambda \gg 1$, there is another approximate solution proposed in the literature [379]. In this case, the *x-th* magnetization component, m_x, takes on another functional form, given by $m_x(\xi') = \varepsilon_s \sin\Psi(\xi')$, where $\varepsilon_s = V/(R\Delta_s)$, $\Psi(\xi') = 2\arctan\exp\xi'/\Delta_s$, and $\xi' = x - Vt$, where it is necessary to introduce some parameters given by $V = \sqrt{R}\,v$, $V_0 = \sqrt{R}$, $\Delta_s = \sqrt{R/\gamma'}\sqrt{1 - (V/V_0)^2}$, and $V_0 = \sqrt{R}$, framework in which the aforementioned limit takes the form $R^2/\gamma' = \lambda \to \infty$. The newly introduced function, $\Psi(\xi')$, also satisfies a SG-like expression of the form

$$\left(\partial_x^2\Psi\right) - \frac{1}{V_0^2}\ddot{\Psi} = \frac{\gamma'}{2R}\sin 2\Psi, \tag{4.32}$$

equation which constitutes a particular case of Eq. (4.23) for $\Delta_e = \sqrt{R/\gamma'}$. In this context, the previously defined DW width Δ_s, in the limit $\lambda \to \infty$, tends to infinity for any finite velocity, V, as long as it is verified that $V < V_0$, which results in the vanishing of the right-hand side of Eq. (4.32). Particularly, in the aforementioned expression, the maximum speed, V_0, given by $V_0 = (\gamma'\lambda)^{1/4}$, differs from the one introduced in Sec. 4.4.2.1, and it must be equal to $v_- = \sqrt{\lambda}$. In the case in which the parameter γ' is redefined, such that $\gamma' = 1$ [380], it is possible to recover the same form of the SG-like expression exposed in Eq. (4.23). Concerning the small parameter ε_s, basis of the perturbation theory approximation, whose functional form resembles the one introduced in the previous section, given by $\varepsilon = v/\left(\lambda\sqrt{1 - v^2/\lambda}\right)$, it is also singular as the velocity V approaches the critical speed $V_0 = \lambda^{1/4}$ due to the definition of the DW width Δ_s. This shared feature constitutes a signature of all those solutions to Eq. (4.23) in the steady-state Walker-type of solutions framework where $\phi(\xi) = \text{cte}$. However, the solution, parameterized through the parameter Ψ, to Eq. (4.32) presents additional problems due to the assumptions about the anisotropy constants of the system, since it is theorized that K_x is proportional to R and that K_z is proportional to $1/R$, which means that, in the limit $\lambda \gg 1$, the easy-axis anisotropy verifies that $K_z \to 0$, which would imply the disappearance of the DW.

4.4.3 Singularity avoidance going beyond Walker-type of solutions

Based on what has been discussed so far in the context of the Walker-type of solutions, where it is assumed that $\varepsilon(\xi) = \text{cte}$, it is possible to infer that, to properly evaluate the limit $\lambda \gg 1$, $m_x \ll 1$, and to obtain a reasonable SG-like expression for finite velocities, $v < v_-$, it is necessary to assume that the azimuthal angle, $\varepsilon(\xi) \ll 1$, is a function not only of time, but also of space, to solve Eqs. (4.19) and (4.20). In this line, the solutions obtained previously could be refined, avoiding the appearance of the singularity at high speeds at $v \to c$, context in which, if the energy is lower than in the steady-state case where $\varepsilon \neq \varepsilon(x)$, would lead to a stable solution, which could confirm that it is possible to rigorously reduce the DW dynamics in biaxial FM, at least for low velocities, to a SG-like expression. At the moment, although it has been shown heuristically that it is possible to map the LL equation to this kind of form by going beyond the Walker approximation in the perturbation theory framework [381], this attempt is not completely satisfactory since it assumes that the spatial and time derivatives of magnetization are independent [382, 383]. Due to this, this attempt contradicts the parameterization of the steady-state DW motion through the traveling wave *ansatz*, since it is assumed that the spatial derivative of the angular variable is zero, while the temporal one is finite. The most consistent handling of this type of situation is beyond the current theory of 1D magnetic solitons.

4.4.4 Antiferromagnetic-like kinetic term scenario

In our quest to find a SG-like dynamical equation for FM, we have to address what functional form the kinetic term, $\mathcal{L}_{\text{kin}}$, has to have in order to obtain a consistent theory. The goal should be to get the same as in AFM in the nonlinear σ-model framework, where $\mathcal{L}_{\text{kin}} \propto \dot{\theta}^2$, as it was shown in Eq. (3.59) [384]. Interestingly, for FM, it is possible that the term of the LL equation that accounts for the time evolution can be written, indistinctly, through two options, given by

$$\mathcal{L}_{\text{kin}} = -\cos\theta\,\dot{\phi}, \qquad \mathcal{L}_{\text{kin}} = -\phi\sin\theta\,\dot{\theta}, \tag{4.33}$$

which, after applying the EL equation, give rise to

$$\frac{\partial \mathcal{L}_{\text{kin}}}{\partial \theta} - \partial_t \left(\frac{\partial \mathcal{L}_{\text{kin}}}{\partial \dot{\theta}} \right) = 0 \rightarrow \sin\theta\, \dot{\phi} = 0, \tag{4.34}$$

$$\frac{\partial \mathcal{L}_{\text{kin}}}{\partial \phi} - \partial_t \left(\frac{\partial \mathcal{L}_{\text{kin}}}{\partial \dot{\phi}} \right) = 0 \rightarrow \sin\theta\, \dot{\theta} = 0, \tag{4.35}$$

for both parameterizations of the geometric term. Evaluating Eq. (4.3) for the azimuthal angle parameterization introduced in Sec. 4.4.2.1, such that $\phi(\xi) = \pi/2 - \varepsilon(\xi)$, for the Walker-type of solutions, in the limit $\varepsilon \ll 1$, it can be found that

$$\sin\theta\, \dot{\theta} = \lambda \sin^2\theta \cos\phi \sin\phi \simeq \lambda\varepsilon \sin^2\theta, \tag{4.36}$$

from where it can be deduced that $\sin\theta = \dot{\theta}/(\varepsilon\lambda)$, which results in that the second expression in Eq. (4.33) can be rewritten as $\mathcal{L}_{\text{kin}} = \dot{\theta}^2/\lambda$. Accordingly, the Lagrangian density, given in this case by $\mathcal{L} = e(\theta,\phi) - \dot{\theta}^2/\lambda$, where the energy density $e(\theta,\phi)$ is depicted in Eq. (4.1), can be expressed, within the limit $m_x \ll 1$, as

$$\mathcal{L} = \left(\partial_x^2\theta\right) - \frac{1}{c^2}\ddot{\theta} + \sin^2\theta, \tag{4.37}$$

expression which is compatible with a SG equation, where it has been taken into account that $c = \sqrt{\lambda}$, in accordance with what is stated in Sec. 4.4.2.1.

On the other hand, for the uniaxial AFM case, the SW dispersion relation is given, as opposed to the biaxial FM case exposed through Eq. (4.11), by

$$\omega^2 = \omega_0^2 + c^2k^2, \tag{4.38}$$

where ω_0 represents the anisotropy-based zero-momentum resonance frequency [385]. Using the same approach as that used in Sec. 4.3.2, where a generalization to complex wavenumbers was used, it is possible to find that the limiting velocities obtained in FM, in this case, are equivalent, $v_\pm = c$, as well as that, in the context of a purely imaginary scalar wavector, κ, the dependency $\kappa(v)$, in units of $\kappa_0 = \omega_0/c$, is given by the Lorentz factor-based functional form

$$\kappa(v) = \frac{1}{\sqrt{1 - \left(\frac{v}{c}\right)^2}}, \tag{4.39}$$

being given the equivalent expression in the case for FM by Eq. (4.14). Through this, it is possible to immediately write a relativistic form for the non-normalized energy, $E_{\text{DW}}(v)$, and DW width, $\Delta(v)$, as it was done in Sec. 4.3.3, in such a way that

$$E_{\text{DW}}(v) = \frac{E_0}{\sqrt{1 - \left(\frac{v}{c}\right)^2}}, \qquad \Delta(v) = \Delta_0 \sqrt{1 - \left(\frac{v}{c}\right)^2}, \tag{4.40}$$

expressions which are exact in contrast to those obtained for the case of biaxial FM [239].

4.5 Field-induced relativistic-like signatures in ferromagnets

As we have discussed in Sec. 4.4, specifically in those cases based on the variational principle, which were exposed in Sec. 4.4.2, the DW contracts during the dynamic

process, getting closer to the Lorentz factor-mediated trend as the dimensionless anisotropy-based parameter λ increases. In real systems, in the presence of dissipative effects governed by the Gilbert damping parameter, α, the movement of the magnetic texture can be induced through a magnetic field or an electric current. As discussed earlier in Sec. 3.2, in the case of FM there is a limit to the stable dynamics of magnetic solitons, known as WB, whose appearance seems to be possible to delay as λ increases. With this in mind, the configurational energy density, given by Eq. (4.1), can be modified to include a magnetic field applied along the positive *z-th* axis, being given by $\boldsymbol{H} = H\,\hat{\boldsymbol{z}}$, such that

$$e\left(\theta,\phi\right) = \frac{1}{2}\left[\left(\partial_x\theta\right)^2 + \left(1+\lambda\cos^2\phi + \left(\partial_x\phi\right)^2\right)\sin^2\theta\right] - h\cos\theta, \tag{4.41}$$

where $h = H/H_{\mathrm{a}}$ represents the reduced magnetic field. Accordingly, the dynamic description given by Eqs. (4.3) and (4.4) can be rewritten, taking into account the LLG equations in spherical coordinates

$$\sin\theta\,\dot{\theta} = -\frac{\delta e}{\delta\phi} - \alpha\sin^2\theta\,\dot{\phi}, \qquad\qquad \sin\theta\,\dot{\phi} = \frac{\delta e}{\delta\theta} + \alpha\dot{\theta}, \tag{4.42}$$

for the Walker-type of solutions, $\left(\partial_x\phi\right) = 0$, such as

$$\dot{\theta} = \lambda\,\cos\phi\,\sin\phi\,\sin\theta, \tag{4.43}$$

$$\alpha\dot{\theta} - h\sin\theta = \left(1+\lambda\,\cos^2\phi\right)\cos\theta\,\sin\theta - \left(\partial_x^2\theta\right), \tag{4.44}$$

where it can be seen through the left-hand side of Eq. (4.44) that for the system to accommodate the same kind of soliton-like solutions as those for Eqs. (4.3), (4.4), (4.19), and (4.20), it is necessary that the dissipative and the Zeeman terms compensate each other, such that $\alpha\dot{\theta} = h\sin\theta$, which implies that the DW experiences a steady-state motion. Taking into account that, for a constant azimuthal angle, $\phi = \phi_0$, the solutions to the system given by Eqs. (4.19) and (4.20) were given by $\eta\left(\xi\right) = \xi/\Delta\left(v\right)$, it is possible to combine Eq. (4.19) and (4.43) to get

$$\frac{\dot{\theta}}{\sin\theta} = \lambda\cos\phi_0\,\sin\phi_0 = \frac{v}{\Delta\left(v\right)} = \frac{h}{\alpha}, \tag{4.45}$$

where the velocity-dependent DW width, $\Delta\left(v\right) = 1/\kappa\left(v\right)$, will be dictated by Eq. (4.14). Finally, the previous expression can be restructured in such a way that it is found, for a steady-state process, how the magnetic soliton velocity, v, evolves as a function of the magnetic field, h, such that

$$v\left(h\right) = \frac{h}{\alpha\sqrt{1+\left(\frac{h}{\alpha c}\right)^2}}. \tag{4.46}$$

To test how well reality fits the exposed theory, we perform ASDS, in which the LLG equation is solved numerically, site by site, through a fifth-order Runge-Kutta method, since it is foreseeable that the DW shrinks, for high velocities, to widths of the order of 1 nm, failing the continuum approximation. The simulated system consists of a 1D FM chain composed of 60000 atomic sites, in which the layered AFM Mn_2Au is taken as a reference, being the AFM exchange bonds nullified, being characterized by an exchange integral $I = 1.588\cdot10^{-21}$ J, an atomic magnetic moment $\mu_{\mathrm{s}} = 4\mu_{\mathrm{s}}$, and a lattice constant $a_0 = 3.328$ Å [386, 387]. Additionally, atomistically, it

has been taken into account that the hard-axis anisotropy is given by $|K_x|a_0^3 = I$, that the easy-axis anisotropy constant has a value given by $K_z a_0^3 = 1.302 \cdot 10^{-24}$ J, and that the Gilbert damping parameter is expressed by $\alpha = 0.001$. It should be noted that these values have been adopted to ensure the validity of the limit $m_x \ll 1$, $\lambda \gg 1$, verifying that the dimensionless parameter λ is given by $\lambda = 1221$. Rewriting the atomistic parameters as micromagnetic ones, it is possible to find that $M_s = 1006$ kA/m, $A = 4.77$ pJ/m, $|K_x| = 43.08$ MJ/m^3, and $K_z = 0.0353$ MJ/m^3, from which it can be deduced that the critical velocity limiting the stable DW motion takes the value $v_- = 4.869$ km/s, the latter one being in very good agreement with the simulated maximum magnon group velocity, $c = 4.981$ km/s. Taking into account that the velocity-dependent magnetic soliton spatial extension, Δ, can be denoted, in the limit $\lambda \gg 1$, as in the case exposed in Eq. (4.30), with the simulated DW width at rest given by $\Delta_0 = 11.62$ nm, it is possible to see how well these expressions fit the simulations, which is shown in Fig. 4.6. As it can be seen, the agreement is very good, verifying the saturation of the speed of the magnetization texture as the value of the magnetic field increases, which is exposed in Fig. 4.6 (a), at the same time that a relativistic-like contraction of the spatial extension is observed in Fig. 4.6 (b). The velocity, $v(h)$, as depicted in Eq. (4.46), is no longer an arbitrary parameter, contrary to what was seen in previous sections, being qualitatively equivalent, for low fields, to what is expected for small ratios λ. Additionally, it shows the same type of behavior, at high values of the external stimulus, than in the case of weak FM-like $YFeO_3$, where the mobility, v/H, is different, since it is governed by the exchange and the DMI [388]. The fact that there is a good correspondence between the analytical expressions and the simulated results for the studied case indicates that the effect of the out-of-easy-plane variable, ε, is negligible, so that the Walker-type of solutions framework is a good approximation up to, at least, v_- as long as $\lambda \gg 1$.

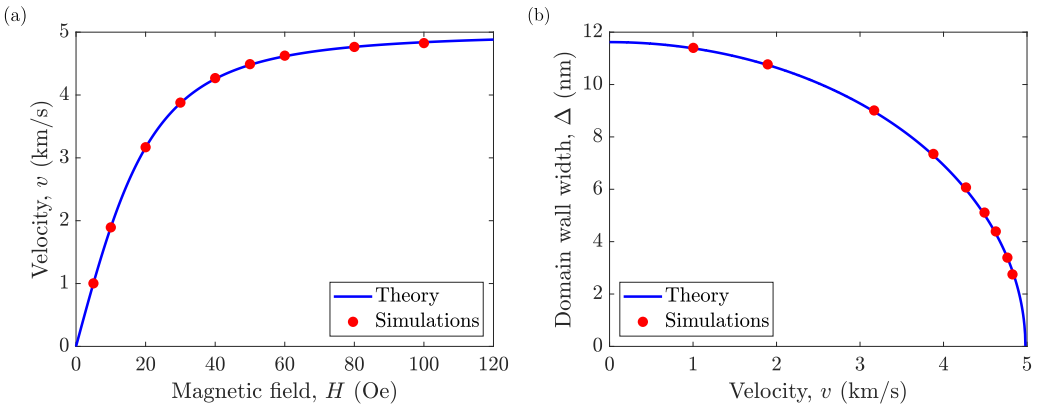

Figure 4.6: Comparison with ASDS for a FM layer with $\lambda = 1221$ of the relativistic-like signatures for steady-state DW dynamics theoretically obtained through (a) its speed, v, saturation as the applied magnetic field, H, increases, accordingly to Eq. (4.46), and (b) the contraction of its spatial extent, Δ, as the speed of the magnetic soliton increases, obtained from Eq. (4.30).

4.6 Conclusions

In this chapter, we have addressed the reduction of the dynamic LL equation to a relativistic SG-like expression for the case of a biaxial FM in search of mimicking the absence of the WB in AFM through the avoidance of the magnetization tilting from

the DW plane at rest. For this, we have used the possibility of accurately characterizing the energy and spatial extension of the magnetic soliton through the dispersion relation of the linear SW with imaginary wavenumber and frequency that live in its tails, its speed being limited by the maximum phase velocity of these low-energy excitations of the magnetic medium. In the Walker-type of solutions framework, it is possible to find that the reduction of the system equation to a SG-like expression is formally possible, whether or not an assumption is made about the value of the dimensionless hard-axis to easy-axis anisotropy ratio. However, only in the case in which this anisotropy-based parameter is very large is it possible to find a physically consistent result, where the assumption of negligible cantings of the out-of-easy-plane angle is essential to obtain an appropiate functional form of the kinetic Lagrangian term. Nevertheless, this description of the steady-state DW motion is only valid for the case in which its speed is small enough compared to the critical velocity of the system, asymptotically tending its energy and width to the exact expressions. To avoid the hypothetical small canting angle divergence, it is necessary, a priori, to work outside the Walker-type of solutions framework, which is beyond the current 1D theory of magnetic solitons, where the spatial and temporal derivatives of the magnetization cannot be considered as independent to verify the traveling wave *ansatz*. Through ASDS, the relativistic-like signatures of the DW dynamics in biaxial FM have been verified for high values of the hard-axis to easy-axis anisotropy ratio, such as the velocity saturation as the applied external stimulus increases and its consequent contraction following a Lorentz-based trend. The fact that the use of micromagnetic simulations is avoided is due to the predicted shrinkage of the spatial extension of the magnetic soliton to values where the continuum approximation fails, which highlights that this type of process must be taken into account when choosing the computational discretization method of the system, even in the case of FM in the absence of temperature. These remarkable results open the door to implementing real biaxial FM-based experiments with high values of hard-axis to easy-axis anisotropy ratios to delay the extinction of the stable steady-state DW motion without using complicated geometries.

Chapter 5

Inertial domain wall characterization in layered multisublattice antiferromagnets

5.1 Massive magnetic soliton dynamics in antiferromagnets

In those spintronics devices that use DW as information carriers, it is desired to have ultrafast magnetization dynamics with the shortest possible response time for a reasonable magnitude of the external stimulus to optimize its operability. This being the case, the use of AFM textures is advantageous due to the high velocities achievable in the special relativity framework [133, 134], being, however, not only important how fast they can move, but also how long it takes them to move stably at a certain speed. In this context, interestingly, AFM show a low exchange-mediated static DW mass and a weak motion-based deformation tendency [306, 371], and it is usually possible to describe their dynamics through a Newton-like second-order differential equation of motion [307, 389], as it can be seen in Eq. (3.64). Because of this, in the presence of dissipation and external forces, the accurate characterization of the magnetic soliton position is limited by the inherent inertial effects. Accordingly, it is essential to characterize in detail how a DW evolves in the acceleration and deceleration processes under the action of different time-dependent stimuli. However, in the literature there is a clear absence of analysis about the dynamic inertial signatures of a magnetic texture in real AFM materials with an invariant spin space, without time-dependent anisotropy energy gradients in the sample [390], where the complete set of exchange interactions are taken into account, and there are also certain claims about a hypothetical universal AFM DW massless-like behavior [391]. Additionally, the main problem in taking advantage of this type of system lies in its low magnetic susceptibility, which makes it extremely difficult to stimulate them through static magnetic fields [140, 141], as it can be deduced from what it is exposed in Sec. 3.3. To directly excite an AFM it is necessary to generate an effective magnetic field that is staggered, that is, that its relative direction in each magnetic sublattice is antiparallel with respect to each other. Interestingly, this occurs naturally in the case of Mn_2Au and CuMnAs, a pair of complex layered metallic AFM that can be excited efficiently through current-induced SO fields [148, 149], and whose magnetic state can be characterized by combining conventional MR effects with image characterization in real space [153, 340, 392, 393], as it is discussed in Sec. 3.6. The fact that it has been possible to experimentally visualize DW in these type of materials [170, 394, 395], as well as that there are proposals based on thermoelectric effects to

track their positioning [164, 165], which it is proposed in Sec. 3.6.3, motivates their theoretical dynamic exploration keeping in mind their potential for AFM DW-based racetrack memories, all-spintronics architectures, or memristive-like neuromorphic computing approaches [114, 116, 166].

5.2 Magnetic and crystallographic description of the layered antiferromagnet Mn_2Au

To carry out our study, we will take into consideration the layered collinear AFM Mn_2Au, which stands out for being a good conductor, having a strong magnetocrystalline anisotropy [161, 387, 396], and a Néel temperature well above the room temperature [386]. To characterize this system, which is shown in Fig. 5.1 (a) [397], it is possible to write the interactions that make up its configurational energy, E, for its conventional tetragonal unit cell [139, 150], which will be given by

$$E = -\sum_{\langle i,j\rangle} \mathcal{J}_{ij}\, \boldsymbol{m}_i \cdot \boldsymbol{m}_j - K_{2\perp} \sum_i (\boldsymbol{m}_i \cdot \hat{\boldsymbol{z}})^2 - K_{2\parallel} \sum_i (\boldsymbol{m}_i \cdot \hat{\boldsymbol{y}})^2 - \frac{K_{4\perp}}{2} \sum_i (\boldsymbol{m}_i \cdot \hat{\boldsymbol{z}})^4 - \frac{K_{4\parallel}}{2} \sum_i \left[(\boldsymbol{m}_i \cdot \hat{\boldsymbol{u}}_1)^4 + (\boldsymbol{m}_i \cdot \hat{\boldsymbol{u}}_2)^4 \right] - \mu_0 \mu_s \sum_i \boldsymbol{m}_i \cdot \boldsymbol{H}_i^{SO}, \tag{5.1}$$

where the unit vectors $\hat{\boldsymbol{u}}_{1,2}$ represent the in-plane xy-based directions $\boldsymbol{u}_1 = [110]$ and $\boldsymbol{u}_2 = [1\bar{1}0]$. As it can be seen in Fig. 5.1 (a), the lattice constant along the *x-* and *y-th* spatial directions in the basal planes is given by $a_0 = 3.328$ Å, while the height of the unit cell along the *z-th* axis is characterized by $c = 8.539$ Å [386]. Considering the conventional unit cell, it is possible to appreciate that there are two Mn atoms per each type of sublattice, denoted as A and B, which gives rise to a total of four magnetic atoms. In fact, the magnetic moment associated with each of these Mn atoms, which coincides with the contribution per FM layer in the unit cell, would be given by $\mu_s = 4\mu_B$ [387]. Additionally, as it is represented in Fig. 5.1 (a), there are three different types of exchange contributions between the magnetic moments $\boldsymbol{m}_i$ and $\boldsymbol{m}_j$ in the unit cell, which are represented by the exchange integrals $\mathcal{J}_{ij}$. This set is composed of two AFM interactions, which are given by $\mathcal{J}_1 = -(396\,\mathrm{K})\,k_B$ and $\mathcal{J}_2 = -(532\,\mathrm{K})\,k_B$, and a third one of FM origin, being represented by $\mathcal{J}_3 = (115\,\mathrm{K})\,k_B$ [386, 387, 396]. On the other hand, it is possible to appreciate the existence of two types of tetragonal anisotropies in the system, given by $K_{4\parallel} = 1.8548 \times 10^{-25}$ J and $K_{4\perp} = 2K_{4\parallel}$, and two others of a uniaxial nature, denoted by $K_{2\perp} = -1.303 \times 10^{-22}$ J and $K_{2\parallel} = 7K_{4\parallel}$ [139, 161, 165]. The last term in Eq. (5.1) accounts for the Zeeman-like contribution, where $\boldsymbol{H}_i^{SO}$ is the staggered SO field on each *i-th* lattice site, which, due to locally broken inversion symmetry along the *z-th* spatial direction, results in $\boldsymbol{H}_{A,B}^{SO} = \pm H_y^{SO}\hat{\boldsymbol{y}}$ when the electric current density, $\boldsymbol{j}$, is injected along $\boldsymbol{j} \parallel \hat{\boldsymbol{x}}$, and $\boldsymbol{H}_{A,B}^{SO} = \mp H_x^{SO}\hat{\boldsymbol{x}}$ when $\boldsymbol{j} \parallel \hat{\boldsymbol{y}}$ [148].

5.3 Analytically-based magnetic texture dynamics in complex antiferromagnets

5.3.1 Reduction to a two sublattices-based order parameter description

Due to the existence of the different magnetic interactions collected in Eq. (5.1), the magnetization is constrained in the xy plane for each Mn-based FM layer in the

form of stable 1D 180° Néel-like DW, as it is exposed in Fig. 5.1 (b). When it is addressed how the magnetic soliton dynamics can be characterized analytically in Mn_2Au, it is worth noting that the conventional unit cell consists of four staggered magnetized layers along the *z-th* spatial direction, which are connected through two types of AFM exchange contributions, given by $\mathcal{J}_1$ and $\mathcal{J}_2$, which makes it difficult to define a unique Néel order parameter in the system, contrary to what it is stated in Sec. 2.4.3 for the case of an AFM spin chain. However, due to the symmetric inequivalence of the magnetic and crystallographic unit cells, it is feasible to reduce their characterization to a two sublattices single staggered vector-based description. To proceed with this discussion, let us take into account the numbering of the Mn planes exposed in Fig. 5.1 (b). At this point, it is necessary to differentiate between two crystallographically identical Mn-based groups: one consisting of planes 1 and 4, and the other by sheets 2 and 3. Interestingly, if a spatial inversion transformation is performed with respect to the unit cell center position, an operation which will be characterized by the position vectors, $\boldsymbol{r}_i$, of each magnetic layer, it will be possible to appreciate that, crystallographically, the Mn atoms of plane 1 become those of layer 4, and vice versa (this is, $\boldsymbol{r}_{1,4} \rightarrow \boldsymbol{r}_{4,1}$). Accordingly, this can be extrapolated to the case of Mn atoms residing in sheets 2 and 3 (which will be expressed as $\boldsymbol{r}_{2,3} \rightarrow \boldsymbol{r}_{3,2}$). However, if the orientation of the magnetic moments in each Mn site is taken into account, the crystallographic symmetry is not preserved, since the AFM ordering forces the magnetization in the 1-4 and 2-3 planes to be antiparallel with respect to each other within the exchange approximation. It is precisely this broken inversion symmetry which gives rise to the existence of the staggered SO field, $\boldsymbol{H}_i^{\mathrm{SO}}$, in each magnetic sublattice, which was included in Eq. (5.1), which allows to induce the AFM dynamics.

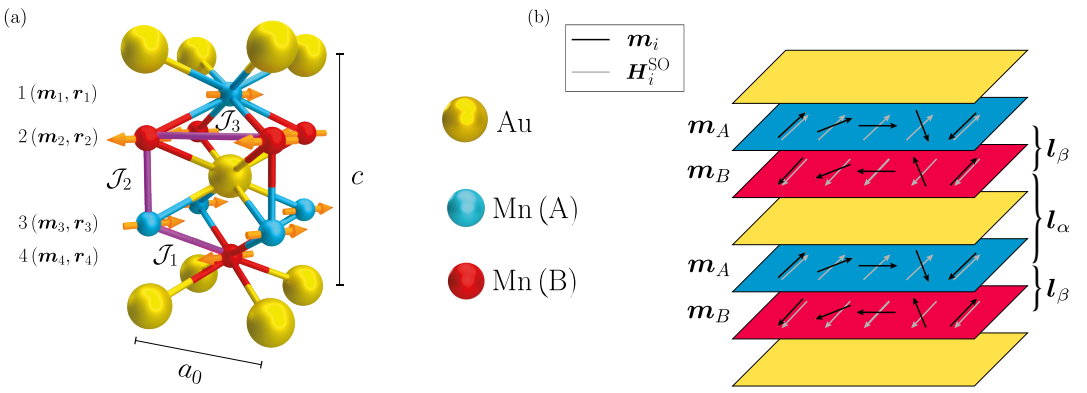

Figure 5.1: (a) Crystal and spin structure of the Mn_2Au tetragonal unit cell along with the different types of atoms and sublattices in the system, where the magnetic Mn-based layers are numbered and displayed along with their corresponding unit magnetization, $\boldsymbol{m}_i$, and position vectors, $\boldsymbol{r}_i$. Distribution of the different exchange bonds of AFM origin, $\mathcal{J}_1$ and $\mathcal{J}_2$, connecting different sublattices, and the one of FM nature, $\mathcal{J}_3$, as well as the in-plane xy basal lattice period, a_0, and the out-of-plane height, c, parameters. (b) Distribution of the Néel-like DW magnetization, $\boldsymbol{m}_i$, and the SO field, $\boldsymbol{H}_i^{\mathrm{SO}}$, in each of the magnetic sublattices, denoted by A and B, along with the definition of the two types of Néel order parameters involving different layers, $\boldsymbol{l}_\alpha = (\boldsymbol{m}_3 - \boldsymbol{m}_2)/2$ and $\boldsymbol{l}_\beta = (\boldsymbol{m}_{1,3} - \boldsymbol{m}_{2,4})/2$.

Taking into account that Mn_2Au is a magnetically-based centroasymmetric AFM, it is possible to define four vectors to describe the system, one FM, $\boldsymbol{n}_{\mathrm{a}}$, and three

AFM, $\boldsymbol{l}_i$, result of linear combinations of the four sublattices magnetization vectors, $\boldsymbol{m}_i$, such that they will be given by: $\boldsymbol{n}_{\mathrm{a}} = (\boldsymbol{m}_1 + \boldsymbol{m}_2 + \boldsymbol{m}_3 + \boldsymbol{m}_4)/4$, $\boldsymbol{l}_{\mathrm{a}} = (\boldsymbol{m}_1 - \boldsymbol{m}_2 - \boldsymbol{m}_3 + \boldsymbol{m}_4)/4$, $\boldsymbol{l}_{\mathrm{b}} = (\boldsymbol{m}_1 - \boldsymbol{m}_2 + \boldsymbol{m}_3 - \boldsymbol{m}_4)/4$, and $\boldsymbol{l}_{\mathrm{c}} = (\boldsymbol{m}_1 + \boldsymbol{m}_2 - \boldsymbol{m}_3 - \boldsymbol{m}_4)/4$ [242]. In fact, one of the AFM vectors, namely $\boldsymbol{l}_b$, can be used as the main one to define the system due to the specific magnetic symmetry of the Mn_2Au unit cell. Since the 1-3 and 2-4 planes are magnetically equivalent, it is possible to introduce a two sublattices model consisting of Mn-based layers 2 and 3 (or type B and A according to Fig. 5.1 (b), respectively) taking into account that $\boldsymbol{m}_1 = \boldsymbol{m}_3$ and $\boldsymbol{m}_2 = \boldsymbol{m}_4$. This results in the AFM vectors now being given by $\boldsymbol{l}_{\mathrm{a,c}} = 0$ and $\boldsymbol{l}_{\mathrm{b}} = (\boldsymbol{m}_3 - \boldsymbol{m}_2)/2$, while the FM one will be represented by $\boldsymbol{n}_{\mathrm{a}} = (\boldsymbol{m}_3 + \boldsymbol{m}_2)/2$. In this way, it is possible to describe the DW dynamics in the layered AFM Mn_2Au through a two sublattices formalism taking into account only the two FM embedded layers 2 and 3, excluding for this purpose sheets 1 and 4, in such a way that it is possible to define the main AFM vector as $\boldsymbol{l}_\alpha = \boldsymbol{l}_{\mathrm{b}} = (\boldsymbol{m}_3 - \boldsymbol{m}_2)/2$ and the total magnetization vector as $\boldsymbol{n}_\alpha = \boldsymbol{n}_{\mathrm{a}} = (\boldsymbol{m}_3 + \boldsymbol{m}_2)/2$. Additionally, it is possible to introduce a more general definition of the aforementioned variables in terms of the two types of magnetic layers of the system, A and B, in accordance with what is exposed in Fig. 5.1 (b), in such a way that we obtain that $\boldsymbol{l} = (\boldsymbol{m}_{\mathrm{A}} - \boldsymbol{m}_{\mathrm{B}})/2$ and $\boldsymbol{n} = (\boldsymbol{m}_{\mathrm{A}} + \boldsymbol{m}_{\mathrm{B}})/2$, which is consistent with the $\boldsymbol{l}_\alpha$ and $\boldsymbol{m}_\alpha$ characterization, respectively.

5.3.2 First nearest neighbors-governed exchange energy construction

To address the analytical description of the system, it is necessary to evaluate how the different nearest neighbors exchange-based bonds impact the inhomogeneous DW transition. To do this, taking as a reference Fig. 5.2 (a), which shows a top view of the conventional unit cell, we will focus on the number of relevant first nearest neighbors for a Mn atom of the embedded layer 2, which enclose all the possible exchange-based interactions, in an arbitrary position x_i, being its magnetization vector characterized by $\boldsymbol{m}_2(x_i)$. This being the case, it is possible to see that this reference atom has four intersublattice first neighbors on sheet 1, at a distance $a_0/2$ along the *x-th* axis, which are depicted as $\boldsymbol{m}_1(x_{i\pm1/2})$, being mediated by the AFM exchange interaction given by $\mathcal{J}_1$. Additionally, the aforementioned atomic position has two intrasublattice first neighbors along the *x-th* transition direction, at a distance a_0, which are characterized through $\boldsymbol{m}_2(x_{i\pm1})$, interacting through the FM exchange $\mathcal{J}_3$ contribution. In this sense, it should be noted that both, the first neighbors in layer 2 along the *y-th* axis, characterized by the FM $\mathcal{J}_3$ parameter, and the only intersublattice first neighbor in sheet 3, whose contribution is given by the AFM exchange $\mathcal{J}_2$ constant, are not taken into account because they do not impose any type of exchange penalty when determining the static and dynamic DW configuration in each magnetic sublattice of the system.

This being the case, we can first characterize the $\mathcal{J}_1$-mediated contribution to the exchange energy of the system, E_{exc}, through the introduction of the interaction between the unit magnetization vectors $\boldsymbol{m}_1(x_{i\pm1/2})$ and the reference unit magnetization vector $\boldsymbol{m}_2(x_i)$, giving rise to

$$E_{\mathrm{exc}}(\mathcal{J}_1) = -2\mathcal{J}_1 \boldsymbol{m}_2(x_i) \cdot [\boldsymbol{m}_1(x_{i-1/2}) + \boldsymbol{m}_1(x_{i+1/2})], \tag{5.2}$$

where it is important to note that the factor 2 that appears on the right-hand side is due to the existence of two first neighbors on each side of the reference Mn-based atom located at x_i at a distance $a_0/2$. Performing a 1D Taylor series decomposition up to second order for the atoms belonging to layer 1 with respect to the position x_i

of the reference atom, we obtain that

$$E_{\text{exc}}\left(\mathcal{J}_1\right) = 4|\mathcal{J}_1|\,\boldsymbol{m}_2\left(x_i\right)\cdot\left[\boldsymbol{m}_1\left(x_i\right)+\frac{1}{2}\left(\frac{a_0}{2}\right)^2\left(\partial_x^2\boldsymbol{m}_1\left(x_i\right)\right)\right], \tag{5.3}$$

expression which can be rewritten in terms of the total magnetization vector, $\boldsymbol{n} = \left(\boldsymbol{m}_{\text{A}}+\ \boldsymbol{m}_{\text{B}}\right)/2$, and the Néel order parameter, $\boldsymbol{l} = \left(\boldsymbol{m}_{\text{A}}-\boldsymbol{m}_{\text{B}}\right)/2$, taking into account, as expressed in Sec. 5.3.1, the existing equivalence between the magnetic sublattices 1-3, which we can refer to generically as type A, according to Fig. 5.1 (b), and sheets 2-4, which can be classified in the category called B, in such a way that the orthogonal set of unit vectors $\boldsymbol{n}$ and $\boldsymbol{l}$ will be defined as $\boldsymbol{n} = \left(\boldsymbol{m}_1+\boldsymbol{m}_2\right)/2$ and $\boldsymbol{l} = \left(\boldsymbol{m}_1-\boldsymbol{m}_2\right)/2$. Considering that $\boldsymbol{n}^2+\boldsymbol{l}^2 = 1$ and that we are working on the exchange limit regarding the exchange parameter $\mathcal{J}_1$ ($\boldsymbol{n}^2 \ll \boldsymbol{l}^2$) [144, 241], it is possible to obtain, after neglecting the spatial indices, that the aforementioned exchange interaction can be reduced to

$$E_{\text{exc}}\left(\mathcal{J}_1\right) = 8|\mathcal{J}_1|\left[\boldsymbol{n}^2-\frac{1}{4}\left(\frac{a_0}{2}\right)^2\boldsymbol{l}\cdot\left(\partial_x^2\boldsymbol{l}\right)\right], \tag{5.4}$$

which can be rewritten taking into account that, since both $\boldsymbol{n}$ and $\boldsymbol{l}$ are two fixed length vectors, it is possible to show that $\boldsymbol{l}\cdot\left(\partial_x^2\boldsymbol{l}\right) = -\left(\partial_x\boldsymbol{l}\right)^2$, such that

$$E_{\text{exc}}\left(\mathcal{J}_1\right) = 8|\mathcal{J}_1|\left[\boldsymbol{n}^2+\frac{a_0^2}{16}\left(\partial_x\boldsymbol{l}\right)^2\right]. \tag{5.5}$$

Similarly, the functional form of the intrasublattice FM exchange $\mathcal{J}_3$ contribution to the system can be analyzed analogously to the case in which the first neighbors of layer 1 were taken into account. In this case, the interaction between atoms of the same sheet located at a distance a_0 on both sides of the reference atom located at x_i can be modeled as

$$E_{\text{exc}}\left(\mathcal{J}_3\right) = -\mathcal{J}_3\,\boldsymbol{m}_2\left(x_i\right)\cdot\left[\boldsymbol{m}_2\left(x_{i-1}\right)+\boldsymbol{m}_2\left(x_{i+1}\right)\right], \tag{5.6}$$

where it can be seen that, unlike the case presented in Eq. (5.2), there is no factor 2 on its right-hand side since there is only one neighbor on each side of the reference atom. Performing a Taylor series expansion up to second order along the *x-th* spatial direction for the intrasublattice first nearest neighbors of layer 2 located at a distance a_0 from the reference atom, it is possible to obtain that

$$E_{\text{exc}}\left(\mathcal{J}_3\right) = -2\mathcal{J}_3\,\boldsymbol{m}_2\left(x_i\right)\cdot\left[\boldsymbol{m}_2\left(x_i\right)+\frac{a_0^2}{2}\left(\partial_x^2\boldsymbol{m}_2\left(x_i\right)\right)\right], \tag{5.7}$$

expression which can be rewritten in terms of the AFM vectors $\boldsymbol{n}$ and $\boldsymbol{l}$ taking into account that all the considered atoms belong to the same magnetically-based category denoted by type B. Taking into account, again, that we are working on the exchange limit, that the $\boldsymbol{n}$ and $\boldsymbol{l}$ variables form an orthogonal unit set ($\boldsymbol{n}\cdot\boldsymbol{l} = 0$), and that both are two fixed length vectors, we obtain that

$$E_{\text{exc}}\left(\mathcal{J}_3\right) = \mathcal{J}_3 a_0^2\left(\partial_x\boldsymbol{l}\right)^2. \tag{5.8}$$

Finally, it is possible to group both exchange-based contributions, given by Eqs. (5.5) and (5.8), which will govern the static and dynamic DW configuration in each

of the FM layers of the conventional unit cell, giving rise to

$$E_{\text{exc}} = \frac{1}{2} A \boldsymbol{n}^2 + \frac{1}{8} a \left(\partial_x \boldsymbol{l}\right)^2, \tag{5.9}$$

where we have introduced the homogeneous AFM exchange parameter, $A = 16|\mathcal{J}_1|$, and the inhomogeneous FM-like exchange constant, given by $a = 8a_0^2 \left(\mathcal{J}_3 + |\mathcal{J}_1|/2\right)$.

5.3.3 Effective version of the nonlinear σ-model in the rigid profile approximation

In addition to the plethora of different exchange interactions connecting the different magnetic sublattices of the system, there are also various anisotropy-based contributions with different directionality. Due to the relative order of magnitude of the uniaxial anisotropy constants compared to the tetragonal ones, being given by $K_{2\perp}/K_{4\perp} = 351$ and $K_{2\parallel}/K_{4\parallel} = 7$, the fourth-order anisotropies will be neglected in the main approximation from now on. In order to readjust the configurational energy given by Eq. (5.1) for the case of a two sublattices-based description in terms of the set of the orthogonal unit vectors defined by $\boldsymbol{n}$ and $\boldsymbol{l}$, it is necessary to take into account that these variables are constructed in terms of the two embedded FM layers 2 and 3 of the unit cell, being denoted as $\boldsymbol{n}_\alpha$ and $\boldsymbol{l}_\alpha$. However, it is important to keep in mind that, in our case, in Mn_2Au, the description of the DW dynamics must reflect that it occurs entirely in a single FM layer of the system, while the definition of the vectors $\boldsymbol{n}$ and $\boldsymbol{l}$ implicitly assume that this occurs across both sublattices, as in the case of the AFM spin chain presented in Secs. 2.4.3 and 3.3. To adapt this to our particular problem, we must halve the resulting magnetic anisotropy and Zeeman-like energies after adding the contributions of the two individual embedded sublattices. This, in conjunction with the exchange energy part exposed in Eq. (5.9), within an effective version of the nonlinear σ-model [135, 136, 398], due to the non-inclusion of the AFM exchange interaction encoded by the $\mathcal{J}_2$ parameter, which is defined along the c-axis of the system, in the exchange limit [144, 243], gives rise to

$$E = \frac{1}{2} A \boldsymbol{n}^2 + \frac{1}{8} a \left(\partial_x \boldsymbol{l}\right)^2 + w_{\text{ani}}\left(\boldsymbol{l}\right) - 2\gamma\hbar \, \boldsymbol{l} \cdot \boldsymbol{H}^{\text{SO}}, \tag{5.10}$$

where the term $E_{\text{ani}}\left(\boldsymbol{l}\right)$ encapsulates the uniaxial anisotropy contributions of the system, $E_{\text{ani}}\left(\boldsymbol{l}\right) = |K_{2\perp}| \left(\boldsymbol{l} \cdot \hat{\boldsymbol{z}}\right)^2 - K_{2\parallel} \left(\boldsymbol{l} \cdot \hat{\boldsymbol{y}}\right)^2$, where the electric current has been chosen to be injected along $\boldsymbol{j} \parallel \hat{\boldsymbol{x}}$, so $\boldsymbol{H}^{\text{SO}} = H_y^{\text{SO}} \hat{\boldsymbol{y}}$, inducing the DW motion along the x-*th* spatial direction, and where it has been taken into account, when rewriting the Zeeman-like term of Eq. (5.1), that, for the specific case of Mn_2Au, $\mu_0 \mu_s = 2\gamma\hbar$.

Along the same line, due to the transition to a two sublattices-based description of the system, it is necessary to work within the framework governed by the AFM LLG equations, which describe the dynamic behavior of the staggered, $\boldsymbol{l}$, and total magnetization, $\boldsymbol{n}$, vectors, which, in the exchange limit [144, 241], are given, respectively, by Eqs. (3.49) and (3.50). It should be noted that, in this case, the effective magnetic fields associated to the variables $\boldsymbol{n}$ and $\boldsymbol{l}$, which are represented by $\boldsymbol{H}_{\boldsymbol{n},\boldsymbol{l}}^{\text{eff}}$, will be expressed as $\boldsymbol{H}_{\boldsymbol{n},\boldsymbol{l}}^{\text{eff}} = -\frac{1}{2\gamma\hbar} \frac{\delta E}{\delta(\boldsymbol{n},\boldsymbol{l})}$. Through Eq. (3.49), it is possible to find that

$$\boldsymbol{n} = \frac{2\hbar}{A} \left(\dot{\boldsymbol{l}} \times \boldsymbol{l}\right), \tag{5.11}$$

expression which can be substituted into Eq. (3.50) to obtain a second-order differential equation entirely in terms of the Néel order parameter, $\boldsymbol{l}$, which can be denoted as

$$\boldsymbol{l} \times \left[\left(\partial_x^2 \boldsymbol{l} \right) - \frac{1}{v_{\mathrm{m}}^2} \ddot{\boldsymbol{l}} + \boldsymbol{h} - \frac{4}{a} \frac{\partial E_{\mathrm{ani}} \left(\boldsymbol{l} \right)}{\partial \boldsymbol{l}} - \eta \, \dot{\boldsymbol{l}} \right] = 0, \tag{5.12}$$

where v_{m} represents the maximum magnon group velocity of the medium, which in this case is given by

$$v_{\mathrm{m}} = \frac{\sqrt{aA}}{4\hbar} = \frac{2a_0}{\hbar} \sqrt{2|\mathcal{J}_1| \left(\mathcal{J}_3 + \frac{|\mathcal{J}_1|}{2} \right)}, \tag{5.13}$$

whose value in the case of Mn_2Au, in view of what is stated in Sec. 5.2, is 43.39 km/s, while $\boldsymbol{h}$ encodes the reduced SO field as $\boldsymbol{h} = 8\gamma\hbar \boldsymbol{H}^{\mathrm{SO}}/a$, and η denotes the dissipative parameter expressed as $\eta = 8\alpha\hbar/a$. Interestingly, it should be noted that there are studies predicting that an intersublattice AFM exchange interaction such as the one encoded by $\mathcal{J}_2$, perpendicular to the inhomogeneous DW transition, should govern the value of v_{m}, both within and outside of the standard nonlinear σ-model [389, 399, 400], as opposed to what it is exposed in Sec. 5.3.2 in the construction of the exchange-based energy of the system.

Consistent with what it is shown in Fig. 5.2 (b), it is possible to parameterize the Néel order parameter in spherical coordinates taking into account the in-plane easy-axis direction dictated by $K_{2\parallel}$, giving rise to

$$\boldsymbol{l} = \left(\sin\varphi \, \cos\varepsilon, \cos\varphi \, \cos\varepsilon, -\sin\varepsilon \right), \tag{5.14}$$

where φ represents the azimuthal angle, which accounts for the rotation of the magnetization in the xy plane being measured from the y-th axis, while ε expresses the polar angle, which describes the out-of-plane canting characterized from the xy plane. Since we are working on the exchange limit, it is possible to predict that the tilting from the easy-plane is negligible, such that it can be assumed that $\varepsilon \simeq 0$, so the reduced AFM vector can be expressed as $\boldsymbol{l} \simeq (\sin\varphi, \cos\varphi, 0)$. This being the scenario, it is possible to reduce Eq. (5.12) to a SG wave-like equation [303, 401], which has the following functional form

$$\frac{1}{v_{\mathrm{m}}^2} \ddot{\varphi} - \left(\partial_x^2 \varphi \right) + \frac{1}{2\Delta_0^2} \sin 2\varphi + h \, \sin\varphi = -\eta \, \dot{\varphi}, \tag{5.15}$$

where Δ_0 stands for the DW width at rest, which is given in this case by

$$\Delta_0 = \sqrt{\frac{a}{8K_{2\parallel}}} = a_0 \sqrt{\frac{\left(\mathcal{J}_3 + |\mathcal{J}_1|/2 \right)}{K_{2\parallel}}}, \tag{5.16}$$

which, for the particular case of Mn_2Au, taking into account the parameters exposed in Sec. 5.2, yields a value of 19.17 nm, and where $h = 8\gamma\hbar \, H_y^{\mathrm{SO}} / \, a$ denotes the reduced scalar SO field.

At this point, it is convenient to consider the magnetic texture dynamics in the framework of the well-known collective coordinates approach [230]. For this, it is usual to introduce what is known as Walker-like rigid profile through the angular variable that defines the spatio-temporal evolution of the magnetization, which will be given, in accordance with what is stated in Eq. (2.30), by $\varphi\left(x,t\right) = 2 \arctan \exp \left[\left(x - X\left(t\right) \right) / \Delta\left(t\right) \right]$. Due to the Lorentz invariance shown by Eqs. (5.12) and (5.15),

the magnetic soliton dynamics in AFM present emergent special relativity signatures, so it will be verified that, as the velocity of the magnetic texture, $\dot{X}$, increases, the DW width, Δ, will decrease, which will be governed by $\Delta(t) = \Delta_0 \beta(t)$, where $\beta(t) = \sqrt{1 - \left(\dot{X}(t)/v_m\right)^2}$ represents the symmetric Lorentz factor. In order to avoid the excitation of internal modes of the magnetic texture, we will focus on quasistatic processes, so that potential asymmetries do not appear in its envelope, so we can neglect the time derivatives of its spatial extent, Δ. In this way, we obtain that

$$\frac{1}{\Delta v_m^2}\ddot{X} + \frac{\eta}{\Delta}\dot{X} - h = 0, \tag{5.17}$$

expression which is a Newton-like second-order differential equation for the time evolution of the DW center position, X, which reveals the inertial nature of the magnetic texture [307, 389]. In the particular case in which a constant SO field is applied, it is possible to access a steady-state-like regime after the accommodation of the magnetic soliton to its new dynamic regime. In this sense, we can reduce the previous equation to a compact expression that describes the steady-state DW velocity, which we will denote from now on as $\dot{X} = v$, which will be given by

$$v = \frac{v_m}{\sqrt{1 + (v_m/v_0)^2}}, \tag{5.18}$$

where $v_0 = h\Delta_0/\eta$.

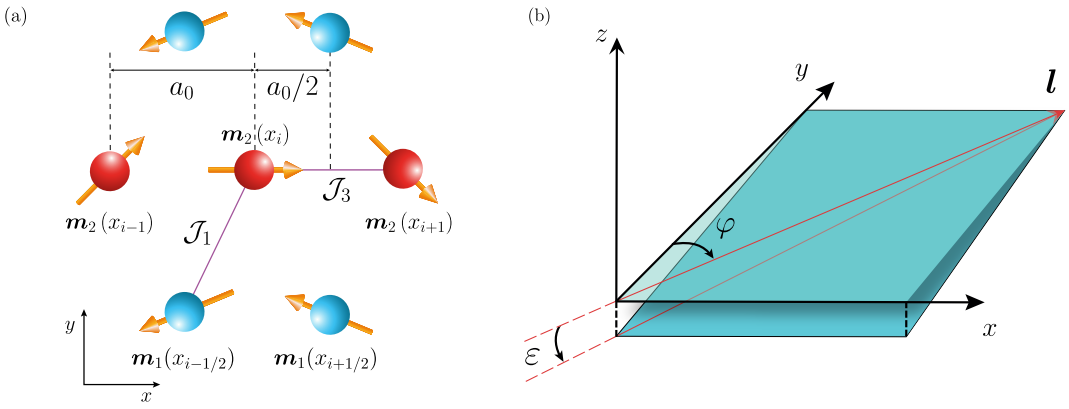

Figure 5.2: (a) View from the top of the unit cell along the *z-th* spatial direction of the distribution of the first nearest neighbors of the Mn atom of layer 2 located at the position x_i along the *x-th* axis, characterized by $\boldsymbol{m}_2(x_i)$. Those neighbours of its same sublattice, at a distance a_0, are denoted by $\boldsymbol{m}_2(x_{i\pm1})$, being mediated by the FM exchange interaction $\mathcal{J}_3$, and those from layer 1, located at an in-plane spacing $a_0/2$, are represented by $\boldsymbol{m}_1(x_{i\pm1/2})$, and are connected through the AFM exchange contribution encoded by $\mathcal{J}_1$. (b) Description of the unit AFM vector, $\boldsymbol{l} = (\boldsymbol{m}_A - \boldsymbol{m}_B)/2$, in terms of the polar out-of-plane ε and in-plane azimuthal φ angles relative to the Cartesian coordinate system.

5.3.4 Simulated exchange-dependent static and dynamic domain wall properties

To try to validate the qualitative argument made in Sec. 5.3.2 about the non-impact of the intersublattice AFM exchange interaction dictated by the $\mathcal{J}_2$ constant in the

temperature-independent DW properties, we will use ASDS. To do this, the LLG equation of motion, given by Eq. (2.14), will be solved numerically, site by site, through a fifth-order Runge-Kutta method, assuming that the damping parameter is $\alpha = 0.001$ [139, 165, 402]. In this case, the computational domain is composed of 60000 cells along the *x-th* propagation direction, one cell width with periodic boundary conditions along the *y-th* direction, and one cell thick along the *z-th* axis. At this point, it should be noted that the absence of periodicity along the *z-th* spatial direction in the simulated ultrathin film does not guarantee the condition $\boldsymbol{m}_{1,2} = \boldsymbol{m}_{3,4}$ used in Sec. 5.3.1, which allowed us to reduce the system description to a two sublattices-based nonlinear σ-model. Through the variation, mediated by a numerical scaling factor given by κ, of the different exchange parameters of the system, where in each case only one of these is modified at each time, it is possible to compare the analytical expressions obtained in Sec. 5.3.3 with the results obtainable through the simulations. In this line, and it as can be seen in Fig. 5.3 (a), the simulated DW width at rest, Δ_0, does not depend on the considered scaling magnitude applied to the AFM $\mathcal{J}_2$ constant, since this interaction only guarantees that contiguous sublattices are perfectly antiparallel, while $\mathcal{J}_1$ and $\mathcal{J}_3$ characterize the relative angle between in-plane spins and hence the spatial soliton extent [395]. This is consistent with what it is stated in Eq. (5.16), according to which the DW width at rest does not depend on the contribution governed by $\mathcal{J}_2$, whose trend clearly coincides with the one shown by the simulations. It is worth noting that the small discrepancy between them may be due to the non-inclusion in the analytical model, for simplicity, of the in-plane tetragonal anisotropy contribution encoded by $K_{4\parallel}$. On the other hand, we can explore the SW dispersion relation of the system by varying only the $\mathcal{J}_2$ parameter, so that we can see how this affects the functional form of the low-frequency acoustic branch from which it can be extracted the maximum magnon group velocity, v_m, of the medium, which is characterized as $v_\mathrm{m} = (\mathrm{d}f/\mathrm{d}k)_{\mathrm{max}}$, where f expresses the SW frequency and k represents the associated wavenumber along the propagation direction. As it can be seen in Fig. 5.3 (b), the acoustic branch is independent of the associated magnitude of the exchange interaction governed by $\mathcal{J}_2$, while the high-frequency optical branch maintains its functional form for $\kappa\mathcal{J}_2 \neq 0$, shifting to higher frequencies as the aforementioned combined variable increases. When $\kappa = 0$, the optic branch disappears, so it strongly depends on the presence of $\mathcal{J}_2$. However, the maximum slope of the differentiated SW dispersion relation is always founded on the $\mathcal{J}_2$-independent acoustic branch, so the maximum magnon group velocity, v_m, does not depend on this interaction.

Regarding the dynamic behavior of the magnetic texture under the action of a constant current-induced SO field, as explained in Sec. 5.3.3, its steady-state velocity, v, given by Eq. (5.18), has a functional form such that $v = v(\Delta_0, v_\mathrm{m})$, so no dependency on $\mathcal{J}_2$ is expected. Accordingly, for a SO field of magnitude $H_y^{\mathrm{SO}} = 60$ mT, it is possible to see, as it is shown in Fig 5.4 (a), that there is a good correspondence between the simulated and the analytically-predicted values for the steady-state velocity v for different numerical scalings in the exchange parameters $\mathcal{J}_1$, $\mathcal{J}_2$, and $\mathcal{J}_3$. While it does not depend on the AFM intersublattice exchange contribution $\mathcal{J}_2$, it is strongly dependent on the magnitude of the AFM interlayer interaction $\mathcal{J}_1$, which is consistent with the analytical form exposed in Eq. (5.18), and it is affected by changes in the value of the intrasublattice FM exchange term encoded by $\mathcal{J}_3$. On the other hand, since the theoretically-predicted steady-state DW width, Δ, is entirely conditioned by its rest state value, Δ_0, the corresponding speed v to the applied SO field H_y^{SO}, and the maximum magnon group velocity of the medium, v_m, since $\Delta = \Delta_0\,\beta$, again the encoded AFM exchange interaction via the $\mathcal{J}_2$ parameter

should not play any role in its determination. Consequently, and as it can be seen in Fig. 5.4 (b), the simulated steady-state DW width follows the theoretically-predicted trend, only existing, as in the case of the DW width at rest Δ_0 shown in Fig. 5.3 (a), a small constant shifting between the simulated and analytical values. Thus, the role of $\mathcal{J}_2$ consists of acting as a hard-axis anisotropy, strongly constraining the magnetization in the Mn-based planes of the conventional unit cell, since this interaction is the dominant one in magnitude of the system, but does not intervene in the static and dynamic DW configurational properties.

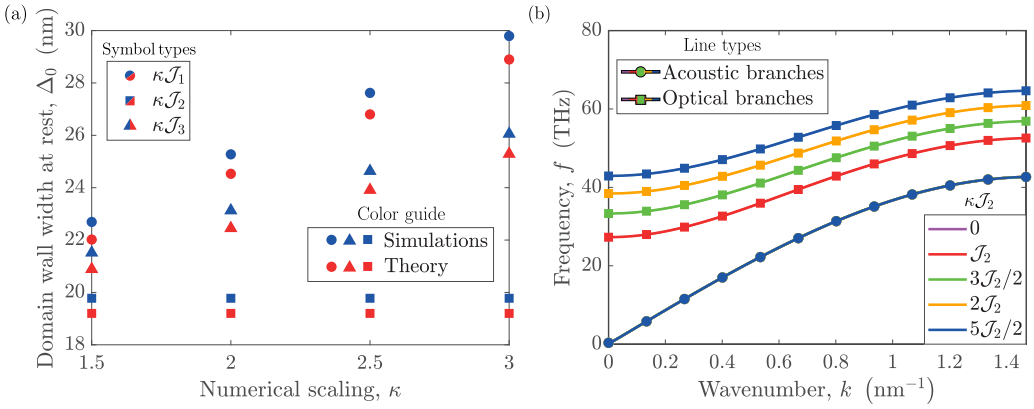

Figure 5.3: (a) Comparison between the simulated and the theoretically-predicted DW width at rest, Δ_0, for different numerical scalings, κ, of, at each time, one of the exchange parameters of the system, $\mathcal{J}_1$, $\mathcal{J}_2$, and $\mathcal{J}_3$. (b) Simulated SW dispersion relations, including the high-frequency optical and low-frequency acoustic branches, characterized through the associated SW frequency f and wavenumber k, for different numerical scalings through the κ parameter of the AFM exchange interaction governed by $\mathcal{J}_2$.

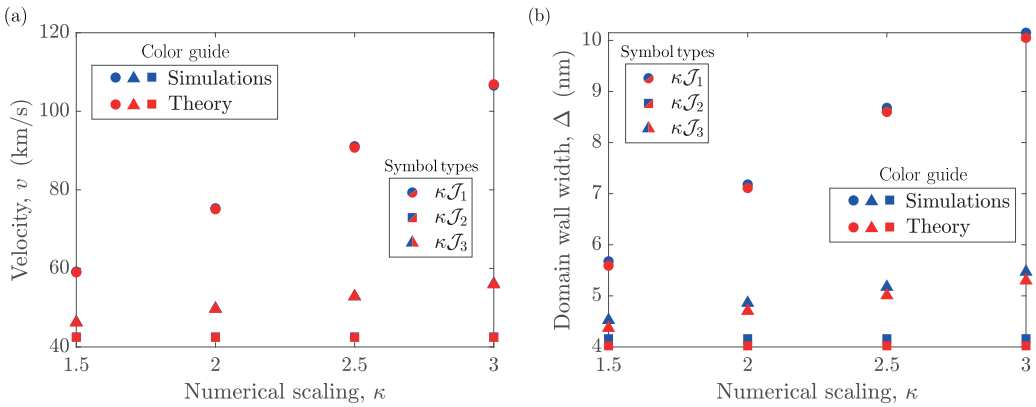

Figure 5.4: Comparison between the simulated and the analytically-calculated (a) steady-state velocity v and (b) DW width Δ, for the case of a SO field of $H_y^{\mathrm{SO}} = 60$ mT, for different numerical scalings controlled by the κ parameter, affecting, individually in each case, one of the exchange interactions of the system, characterized by $\mathcal{J}_1$, $\mathcal{J}_2$, and $\mathcal{J}_3$.

5.4 Relativistic pseudoparticle behavior of antiferromagnetic magnetic textures

5.4.1 Emergent special relativity-like signatures

In line with what it is shown in Figs. 5.4 (a) and (b), where the effective version of the nonlinear σ-model introduced in Sec. 5.3.3 was compared with ASDS, where it is verified the great correspondence of the steady-state DW velocity, v, and width, Δ, predictions, respectively, it is possible to certify that, as inferred from Eqs. (5.12) and (5.15), the system shows special relativity signatures. Taking into account that our analytical formalism is based on the simple functional forms in terms of the intrinsic parameters of the material of the maximum magnon group velocity of the medium, v_{m}, and the DW width at rest, Δ_0, given by Eqs. (5.13) and (5.16), respectively, these expressions can be compared directly with the values obtained through simulations. In accordance with what it is shown in Fig. 5.3 (a) for the case in which the magnitude of the AFM exchange parameter $\mathcal{J}_2$ was varied through the numerical scaling factor κ, it can be found that $\Delta_0 = 19.78$ nm, while through the slope of the low-frequency acoustic branch of the differentiated SW dispersion relation of Fig. 5.3 (b) it can be obtained that $v_{\mathrm{m}} = 43.3$ km/s. In this way, the simulated DW width at rest, Δ_0, shows a good correspondence with the theoretically-predicted value obtained through Eq. (5.16), differing only by a 3.1%, while, on the other hand, the maximum magnon group velocity, v_{m}, obtained analytically, according to Eq. (5.13), and by simulations coincide in a 99.93%, which supports the non-inclusion in our formalism of the AFM exchange interaction along the c-axis of the unit cell given by $\mathcal{J}_2$. Taking into account the functional form of the dynamic spatial extent of the magnetic soliton, Δ, governed by the symmetric Lorentz factor such that $\Delta = \Delta_0\,\beta$, it is possible to verify that the system really shows relativistic traces, as expected from what it was shown analytically. As it can be seen in Fig. 5.5, the saturation of the magnetic texture velocity, v, as it is predicted by Eq. (5.18), and the contraction of the DW width, Δ, as the SO field, H_y^{SO}, increases are verified, showing the theoretically-predicted trend.

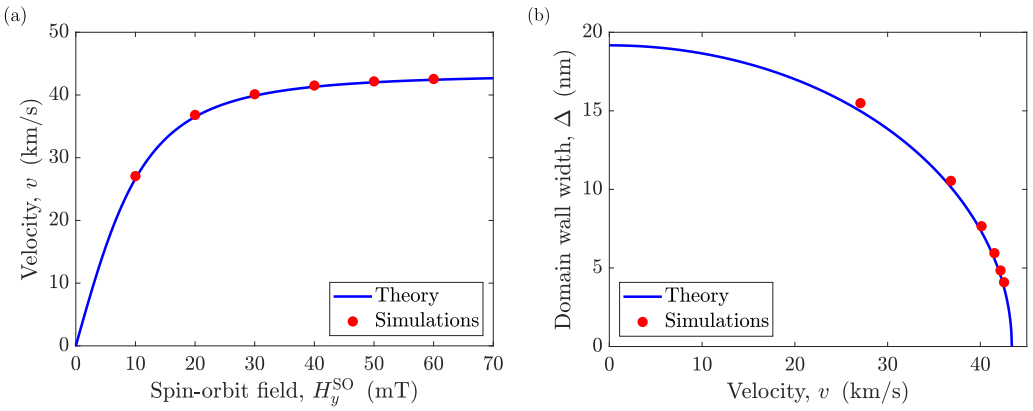

Figure 5.5: Comparison of the relativistic signatures for steady-state processes in Mn_2Au obtained through ASDS and theory. (a) Saturation of the velocity, v, of the magnetic texture as the SO field, H_y^{SO}, increases, being based the analytical formalism in Eq. (5.18). (b) DW width, Δ, contraction as the speed v of the magnetic soliton increases, the theoretical prediction coming from the combination of the relativistic expression $\Delta = \Delta_0\,\beta$ and Eq. (5.18).

5.4.2 Quasistatic inertial stable magnetic soliton dynamics

To explore the inertial signatures in the system, we have used time-dependent SO field-based excitation regimes, which are represented in Fig. 5.6 (a). As it can be seen, there are three well-differentiated regions. In the first one, which covers the interval $t \in [0, t_r)$, being t_r the time taken to reach a constant value of the field of $H_y^{SO} = 60$ mT, which we will denote as ramping time, the rest state of the magnetic texture is perturbed by a SO field that increases linearly with time. We will denote this regime as region I, and each colored dashed line in Figs. 5.5 and 5.6, and in Fig. 5.7 (a), correspond to a certain t_r that defines the aforementioned domain. Consistent with Eq. (5.17), which implicitly shows the existence of a non-zero DW mass, the initial response of the magnetic texture to the external stimulus is fast, but not instantaneous, as it can be seen in Figs. 5.6 (b) and 5.7 (a). At the time when a constant field value of 60 mT is reached, that is, at $t = t_r$, the magnetic soliton will tend to a steady-state regime (region II), which covers the interval $t \in [t_r, 100\,\text{ps})$. This upper limit is denoted by a black dashed line where appropriate in Figs. 5.6 and 5.7 (a). In this case, it is possible to observe in Figs. 5.6 (b) and 5.7 (a) that, in the region II, after a brief adaptation period to the new dynamic regime, which is a sample of the inertial nature of the process, the magnetic texture moves steadily at a speed of $v = 42.56$ km/s. This is very close to the maximum magnon group velocity of the medium, corresponding to a 98% of it, while it shrinks to a spatial extension of $\Delta = 4.08$ nm, which represents a shrinkage of 80% with respect to the simulated DW width at rest. Finally, at $t = 100$ ps, the SO field is abruptly switched off, which allows us to observe that the magnetic texture is able to initiate an after-pulse displacement in the absence of an external stimulus at the same time that its width expands until it stops completely, as it can be seen in Figs. 5.6 (b) and 5.7 (a). We denote this regime as region III, which covers the interval $t \in [100, 140]$ ps.

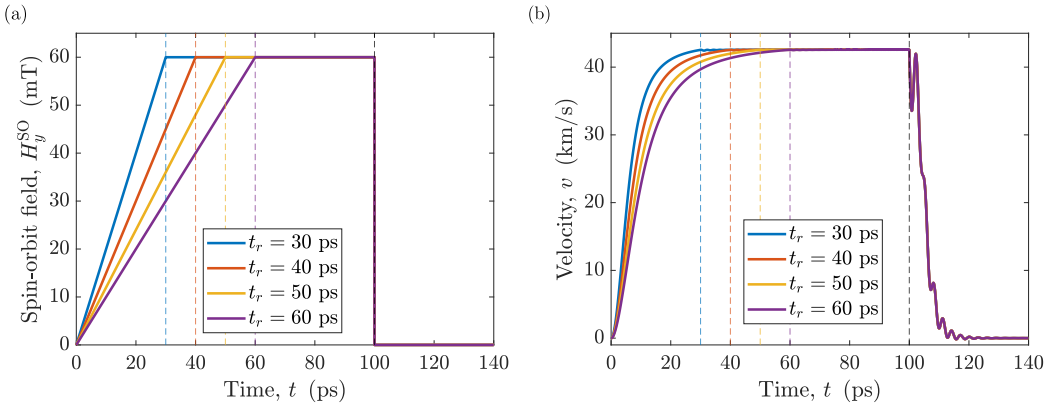

Figure 5.6: (a) Time-dependent staggered SO field-based excitation protocol, $H_y^{SO}(t)$, applied in each Mn-based FM layer of Mn_2Au for different ramping times, t_r. (b) Dynamic time evolution of the DW velocity v obtained through ASDS for different ramping times t_r.

The range of values considered for the ramping time t_r has been chosen to avoid the excitation of internal DW modes during the acceleration process, in such a way that the simulations were comparable with the quasistatic scenario exposed in Sec. 5.3.3 through Eq. (5.18). As it can be seen in Figs. 5.7 (b) and 5.8 (a), in these circumstances there is a close correspondence between the simulated and theoretically-predicted velocity of the magnetic texture, v, and its extent , Δ, in regions I and II.

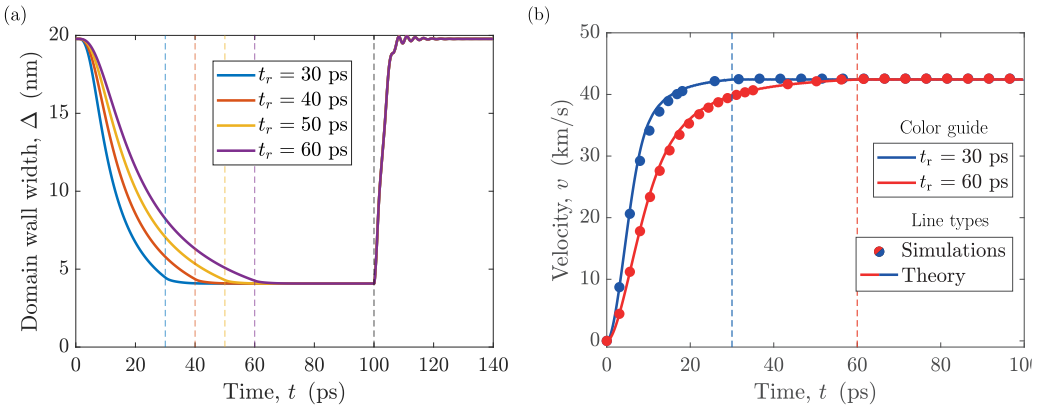

Figure 5.7: (a) Dynamic time evolution of the DW width Δ obtained through ASDS for different ramping times t_r. (b) Comparison of the dynamic time evolution of the DW velocity v for ASDS and the analytical expressions given by Eq. (5.17) and $\Delta = \Delta_0\,\beta$ for two ramping times, $t_r = 30$ and 60 ps. Each vertical colored dashed line represents the end of the ramped process for the different ramping times t_r, while the dashed black line denotes the instant $t = 100$ ps at which the driving SO field H_y^{SO} is abruptly turned off.

5.4.3 After-pulse complex translational displacement

If attention is paid to Figs. 5.6 (b) and 5.7 (a) in region III, it is possible to appreciate the presence of ripples once the SO field H_y^{SO} is turned off. These ripples observed in the simulated DW velocity and width in region III cause longer decay times than those predicted through a Newton-like pseudoparticle behavior. Because of this, we avoid the analytical evaluation of this region through Eq. (5.17) because the magnetic soliton is not fulfilling the imposed rigid profile constraint anymore. However, the after-pulse displacement that the magnetic texture experiences in region III is related to the SO field-mediated increase in the exchange-based relativistic DW mass obtained during the acceleration process in region I while its width shrank. This is a purely inertial phenomenon, which is consistent with the massive pseudoparticle behavior captured by Eq. (5.17), according to which the greater the dynamic DW mass after turning off the external stimulus, the greater is the braking distance traveled by it. Interestingly, it is the fact that the magnetic soliton moves along a particular direction which sets how this stored relativistic exchange energy is transformed into a translational displacement, manifesting its massive particle-like behavior rather than being dissipated into a breather-like fashion or through the emission of SW without prolonging its mobility. For different values of the SO field during region II, we have found through simulations that there is a quasilinear relationship between the after-pulse distance traveled by the magnetic texture, x, normalized to its steady-state DW width, Δ, and its steady-state DW mass, m_{DW}, normalized to its rest state value, m_{DW}^0, this is, $m_{DW}/m_{DW}^0 = 1/\beta$ according to Eq. (5.17), which can be seen in Fig. 5.8 (b) and can be expressed as

$$\frac{x}{\Delta} = b\,\frac{m_{DW}}{m_{DW}^0} + d, \tag{5.19}$$

where b and d are two fitting-dependent parameters, which are given, accompanied by their associated uncertainties, by $b = 13.81(27)$ and $d = -13.92(89)$. It is

remarkable that the DW is capable of undertaking exchange-based after-pulse displacements of the order of 4 to 11 times greater than the DW width at rest, Δ_0, for SO fields between $10 - 60$ mT.

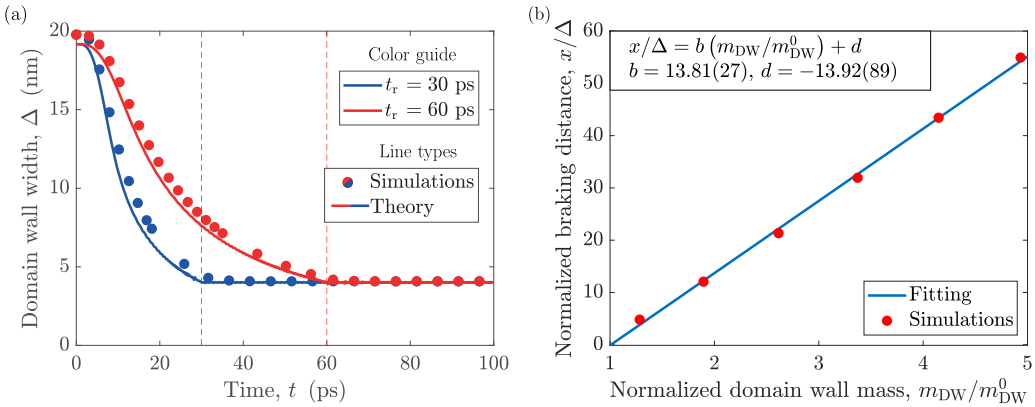

Figure 5.8: (a) Comparison of the dynamic time evolution of the DW width Δ for ASDS and the analytical expressions given by Eq. (5.17) and $\Delta = \Delta_0\,\beta$ for two ramping times, $t_r = 30$ and 60 ps. Each vertical colored dashed line represents the end of the ramped process for the different ramping times t_r, while the dashed black line denotes the instant $t = 100$ ps at which the driving SO field H_y^{SO} is abruptly turned off. (b) Quasilinear correspondence between the normalized relativistic DW mass, m_{DW}/m^0_{DW}, where m_{DW} and m^0_{DW} represent the aforementioned mass in steady-state and at rest, respectively, and the normalized braking distance, x, traveled by the magnetic texture once the SO field is turned off abruptly, x/Δ, in terms of the steady-state DW width, Δ, characterized by a linear fitting where b and d represent the adjustment parameters, together with their corresponding uncertainties.

5.5 Conclusions

We have addressed the theoretical characterization of the dynamic evolution of a 1D Néel-like DW in one of the FM sheets of the layered collinear multisublattice AFM Mn_2Au driven by current-induced SO fields. Despite the complexity of the system, we have exploited the symmetric inequivalence between the crystallographic and magnetic unit cells to reduce its description to a two sublattices-based problem. Since the AFM exchange interaction directed along the c-axis of the system, which is encoded via $\mathcal{J}_2$, has a null projection along the 1D inhomogeneous magnetic texture transition, it will have no impact on the temperature-independent nonlinear σ-model. Because the standard procedure would predict the opposite, we have worked within an effective theory framework avoiding its inclusion, a methodology which can be extrapolated to layered multisublattice AFM with different exchange-oriented contributions. In the rigid profile approximation, we have shown that it is possible to reduce the dynamic magnetic soliton description to a Newton-like second-order differential equation of motion. By comparing our formalism with ASDS, we have been able to replicate with a high degree of accuracy the relativistic and inertial signatures of the magnetic texture motion during quasistatic dynamic processes within the framework of our effective model. After the abrupt shutdown of the SO field in simulations, the rigid DW profile approach is no longer supported and our analytical formalism fails to describe the after-pulse inertial dynamic

regime. Interestingly, during the deceleration process, the relativistic exchange energy accumulated during the previous dynamic evolution of the magnetic texture is converted into translational mobility, rather than being released in a breather-like fashion or through the emission of SW with non-associated displacement. We have found a quasilinear relationship that allows us to predict, for the range of simulated SO fields, the value of the braking distance traveled by the DW through the knowledge of its relativistic mass before turning off the external stimulus. This detailed dynamic characterization of the 1D magnetic texture in the complex multisublattice AFM Mn_2Au is of potential interest for AFM DW-based technological applications, where the accurate control over the positioning of the magnetic soliton is of paramount interest.

Chapter 6

Walker-like domain wall breakdown in layered antiferromagnets

6.1 Beating the magnonic barrier through topologically-preserved processes

Within a general physical context, topological solitons are entities that interpolate between two degenerate minima, their core region being characterized by a spatially-inhomogeneous field configuration while in their outer domains the order parameter varies smoothly [230, 403], as it was exposed in Sec. 2.4.2.2. Beyond those magnetic textures that live in spin space, they also exist, for example, in the form of vortices in superfluid helium or as dislocations in periodic crystal structures [404–407]. In the field of irregularities in solid arrangements, the property that outlines the resistance of the defect to be eradicated in infinitely extended media is known as the Burgers vector, which is quantified in multiples of the atomic spacing of the system [408], whose role is analogous to that of winding number in magnetically-based scenarios [81], which was introduced in Sec. 2.5. As it happens in long-range FM ordered media, the topological-like protection of the solitary waves in real finite systems is not at odds with the appearance of instabilities, which is manifested through the existence of the WB at relatively low speeds, which limits the stable DW motion under a certain external stimulus-based threshold [91–93], as it was discussed in Sec. 3.2. In a similar fashion, in the case of dislocations in non-magnetic periodic structures, while for small stresses the crystal defect presents a quasilinear relationship between its velocity and the external stimulus [409], for high strains the phonon-based sonic barrier of the medium can be exceeded by means of the nucleation of mother-daughter secondary kinks with opposite Burgers vectors, preserving the overall topology of the system [410–413]. Even though it is possible to provide the FM DW with a DMI-induced stability, which delays the appearance of the WB, being its dynamics limited by the minimum SW phase velocity of the medium [102, 108], AFM materials present this characteristic intrinsically without the need for complicated structures, since the magnetization is strongly constrained in the DW plane at rest due to the existing exchange interaction [308, 309, 371]. In this case, the dynamic behavior of AFM textures is naturally described through the nonlinear σ-model, which is why they experience special relativity signatures, being their speeds theoretically limited by the maximum magnon group velocity of the medium [135, 136], as it can be induced from the relativistic-like dynamic framework

found in Sec. 3.3. However, it would be very appealing to investigate the behavior of AFM solitons under high amplitude excitations to try to replicate what has already been exposed in dislocation theory, leading to the appearance of a superluminal-like regime where the stable DW motion is interrupted due to the nucleation of at least two magnetic textures of opposite chirality.

6.2 Domain wall pair generation through moderate stresses

6.2.1 Magnetic soliton mother-daughter processes in antiferromagnets

To carry out our investigations, we will take as reference the layered AFM Mn_2Au, which was previously introduced in Sec. 5.2, in which it is possible to induce the Néel-like 180° DW dynamics through the action of current-induced staggered SO fields in each FM sublattice of the system [148, 165, 414]. Just as it was done in Sec. 5.3.4, we will use for this purpose ASDS, for which we will solve, site by site, the LLG equation, given by Eq. (2.14), taking into account the functional form of the atomistic energy exposed in Eq. (5.1), via a fifth-order Runge-Kutta method, with the damping parameter given by $\alpha = 0.001$ [139, 165, 402]. In the same line, again, the computational domain will be made up of 60000 lattice sites along the *x-th* propagation direction, one unit cell width with periodic boundary conditions along the *y-th* axis, and one unit cell height along the *z-th* spatial direction. To break the rest state of the magnetic texture we will use in this case an excitation protocol in which we will ramp the applied SO field for 10 ps to a maximum value of $H_y^{SO} = 65$ mT, which we will maintain until the end of the simulations, as it is depicted in Fig. 6.1 (a). Contrarily, in Sec. 5.4.2, because we were interested in analyzing the inertial signatures of the DW motion, we abruptly shutdown the external stimulus after the steady-state regime to assess the after-pulse magnetic soliton dynamics. As it can be seen in Fig. 6.1 (b), where the space-time winding number density, w, evolution is evaluated, the steady-state regime reached after the ramping process it is eventually interrupted due to the appearance of a different dynamic regime where the nucleation of a DW pair with trivial winding number density occurs, which preserves the initial overall topological charge of the system, according to what is shown in Fig. 6.1 (a). This strongly nonlinear phenomenon involving the spontaneous appearance of additional particles has been reported under different conditions in FM media, either through the DW WB mediated by a vortex-antivortex generation or through the vortex core reversal in spin-torque oscillators in nanodots and nanocontacts [109, 415, 416]. However, its occurrence in AFM has never been reported or proposed.

6.2.2 Dynamically-induced kinetic field-based torque on magnetization

In the specific case of the vortex core reversal in submicron-sized FM dots, which is mediated by a vortex-antivortex creation and subsequent annihilation, its physical origin has been associated with the emergence of an effective gyrotropic magnetic field of a purely dynamic nature which can be characterized through the kinetic part of the Lagrangian [415]. In our case, we can try to argue that the nucleation of the DW pair is related to the torque exerted in the spin space by the effective magnetic field resulting from the, in this case, translational motion of the original magnetic soliton along one of the FM basal planes of the layered AFM Mn_2Au. To formalize this problem, it is possible to write the kinetic part of the Lagrangian, L_{kin}, in a magnetization-invariant form parameterization similar to how it is done in

evaluating spin coherent states [417, 418], form which will be given by

$$L_{\text{kin}} = \frac{\mu_0 \mu_{\text{s}}}{\gamma} \frac{\hat{\boldsymbol{n}} \cdot (\boldsymbol{m} \times \dot{\boldsymbol{m}})}{1 + \boldsymbol{m} \cdot \hat{\boldsymbol{n}}}, \tag{6.1}$$

where $\hat{\boldsymbol{n}}$ is a unit vector defined along an arbitrary direction, which in the particular case of the Néel-like DW dynamics seems to be definable along the *z-th* axis, such that $\hat{\boldsymbol{n}} = \hat{\boldsymbol{z}}$, giving rise to a singularity known as a Dirac string, which is related to the Berry phase of the system. In this context, it is possible to rewrite the previous expression in a Zeeman-like energy term fashion, such that $L_{\text{kin}} = \mu_0 \mu_{\text{s}}\, \boldsymbol{m} \cdot \boldsymbol{h}^{\text{kin}}$, whereby the effective kinetic magnetic field, $\boldsymbol{h}^{\text{kin}}$, can be displayed as

$$\boldsymbol{h}^{\text{kin}} = \frac{1}{\mu_0 \mu_{\text{s}}} \frac{\delta L_{\text{kin}}}{\delta \boldsymbol{m}} = \frac{1}{\gamma (1 + \hat{\boldsymbol{u}} \cdot \boldsymbol{m})^2} \left[-\boldsymbol{m} \times \dot{\boldsymbol{m}} + (\dot{\boldsymbol{m}} \times \hat{\boldsymbol{u}}) (1 + \hat{\boldsymbol{u}} \cdot \boldsymbol{m}) \right], \tag{6.2}$$

where the first term of the right-hand side of the previous equation represents the longitudinal component of the field with respect to the arbitrary direction $\hat{\boldsymbol{n}}$ while the second part encapsulates its transversal contribution, both being directly proportional to the time variation of the magnetization vector, $\dot{\boldsymbol{m}}$, or in other words, to the translational speed of the magnetic texture, v.

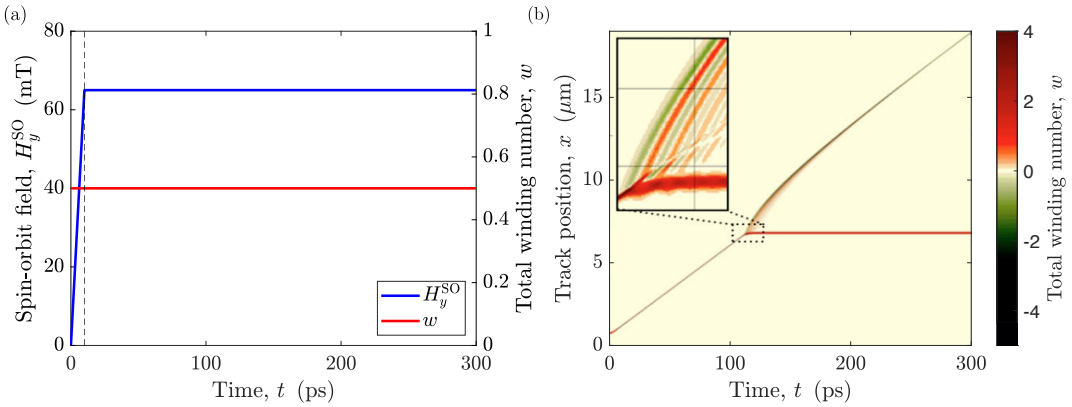

Figure 6.1: (a) Time-dependent SO field-based excitation protocol, H_y^{SO}, applied in each Mn-based FM sheet of the layered AFM Mn_2Au, for the case in which the external stimulus ramps for 10 ps up to a maximum value of $H_y^{\text{SO}} = 65$ mT, which remains constant from then on, together with the time evolution of the winding number density, w, of the system. (b) Simulated space-time evolution of the winding number density, w, for the case in which there was, initially, a single DW in the system which was subjected to a ramping of the SO field for 10 ps up to a maximum value of the SO field of $H_y^{\text{SO}} = 65$ mT, which remains constant thereafter.

Interestingly, the spatial extent and specific form of the kinetic field profile depends on the instantaneous dynamical configuration that the magnetic texture is in throughout the SO field-based ramped process. As it can be seen in Fig. 6.2 (a), in the first 10 ps of the ultrafast acceleration, the *z-th* kinetic field component, h_z^{kin}, is behind the magnetic soliton, moving smoothly from the back to the center when it is in the steady-state regime at constant velocity as for $t = 90$ ps, as it is shown in Fig. 6.3 (a), mimicking the DW profile. Shortly after crossing the 100 ps barrier, it is possible to see that, coinciding with the nucleation of the DW pair, process which involves a time scale of the order of 1 ps, the *z-th* kinetic field component is placed at the forefront of the magnetic texture, as it can be seen for $t = 110$ ps in Fig. 6.4 (a). During

the magnetic soliton motion prior to the appearance of additional magnetic textures, it can be seen that while the x- and y-*th* kinetic components, h_x^{kin} and h_y^{kin}, reach a maximum absolute value of approximately 6 and 3.5 mT, respectively, as it can be noted in their spatial distributions for different instants of time in Figs. 6.6 and 6.7, its projection along the z-*th* spatial direction, h_z^{kin}, reaches an approximate value of up to 35 T in absolute value prior to the nucleation phenomenon, as it is depicted in Fig. 6.3 (a). This is consistent with the magnetization distribution of the Néel-like DW that live in the xy FM basal planes of the conventional unit cell, which is why it can be considered that the z-*th* magnetization component is negligible during the original isolated magnetic soliton motion, $m_z \simeq 0$, which constitutes the same type of approach that the one made in Sec. 5.3.3 when the dynamic behavior of the 1D magnetic texture was evaluated for quasistatic processes.

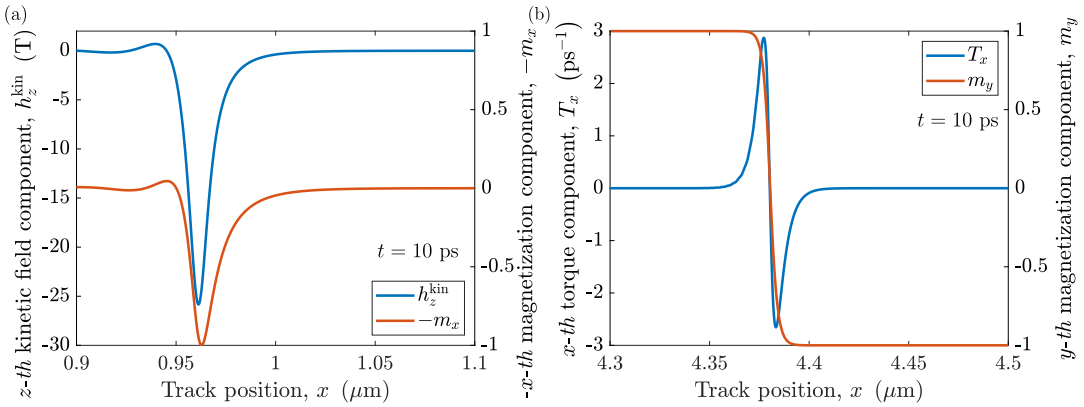

Figure 6.2: Spatial distribution of, on the one hand, (a) the z-*th* kinetic field, h_z^{kin}, and x-*th* magnetization, m_x, components and, on the other hand, of (b) the y-*th* magnetization, m_y, and x-*th* torque, T_x, components, respectively, for an instant of time of $t = 10$ ps, which were obtained by combining simulations together with Eq. (6.2), for the case in which the motion of a single DW was excited through a SO field which was ramped during 10 ps up to a maximum value of $H_y^{\text{SO}} = 65$ mT, which remains constant from then on.

Contrary to what happens in FM where the magnetic soliton absorbs the Zeeman-like energy from the kinetic field, we propose that the nucleation of the DW pair is due to the torque exerted by the dynamic-based field onto the local magnetization, a process which is governed by its z-*th* component due to its order of magnitude. Because the magnetization in front of the primal magnetic soliton prior to the fragmentation process is completely polarized along the $-y$-*th* axis, such that $\boldsymbol{m} \simeq -m_y\,\hat{\boldsymbol{y}}$, the kinetic field, which can be expressed as $\boldsymbol{h}^{\text{kin}} \simeq -\left|h_z^{\text{kin}}\right|\hat{\boldsymbol{z}}$, locally exerts a torque along the x-*th* spatial direction, T_x, given by $T_x = -\gamma\left(\boldsymbol{m}\times\boldsymbol{h}^{\text{kin}}\right) \simeq -\gamma m_y\left|h_z^{\text{kin}}\right|$, whose spatial distribution can be seen, for different instants of time, in Figs. 6.2, 6.3, 6.4, and 6.5 (b). This gives rise to a reversed domain in front of the DW along the $-x$-*th* axis, which has a spatial extension prior to the process of generating additional magnetic textures, in the moving frame, comparable to the exchange length, l_{exc}, of the system. This spatial scale can be defined as $l_{\text{exc}} = \sqrt{a/\left(8K_{2\parallel}\right)}$, where the inhomogeneous FM-like exchange constant, a, and the uniaxial second-order anisotropy, $K_{2\parallel}$, were introduced in Secs. 5.3.2 and 5.2, giving as a result that $l_{\text{exc}} = 19.78$ nm. Coincidentally, this length extent, which, in the rest frame, corresponds to more than

twice l_{exc}, is sufficient to support the existence of a DW pair whose widths at the moment of the nucleation process are around 11 nm, according to what it is exposed in Fig. 6.8. Thus, it would not only be crucial for the original magnetic texture to reach a certain speed for a certain SO-based external stimulus to generate a sizable kinetic field magnitude, but also for the dynamic-based field to extend spatially enough to accommodate the DW pair.

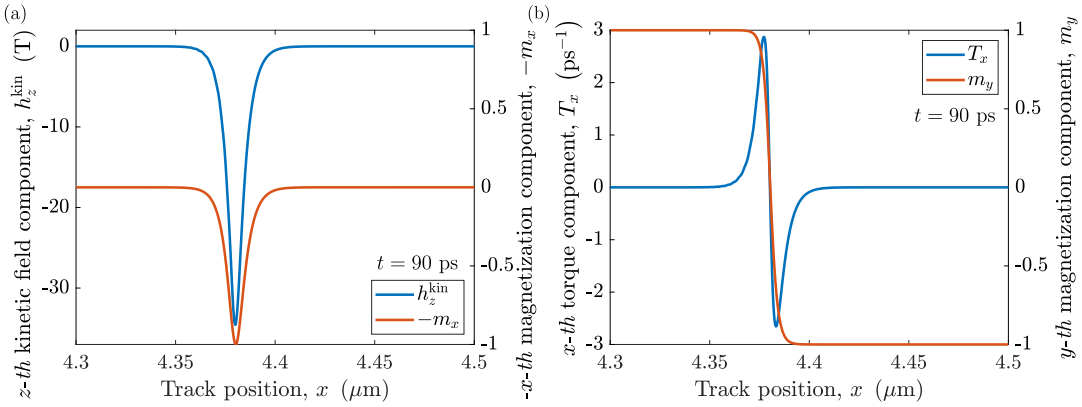

Figure 6.3: Spatial distribution of, on the one hand, (a) the *z-th* kinetic field, h_z^{kin}, and *x-th* magnetization, m_x, components and, on the other hand, of (b) the *y-th* magnetization, m_y, and *x-th* torque, T_x, components, respectively, for an instant of time of $t = 90$ ps, which were obtained by combining simulations together with Eq. (6.2), for the case in which the motion of a single DW was excited through a SO field which was ramped during 10 ps up to a maximum value of $H_y^{\text{SO}} = 65$ mT, which remains constant from then on.

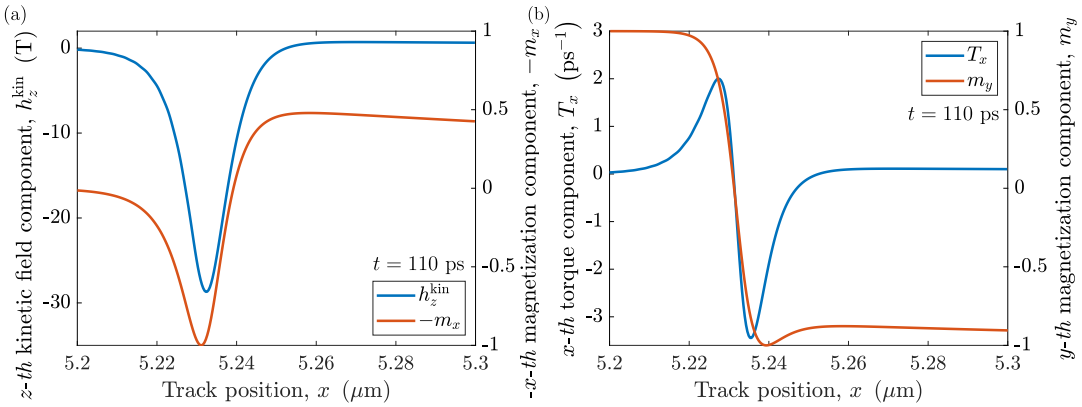

Figure 6.4: Spatial distribution of, on the one hand, (a) the *z-th* kinetic field, h_z^{kin}, and *x-th* magnetization, m_x, components and, on the other hand, of (b) the *y-th* magnetization, m_y, and *x-th* torque, T_x, components, respectively, for an instant of time of $t = 110$ ps, which were obtained by combining simulations together with Eq. (6.2), for the case in which the motion of a single DW was excited through a SO field which was ramped during 10 ps up to a maximum value of $H_y^{\text{SO}} = 65$ mT, which remains constant from then on.

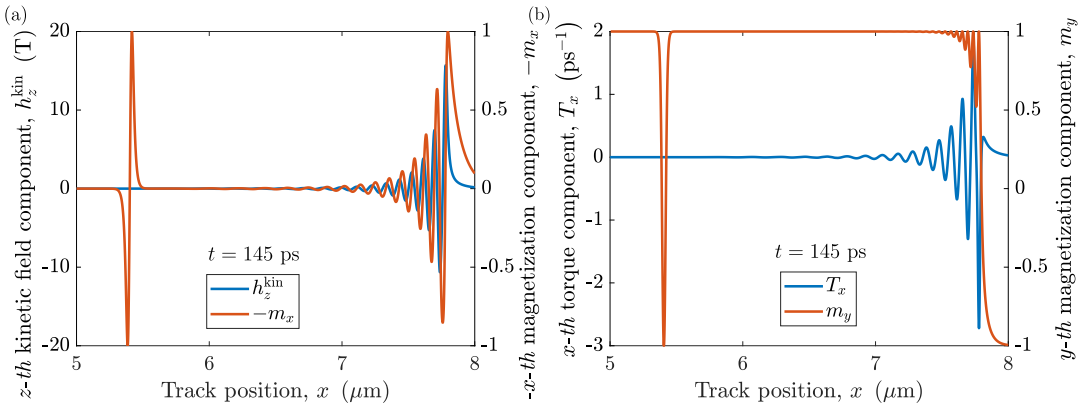

Figure 6.5: Spatial distribution of, on the one hand, (a) the z-*th* kinetic field, $h_z^{\rm kin}$, and x-*th* magnetization, m_x, components and, on the other hand, of (b) the y-*th* magnetization, m_y, and x-*th* torque, T_x, components, respectively, for an instant of time of $t = 145$ ps, which were obtained by combining simulations together with Eq. (6.2), for the case in which the motion of a single DW was excited through a SO field which was ramped during 10 ps up to a maximum value of $H_y^{\rm SO} = 65$ mT, which remains constant from then on.

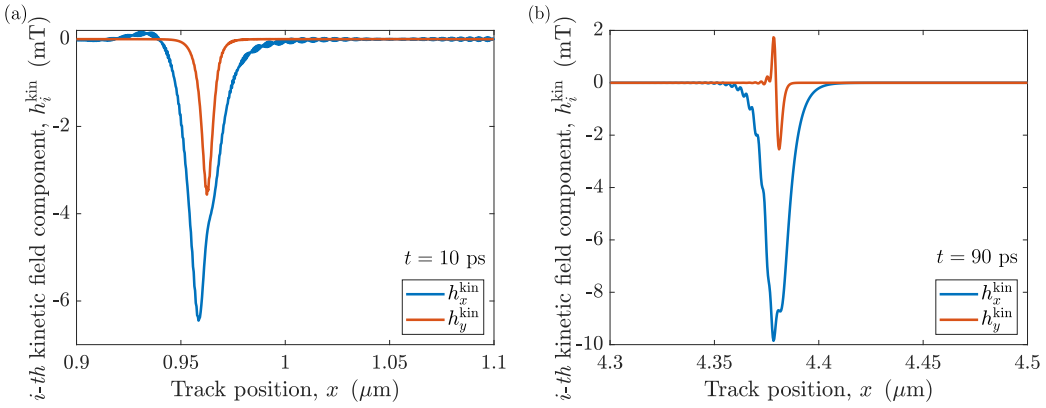

Figure 6.6: Spatial distribution of the x- and y-*th* kinetic field, $h_x^{\rm kin}$ and $h_y^{\rm kin}$, components, correspondingly, for two different instants of time, (a) $t = 10$ ps and (b) $t = 90$ ps, respectively, obtained for the case in which there was initially a single DW, which was subjected to ramping of the SO-based external stimulus for 10 ps up to a maximum value of $H_y^{\rm SO} = 65$ mT, which remains constant thereafter, obtained through the simulated magnetization components in conjunction with Eq. (6.2).

6.2.3 Energetically-favored nucleated magnetization configuration

Regarding the breaking of the reversed magnetic domain into a DW pair that preserves the overall winding number density of the system, giving rise to both having opposite chiralities, there are, in principle, different types of magnetic configurations that can fit according to the boundary conditions of the region where they nucleate. At the forefront of the seed-like magnetic soliton just before the generation of the new magnetic textures, the in-plane magnetization is entirely polarized along the $-y$-*th* axis, which is preserved after the fragmentation process, since the resulting configuration must start and end with the magnetic moment pointing along the aforementioned direction. Through the simulations, it can be seen that the nucleated

DW that is located just in front of the primal magnetic soliton shares its same topological charge, which is, in fact, what could be expected if one attends to the minimization of the different energy contributions of the system, formed by the FM-like exchange interaction and the Zeeman-like term formed by the SO and the kinetic fields. While the FM-like exchange contribution dictates that the central spins of both magnetic textures must be parallel to each other, the SO field dictates that the homogeneous magnetic region between them must be directed along the positive *y-th* axis, matching its current-induced application direction. On the other hand, as we discussed in Sec. 6.2.2, due to the magnitude of the *z-th* component of the dynamically-generated kinetic field, it exerts a torque that forces the magnetization to go along the $-x$*-th* axis during its in-plane rotation between its definition domains directed along the *y-th* spatial direction to minimize the related energy. The balance resulting from all these terms is completely coincident with the distribution of the generated DW with different chirality in front of the primal magnetic texture, which it is shown in Fig. 6.9 (a).

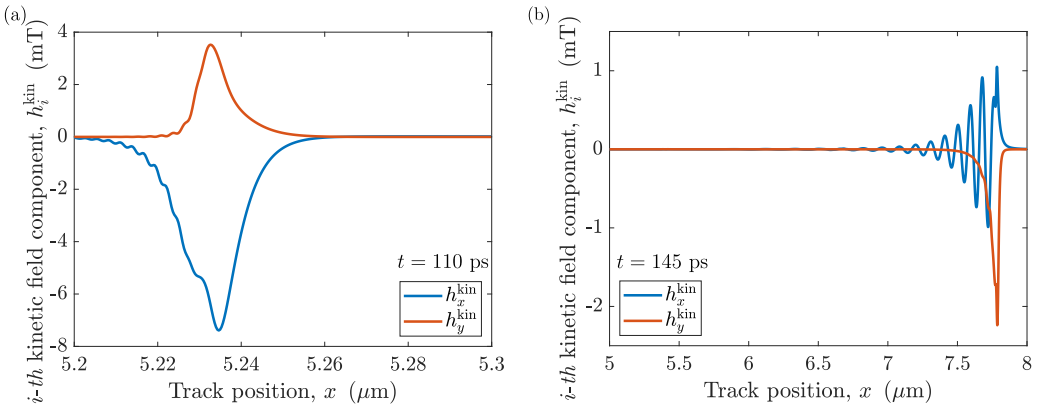

Figure 6.7: Spatial distribution of the *x-* and *y-th* kinetic field, $h_x^{\rm kin}$ and $h_y^{\rm kin}$, components, correspondingly, for two different instants of time, (a) $t = 110$ ps and (b) $t = 145$ ps, respectively, obtained for the case in which there was initially a single DW, which was subjected to ramping of the SO-based external stimulus for 10 ps up to a maximum value of $H_y^{\rm SO} = 65$ mT, which remains constant thereafter, obtained through the simulated magnetization components in conjunction with Eq. (6.2).

6.3 Non-relativistic radiant magnetic soliton boosting

6.3.1 Spatially stuck magnetic textures with the same chirality

The temporal evolution of the system is dramatically affected due to the appearance of the dynamically-generated DW pair compared to how the primal magnetic soliton evolved in a steady-state trend prior to this phenomenon. Due to the energetically-favored arrangement of the magnetic textures, spatially close to the original DW, which we will denote from now on as DW_1, will be the nucleated magnetic soliton with the same chirality as the seed-like one, being characterized as DW_2. Immediately after the fragmentation process, DW_1 and DW_2 perform a few oscillations and then get stuck, evolving in time but not in space as long as the SO field remains active, as it is depicted in Fig. 6.9 (b). This is due to the energy competition between the repulsive FM-like exchange interaction between both magnetic textures, since both reside in one of the basal planes of the layered AFM, their central spins being antiparallel arranged due to having the same topological charge, and the attractive

SO-based external stimulus, which will try to minimize the antiparallel-oriented homogeneously magnetized domain between both magnetic solitons, being important to note that the kinetic field contribution is zero because both DW are static. In this sense, it is possible to see that if the SO field is turned off after the nucleation process of the pair of magnetic textures has occurred, being already the DW_1 and DW_2 spatially localized, the repulsive exchange interaction will separate them, as it is shown in Fig. 6.10 (a). In order to elucidate which is the global minimum resulting from these competing forces, which will characterize, for a certain SO field, the equilibrium distance between the spatially-localized magnetic solitons, it is necessary to analyze the exchange interaction between both based on their mutual separation. For two magnetic solitons far enough apart that their envelopes do not overlap, it is possible to characterize their spatial distributions through the linear superposition of their dynamic individual profiles, $\varphi_i(x,t)$, like the one shown in Eq. (2.30), which is given by

$$\sum_i \varphi_i = 2\arctan\,\exp\left[\frac{Q_1\left(x-X_1\left(t\right)\right)}{\Delta_1\left(t\right)}\right] + 2\arctan\,\exp\left[\frac{Q_2\left(x-X_2\left(t\right)\right)}{\Delta_2\left(t\right)}\right], \tag{6.3}$$

where $Q_{1,2}$, $X_{1,2}$, and $\Delta_{1,2}$ denote the topological charges, center positions, and spatial extensions of the DW_1 and DW_2, respectively. Accordingly, the overall FM-like exchange energy, E_{exc}, concerning both magnetic textures can be characterized as

$$E_{\text{exc}} = \frac{a}{8a_0}\int_{-\infty}^{+\infty}\left(\sum_i \partial_x\varphi_i\right)^2 \mathrm{d}x = \frac{a}{8a_0\Delta^2\left(t\right)}\int_{-\infty}^{+\infty}\left[\operatorname{sech}^2\,\frac{x-X_1\left(t\right)}{\Delta\left(t\right)} + \operatorname{sech}^2\,\frac{x-X_2\left(t\right)}{\Delta\left(t\right)} + 2Q_1Q_2\operatorname{sech}\,\frac{x-X_1\left(t\right)}{\Delta\left(t\right)}\,\operatorname{sech}\,\frac{x-X_2\left(t\right)}{\Delta\left(t\right)}\right]\mathrm{d}x, \tag{6.4}$$

where it has been assumed, for simplicity, that after the nucleation process both DW have the same width, Δ, and that these will evolve over time analogously. Interestingly, the first two terms on the right-hand side of the previous expression denote the self exchange energy of the individual magnetic textures, while the last contribution represents the interaction energy between both magnetic solitons, which we will denote as E_{exc}^{12}.

To deal with the product of hyperbolic functions involved in the definition of the exchange-mediated DW interaction, it is possible to take advantage of the relation

$$\cosh\,\xi_1\,\cosh\,\xi_2 = b + b\cosh\,2\xi_1 + d\sinh\,2\xi_1, \tag{6.5}$$

where the involved parameters b and d can be expressed as

$$b = \frac{1}{2}\cosh\,\frac{X_1\left(t\right)-X_2\left(t\right)}{\Delta\left(t\right)}, \qquad d = \frac{1}{2}\sinh\,\frac{X_1\left(t\right)-X_2\left(t\right)}{\Delta\left(t\right)}, \tag{6.6}$$

while it has been defined that $\xi_i\left(x,t\right) = \left(x-X_i\left(t\right)\right)/\Delta\left(t\right)$. In line with the preceding notation, it is possible to rewrite the interaction term, E_{exc}^{12}, made explicit in Eq. (6.4), such that

$$E_{\text{exc}}^{12} = \frac{Q_1Q_2a}{4a_0\Delta^2}\int_{-\infty}^{+\infty}\frac{\mathrm{d}x}{b+b\cosh\,2\xi_1+d\sinh\,2\xi_1} = \frac{Q_1Q_2a}{4a_0\Delta^2}\,I, \tag{6.7}$$

where I represents, after the change of variable $y = 2\xi_1$, the sum of the two integrals

$$I = \frac{\Delta}{2}\left[\int_0^{+\infty} \frac{\mathrm{d}y}{b + b\cosh\, y + d\sinh\, y} + \int_0^{+\infty} \frac{\mathrm{d}y}{b + b\cosh\, y - d\sinh\, y}\right] = \frac{\Delta}{2}\left[I\left(b, b, d\right) + I\left(b, b, -d\right)\right], \tag{6.8}$$

which, as tabulated [419], have a solution given by

$$I\left(b, b, \pm d\right) = \pm\frac{1}{d}\ln\,\frac{b \pm d}{b}, \tag{6.9}$$

which allows us to reexpress Eq. (6.7) as

$$E_{\mathrm{exc}}^{12} = \frac{Q_1 Q_2 a\left(X_1\left(t\right) - X_2\left(t\right)\right)}{2a_0\Delta^2\left(t\right)}\,\mathrm{csch}\,\frac{X_1\left(t\right) - X_2\left(t\right)}{\Delta\left(t\right)}, \tag{6.10}$$

where, depending on the resulting sign of the product of the individual topological charges, the contribution will be repulsive, if $Q_1 Q_2 = +1$, or attractive, if $Q_1 Q_2 = -1$.

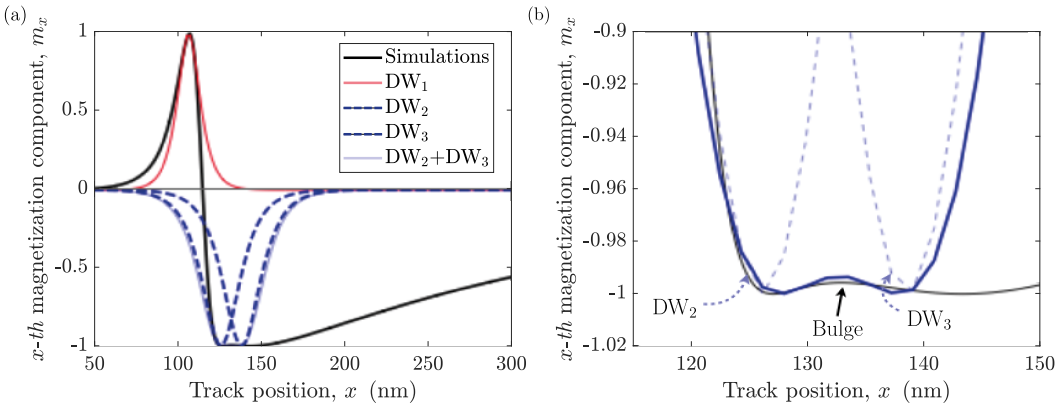

Figure 6.8: (a) Simulated spatial distribution of the *x-th* magnetization component, m_x, to which the analytical DW profiles, as the one given by Eq. (2.30), of the primal magnetic soliton, DW_1, and the pair of nucleated magnetic textures, DW_2 and DW_3, have been superimposed before the fragmentation process. (b) Simulated spatial distribution of the *x-th* magnetization component, m_x, for the instant in which a small bulge is observed for the first time, which suggests the potential generation of the DW pair formed by DW_2 and DW_3 on which has been superimposed an analytic linear combination of their individual profiles like the one given by Eq. (2.30). In both cases there was a single magnetic soliton at the beginning whose dynamics were triggered by ramping the SO field for 10 ps up to a maximum value of $H_y^{\mathrm{SO}} = 65$ mT.

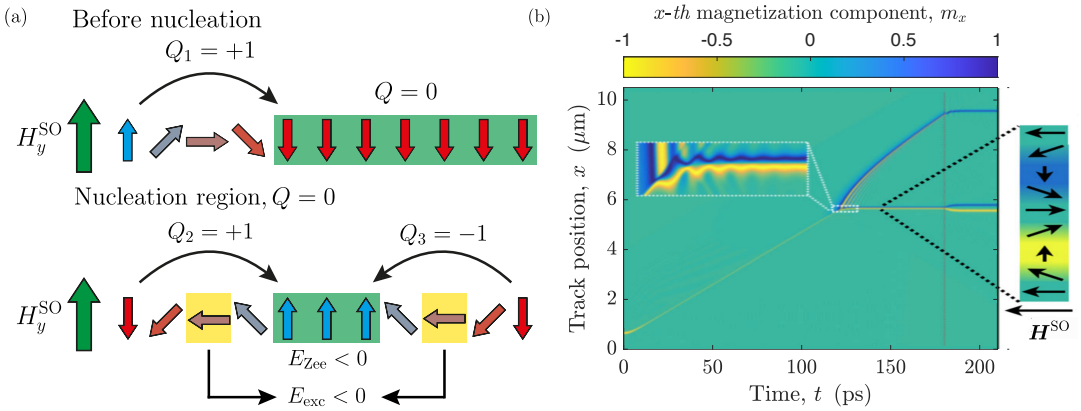

Figure 6.9: (a) Spatial distribution of the original magnetic texture, DW_1, together with the pair of nucleated magnetic solitons, DW_2 and DW_3, which is consistent with the energy minimization principle taking into account account the overall topological charge conservation of the system, the Zeeman-like kinetic and SO field contributions, E_{Zee}, and the FM-like exchange interaction, E_{exc}. (b) Simulated space-time distribution of the x-th magnetization component, m_x, in the region where the DW pair with the same chirality, DW_1 and DW_2, remain spatially stuck together with the oscillations they make around their final equilibrium positions dictated by the competition between the SO field, which has a magnitude of $H_y^{SO} = 65$ mT, and the FM-like exchange interaction.

To the FM-like exchange interaction between both magnetic solitons, given by Eq. (6.10) for the repulsive scenario, $Q_1 Q_2 = +1$, it is necessary to add the SO field-based Zeeman energy term, E_{Zee}, which will try to attract them through the in-between domain shrink, as a function of the distance between both DW, encoded through $X_1 - X_2$. In this way, the involved energy balance, ΔE, will be given by

$$\Delta E = \frac{2\gamma\hbar H_y^{SO}}{a_0}\left(X_1 - X_2\right) + \frac{a\left(X_1(t) - X_2(t)\right)}{2a_0\Delta^2(t)}\,\mathrm{csch}\,\frac{X_1(t) - X_2(t)}{\Delta(t)}, \tag{6.11}$$

from which it is possible to extract the existence of a global minimum that characterizes the stable configuration distance between both magnetic textures. Accordingly, Fig. 6.10 (b) shows how the distance between the centers of mass of both DW depends as a function of the SO-based external stimulus, and it can be seen that, as its magnitude increases, the separation between both entities decreases because the related Zeeman energy requires a smaller extension of the homogeneously magnetized domain between both magnetic solitons to compensate for the repulsive FM-like exchange interaction between them. For the specific case in which the appearance of the nucleation process was observed for $H_y^{SO} = 65$ mT, it is possible to extract from simulations that the DW are at a stable distance of 32 nm as long as the SO field remains present, while the separation obtained analytically through Eq. (6.11), using their simulated spatial extension values of, approximately, $\Delta = 11$ nm, is 38.4 nm, which is a good estimate of the underlying mechanisms.

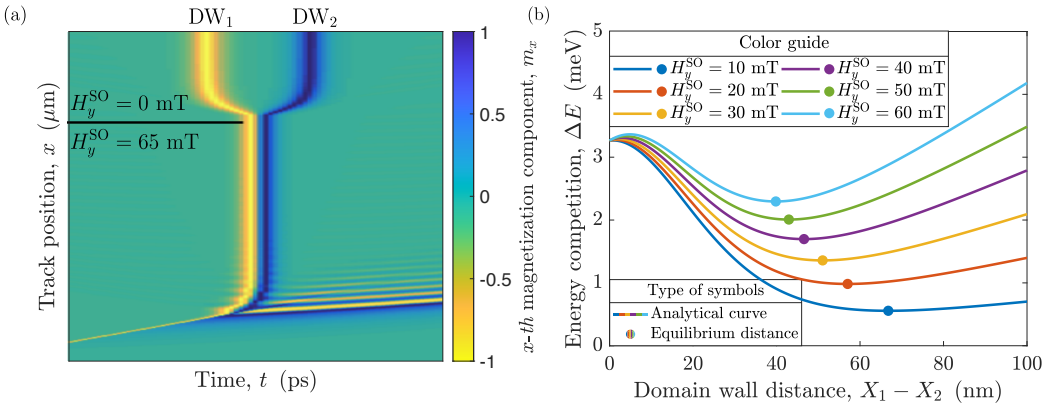

Figure 6.10: (a) Simulated space-time distribution of the *x-th* magnetization component, m_x, in the region where the DW pair with the same chirality, DW_1 and DW_2, are located, where it can be seen that, when the constant SO-based external stimulus of $H_y^{SO} = 65$ mT is turned off, the distance between them increases due to the dominance of the repulsive FM-like exchange interaction. (b) Spatial energy distribution, ΔE, composed of the balance between the attractive SO field and the repulsive FM-like exchange contributions in terms of the distance between the center of mass of the pair of magnetic textures with the same topological charge, DW_1 and DW_2, given by $X_1 - X_2$, obtained analytically through Eq. (6.11) for different magnitudes of the external stimulus, H_y^{SO}. Each colored solid circle corresponds to the global energy-based minimum that marks the equilibrium distance between both magnetic solitons for different SO fields.

6.3.2 Broken Lorentz invariance-based superluminal propulsion

Concerning the magnetic texture with opposite chirality with respect to the one carried by the seed-like original magnetic soliton, which we will denote as DW_3 from now on, after its generation it propagates forward experiencing a velocity boost that causes it to move faster than the maximum magnon group velocity of the medium, as it is shown in Fig. 6.11 (a). As it can be seen in Fig. 6.1 (b), this process is transient, lasting several tens of ps, which is enough for this magnetic texture to cover a distance of, approximately, 3 µm. As it was previously explained in Sec. 6.3.1 and shown in Fig. 6.9 (a), the spatially stuck pair of magnetic textures formed by DW_1 and DW_2 is subject a to mutual repulsion due to the FM-like exchange interaction between them due to their coexistence in one of the basal planes of Mn_2Au, which would promote a potential motion of both magnetic solitons in opposite directions, moving away from each other. Despite this fact, they barely move due to the attractive effect of the current-induced SO field, which would result in all this stored exchange-based energy that is not transformed into a translational displacement of the localized DW pair being transferred from DW_2 to DW_3, similar to how SW can transmit linear momentum to a given magnetic texture [420]. Under this perspective, the mobility of DW_3 at the moment of the nucleation would consist of the speed provided by the primal magnetic texture in its steady-state motion just before the generation process of additional pseudoparticles together with a boost from the momentum transfer resulting from the repulsion between the spatially stuck magnetic soliton pair.

To characterize this phenomenon, it is possible to generalize what it is stated in Eq. (6.11), which is ascribed to the case of exchange-mediated repulsion between two magnetic textures with the same chirality, to an attractive situation in which

DW_2 and DW_3 have opposite topological charges, case reflected in Eq. (6.10). In this context, in the presence of the SO field-based contribution, which will want them as far away as possible, it would be necessary to characterize, through the collective coordinates approach in combination with the EL formalism in the presence of dissipation processes encapsulated by the Rayleigh dissipation function, R, which is the impact of the repulsive exchange interaction between the spatially localized magnetic textures, characterized by Eq. (6.10), in the dynamics of the DW_3. For this, however, it must be taken into account that to the Zeeman-like contribution of the right-hand side of Eq. (6.11) it has to be added a factor 2, since in this case it refers to the case of a single magnetic soliton, situation for which the configurational energy given by Eq. (5.10) must be spatially integrated taking into account, for this, which is stated in Eqs. (3.19) and (3.23). In this line it is possible to obtain that the speed of the boosted magnetic soliton, v_{DW_3}, will be given by

$$v_{DW_3} = \frac{\gamma H_y^{SO} \Delta_{DW_1}}{\alpha} + \frac{a}{8\alpha\hbar\Delta_{DW_3}^2}\left[x\left(t\right) \text{ cotanh } \frac{x\left(t\right)}{\Delta_{DW_3}} - \Delta_{DW_3}\right] \text{csch } \frac{x\left(t\right)}{\Delta_{DW_3}}, \quad (6.12)$$

where Δ_{DW_1} represents the simulated dynamically-based spatial extent of the DW_1 during its steady-state trend, while Δ_{DW_3} denotes the width of the boosted magnetic texture at the time of nucleation extracted through simulations, and $x\left(t\right)$ corresponds to the distance between the centers of mass of the aforementioned magnetic solitons, $x\left(t\right) = X_1\left(t\right) - X_3\left(t\right)$. The first term of the right-hand side of the previous expression is consistent with the assumption that, in the simulations, the magnetization dip that will eventually fragment to produce the DW_2 and DW_3 pair moves at the same velocity as the seed-like magnetic soliton, v_{DW_1}. The global velocity profile, represented in Fig. 6.11 (b), shows that, in fact, the maximum attainable speed due to the transfer of linear momentum between the DW_1-DW_2 pair and DW_3 does not occur when they coincide in space, which can be linked to the fact that the magnetic textures have a finite width.

Through the simulations, it is possible to appreciate that the distance between the DW_1 and DW_3, at the moment of nucleation, is 17 nm, while the numerically-extracted speed of the magnetic texture in the supermagnonic regime is approximately 177 km/s, that is, four times higher than the maximum magnon group velocity, v_m, of the medium in Mn_2Au, which is given by $v_m = 43.3$ km/s. The maximum analytically achievable speed, v_{DW_3}, according to Eq. (6.12), that DW_3 can reach as a function of the distance between the considered DW pair is about 133 km/s when its separation with respect to the primal magnetic texture is 16.1 nm, which shows that this interpretation is efficient when elucidating the balance of forces that act on the boosted magnetic soliton in its breaking process of the magnonic barrier. At this point, it is appealing to think that the special relativity theory is being violated since no magnetic soliton is, in principle, allowed to propagate faster than the light-like velocity of the magnons in spin space. However, as soon as the pair of magnetic textures, represented by DW_2 and DW_3, is nucleated, additional interactions appear in the system, as it can be seen in Eq. (6.10), which mean that the Lagrangian is no longer Lorentz invariant, which has as a consequence that the constriction imposed by the maximum magnon group velocity of the medium must be lifted up. As the boosted magnetic texture moves away from the spatially stuck DW pair, the exchange-based linear momentum transfer will be weaker due to its short-range character. In this way, as it moves away, the Lorentz invariance is gradually recovered due to the energy dissipation that it experiences through the SW emission, and it becomes possible to define, again, the limit ascribed to the maximum magnon

group velocity of the medium.

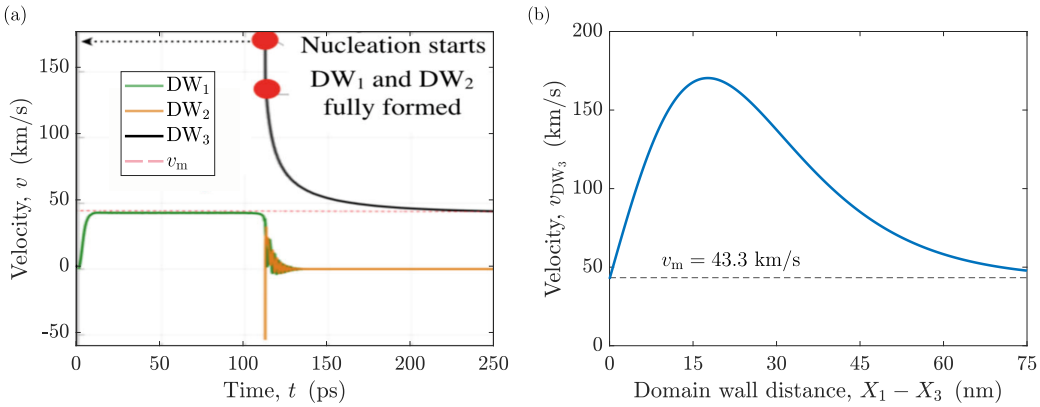

Figure 6.11: (a) Time evolution of the velocity of DW_1, DW_2, and DW_3, represented, respectively, by v_{DW_1}, v_{DW_2}, and v_{DW_3}, extracted through the simulations together with the relativistic limit imposed by the maximum magnon group velocity of the medium, v_m. (b) Dependence of the speed of the DW_3, v_{DW_3}, as a function of the distance between this magnetic texture and DW_1, given by $X_1 - X_3$, obtained analytically through Eq. (6.12), compared to the maximum magnon group velocity of the medium, v_m.

6.3.3 Cherenkov and Bremsstrahlung spin wave mixed radiation

Accompanying the DW_3 in its supermagnonic regime of motion, we can observe the existence of a sudden emission of SW that spreads along with the aforementioned magnetic soliton, but never exceeds it, as it can be seen in Fig. 6.5 for $t = 145$ ps. Interestingly, this phenomenon has also been reported in the case of mechanical systems where dynamic edge dislocations under shear stress may be accompanied by spontaneous emission of radiation [421, 422]. In our case, we attribute the origin of the emitted SW to a mixture of the so-called Bremsstrahlung effect [423], which is also known as braking radiation, and the spin Cherenkov effect [424]. On the one hand, the Bremsstrahlung effect is due to the acceleration/deceleration of a charged particle, which is why it could be hypothesized that, in spin space, a deceleration could lead to an excitation of the medium. On the other hand, through the simulations it is possible to appreciate that the boosted DW_3 not only overcomes the magnonic barrier during its propagation, but it also gets to move faster than the phase velocity of the magnons in the medium, as it is shown in Fig. 6.12 (a), which is the necessary condition for the existence of the spin Cherenkov effect. As a consequence, in our case it is difficult to clearly separate the individual existence of the spin Cherenkov and braking radiations due to their hypothetical mixture. We also note that the number of oscillations that the DW_1 and DW_2 pair perform with respect to their equilibrium distance coincides with the number of SW ripples traveling together with the DW_3 and, additionally, that the decay of these ripples seem to stretch over a rather long time. Therefore, one possibility for the coexistence of both types of radiation would be that the spin Cherenkov-based SW act in an anti-damping fashion in the Bremsstrahlung radiation, since in the case in which there is only acceleration/deceleration radiation it decays faster than what it is observed in this case, which would be combined with the fact that the radiated ripples do not propagate in the opposite direction to the DW_3.

6.4 Domain wall lattice generation and decompression

6.4.1 Supermagnonic soliton-triggered nucleations cascade

So far, we have evaluated the case in which a primal DW seed, under the action of a ramping process of 10 ps after which the SO field is kept constant at a value of $H_y^{SO} = 65$ mT until the end of the simulation, see its steady-state regime of motion interrupted by the nucleation of a magnetic soliton pair preserving the overall topological charge, as it was explained in Sec. 6.2. However, it is pertinent to assess how the system behaves when it has at its disposal additional current-induced pumped energy. Under this pretext, we will employ an excitation protocol with a rising time of 5 ps until reaching a SO field-based maximum value of $H_y^{SO} = 100$ mT, which is held constant by the next 50 ps after which it is reduced to zero with a falling time of 5 ps. After this, the external stimulus will remain off for 50 ps before starting this pattern again three times in a row, as it is shown in Fig. 6.12 (b). Interestingly, once the first generation process of a single DW pair occurs, the magnetic texture that propagates at supermagnonic velocities from the fragmentation point becomes a new breeder and gives rise to a new couple of magnetic textures, which gives rise to an avalanche of nucleation phenomena preserving the original winding number density, which it is depicted in Fig. 6.13 (a). This situation is repeated 13 times throughout the simulation, which results in the appearance of 26 additional magnetic solitons. It is worth noting that the magnetic textures, once nucleated, do not rearrange into a more stable configuration as long as the SO field is maximum, giving rise to a DW lattice-like structure in which the distance between spatially stuck magnetic soliton pairs depends on the external stimulus-based pulse pattern. In this line, the average magnetic texture number density per pulse is 0.013 DW/nm, taking approximately 20 ps to generate the complete magnetic soliton-based network, which it is shown in Fig. 6.12 (b) through closed blue circles.

As it can be noted in Fig. 6.13 (b), when in each cycle the SO field begins to decrease, the lattice suffers a decompression due to the mitigation of this attractive mechanism between DW with identical topological charge, which coexists with the FM-like exchange interaction which favors the annihilation of magnetic textures with opposite chirality, since their central spins are parallel. Every time the external stimulus starts to decrease progressively from the constant value regime, it is possible to see that approximately the same number of DW are recombined in each cycle, as it can be seen through the solid orange circles in Fig. 6.12 (b). In the same way, it is possible to appreciate that the number of magnetic solitons between pulses, while the SO field is zero, just before reinjecting the electric current, increases after each cycle, which it is represented by solid green circles in Fig. 6.12 (b), which denotes that only those magnetic textures with opposite topological charge that are located spatially close will annihilate, being separated again when the external stimulus reappears, which implies that not all the generated DW are recombined. After finishing the fourth pulse, it is possible to obtain that the number of magnetic solitons in the system is 8, ranging the spacing between the magnetic textures from hundreds of nm to few μm. More complex DW lattices can be generated through the variation of the pulse duration and the sign of the SO field, showing the rich magnetization dynamics in these type of systems. However, it is important to note that there does not seem to be a clear correlation between the strength of the external stimulus, H_y^{SO}, and the number of magnetic solitons generated, nor for the instant of time and the point of the space where the fragmentation process takes place. This opens the possibility that, under certain circumstances, a potential chaotic behavior in the system

can be appreciated.

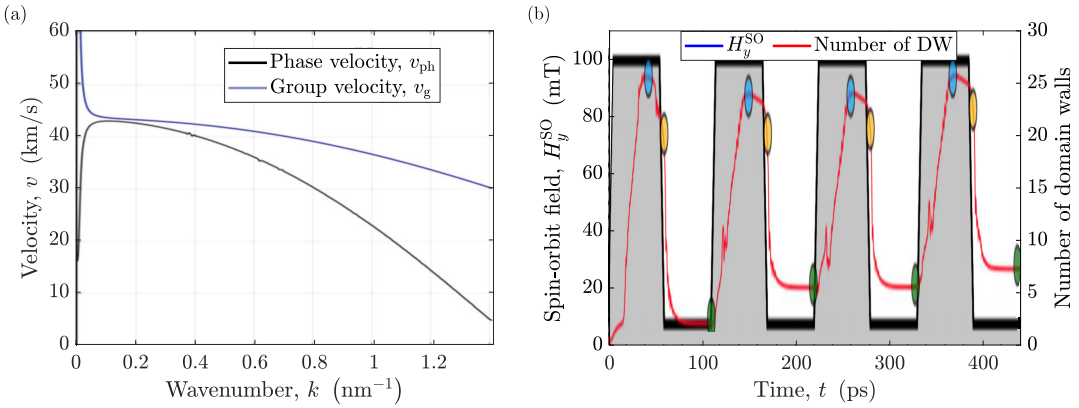

Figure 6.12: (a) Phase, v_{ph}, and group, v_g, velocities of the magnons of the medium as a function of the wavenumber, k, extracted through simulations under a SO field of $H_y^{SO} = 100$ mT. (b) Time-dependent staggered SO field-based excitation protocol, H_y^{SO}, applied in each Mn-based FM sheet of the layered AFM Mn_2Au, for the case in which the external stimulus ramps for 5 ps up to a maximum value of $H_y^{SO} = 100$ mT, which is maintained for 50 ps, after which it decreases to zero with a falling time of 5 ps, state in which it remains for another 50 ps. This process is repeated three times in a row. Additionally, the closed blue circles represent the number of magnetic solitons in each pulse, while the orange and green ones denote the number of magnetic textures when the SO field begins to decrease and when it is about to increase again from a zero value, respectively.

6.4.2 Experimental fragmentation-induced resistance variations

A recent experimental work has reported current-induced resistance changes in the layered AFM CuMnAs, which shares with Mn_2Au the possibility of being excited through SO fields due to the symmetric inequivalence between its crystallographic and magnetic unit cells, which are attributed to the fragmentation and recovery of the domain structure [170, 353]. In particular, what was observed was a gradual increase in the resistance in response to repeated pulsing and a slow relaxation of it towards lower values when the excitation is completely turned off. Provided that finite size effects can be excluded and that the topological charge is globally conserved, it should be possible to return to the original state through the application of a reversed field with a magnitude below which the AFM DW WB takes place, which would allow to completely recover the initial value of the resistance, that is, to achieve a complete reset of the system. However, what is observed experimentally is that the relaxed resistance after a long waiting time was higher than the original one, which could imply that there are residual DW in the medium, as in our case, which is represented by solid green circles in Fig. 6.12 (b) and in Fig. 6.13 (b). If the interpretation that the observed resistance changes are due to domain fragmentation and recovery/recombination up to the initial state, we cannot help but to speculate on the possibility of experimentally characterizing the phenomenology contemplated in this chapter. Moreover, if this was confirmed, it could also be shown that the reported resistance changes can be explained entirely through magnetic effects, which is under discussion due to alternative explanations based on current-induced heat effects [363], electromigration [425], and rapid quenching-induced structural and magnetic modifications [170, 426]. Although in our case the phenomenon of

magnetic texture nucleation occurs in a perfect crystal in the absence of temperature and without taking into account the current-induced Joule heating, if the pinning and heating effects inherent to a real system could be isolated experimentally, these changes in the detected resistance could constitute an indirect detection method of the AFM DW WB as well as the associated generation of supermagnonic solitons, since the SO field contribution appears to be the leading one in the switching mechanism [427].

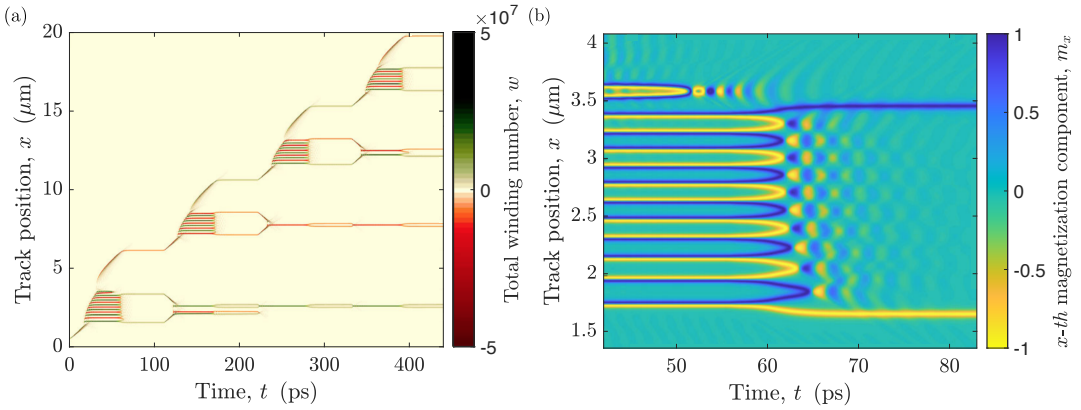

Figure 6.13: (a) Simulated space-time evolution of the winding number density, w, for the case in which there was, initially, a single DW in the system which was subjected to a ramping of the SO field for 5 ps up to a maximum value of the SO field of $H_y^{\mathrm{SO}} = 100$ mT, which remains constant for 50 ps, and then gradually decreases to zero for 5 ps, remaining in this state for another 50 ps. This excitation process is repeated three times in a row. (b) Simulated space-time distribution of the x-th magnetization component, m_x, in a region full of DW pairs with opposite chirality whose constituents, after the gradual decrease and eventual shutdown of external stimulus, annihilate each other.

6.4.3 Exchange-mediated pairwise gas approximation

It should be noted that, for a ramping time of 10 ps, there are no signatures of nucleation of pairs of magnetic textures below a SO-based external stimulus of $H_y^{\mathrm{SO}} = 65$ mT, which indicates that the critical field depends on the raising time rather than the absolute value of the energy pumped in the system. As it is shown in Fig. 6.13 (b), once the DW lattice has formed and the SO field is turned off, a process of multiple annihilations takes place, leading to the reduction of the existing 13 pairs of magnetic solitons to just one of them. Due to the existence of a distribution of separations between the closest magnetic textures with opposite topological charges, it is possible to observe that there will be a manifold of recombination times in the after-pulse exchange-mediated process, as it is depicted in Fig. 6.14 (a). Analytically, it is possible to obtain the annihilation time, t_{r}, as a function of the distance between magnetic solitons assuming that the decompression phenomenon in the absence of SO field results in a phase transition from a DW lattice to a gas-like system for a transient time. In this line, the recombination time will depend only on the intrinsic parameters of the medium, such as the FM-like exchange interaction, the damping, and the distance to the closest magnetic textures with opposite chirality, ruling out the effect of the rest of the DW pairs in the system.

A general expression for the annihilation time can be derived through the general functional form for the exchange-based velocity boost between two magnetic

solitons with opposite topological charge, that is, for the case in which the exchange-based part in Eq. (6.12) is attractive without taking into account the SO field-based steady-state contribution, such as

$$t_{\mathrm{r}}(l) = \int_{t_0}^{t_{\mathrm{r}}} \mathrm{d}t = -\frac{8\alpha\hbar\Delta^2}{a} \int_{l}^{l_0} \frac{\mathrm{d}x}{\left(\Delta - x\,\mathrm{cotanh}\,\frac{x}{\Delta}\right)\,\mathrm{csch}\,\frac{x}{\Delta}}, \tag{6.13}$$

where Δ and l are the spatial extent of both magnetic solitons and the distance between them just before turning off the SO field, respectively, which occurs at t_0, which can be set to $t_0 = 0$ as a reference. On the other hand, t_{r} represents the recombination time, which will be assumed to occur when the centers of mass of both magnetic textures are at a cut-off distance of $l_0 = 1$ nm, having chosen this length scale as a compromise between the fully contracted DW width in the steady-state trend and the minimum interatomic distance given by a_0 due to their non-point nature. We note that, as it is shown in Fig. 6.14 (a), the theoretically-predicted recombination time quantitatively reproduces the values extracted from the ASDS, which validates the hypothesis of a 1D DW pairwise gas approximation. For distances in the range of a few hundred nm, the annihilation time is of the order of a few ps, since the exchange interaction is a short-range contribution. However, it is possible to appreciate in Fig. 6.13 (b) that, after all the simulated decompression process, there are still magnetic solitons in the system that are separated by a few of µm. For a distance of 1.8 µm, the expected recombination time lies in the range of, approximately, 6 days, which suggests that, in the ideal scenario in which pinning and thermal effects are not present, the stability of such configuration is guaranteed thanks to the absence of long-range interactions.

6.4.4 Recombination-induced breather-like excitation

From Fig. 6.13 (b), it is possible to appreciate that, when the SO field is set to zero, the recombination process of each DW pair led to an excitation in the continuum spectrum that oscillates over time with a very precise frequency. The emergence of this breather-like state is due to the kinetic energy carried by each magnetic texture involved in the collision, which is insufficient to escape the attractive potential provided by its antiparticle. By mapping this bounded excitation into a single damped harmonic oscillator, which would be given by

$$m_x = B\,\cos\left(ft - \phi\right)\,e^{-t/t_{\mathrm{d}}}, \tag{6.14}$$

we obtain a good quantitative agreement over its lifetime, as it is shown in Fig. 6.14 (b). The breather decay occurs in $t_{\mathrm{d}} =$ 20-30 ps and is governed by the Gilbert damping. Moreover, the characteristic frequency of this state is $f = 544$ GHz, which lies within the linewidth of the simulated SW band gap for $H_y^{\mathrm{SO}} = 100$ mT, that is, the frequency at zero wavenumber, $k = 0$. Therefore, we are compelled to assign the breather frequency to the band gap.

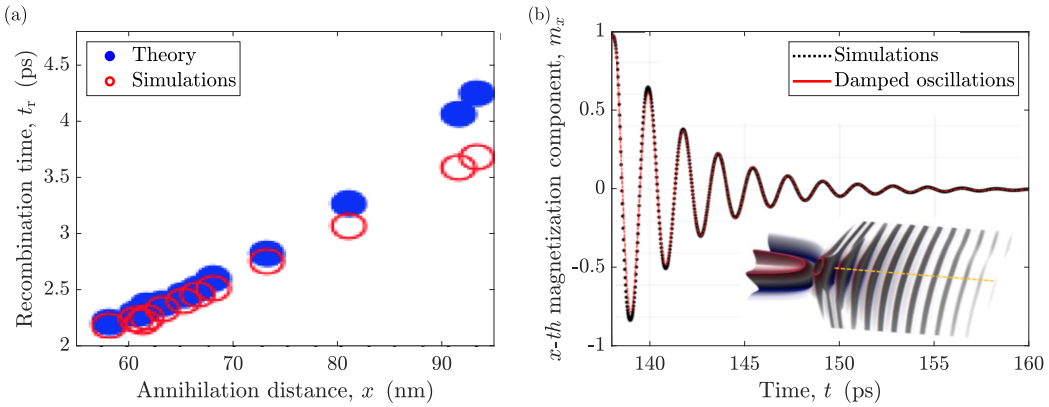

Figure 6.14: (a) Comparison of the recombination time, t_r, extracted through simulations and the one estimated analytically through Eq. (6.13) as a function of the distance traveled by each DW with opposite chirality before culminating in the annihilation process. (b) Comparison of the simulated time evolution of the *x-th* magnetization component, m_x, at the annihilation point of a pair of magnetic textures with opposite topological charge with an analytically-based damped harmonic oscillator expression given by Eq. (6.14).

6.5 Conclusions

We have sought to mimic in spin space the entry of dislocations in non-magnetic periodic structures under the action of high strains into a highly nonlinear regime of motion, case in which the steady-state dynamic trend is extinguished through the beating of the phonon-based sonic barrier by means of the nucleation of mother-daughter secondary kinks with opposite Burgers vectors. In this sense, through ASDS, it has been found that, despite the energy-based topological protection of the Néel-like DW residing in the FM sheets of the layered AFM Mn_2Au, for a certain combination of the SO field magnitude and the raising time, a phenomenon analogous to the WB in FM occurs, interrupting the stable magnetic texture dynamics. This results in the generation of an additional DW pair preserving the overall topological charge of the system, a process which can be related to the torque exerted by the dynamically-based kinetic field generated by the primal magnetic soliton during its translational propagation. That nucleated magnetic texture that has the same chirality as the seed one will stay spatially stuck next to the original one due to the energy balance between the repulsive FM-like exchange interaction and the attractive SO field, while the other generated DW moves away from the breakdown point at speeds that far exceed the maximum magnon group velocity of the medium. This supermagnonic boost is due to the fact that, in addition to the speed at which the primal magnetic soliton was moving just before the fragmentation process, the stored exchange-based energy that is not transformed into translational displacement by the localized DW pair is transferred to the free magnetic texture. At such high speeds it is possible to appreciate the existence of a radiative tail traveling together with the boosted magnetic soliton, which seems to be due to the spin Cherenkov, because the DW eventually exceeds the SW phase velocity of the system, and the Bremsstrahlung, due to the rapid deceleration of the primal magnetic texture at the nucleation instant, effects. We observe the existence of oscillations in the positions of the spatially stuck DW pair whose number coincides with the radiative ripples traveling with the boosted magnetic soliton, which opens the possibility that

the spin Cherenkov radiation acts in an antidamping fashion in the braking-based SW emission, explaining the rather slow decay of the undulations. If the magnitude of the SO field is increased using the same ramping time, it is possible to appreciate the creation of a DW lattice due to the appearance of a cascade of nucleations where each supermagnonic magnetic texture acts as a new seed, proceeding to decompress when the external stimulus is progressively decreased due to the annihilation of pairs of magnetic solitons with opposite chirality. This type of scenario points to a potential application in the field of information processing, which could be codified through the creation of different patterns. Provided that the separation between nucleated magnetic textures with the same topological charge is large enough, residual magnetic solitons may remain in the system when the SO field is completely turned off, leading to recombination times well beyond of those possibly simulated because the exchange-based attractive mechanism is a short-range one. This type of observation is in line with the experimentally reported resistance variations in these types of materials under the action of pulsed excitations as well as a remnant signal when the external stimulus has been extinguished, which is attributed to a fragmentation of the spin space, phenomenon which would not require the action of Joule heating or temperature to explain it according to our results.

Chapter 7

Topologically-mediated energy release by relativistic antiferromagnetic solitons

7.1 Energy tuning and release by domain walls in spin space

Solutions for an efficient energy control are based on identifying the related prevailing carriers, transfer mechanisms, and release pathways on the relevant time and space scales. In the field of nanoelectronics, which is based on exploiting the electric charge of the electron, many concepts have been proposed to achieve this end [428], but the use of its quantum-based spin in this sense has not been so widely discussed. Based on the same topological-like protection functionality for which localized spin structures have been envisioned as information vectors [82, 429], there are some proposals in which they are also proposed as stationary energy storing units [430–432]. However, the use of them as dynamic carriers as well as possible ways to release the accumulated energy at will have not been addressed. Beyond the potential stability of magnetic solitons like DW, it is also possible to highlight the plethora of well-characterized methods through which it is possible to excite their translational motion as well as the fact that their self energies can be tuned through the control of their width [96, 175, 207, 433, 434]. This last statement is due to the fact that, as the angle between neighboring spins increases, which implies that the spatial extension of the considered magnetic texture is reduced, the exchange-based energy is enhanced. Unlike in the case of FM, where no sizable DW width contractions down to almost the atomic scale have been reported even for relatively high velocities [435], AFM do present it intrinsically without complicated engineered geometries [436]. This is because, in AFM, it is possible to reach speeds very close to the limiting maximum magnon group velocity of medium dictated by the special relativity principles, which leads to very narrow DW widths and, therefore, high exchange-based self energies [134, 414]. Due to the inherent topological selection rules in spin space, it is expected that, as in the case of FM, if two 1D magnetic textures with the same relative topological charges collide they will not be able to annihilate each other, but for the case in which the DW pair have opposite chiralities, as long as their kinetic energies are not enough to escape the attractive potential created by their counterpart, they will recombine [86, 437, 438]. In this way, it is possible to merge the relativistic Lorentz factor-governed width tuning together with the energy release in nanometric localized spots on the ps time scale through inelastic DW collisions in AFM.

7.2 Topological selection rules for antiferromagnetic solitons

7.2.1 Simulated chirality-dependent magnetic textures collision

Just as it was done previously in, namely, Chaps. 5 and 6, we will take as the study system the layered AFM Mn_2Au, in which 180° DW can be stabilized in each FM sheet of the unit cell, as it was schematized in Fig. 5.1 (b), the dynamics of which can be excited through a current-induced SO field [139, 148]. To, firstly, certify that the topological selection rules, as expected, are also verified in AFM, we perform ASDS, taking into account the functional form of the atomistic energy given by Eq. (5.1), being defined the associated parameters in Sec. 5.2, in which the LLG equation given by Eq. (2.14) is solved numerically, site by site, through a fifth-order Runge-Kutta method, assuming that the damping parameter is $\alpha = 0.001$ [165, 402]. The simulated magnetic domain will consist of 60000 unit cells along the *x-th* movement direction, one cell width with periodic boundary conditions along the *y-th* direction, and one cell thick along the *z-th* axis. Initially, two DW are stabilized at an approximate distance of 1.5 µm, with the same or the opposite relative topological charges, and through a SO-based external stimulus protocol, applied along the *y-th* spatial direction, based on ramping the field for 10 fs up to a maximum value, H_y^{SO}, which will hold until the end of the simulation, they are made to collide at the midpoint of the track. As it can be seen in Fig. 7.1, both magnetic solitons undergo a strong initial acceleration process which is accompanied by the emission of SW, contrary to what happened in Sec. 5.4.2, where this scenario was avoided by employing a sufficiently long raising time to ensure that the magnetic texture evolved in a quasistatic trend, as it can be seen in Figs. 5.6 and 5.7 (a). After a brief period of acclimation after which both DW move at a constant speed, reaching values very close to the maximum magnon group velocity of the medium from SO field amplitudes of $H_y^{SO} = 20$ mT, which it can be seen in Fig. 5.5 (a), they reach the impact spot after a few tens of ps. Depending on the relative topological charges, Q_i, between both magnetic solitons, they will suffer an elastic collision if they have the same winding numbers, that is, $Q_1Q_2 = +1$, both remaining in the system after it, while if their chiralities are the opposite, that is, $Q_1Q_2 = -1$, both of them will suffer an inelastic impact that results in their deletion, giving rise to a breather-like excitation, as it is shown, for a maximum SO field of $H_y^{SO} = 60$ mT, in Figs. 7.1 (a) and (b), respectively.

7.2.2 Energy-based perspective on the pseudoparticles impact outcome

The notion of topological protection and, therefore, the assignment of a certain topological charge to a magnetic soliton, responds to its behavior in the presence of an external field, since, for a moderate external stimulus that is collinear to the domains between which this is defined, the torque outside the inhomogeneous DW transition will be zero, which allows it to prevail in the system, as it is shown in Fig. 2.5 (b). Furthermore, regardless of the relative winding numbers between the two considered magnetic textures, the domain between them is antiparallel to the applied SO field, as it is depicted in Fig. 7.2 (a), so, to minimize the associated Zeeman energy, this region between them should be as short as possible, leading to the collision of both magnetic solitons. However, this is not the only energy contribution to take into account to envision how will be the impact of two DW as the in-between domain shrinks, being also dictated by the FM-like exchange interaction. Since both magnetic textures, irrespective of their relative chiralities, live in a FM sheet, if their central spins are parallel, the exchange contribution will cause them to attract each

other (as in the case in which $Q_1Q_2 = -1$), while if they are arranged antiparallel to each other they will tend to repel each other (scenario corresponding to case in which $Q_1Q_2 = +1$), as it is shown in Fig. 7.2 (a). It is, therefore, the simultaneous action of these two energy contributions which dictates which will be the outcome of the collision of two DW depending on what their relative topological charges are, approaching each other due to the action of the SO field and being able to recombine or not depending on the relative orientation of their central spins through the FM-like exchange interaction, as it is shown by the simulations in Fig. 7.1. This type of reasoning was also implicit in the discussions of the creation and decompression of the DW lattice in Chap. 6, both in the case of stuck pairs of magnetic textures with the same topological charge, as discussed in Sec. 6.3.1, and in the case in which magnetic solitons with opposite topological charges begin to recombine when the SO field is turned off, as it is shown in Sec. 6.4.1. In this line, the balance between both energy contributions has been collected by Eqs. (6.10) and (6.11). Due to the attractive or repulsive nature of the FM-like exchange interaction between two DW depending on their relative chiralities, it could be hypothesized if this short-range contribution has an impact on the velocity of the magnetic solitons when they are close enough to each other. However, if this it is evaluated through the simulations, for different maximum values of the external stimulus, H_y^{SO}, it is possible to see that, regardless of whether the impact is elastic or inelastic, the collision time, t_c, given that the initial distance between the two DW is always the same, depends entirely on the SO field magnitude, and it does not appear that the exchange interaction causes an appreciable boost or delay in the process, as it can be seen in Fig. 7.2 (b). This is because the exchange interaction is a short-range one, so the magnetic solitons might not have enough time to get an exchange-based variation in their speeds due to the continuous presence of the SO field, which makes them to move at speeds of the order of tens of km/s.

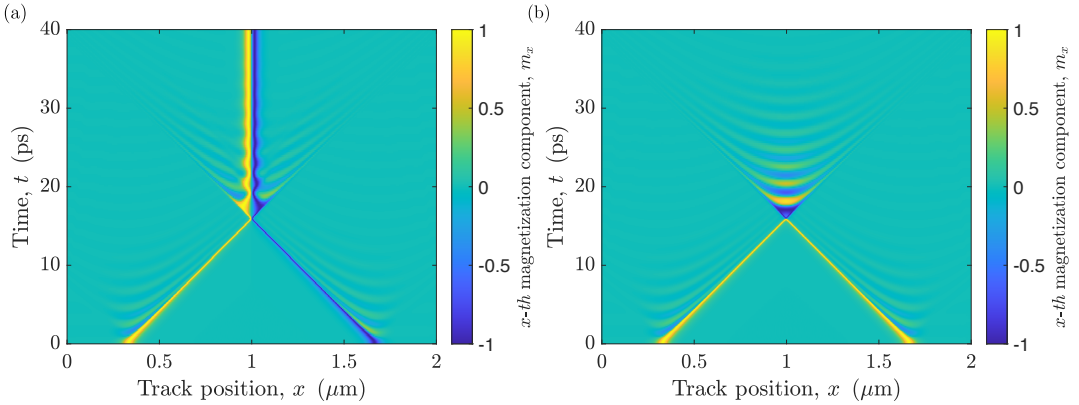

Figure 7.1: Simulated space-time evolution of the *x-th* magnetization component, m_x, for the case in which the two initially stabilized DW in the system have (a) the same or (b) the opposite topological charges, $Q_1Q_2 = +1$ or $Q_1Q_2 = -1$, respectively. In both cases, the SO field ramps for 10 fs up to a maximum value of $H_y^{\mathrm{SO}} = 60$ mT, which remains active until the end of the simulations.

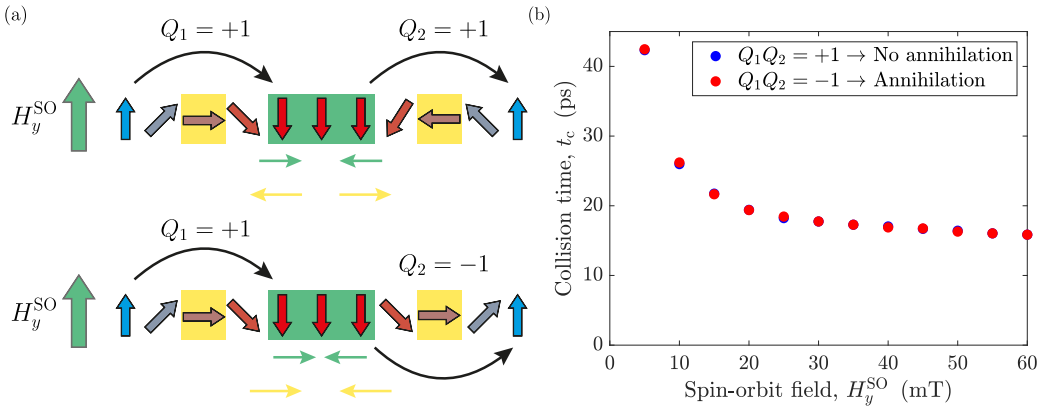

Figure 7.2: (a) Balance of the SO field, H_y^{SO}, and FM-like exchange energy contributions depending on the relative topological charges, Q_i, of both DW, which dictates whether the pair of magnetic textures will recombine or not in each situation. In this case, the colored rectangular regions indicate the main area of influence of each term, while the associated colored arrows represent in which direction each energy contribution prompts them to move. (b) Simulated evolution of the collision time, t_c, for different maximum SO fields, H_y^{SO}, both for the case of an elastic ($Q_1Q_2 = +1$) and an inelastic ($Q_1Q_2 = -1$) collision between both magnetic solitons.

7.3 Magnetic textures as local heating probes in metals

7.3.1 Electronic- and phononic-governed kinetic two temperature model

Heat production at the nanoscale has been shown to be crucial for the existence of several emerging non-disruptive technologies, ranging from cancer treatments to information storage through heat-assisted magnetic recording schemes [439, 440]. In this sense, it is still a challenge to find not only ways to control the level of heating, but also to do it in a fast, energy-efficient manner at ever decreasing length scales. Interestingly, the electrically-driven DW motion through a viscous-like medium is inherently subject to an energy redistribution process to its surroundings in a similar way as in the case of the Joule heating generated by applying an electric current to a resistive material. If the considered material is metallic, due to the low associable electronic specific heat and the efficient coupling of the spin and electronic degrees of freedom [441, 442], the electron subsystem can be heated, due to the energy dissipated during the magnetization dynamics, in the subpicosecond time scale, as it has been reported for the case of the layered AFM Mn_2Au [165]. In this sense, it is important to point out that, if an AFM insulator were considered, the magnetic energy would be absorbed by the magnon bath, whose relaxation is slow, being comparable to the thermal diffusion, instead of being transferred to the electronic degree of freedom [443]. In metals, due to the excess of energy of the heated electrons adjacent to the spatial region located around the magnetic soliton, not only the thermalization of the electronic subsystem occurs through inelastic scattering events [444], but also an energy transfer between them and the colder lattice takes place through the electron-phonon coupling [445, 446], a process which can take several ps [165]. It is important to note that the heating of the phononic reservoir occurs indirectly, since the source of energy in the physical system, embodied by the magnetic texture, lives in spin space, which is weakly coupled to the lattice, the latter being however in relevant connection with the electronic bath. All this succession of events have been outlined in Fig. 7.3 (a). If the external stimulus that incites the movement of the

magnetic texture, which acts as a local heating probe, ceases its activity, it will stop pumping energy to the electronic reservoir and, therefore, the electron temperature will decrease until it equals the one of the phononic subsystem, being the time scale of the process governed by the strength of the coupling between both degrees of freedom. All the phenomenology exposed so far can be described within the so-called two temperature model, which deals with the electronic and phononic systems as coupled heat baths [447]. In this context, the time evolution of the temperature of the electronic and phononic reservoirs can be described through two coupled heat equations, such that

$$C_{\mathrm{el}}\frac{\mathrm{d}T_{\mathrm{el}}}{\mathrm{d}t} = -G_{\mathrm{el-ph}}\left(T_{\mathrm{el}} - T_{\mathrm{ph}}\right) + \kappa\frac{\partial^2 T_{\mathrm{el}}}{\partial x^2} + \dot{q}, \tag{7.1}$$

$$C_{\mathrm{ph}}\frac{\mathrm{d}T_{\mathrm{ph}}}{\mathrm{d}t} = G_{\mathrm{el-ph}}\left(T_{\mathrm{el}} - T_{\mathrm{ph}}\right), \tag{7.2}$$

where C_{el} and T_{el} represent, respectively, the electron specific heat and temperature, while C_{ph} and T_{ph} exercise the same roles but referred to the phonon reservoir. On the other hand, $G_{\mathrm{el-ph}}$ denotes the coupling constant between the electronic and phononic systems, $\dot{q}$ quantifies the heat dissipation rate per spin, and κ, the electronic thermal conductivity, refers to the diffusion of the excess of energy from the hot electrons to the colder ones. It should be noted that this last mechanism, in the case in which the pumping of energy to the system stops, which would lead to an eventual cessation of the dynamics of any spin texture in the magnetic medium, would allow the heat to be spatially delocalized on the time scale of hundreds of ps. Regarding its phononic analogue, its absence in the preceding expressions is due to the fact that it is significantly slower than the one involving the electron subsystem [216].

7.3.2 Dynamically-induced dissipation through the spin Peltier effect

The theoretically-calculated energy dissipation by the SO field-induced dynamics of a single DW in one of the FM layers of the metallic AFM Mn_2Au has been previously reported through the combination of ASDS, based on the numerical resolution of the LLG equation, given by Eq. (2.14), and the kinetic model encoded by Eqs. (7.1) and (7.2), being the relaxation rate proportional to the so-called Gilbert damping parameter, α [165]. In this case, it was observed that, through the SPE, the creation of a localized electronic-based heat wave takes place, which accompanies the fast moving magnetic texture, slightly lagging the DW center position. At the same time, the phononic temperature shows a much smoother profile owing to the indirect coupling to the heat source, represented by the moving magnetic texture, through the electron-phonon channel. Interestingly, it is possible to estimate the time scale associated with the temporal delay between the electronic and phononic temperature profiles through the electron-phonon relaxation time, $\tau_{\mathrm{el-ph}} \simeq G_{\mathrm{el-ph}}/C_{\mathrm{el}}$, which, for the parameters considered in the aforementioned work, will be given by $\tau_{\mathrm{el-ph}} = 1.2$ ps [165]. Along the same lines, the characteristic length scale for which both thermal profiles are different, $l_{\mathrm{el-ph}}$, can be calculated considering that the DW moves close to the maximum attainable speed in the medium, which is around $v = 40$ km/s, being, in this case, given by $l_{\mathrm{el-ph}} \simeq \tau_{\mathrm{el-ph}}\, v = 48$ nm. Leaving aside the advantages associated with using a metal and focusing on why to use AFM materials, it is possible to characterize, through the Rayleigh dissipation function, which we will denote in the rest of the chapter as $\dot{q}$, given by Eq. (2.18), which

will be the spatio-temporal electronic, T_{el}, and phononic, T_{ph}, temperature distributions. To analytically quantify the dynamically-based heat dissipated per atomic spin, $\dot{q}_{\mathrm{dyn}}$, it is possible to combine the parameterization in spherical coordinates of the Néel order parameter, given by Eq. (5.14), taking into account its negligible associated out-of-plane component, with the stationary symmetric Walker-like profile of a magnetic soliton, which is characterized by Eq. (2.30). In this line, its spatially localized dynamic profile, $\dot{q}_{\mathrm{dyn}}$, for steady-state processes can be found to be given by

$$\dot{q}_{\mathrm{dyn}} = 2\alpha\hbar \left(\frac{v}{\Delta}\right)^2 \operatorname{sech}^2 \frac{x - X}{\Delta}, \tag{7.3}$$

expression through which, after integration over time, it is possible to extract the associated electronic and phononic temperatures, $T_{\mathrm{el,ph}}$, that will accompany the magnetic texture, such that

$$\left|T_{\mathrm{el,ph}}\right| = \frac{4\alpha\hbar v}{C_{\mathrm{el,ph}}\,\Delta} \tanh \frac{x - X}{\Delta}, \tag{7.4}$$

where it should be noted that the factor 2 in the numerator has been artificially added to encompass a greater number of spins of the inhomogeneous transition that defines the magnetic soliton, since the Bloch definition of the DW width, $\Delta_0 = \sqrt{a/\left(8K_{2\parallel}\right)}$, does not give a good account of the whole dissipative region [165].

Because in Eq. (7.4) the temperature scales with the ratio v/Δ, it can be appreciated that the DW dynamics in AFM is advantageous in terms of heating level, since in this type of materials it is possible to reach ultrafast magnonic velocities and Lorentz-governed width contractions down to the atomic scale [134, 414]. In fact, it has been reported that, through an excitation protocol that induces the back and forth motion of a magnetic soliton in one of the FM sheets of the layered AFM Mn_2Au, a maximum electronic temperature peak of $T_{\mathrm{el}} = 1.2$ K can be reached for $H_y^{\mathrm{SO}} = 60$ mT, as well as electronic and phononic temperatures, after the thermalization process when the dynamics in the spin space are extinguished, of the order of $T_{\mathrm{el,ph}} = 0.8$ K in the center of the track for a mean velocity and width of, respectively, $\langle v \rangle = 33.15$ km/s and $\langle \Delta \rangle = 12.72$ nm [165]. It should be noted that, for FM, the heating induced by a moving magnetic soliton will not be as efficient as in AFM materials. For the standard case of permalloy, for example, it can be estimated that the maximum temperature that the electrons can carry due to the dissipation generated by the movement of the magnetic soliton will be of the order of 1 mK, which is due to the lower order of magnitude of the ratio v/Δ in Eq. (7.4) compared to the one expected in AFM due to the speeds and widths achievable in each scenario. Moreover, in FM, the thermal diffusion will play an important role when it comes to delocalizing the generated heat wave. The heat diffusion rate can be defined as $\eta = D_{\mathrm{el}}/\left(v\Delta\right)$, where $D_{\mathrm{el}} = \kappa/C_{\mathrm{el}}$ represents the electron thermal conductivity, and it expresses that, the larger this parameter is, the more efficiently the thermal diffusion takes the temperature away from the generation region. Considering a typical value of the electron thermal conductivity for a metal, that is, $D_{\mathrm{el}} = 10^{-4}$ m^2/s, the aforementioned parameter will be $\eta \gg 1$ for permalloy and $\eta < 1$ for Mn_2Au [165]. This has as a consequence that the negligible heat wave accompanying the magnetic texture during its dynamics in permalloy will be completely delocalized, contrary to the case of Mn_2Au.

In our case, it is possible to calculate the dissipation rate per spin, $\dot{q}$, through Eq. (2.18), from the ASDS explained in Sec. 7.2.1 and displayed in Fig. 7.1, both for the situation in which both DW have the same relative topological charges, $Q_1Q_2 = +1$,

as it is shown in Figs. 7.3 (b) and 7.4 (a), as well as for the situation in which they have opposite winding numbers, $Q_1 Q_2 = -1$, which is depicted in Figs. 7.4 (b) and 7.5 (a). In view of Fig. 7.1, it is possible to see that, in both cases, there is a SW emission during the acceleration process of both magnetic textures due to the application of a short ramping time of 10 fs, which gives rise to the creation of an additional dissipation channel in the system, transporting energy away from the heat source, although its effect is practically negligible, as it can be seen in Figs. 7.3 (b) and 7.4 (b). Given this scenario, in order to characterize the temperature of the electronic and phononic baths through Eqs. (7.1) and (7.2), it will be adopted in the following that the parameters involved in the aforementioned expressions will be given by $C_{\mathrm{el}} = 10^3\ \mathrm{J}/\left(\mathrm{K}\cdot\mathrm{m}^3\right)$, $C_{\mathrm{ph}} = 1.5\times 10^6\ \mathrm{J}/\left(\mathrm{K}\cdot\mathrm{m}^3\right)$, $G_{\mathrm{el-ph}} = 2.5\times 10^{17}\ \mathrm{W}/\left(\mathrm{K}\cdot\mathrm{m}^3\right)$, and $\kappa = 200\ \mathrm{W}/\left(\mathrm{m}\cdot\mathrm{K}\right)$ [165, 448]. Regardless of the relative chiralities between the two magnetic solitons, before the collision both cases are completely coincident, as it can be seen from the fact that, for $t = 14$ ps, even though the spatial distributions of the *x-th* magnetization component are different in each case, as it can be appreciated in Figs. 7.5 (b) and 7.6 (b), the electronic, T_{el}, and phononic, T_{ph}, temperature profiles are the same, as it is depicted in Figs. 7.6 (a) and 7.7 (a), which is because both at this point only show a dynamic contribution. These exposed thermophysical processes may allow the traceability of the magnetic texture dynamics in AFM due to the accompanying nanoscale confined heat wave through, for example, scanning thermal microscopy, as it has been proposed with the case of the SPE [449, 450]. This is in line with the recently reported thermal detection, through the anomalous Nerst effect, of the FM DW motion, albeit on much larger time scales than those governing the Mn_2Au case [451]. In addition, the localized phonon temperature profile will be associated with the creation of phononic waves, which could be measured in a similar way as in the reported ultrafast Einstein-de Haas effect [452].

7.3.3 Topologically-induced exchange domain wall energy release

As it can be seen in Figs. 7.3 (b) and 7.4 (b), regardless of the relative chiralities of the DW in the system and the outcome of the eventual collision process, it is possible to transport in an efficient and ultrafast manner the exchange-based self energy carried by each magnetic soliton. This is because, in AFM, the magnetic textures show special relativity signatures, which results in their widths and free energies strongly depending on the speeds at which they are moving through the medium. In particular, the dynamically-dependent DW energy can be obtained through the spatial integration of either one of the first two terms of the right-hand side of Eq. (6.4), which do not depend on the involved topological charges due to the fact that the present hyperbolic function is even. Thus, the exchange-based self energy of an *i-th* magnetic soliton, E^i_{exc}, will be given by

$$E^i_{\mathrm{exc}} = \frac{a}{8a_0\Delta^2}\int_{-\infty}^{+\infty}\mathrm{sech}^2\,\frac{x-X_i}{\Delta}\,\mathrm{d}x = \frac{a}{4a_0\Delta}, \tag{7.5}$$

whose functional behavior, for quasistatic processes, can be found in Fig. 3.4 (a). The dynamic DW width is governed by a symmetric Lorentz-like functional form such as $\Delta = \Delta_0\,\beta = \Delta_0\sqrt{1-(v/v_{\mathrm{m}})^2}$, being given, at the same time, the velocity, v, of the magnetic texture in quasistatic processes through Eq. (5.17) or, in the case where the DW moves in a steady-state trend, through Eq. (5.18). Due to the small DW mass in the layered AFM Mn_2Au, which is implicit in the functional form of the Newton-like second-order differential equation given by Eq. (5.17), being inversely proportional

to the inhomogeneous FM-like exchange constant, a, a magnetic texture in one of the basal planes of the unit cell will present small inertial in its adaptation to a new dynamic regime in the presence of a time-dependent external stimulus, as it can be seen in Figs. 5.6 (b) and 5.7 (a). This is also true for the case we are currently studying, given by the simulations explained in Sec. 7.2.1 and shown in Fig. 7.1, where the SO field is ramped for 10 fs up to a maximum value of $H_y^{\mathrm{SO}} = 60$ mT, taking only a few ps to acclimatize to the imposed stationary regime, in which case no significant SW emission is observed after the acceleration process. In this line, in the steady-state regime prior to the collision process of both magnetic solitons, they reach speeds given by $v = 42.56$ km/s, which constitutes a 98% of the maximum magnon group velocity of the medium, v_{m}, while its spatial extents shrink to a value of $\Delta = 4.08$ nm, which represents 80% of the DW width at rest, Δ_0, as it was previously discussed in Sec. 5.4.2. This has as a result that, at this dynamic stage, both magnetic textures increase their exchange-based self energies, E^i_{exc}, up to a 485% compared to their resting values, which shows that it is possible, in fact, not only to displace their free energies through the track, but also to charge them through an externally applied electric current.

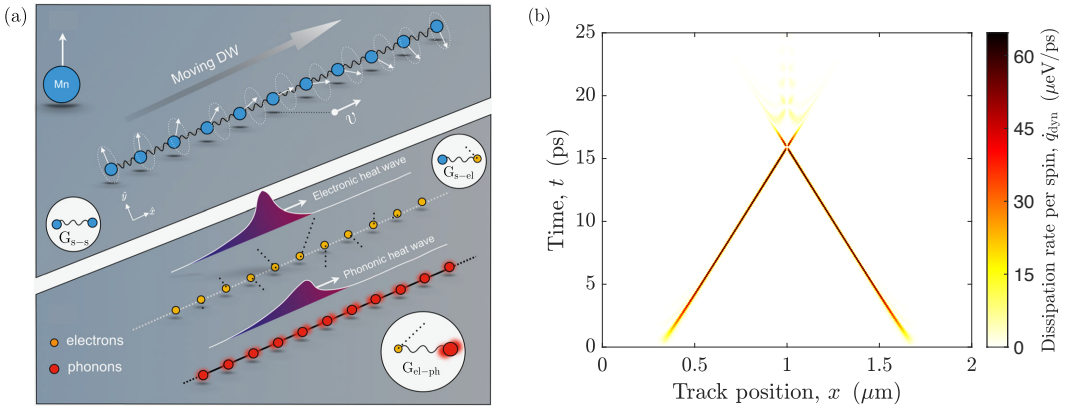

Figure 7.3: (a) The current-induced dynamics of each DW through one of the FM sheets of the layered AFM Mn_2Au, being the magnetic Mn atoms whose local spins are connected through the coupling constant $G_{\mathrm{s-s}}$ represented by solid blue circles, causes, due to dissipation processes, an energy redistribution from the magnetic reservoir to the electron (solid yellow circles) and phonon (solid red circles) subsystems. Due to the efficient spin-electron coupling, represented by $G_{\mathrm{s-el}}$, the creation, on the subpicosecond time scale, of a localized heat wave of hot electrons that accompany each moving magnetic soliton takes place. In the following ps, the imbalance between the electron degree of freedom and the colder lattice, which interact through the parameter $G_{\mathrm{el-ph}}$, gives rise to a thermalization process up to an equilibrium temperature. Extracted from [165]. (b) Dynamically-generated simulated space-time evolution of the heat dissipation rate per spin, $\dot{q}_{\mathrm{dyn}}$, for the case in which the two initially stabilized DW in the system have the same relative topological charges, $Q_1Q_2 = +1$. The SO field ramps for 10 fs up to a maximum value of $H_y^{\mathrm{SO}} = 60$ mT, which remains active until the end of the simulations.

As it was shown in Fig. 7.1, the outcome of a collision process between two DW is strongly dependent on their relative topological charges, Q_i. This phenomenon, governed by the topological selection rules, establishes that if both magnetic solitons have the same chirality they will not annihilate when colliding elastically, while if their winding numbers are the opposite, belonging to the same topological class that

the homogeneous state, both will suffer upon impact an inelastic event in which they will eradicate each other, as it was introduced in Sec. 2.5. In the case compiled in Fig. 7.1 (a), where both DW persist in the system after the collision, which occurs approximately at $t = 15.85$ ps, their magnetization profiles are affected when they are close enough, as it can be seen in Fig. 7.5 (b) for the time frame $t = 16$ ps, at the same time that their temperature profiles are combined in the impact point, as it is depicted in Fig. 7.6 (a). This happens in this region despite the fact that both magnetic textures do not merge spatially due to their exchange-based mutual repulsion, as it is shown in Fig. 7.4 (a), where there is no dissipation in this point. After their collision, as it can be seen in Fig. 7.5 (b) for $t = 18$ ps, they are separated up to an equilibrium distance, in line with what is stated in Secs. 6.3.1 and 7.2.2, which leads to an abrupt decrease in their velocities with respect to their values in the stationary trend, which causes the expansion of their widths and, therefore, a significant loss of part of their stored self energies. In this situation, the energy transfer to the system is only partial due to the prevalence of both magnetic textures, as it is depicted in Fig. 7.5 (b), being the dissipation to the medium purely dynamic, $\dot{q}_{\mathrm{dyn}}$, as in the SPE of a single magnetic soliton [165]. This causes that the energy excess that both stored before their impact is redistributed between different subsystems through SW emission, electron-phonon coupling, and lateral thermal conduction, leading to a decrease in the electronic temperature, T_{el}, in the center of the track in its thermalization process, as it shown in Fig. 7.6 (a) for $t = 18$ ps.

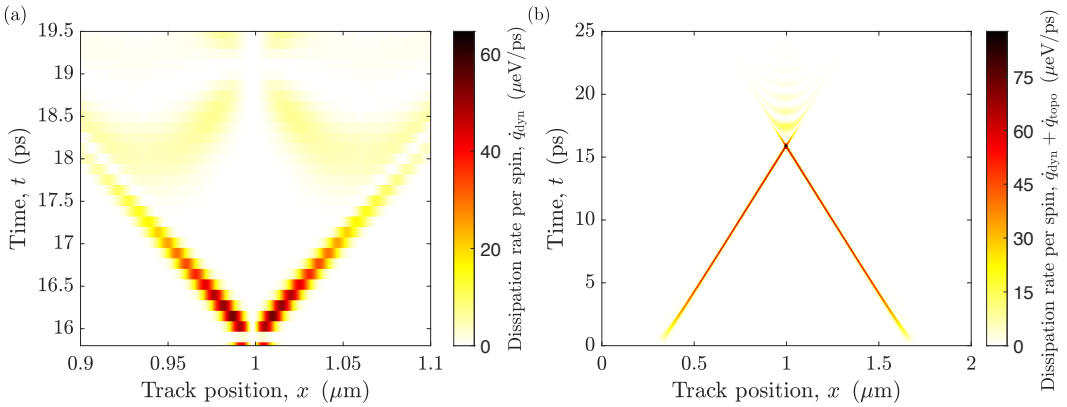

Figure 7.4: (a) Dynamically-generated simulated space-time evolution of the heat dissipation rate per spin, $\dot{q}_{\mathrm{dyn}}$, for the case in which the two initially stabilized DW in the system have the same relative topological charges, $Q_1Q_2 = +1$, in the region where the elastic collision takes place. (b) Dynamically- and topologically-generated simulated space-time evolution of the heat dissipation rate per spin, $\dot{q}_{\mathrm{dyn}} + \dot{q}_{\mathrm{topo}}$, for the case in which the two initially stabilized DW in the system have the opposite relative topological charges, $Q_1Q_2 = -1$. In both cases, the SO field ramps for 10 fs up to a maximum value of $H_y^{\mathrm{SO}} = 60$ mT, which remains active until the end of the simulations.

On the other hand, in the case where both DW have opposite relative topological charges, both magnetization profiles merge at the impact point, as it is shown in Fig. 7.6 (b) for $t = 16$ ps, which means that the temperature profiles overlap at the center of the track, as it is depicted in Fig. 7.7 (a). This results in a total release of the energy carried by both magnetic textures in their previous dynamic history in the impact spot, as it can be seen in Figs. 7.4 (b) and 7.5 (a), which is allowed in this case by the topological selection rules, contrary to what happens in the elastic case. As a result of

the mutual annihilation of both magnetic solitons, a strong dissipation in the form of a magnon emission occurs through the creation of a breather-like excitation [230], as it is depicted in Fig. 7.6 (b) for $t = 18$ ps, which evolves in time, but not in space, the magnon cone being constrained by the trajectory of both magnetic textures before colliding, which is clearly seen in Fig. 7.1 (b), which means that no spin perturbations can exist outside this region [371]. The attenuation of this bounded state, for a SO field of $H_y^{\mathrm{SO}} = 60$ mT, occurs on, approximately, the exchange relaxation time scale, which can be estimated through Eq. (5.17), such as $a/\left(8\alpha\hbar v_{\mathrm{m}}^2\right) \simeq 2.41$ ps, which is in line with the one observed through simulations in Fig. 7.1 (b), which is around $3-4$ ps. Since the stored exchange energies by both DW during their motions are completely released to the medium as these two magnetic textures cease to exist in the spin space, as it can be seen in Figs. 7.1 (b) and 7.6 (b), the dissipation to the medium will not only have a dynamic contribution, $\dot{q}_{\mathrm{dyn}}$, as in the case with an elastic impact shown in Fig. 7.1 (a), but also a topological one, $\dot{q}_{\mathrm{topo}}$. As in the case in which there were two magnetic solitons with the same relative chiralities, the energy excess is redistributed between the different dissipation channels, giving rise to a gradual reduction process of the electronic temperature, T_{el}, in its thermalization as the breather dims, as it is shown in Fig. 7.7 (a) for $t = 18$ ps. In this sense, the topologically-dependent events dependent on the relative DW topological charges are reminiscent of the case of an electric capacitor, in that it is possible to charge them, in this case, of exchange-based energy through their current-induced dynamics, and also to discharge them, either partially or totally depending on the outcome of the collision between them, as it is schematized in Fig. 7.7 (b). The footprint of both scenarios governed by the topological selection rules can potentially be discerned experimentally, since there are appreciable differences in the temperature of the electronic, T_{el}, and phononic, T_{ph}, baths, being possible to achieve an maximum increase of a 51% of T_{el} and of a 30% of T_{ph} if there is a total discharge of energy to the medium compared to the case in which both remain in the system as well-differentiated entities, which it is shown, respectively, in Figs. 7.8 (a) and (b).

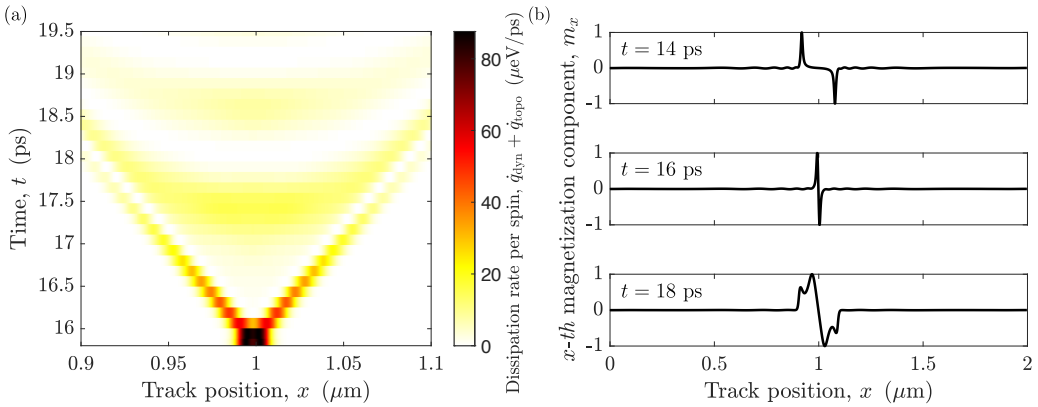

Figure 7.5: (a) Dynamically- and topologically-generated simulated space-time evolution of the heat dissipation rate per spin, $\dot{q}_{\mathrm{dyn}} + \dot{q}_{\mathrm{topo}}$, for the case in which the two initially stabilized DW in the system have opposite relative topological charges, $Q_1Q_2 = -1$, in the region where the inelastic collision takes place. (b) Simulated spatial distribution for different time frames of the x-th magnetization component, m_x, for the case of two DW with the same relative winding numbers, $Q_1Q_2 = +1$, during their dynamic evolutions until they collide elastically, event that occurs at approximately $t = 15.85$ ps. The SO field ramps for 10 fs up to a maximum value of $H_y^{\mathrm{SO}} = 60$ mT, which remains active until the end of the simulations.

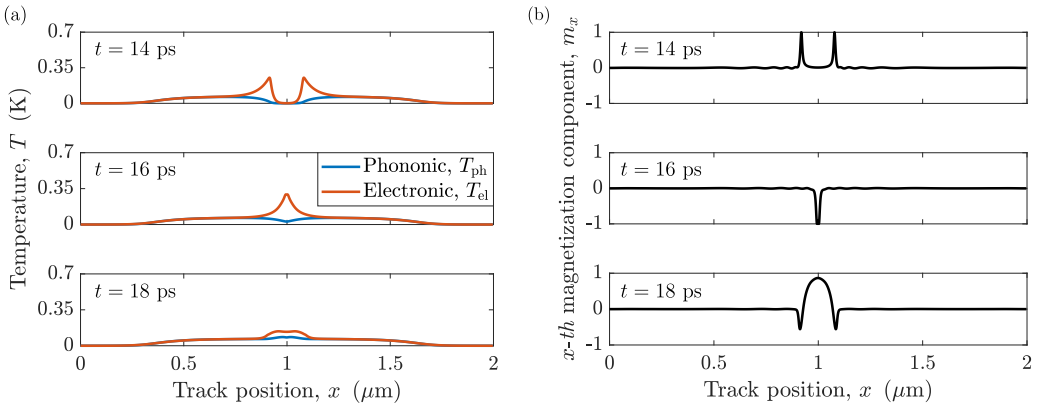

Figure 7.6: (a) Simulated spatial distribution for different time frames of the electronic, T_{el}, and phononic, T_{ph}, temperatures for the case of two DW with the same relative topological charges, that is, $Q_1Q_2 = +1$, during their dynamic evolutions until they collide elastically, event that occurs at approximately $t = 15.85$ ps. (b) Simulated spatial distribution for different time frames of the x-th magnetization component, m_x, for the case of two DW with opposite relative topological charges, that is, $Q_1Q_2 = -1$, during their dynamic evolutions until they collide inelastically. In both cases, the SO field ramps for 10 fs up to a maximum value of $H_y^{SO} = 60$ mT, which remains active until the end of the simulations, process during which the impact between both magnetic solitons takes place at approximately $t = 15.85$ ps.

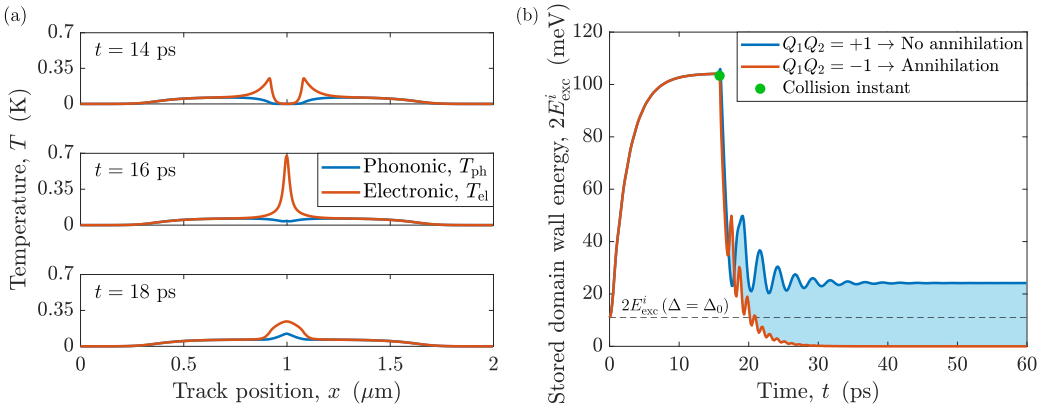

Figure 7.7: (a) Simulated spatial distribution for different time frames of the electronic, T_{el}, and phononic, T_{ph}, temperatures for the case of two DW with opposite relative topological charges, that is, $Q_1Q_2 = -1$, during their dynamic evolutions until they collide inelastically. (b) Simulated comparison of the time evolution of the stored exchange-based energy by both magnetic textures, $2E^i_{exc}$, for the cases in which they have the same relative topological charges, that is, $Q_1Q_2 = +1$, undergoing an elastic collision, or the opposite relative winding numbers, $Q_1Q_2 = -1$, giving rise to an inelastic event. The in-between blue region corresponds to the net topological contribution resulting from the total release of the self energy of both DW due to their mutual annihilation, while the solid green circle represents the collision point. In both cases, the SO field ramps for 10 fs up to a maximum value of $H_y^{SO} = 60$ mT, which remains active until the end of the simulations, process during which the impact between both magnetic solitons takes place at approximately $t = 15.85$ ps.

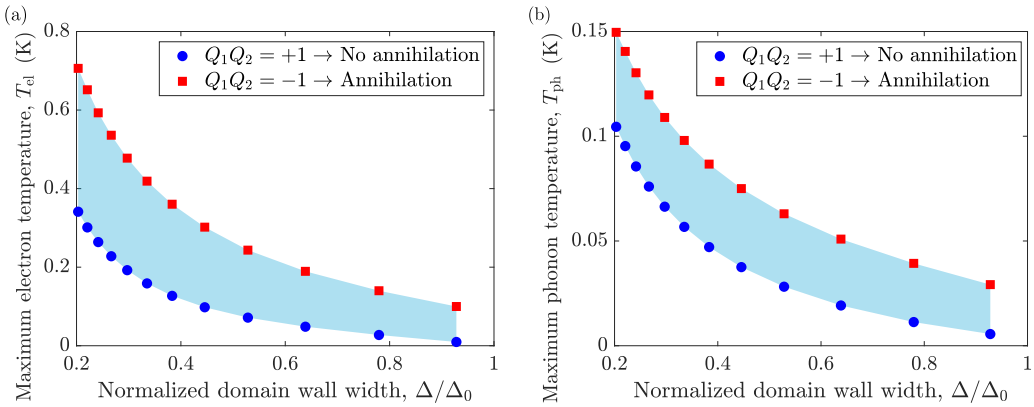

Figure 7.8: Comparison of the simulated maximum (a) electronic, T_{el}, and (b) phononic, T_{ph}, temperatures in terms of the normalized DW widths, Δ/Δ_0, being Δ and Δ_0 their values at steady-state and at rest, respectively, obtained for the cases in which the magnetic textures collide elastically, that is, $Q_1Q_2 = +1$, or inelastically, $Q_1Q_2 = -1$, for different constant SO fields, H_y^{SO}, after the ramping process. The in-between blue region corresponds to the net topological contribution resulting from the total release of the self energy of both DW due to their mutual annihilation.

7.4 Post-collision domain wall bounded state features

Regarding the different scenarios emerging from the collision of two magnetic textures depending on their relative topological charges, part of this analysis was carried out when the Walker-like breakdown in the AFM Mn_2Au was evaluated in Chap. 6. This phenomenon consisted in the fact that, initially existing a single DW in the system, this could give rise, in its dynamic process under a certain magnitude of the SO field, to an avalanche of nucleation of magnetic solitons preserving the overall winding number [139]. However, this process and, therefore, what was previously analyzed in this regard, was subject to a certain combination of inputs through the selected time-dependent excitation protocol, both in terms of the used ramping time and the maximum value of the external stimulus reached during the simulations. In the current case that concerns us, where from the beginning we have two DW in each FM sheet of the layered AFM Mn_2Au, we are not constrained in this sense, which makes it possible to carry out a less restricted analysis that is related to the one previously done. As it was qualitatively introduced in Sec. 7.2.2, when both magnetic textures have the same relative topological charges, $Q_1Q_2 = +1$, the SO field-based Zeeman energy will shrink the in-between domain between them, while the FM-like exchange interaction, due to their central spins being antiparallel, will cause them to repel when they are close to each other due to their short-range nature. The equilibrium distance, $X_1 - X_2$, between both magnetic solitons after the collision process can be found through the balance between both energetic contributions, as it was discussed in Sec. 6.3.1 and encapsulated in Eq. (6.11), which is shown in Fig. 7.9 (a) for different maximum magnitudes of the SO field, H_y^{SO}, after the ramping process. The comparison between the outcome obtained through ASDS and the numerical analysis of Eq. (6.11) show an appreciable coincidence, as well as that, as the value of the external stimulus decreases, its separation increases, which implies that the Zeeman-based force needs a greater extension of the magnetic domain to compensate for the exchange repulsion between both magnetic textures. On the other hand, when the two existing DW in the system have the opposite relative

winding numbers, $Q_1Q_2 = -1$, they collide inelastically because not only the SO field will contribute to favoring the annihilation of both magnetic solitons, but also, in this case, it will also be supported by the FM-like exchange interaction due to their mutually parallel central spins, as it was introduced in Sec. 7.2.2. Under these circumstances, after their eradication, a breather-like excitation is formed, as it can be seen in Fig. 7.1 (b), which, as it was explained in Sec. 6.4.4, can be fitted to a simple damped harmonic oscillator as the one described by Eq. (6.14). As it can be induced from Fig. 7.9 (b), the decay time, t_{d}, of the bounded state after its creation does not show a clear correspondence with the externally applied external stimulus, H_y^{SO}, and, in the same line, with the velocity at which the magnetic textures move just before the collision, thus depending solely on the intrinsic parameters of the system such as the damping parameter, α, the homogeneous AFM, A, and the inhomogeneous FM-like, a, exchange constants. Interestingly, through the estimation of the relaxation time related to the breather excitation, which we can consider to be around $3-4$ ps according to Fig. 7.9 (b), it is possible to calculate the size of the energy release spot. For example, for the case in which $H_y^{\mathrm{SO}} = 60$ mT, being the related DW velocity given by, approximately, $v = 42.4$ km/s, the impact-based discharge area will be around $120-160$ nm, as it can be seen in Figs. 7.4 (b) and 7.5 (a). In the case in which the speed of the magnetic solitons at the moment of the collision was lower, the spot size would decrease, but in turn the released energy would be lower due to the reduction in the dissipation contribution, given by $\dot{q}_{\mathrm{dyn}}$ according to Eq. (7.3).

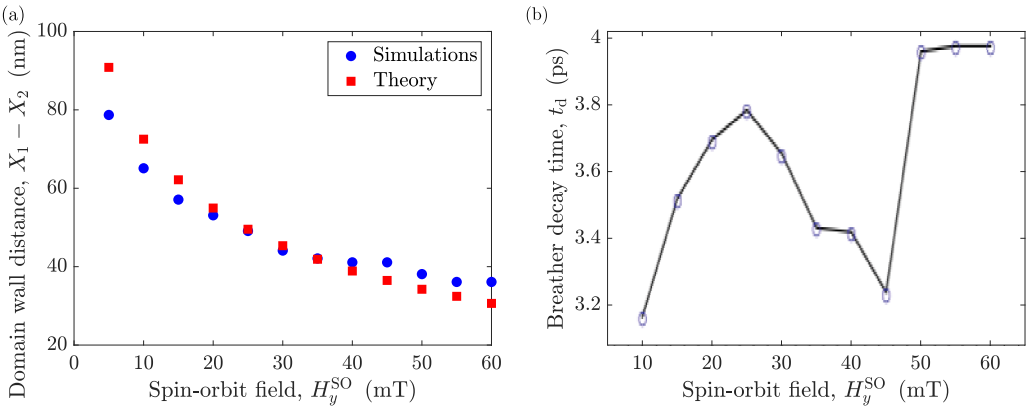

Figure 7.9: (a) Comparison between the equilibrium distances, $X_1 - X_2$, of both DW after their mutual elastic collision in the case in which their relative topological charges are the same, $Q_1Q_2 = +1$, extracted through the simulations and from Eq. (6.11) as a function of the applied SO field, H_y^{SO}. (b) Decay times, t_{d}, for different SO fields, H_y^{SO}, of the breather mode for the case in which two magnetic solitons with opposite relative winding numbers, $Q_1Q_2 = -1$, impact inelastically, obtained by fitting the damped harmonic oscillator expression given by Eq. (6.14) to the simulated data.

7.5 Dissipation-induced magneto Seebeck recoil effect

Prior to the collision between both magnetic textures, regardless of their relative topological charges, both pseudoparticles generate a spin Peltier-based electronic thermal gradient during their ultrafast SO field-induced dynamic motion that is slightly behind the DW center position, X_i, of each soliton [165]. Therefore, there

is a potential feedback response due to the spin Seebeck effect that each magnetic texture would experience, since, to minimize the energy of the system, they would tend to move to the hottest regions of the sample [453, 454]. In our case, these sectors are shifted backwards with respect to the DW centers of mass. To quantify this, one can take advantage of the fact that the thermodynamic properties of FM and AFM are similar because both models only differ in a change of sign of the exchange integral in the Hamiltonian [391, 455]. As in the case of FM, it is possible to estimate the velocity associated with a thermal gradient-induced magnetic soliton dynamics based on the tilting of the magnetization with respect to its plane at rest. In this sense, we will assume that it is possible to linearize the dependence on the electronic temperature, T_{el}, of the exchange stiffness, ρ, as $\mathrm{d}\rho\left(T_{\mathrm{el}}\right)/\mathrm{d}T_{\mathrm{el}} \simeq \rho\left(0\right)/T_{\mathrm{N}}$, where $\rho\left(0\right)$ represents the exchange stiffness at $T = 0$ K and T_{N} expresses the Néel temperature of Mn_2Au. Considering that we are working on the low damping limit, that is, $\alpha^2 \ll 1$, and that we can simplify our problem to the case of a simple cubic lattice of spatial period a_0, parameter which we consider to be the same as in the case of Mn_2Au, which was presented in Sec. 5.2, it is possible to find that the thermally-activated velocity, v_{th}, of a magnetic texture can be expressed as

$$v_{\mathrm{th}} = \frac{a_0^3 \rho\left(0\right)}{\alpha\hbar T_{\mathrm{N}}} \frac{\partial T_{\mathrm{el}}}{\partial x} = -\frac{k_{\mathrm{B}} a_0^2}{2\alpha\hbar} \frac{\partial T_{\mathrm{el}}}{\partial x}, \tag{7.6}$$

where it has been assumed that the exchange stiffness at $T = 0$ K, $\rho\left(0\right)$, of a simple cubic lattice can be represented, in the mean field approximation, as $\rho\left(0\right) = -k_{\mathrm{B}} T_{\mathrm{N}}/\left(2a_0\right)$ [391, 455].

As it was introduced in Sec. 7.3.2, since the study system is a metal, it is possible to assume that the dynamically-based energy dissipated by both DW to the system is directed primarily to the electron bath due to the order of magnitude of the electron heat capacity, C_{el}, a process which occurs in the subpicosecond time scale. This contribution due to the motion of the magnetic solitons through a FM sheet of Mn_2Au prior to their impact can be characterized analytically through Eq. (7.4), which has an associated gradient given by

$$\frac{\partial T_{\mathrm{el}}}{\partial x} = -\frac{4\alpha\hbar v}{C_{\mathrm{el}}\Delta^2} \operatorname{sech}^2 \frac{x - X}{\Delta}, \tag{7.7}$$

where v is the SO field-based steady-state speed of each magnetic texture according to Eq. (5.18). This expression allows to obtain, from Eq. (7.6), assuming that the heat release is maximum and that, therefore, the temperature gradient is the largest possible one, that the spin Seebeck-induced retardation velocity, v_{th}, can be written as

$$v_{\mathrm{th}} = \frac{2k_{\mathrm{B}} a_0^2 v}{C_{\mathrm{el}}\Delta^2}, \tag{7.8}$$

which, as it was the case with the temperature profile exposed by Eq. (7.4), it is potentially greater than in the case of FM because it is proportional to v/Δ^2, being possible to reach speeds of tens of km/s and widths close to atomic spacing in AFM [134, 414]. This last expression can be further simplified by assuming that the dependence between the electron heat capacity, C_{el}, and the Boltzmann constant, k_{B}, is given by the Dulong-Petit law [441], $C_{\mathrm{el}} = 3k_{\mathrm{B}}$, condition under which it is obtained that

$$\frac{v_{\mathrm{th}}}{v} = \frac{2}{3}\left(\frac{a_0}{\Delta}\right)^2, \tag{7.9}$$

ratio which allows us to quantify which is the relative effect on the absolute SO field-induced DW velocity, v, of the thermally-activated one, v_{th}, which it is shown in Fig. 7.10 (a). Because the retardation velocity, v_{th}, due to the spin Seebeck effect reaches values of the order of a few hundred m/s for SO fields between $40-60$ mT, range of the external stimulus for which the magnetic soliton speed is approximately 40 km/s, it is possible to assert that its impact is negligible on the magnetic texture motion, representing, at most, $1/100$ of its current displacement velocity [165].

7.6 Current-induced Joule heating thermal background

Since the excitation method to induce the DW dynamics in the metallic AFM Mn_2Au is carried out through a current-induced SO field, it is unavoidable to consider what the energy losses associated with the Joule heating will be. This is due to the energy transferred by the charge carriers to the atoms of the conducting medium through their collision, which results in the increase of the temperature, which has an impact on the magnetic properties of the system [456, 457]. Assuming that the current-induced power profile would be Gaussian, it is possible to introduce an expression to estimate the increase of the Joule heating-induced temperature, ΔT, in terms of the injected current density amplitude, j, the geometry of the sample, and the thermal properties of the considered substrate [458, 459]. Thus, the associated time-dependent background temperature, ΔT, in a Mn_2Au layer grown on a given surface would be given by

$$\Delta T = \frac{whj^2}{\pi\kappa_s\sigma}\,\text{asinh}\,\frac{2}{\alpha_G w}\sqrt{\frac{\kappa_s t}{\rho_s c_s}}, \tag{7.10}$$

where, on the one hand, one can find the parameters related to the Mn_2Au sample, that is, the film thickness represented by h, the current linewidth expressed by w, and the electrical conductivity denoted by σ. On the other hand, it is also possible to notice the existence of substrate-dependent constants, among which one can appreciate the presence of the mass density represented by ρ_s, the specific heat capacity expressed as c_s, and the heat conductivity denoted by κ_s. Finally, it should be noted that α_G encodes the width of the Gaussian power profile and it must be taken into account that, to obtain a SO field of $H_y^{SO} = 2$ mT in Mn_2Au, it is necessary to inject a current density of the order of $j \simeq 10^7$ A/cm^2 [149]. In this line, we will assume that the Mn_2Au-based parameters will be given by $h = 10$ nm, $w = 4\sqrt{2}$ µm, and $1/\sigma = 73\,\mu\Omega\cdot$cm [459], while the width of the Gaussian power profile has been chosen to be $\alpha_G = 0.5$. On the other hand, in Table 7.1 the values of the mass density, ρ_s, the specific heat capacity, c_s, and the heat conductivity, κ_s, found in the literature for some commonly used substrates have been compiled. To explore this scenario, we will consider for simplicity the case in which the electric current is active only until the instant at which the collision between the magnetic textures occurs, in order to exemplify the case of the lowest possible energy expenditure, still fulfilling the objective of the work. Consequently, Fig. 7.10 (b) shows the different Joule heating-based thermal backgrounds, ΔT, for different Mn_2Au growth surfaces according to Eq. (7.10), depending on the current-induced SO field, H_y^{SO}, where it must be taken into account that, as it was shown in Fig. 7.2 (b), the impact moment of the two magnetic solitons occurs at approximately the same instant of time regardless of which their relative topological charges are. In this line, it could be appreciated that for the case in which an inelastic DW collision occurs for a SO field of $H_y^{SO} = 5$ mT, taking into account the MgO as the employed substrate because it is the one with the lowest

associated Joule heating-based temperature, the maximum electronic temperature, T_{el}, as it is shown in Fig. 7.8 (a), will be about one third of ΔT, which could give a recognizable signal on the homogeneous background to be measured by scanning thermal microscopy. In any case, it must be taken into account that the Néel temperature in the case of Mn_2Au is of the order of $T_N \simeq 1575$ K [386], so we would be far from this limiting scenario.

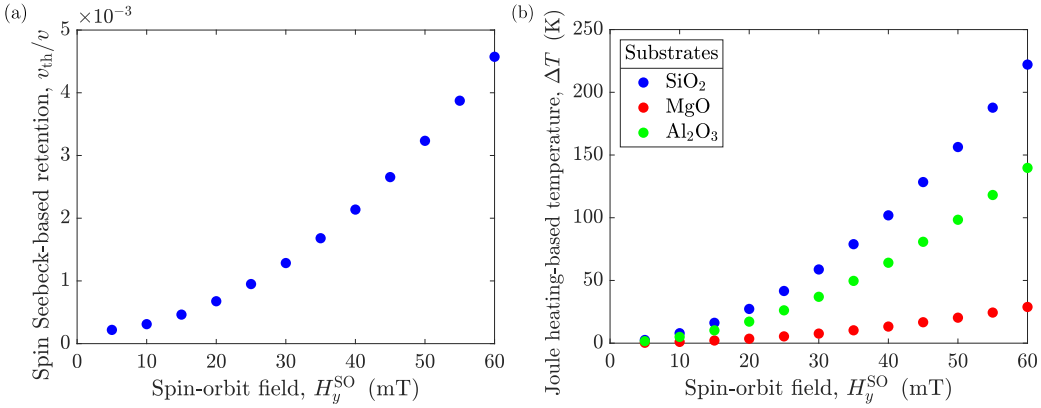

Figure 7.10: (a) Comparison between the analytically-obtained thermally-activated spin Seebeck-based, v_{th}, and SO field-induced steady-state, v, DW velocities according to Eq. (7.9) for different magnitudes of the external stimulus, H_y^{SO}, being given the relationship between the field and the prevailing translational speed by Eq. (5.18). (b) Analytically-calculated Joule heating-based temperature, ΔT, obtained through Eq. (7.10), for the case in which the electric current, j, remains active until the moment of the collision between both magnetic textures for different SO fields, H_y^{SO}, and substrates, of which their associated parameters are shown in Table 7.1.

	Substrates		
	SiO_2 [458]	MgO [459]	Al_2O_3 [460]
Mass density, ρ_{s} $\left(\text{kg}/\text{m}^3\right)$	2200	3580	2950
Specific heat capacity, c_{s} $\left(\text{J}/\left(\text{kg}\cdot\text{K}\right)\right)$	730	930	755
Heat conductivity, κ_{s} $\left(\text{W}/\left(\text{K}\cdot\text{m}\right)\right)$	1.4	40	2.55

Table 7.1: Compilation of the mass density, ρ_{s}, specific heat capacity, c_{s}, and heat conductivity, κ_{s}, parameters associated with some possible substrates on which a Mn_2Au layer could be grown.

7.7 Conclusions

We have addressed the theoretical study of two initially well-separated DW in one of the FM sheets of the layered AFM Mn_2Au under the action of current-induced SO fields, which ranges from their dynamic evolutions far from the region of mutual interaction up to their collision. Analyzing the impact outcome of magnetic textures with different relative topological charges, we have been able to certify that, as expected, the topological selection rules are verified in AFM, which are rooted in the energy balance between the Zeeman contribution and the FM-like exchange interaction between them. In this sense, an elastic collision occurs if they have the same chiralities, remaining in the system after the collision, while when their winding

numbers are the opposite, they annihilate each other, which results in a spatially-localized breather-like excitation when they do not have enough kinetic energy to escape the attractive potential created by the other magnetic soliton. Due to the fact that, in AFM, the DW can be contracted, during their Lorentz-governed dynamic regimes, down to the atomic scale, it is possible to reach increases of up to 485% of their stored exchange-based self energies with respect to their values at rest in the range of considered external stimuli. This, together with the fact that, in this type of long-range magnetically-ordered media, the magnetic textures are not prone to deformations during their motions and that they can reach speeds of up to a few tens of km/s, allows envisioning the magnetic solitons in AFM as potential energy carriers which can be charged and displaced through the application of electrical current pulses. Taking into account that the dynamically-accumulated DW energies can be released through topologically-mediated collision processes, it is possible to use the kinetic two temperature model to obtain a thermal footprint of the heat dissipated by both magnetic textures in their time-dependent evolutions to the electron and phonon baths. Due to the metallic character of Mn_2Au, the energy is redistributed from the spin space to the electronic reservoir on the subpicosecond time scale, giving rise to electron-based temperature peaks lagging slightly behind the ultrafast magnetic solitons, being produced, in turn, the transfer from this subsystem to the phononic one in a few picoseconds. In the case in which the DW collide elastically because they have the same relative topological charges, only a partial release of the energy stored by both magnetic textures occurs because they remain in the system after the impact, while when their relative chiralities are the opposite, there is an additional topologically-based dissipation contribution because both magnetic solitons cease to exist in spin space due to their mutual annihilation, which resembles a hypothetical spin-based version of an electric capacitor. This has as a result that, for the range of considered SO fields, it is possible to find an increase of up to a 51% in the maximum electronic and of up to a 30% in the maximum phononic temperatures when the impact between the DW is inelastic, giving rise to the possibility of experimentally distinguishing both processes through their thermal footprints through techniques such as scanning thermal microscopy. Our proposal opens the door to ultrafast energy management at the nanoscale for future alternative spin-based nanoelectronics as well as the possibility of using magnetic textures as non-disruptive local heating probes, an approach which, unlike in the case of other defects, avoids the inconvenience of overcoming any energy barrier for the particle-antiparticle recombination process, which is ensured in magnetically-based media due to topological and energetical arguments.

Summary and outlook

Concluding remarks

The recently discovered possibility of efficiently manipulating the order parameter of a certain family of AFM metals through current-induced SO fields, whose magnetic morphology is characterizable through conventional MR effects, has fueled the interest in these long-range magnetically-ordered materials with null net magnetization. This is due to the advantages they present compared to their FM counterparts, such as the non-generation of stray fringing fields, inherent frequencies in the elusive THz band, absence of WB due to the tilting of the magnetization with respect to the DW plane at rest, and high critical Néel temperatures. Moreover, AFM have attracted the attention of the scientific community due to their memristive-like multilevel switching behavior and ultrafast topological magnetic solitons not prone to dynamic deformations, which allows envisioning the design of full-AFM all-spintronics devices that beat the current von Neumann architectures in terms of operating speed, energy efficiency, and miniaturization. Of special technological and fundamental interest is the case of magnetic textures propagating in AFM in the special relativity framework, which allows reaching, in stable dynamic regimes, speeds of tens of km/s. Although there are currently no experimental methods that allow to track the movement of magnetic solitons in these types of systems, it is possible to explore their dynamic behavior theoretically for real AFM materials in order to unravel features that may be useful in the near future in hypothetical AFM-based technological implementations. However, the vast majority of works in this sense have been focused on the analytical exploration of 1D spin chains complemented with different discretization-based computational schemes, which cannot always give a good account of the relativistic signatures inherent to complex AFM materials. In this context, it has been exposed, in Chap. 1, a brief summary, from our point of view, of the current state of research in the field of spintronics, with special emphasis on the potential advantages of excitation methodologies based on spin-orbit fields, topologically-protected magnetic textures, and AFM materials. In Chap. 2 it has been introduced how to characterize the dissipative dynamic processes in spin space based on the different magnetic contributions of the system, as well as the conditions under which solitonic solutions exist in long-range magnetically-ordered media whose energetically-induced stabilities can be characterized through topological notions. On the other hand, in Chap. 3 the crucial features that dictate the stability of dynamic DW in both FM and AFM have been discussed, as well as the impact of topology on the propagation of magnetic textures and what kind of computational and experimental approaches exist to characterize these soliton solutions. Finally, our works exposed in this thesis, which are discussed in Chaps. 4, 5, 6, and 7 present insights into fundamental questions such as: (i) the transition from Galilean-governed dynamics in FM to relativistic ones as in the case of AFM, (ii) the accurate theoretical characterization of the motion of magnetic textures in

real layered multisublattice AFM, (iii) the beating of the magnonic barrier in AFM through non-relativistic DW propagation regimes, and (iv) the exploration of thermal gradients-based detection schemes to discern the displacement and presence of magnetic solitons in AFM.

In Chap. 4 we have explored the possibility to emulate analytically some inherent AFM properties in the case of a biaxial FM composed of both easy-axis and hard-axis anisotropy contributions. Among the AFM signatures of interest are their dynamic relativistic traces and the absence of the WB produced by the tilting of the magnetization with respect to the DW plane at rest in its propagation process. In this context, we have been able to find that:

- it is possible to characterize the functional form of the energy and spatial extension of the magnetic soliton through the dispersion relation of the linear SW with imaginary wavenumber and frequency that live in their tails.
- the reduction of the dynamic LL equation to a relativistic SG-like expression is formally obtainable in the Walker-type of solutions framework without the need to make any assumptions about the value of the dimensionless hard-axis to easy-axis anisotropy ratio.
- a physically consistent SG equation is only achieved in the case in which an appropriate functional form of the kinetic Lagrangian term can be obtained, which only happens when the hard-axis anisotropy is large enough, leading to negligible out-of-easy-plane angular deviations.
- the steady-state motion description is only valid for propagation velocities small enough compared to the critical speed of the system given by the maximum phase velocity of SW with imaginary wavevector and imaginary frequency.
- a solution to avoid the small canting angle divergence would be to work outside the Walker-type of solutions framework where the spatial and time derivatives of the magnetization are not independent, verifying the requirements of the traveling wave ansatz.
- relativistic traces such as the saturation of the velocity as the magnetic field increases, together with the consequent contraction of the width of the magnetic texture, have been verified through ASDS for high values of the hard-axis to easy-axis anisotropy ratio.

In this way, for sufficiently large hard-axis to easy-axis anisotropy ratios, it is plausible to delay the appearance of the WB due to the dynamic deviations of the magnetization with respect to the DW plane at rest as well as to appreciate relativistic signatures in the dynamics of magnetic solitons. There should be signatures of this even in real soft FM materials with an induced uniaxial anisotropy like permalloy or YIG without the need for complicated geometries. Moreover, one has to be cautious when choosing the computational discretization method of the spin space in the presence of a strong hard-axis anisotropy, even in FM in the absence of temperature, due to the predicted contraction of the magnetic texture to values that cause the failure of the continuum approximation.

In Chaps. 5 and 6 we have analyzed the behavior of a topologically-protected DW in the layered AFM Mn_2Au, whose dynamics has been excited through SO

fields. This has been motivated by the possibility of using this type of magnetic textures in AFM both to store and process information in all-spintronics architectures, for which it is necessary to have a good understanding of what to expect from the propagation of a magnetic soliton in a real medium. Due to the fact that currently most of the analyses in this regard have been carried out for 1D spin chains, we have used ASDS and analytical tools based on symmetry considerations and on the collective coordinates approach to elucidate its behavior. This being the situation, our investigations have allowed us to find that:

- it is possible to exploit the symmetric inequivalence between the crystallographic and magnetic unit cells to reduce the description of the complex system to a two-sublattices-based problem.
- due to the null-impact of the AFM exchange interaction directed along the c-axis of the system on the temperature-independent static and dynamic properties of the DW, it is necessary to transition to an effective version of the nonlinear σ-model.
- for SO field-excitation protocols that guarantee the transition of the magnetic texture between quasistatic regimes, it is possible to replicate the simulated relativistic and inertial dynamic signatures through a Newton-like second-order differential equation of motion.
- after ceasing the action of the external stimulus, the magnetic soliton undertakes a complex translational regime, being possible to replicate the related after-pulse displacement through the knowledge of its steady-state relativistic mass.
- under a certain combination of the magnitude of the SO field and the ramping time, the existence of a process similar to the WB in FM has been found, where the steady-state motion of the DW is interrupted by a highly nonlinear dynamic regime mediated by the nucleation of pairs of magnetic textures respecting the initial overall topological charge of the system.
- the appearance of additional pairs of magnetic solitons can be related to the torque exerted by the dynamically-based kinetic field generated by the primal DW during its translational propagation.
- the generated magnetic texture with a topological charge opposite to that shown by the primal DW is capable of moving away from the nucleation region at supermagnonic speeds in a non-relativistic dynamic regime, which would be related to a momentum transfer of the exchange-based energy of the two remaining magnetic solitons that are spatially stuck.
- there is a radiative tail traveling together with the boosted magnetic texture, whose origin seems to be due to the spin Cherenkov, because the DW transiently exceeds the SW phase velocity of the system, and to the Bremsstrahlung, due to the sudden deceleration of the original magnetic soliton at the nucleation instant, effects.

In this way, an accurate prediction of the position of the magnetic texture on a real AFM material can be obtained through a single analytical expression without the need to rely on dynamic simulations provided that, in the presence of an external stimulus, the DW transits through quasistatic scenarios. Moreover, the fact that it is

also plausible to predict the after-pulse displacement of the magnetic soliton opens the possibility of using the intrinsic inertial effects of the system to be able to conduct the DW to a specific area of the medium with a lower application time of the SO field than the one that would be needed to produce this event in a steady-state fashion. This is of great importance in the realm of full-AFM racetrack memory schemes, where the magnetic textures themselves encode valuable information in the system, so that, by obtaining an estimate of their propagation, their presence can be traced experimentally over a specific spatial range, with the consequent potential energy saving. On the other hand, by modifying the magnitude of the SO field and the applied ramping time, it is possible to create a DW lattice due to the nucleation of multiple pairs of magnetic solitons where each supermagnonic magnetic texture acts as a new seed. When the external stimulus is progressively decreased, a decompression of the generated network occurs due to the annihilation of nearby DW with opposite topological charges mediated by the attractive short-range exchange interaction between them, process in which residual magnetic solitons may remain in the system for pairs sufficiently far apart from each other. These types of observations are in line with the experimentally-reported resistance changes in these kind of materials under the action of pulsed excitations as well as with the presence of remnant signals after turning off the current-induced SO field, which indicates that this phenomenon could be purely of magnetic origin, not requiring the action of Joule heating, electromigration, or quenching-induced effects to explain it. Moreover, since the number of nucleated magnetic textures depends on the excitation protocol, being the intrapair DW distance non-uniform throughout the sample, it would be possible to encode information in the possible configurable patterns. Likewise, due to the inherent nonlinearities mediated by the exchange interaction between the magnetic textures that make up the created networks, in conjunction with high amplitude excitations, this system could serve as a testbed for the creation of chaotic patterns. In this scenario, the use of magnetic texture-based lattices as computational reservoirs could be envisioned, where the topologically-protected DW would act as virtual neurons, since this type of scheme finds its optimal performance near the phase transition between order and chaos. In this way, self-organized AFM DW-based neural schemes could be configured for purposes such as signal discrimination, temporal classification, and pattern recognition, beating the current von Neumann schemes in terms of power consumption, compactification, and operation time.

In Chap. 7 we have investigated the outcome of the collision of two DW with different relative topological charges in the layered AFM Mn_2Au whose impact is induced by the application of current-induced SO fields. This has been motivated by the possibility of obtaining larger thermal footprints of the electronic and phononic reservoirs than those achieved through the SPE by a single magnetic soliton. To this end, we have used ASDS in combination with the kinetic two temperature model, also employing analytical tools based on the collective coordinates approach. This being the case, we have been able to deduce that:

- the topological selection rules are verified in AFM, which are rooted in the energy balance between the Zeeman contribution and the FM-like exchange interaction between them.

- due to the inherent Lorentz-governed dynamics, increases of up to 485% of the stored exchange-based DW self energies can be achieved with respect to their values at rest for the range of considered external stimuli.

- in addition to the inherent energy redistribution to the electron and phonon reservoirs of the system due to the friction-governed SPE calculated through the two temperature model, there is also a contribution coming from the the impact of the magnetic textures.
- depending on the relative topological charges of both magnetic solitons, there will be a topologically-mediated energy release due to their collision, being partial if it is elastic, due to their sudden deceleration, or total if it is inelastic.
- for the range of considered SO fields, it is possible to reach increases of up to a 51% in the maximum electronic and of up to a 30% in the maximum phononic temperatures when the DW annihilate each other.

As it has been exposed, it is possible to tune the exchange-based self energies of AFM magnetic textures through their relativistic motions, where velocities of the order of several tens of km/s can be reached, while showing great stability during their propagation due to their topological protections. This allows to envision them as dynamic energy carriers whose stored energies can be partially or totally released through topologically-mediated collisions, which resembles a hypothetical spin-based version of an electric capacitor. In the same line, it would also be possible to use magnetic solitons as non-disruptive local heating probes, taking advantage of the fact that, unlike in the case of other defects, the inconvenience of overcoming any energy barrier for the particle-antiparticle recombination is avoided, which it is ensured in magnetically-based media due to topological and energetic arguments. From an experimental point of view, it would be plausible to use, on the one hand, the dynamic spin Peltier-based energy dissipation of a single DW to track its position and, on the other hand, the differentiable thermal footprint produced by the collision of pairs of magnetic textures to distinguish which are their relative topological charges through scanning thermal microscopy techniques. Finally, the impact processes of magnetic solitons, and their possible outcomes, can be used to perform logical operations through the annihilation or prevalence of the DW.

Future prospects

Within the research context exposed in this thesis, beyond some complementary works that would form a kind of logical follow-ups, we have also considered evaluating the dynamic behavior and stability of non-topologically-protected 90° DW in an AFM, being able to take for it the case of Mn_2Au. In this line, it is interesting, in the first place, to find under which application direction and magnitude of the SO field-based excitation the magnetic texture could survive, since in this case it is not possible to apply an external stimulus that exerts a null torque at both ends of the magnetic soliton. It must be taken into account, however, that in this case, if an electric current line is applied across the width of the sample, which is normally around a few tens of nm, the current density necessary to obtain SO-based external stimuli of the order of a few tens of mT would be potentially damaging to the integrity of the system. Because in AFM the dynamics are inherently relativistic, it is interesting to see if it is possible to drive these non-topological DW at speeds for which it is possible to appreciate signatures such as the velocity saturation as the SO field increases and the consequent contraction of its spatial extent. If that it is the case, it will be necessary to check if the considered magnetic texture is capable of surviving in the magnetic medium for SO-based external stimuli greater than the tetragonal in-plane

anisotropy energy landscape, since if this were to happen it could be hypothesized that the relativistic framework provides an additional stability to the magnetic soliton. Finally, it would be interesting to explore which would be the outcome of the collision of a pair of DW with different relative chiralities, being of special interest to verify if it is possible to artificially induce an effective topological 180° magnetic texture if they both have the same "topological" charge. Investigating this scenario is relevant because, currently, multidomain configurations separated by 90° magnetic textures have already been visualized in layered AFM excitable through SO fields such as CuMnAs and Mn_2Au for the case of bulk samples. In this sense, it should be taken into account that, in our case, in order to stabilize the topologically-protected 180° magnetic solitons, we have considered the case of thin films, which are more difficult to engineer, that have an additional strain-induced uniaxial anisotropy.

Resumen

La recientemente descubierta posibilidad de manipular de forma eficiente el parámetro de orden de una cierta familia de materiales antiferromagnéticos metálicos a través de campos de tipo espín-órbita inducidos por corrientes eléctricas, cuyas morfologías magnéticas pueden caracterizarse a través de efectos magnetoresistivos convencionales, ha avivado el interés en este tipo de materiales con ordenamiento magnético de largo alcance con una nula magnetización global. Esto se debe a las ventajas que presentan este tipo de sistemas en comparación con sus contrapartes ferromagnéticas, entre las que se encuentran la inexistencia de campos demagnetizantes significativos, frecuencias inherentes en la banda elusiva del THz, ausencia de la ruptura tipo Walker debido a potenciales desviaciones de la magnetización con respecto al plano en reposo de la pared de dominio y altas temperaturas críticas tipo Néel. Además, los materiales antiferromagnéticos han atraído la atención de la comunidad científica tanto por su comportamiento multinivel tipo memristivo como por la posibilidad de albergar solitones magnéticos ultrarrápidos topológicamente protegidos que no tienden a deformarse durante el proceso dinámico, lo cual permitiría hipotetizar acerca del diseño de aparatos puramente espintrónicos conformados íntegramente por materiales antiferromagnéticos, los cuales podrían superar el rendimiento actual de las arquitecturas de tipo von Neumann en términos de velocidad de operación, eficiencia energética y miniaturización. De especial interés tecnológico y fundamental es el caso de texturas magnéticas propagándose a través de materiales antiferromagnéticos en el marco de la relatividad especial, lo cual permite alcanzar, en regímenes dinámicos estables, velocidades de decenas de km/s. A pesar de que no existen, actualmente, métodos experimentales que permitan caracterizar el movimiento de solitones magnéticos en este tipo de sistemas, es posible explorar su comportamiento dinámico teóricamente en materiales antiferromagnéticos reales con el objetivo de dilucidar propiedades que puedan ser de utilidad en un futuro próximo en la hipotética implementación de tecnologías basadas en estos compuestos. Sin embargo, la mayor parte de los trabajos publicados en este ámbito se centran en la exploración analítica de cadenas unidimensionales de espín, en combinación con diferentes esquemas computacionales con diferentes métodos de discretización del espacio de espín, lo cual no siempre permite evaluar de forma eficiente las trazas relativistas inherentes a los materiales antiferromagnéticos reales más complejos. En este contexto, hemos introducido, en el Capítulo 1, un pequeño resumen, desde nuestro punto de vista, del actual estado de la investigación en el campo de la espintrónica, con especial énfasis en las potenciales ventajas de las metodologías de excitación basadas en campos de tipo espín-órbita, de las texturas magnéticas topológicamente protegidas y de los materiales antiferromagnéticos. En el Capítulo 2, se ha introducido cómo caracterizar los procesos dinámicos disipativos en el espacio de espín tomando en cuenta las diferentes contribuciones magnéticas del sistema, así como las condiciones bajo las cuales pueden existir soluciones

solitónicas en medios magnéticos ordenados de largo alcance cuya estabilidad puede ser descrita a través de nociones topológicas. Por otro lado, en el Capítulo 3, se han discutido las propiedades cruciales que dictan la estabilidad de las paredes de dominio dinámicas, tanto en materiales ferromagnéticos como antiferromagnéticos, así como cuál es el impacto de la topología en la propagación de las texturas magnéticas y qué tipos de aproximaciones computacionales y experimentales se pueden emplear para caracterizar estas soluciones solitónicas. Por último, nuestros trabajos publicados se han discutido en los Capítulos 4, 5, 6 y 7, en los cuales se profundiza sobre cuestiones fundamentales tales como: (i) la transición de una dinámica de tipo galileana en materiales ferromagnéticos a una relativista, como ocurre en los sistemas antiferromagnéticos, (ii) la caracterización teórica precisa del movimiento de texturas magnéticas en materiales antiferromagnéticos laminados reales multi-red, (iii) la existencia de procesos que permitan sobrepasar la barrera magnónica en materiales antiferromagnéticos a través de regímenes de propagación no relativistas de las paredes de dominio y (iv) la exploración de esquemas de detección basados en gradientes térmicos para discernir el desplazamiento y presencia de solitones antiferromagnéticos.

En el Capítulo 4, hemos explorado la posibilidad de emular, analíticamente, algunas de las propiedades inherentes a los materiales antiferromagnéticos en el caso de un material ferromagnético biaxial, compuesto por contribuciones anisotrópicas tanto de tipo eje fácil como difícil. Entre las características de interés de los materiales antiferromagnéticos se encuentran sus trazas dinámicas relativistas y la ausencia de la ruptura tipo Walker producida por la desviación de la magnetización con respecto al plano en reposo de la pared de dominio durante el proceso de propagación. En este contexto, hemos sido capaces de hallar que:

- es posible caracterizar la forma funcional de la energía y la extensión espacial del solitón magnético a través de la relación de dispersión de las ondas de espín lineales, con número de onda y frecuencia imaginarias, que residen en las regiones homogéneamente magnetizadas sitas en sus extremos.

- es formalmente posible reducir la ecuación dinámica de Landau-Lifshitz a una expresión sine-Gordon relativista en el ámbito de las soluciones tipo Walker sin tener que realizar asunciones acerca del valor del parámetro adimensional conformado por el cociente de la contribución anisotrópica de tipo eje difícil entre la de naturaleza fácil.

- solo es posible obtener una ecuación tipo sine-Gordon que sea físicamente consistente en el caso en el cual se pueda proponer una forma funcional apropiada del término cinético del Lagrangiano, lo cual solo sucede cuando la anisotropía de tipo eje difícil es lo suficientemente grande, dando lugar a la existencia de desviaciones angulares despreciables con respecto al plano fácil del sistema.

- la tendencia de movimiento estacionario es solo plausible cuando la velocidad de propagación sea lo suficientemente pequeña en comparación a la velocidad crítica del sistema, la cual viene dada por la máxima velocidad de fase de las ondas de espín con vector de onda y frecuencia imaginarios.

- la solución para evitar la divergencia del ángulo asociado a las pequeñas desviaciones con respecto al plano fácil del sistema sería trabajar fuera del ámbito de las soluciones de tipo Walker, lo cual conllevaría que las derivadas espaciales y temporales de la magnetización no sean independientes, verificándose los requerimientos asociables a una onda viajera.

- las trazas relativistas tales como la saturación de la velocidad a medida que el campo magnético se incrementa, así como la consiguiente contracción de la anchura espacial de la textura magnética, han sido verificadas a través de simulaciones dinámicas de espines atómicos para grandes valores del cociente de la contribución anisotrópica de tipo eje difícil con respecto a la de naturaleza fácil.

De este modo, para cocientes de la contribución anisotrópica de tipo eje difícil entre la de naturaleza fácil que sean lo suficientemente grandes, será plausible retrasar la aparición de la ruptura de tipo Walker debida a las desviaciones dinámicas de la magnetización con respecto al plano en reposo de la pared de dominio y, además, se podrán apreciar trazas relativistas durante la dinámica de los solitones magnéticos. Esto se debería de poder verificar incluso para el caso de materiales ferromagnéticos blandos reales con una anisotropía uniaxial inducida, lo cual sucede en aleaciones de hierro y níquel o en granates de hierro e itrio, sin la necesidad de complicadas geometrías. Asimismo, se ha de ser prudente a la hora de escoger el método de discretización computacional del espacio de espín en presencia de una fuerte anisotropía de tipo eje difícil, incluso en materiales ferromagnéticos en ausencia de efectos térmicos, debido a la predicha contracción espacial de la textura magnética hasta valores que puedan provocar el fallo de la aproximación al continuo.

En los Capítulos 5 y 6, hemos analizado el comportamiento de una pared de dominio topológicamente protegida en un material antiferromagnético laminado conocido como Mn_2Au, cuya dinámica ha sido excitada a través de campos de tipo espín-órbita. La motivación de este estudio recae en la posibilidad de emplear este tipo de texturas magnéticas en materiales antiferromagnéticos tanto para almacenar como para procesar información en arquitecturas completamente basadas en fenómenos de origen espintrónico, para lo cual es necesario comprender qué es lo que se puede esperar de la propagación de un solitón magnético en un sistema real. Debido a que, actualmente, la mayor parte de los análisis que se han llevado a cabo en este sentido han considerado el caso de cadenas de espín unidimensionales, hemos empleado simulaciones dinámicas de espines atómicos y métodos analíticos basados en consideraciones sobre simetría y la aproximación de las coordenadas colectivas para dilucidar su comportamiento. En este contexto, nuestra investigación nos ha permitido descubrir que:

- es posible explotar la inequivalencia existente entre las simetrías de las celdas unidad cristalográfica y magnética para reducir la descripción del sistema complejo a un problema basado en dos redes.

- debido al nulo impacto de la interacción de canje antiferromagnética, dirigida a lo largo del eje c del sistema, en las propiedades estáticas y dinámicas de la pared de dominio en ausencia de efectos térmicos, es necesario transicionar a una versión efectiva del modelo no lineal tipo σ.

- para protocolos de excitación basados en campos de tipo espín-órbita que garanticen la transición de la textura magnética entre regímenes dinámicos de forma cuasiestacionaria, es posible replicar las trazas relativistas e inerciales a través de una ecuación diferencial newtoniana de segundo orden.

- tras extinguirse la acción del estímulo externo, el solitón magnético accede a un régimen traslacional complejo, siendo posible replicar el desplazamiento que esta experimenta tras apagarse el pulso magnético de tipo espín-órbita a través de su masa relativista en estado estacionario.

- bajo cierta combinación de la magnitud y el tiempo de aplicación del campo de tipo espín-órbita hasta alcanzar su máximo valor en el protocolo de excitación escogido, tiene lugar la aparición de un proceso similar a la ruptura tipo Walker típica de materiales ferromagnéticos, lo cual implica que el movimiento estacionario de la pared de dominio sea interrumpido, dando paso a un régimen dinámico altamente no lineal mediado por la nucleación de un par de texturas magnéticas respetando la carga topológica global inicial del sistema.

- la aparición de un par adicional de solitones magnéticos en el sistema puede estar relacionada con el torque ejercido por el campo cinético inducido por la dinámica de la pared de dominio inicial durante su propagación traslacional.

- la textura magnética generada que atesora una carga topológica opuesta a la albergada por la pared de dominio inicial es capaz de alejarse de la región de nucleación a velocidades supermagnónicas en un régimen dinámico no relativista, lo cual estaría relacionado con la transferencia de momento de la energía de tipo canje asociada a los dos solitones magnéticos restantes, los cuales se hallan espacialmente constreñidos.

- existe una estela viajando junto con la textura magnética impulsada, cuyo origen parece ser debido a la radiación de tipo espín Cherenkov, en consonancia con que la pared de dominio excede temporalmente la velocidad de fase de las ondas de espín del sistema, y de frenado, producida por la deceleración abrupta del solitón magnético inicial en el instante en el cual se produce la nucleación.

De este modo, es posible obtener una predicción precisa de la posición de una textura magnética en un material antiferromagnético real a través de una única expresión analítica sin la necesidad de depender de simulaciones dinámicas siempre que, en presencia de un estímulo externo, la pared de dominio transite a través de regímenes cuasiestacionarios. Asimismo, debido a que es plausible predecir el desplazamiento experimentado por el solitón magnético tras la extinción abrupta del campo de tipo espín-órbita, sería posible aprovechar los efectos inerciales intrínsecos del sistema para trasladar la pared de dominio a una región específica del medio a través de un menor tiempo de aplicación del estímulo externo que el que sería necesario si este fenómeno se llevase a cabo a través de procesos estacionarios. Esto es de gran importancia en el ámbito de memorias tipo pista completamente basadas en materiales antiferromagnéticos, donde las texturas magnéticas en sí mismas codifican información relevante del sistema, por lo que, a través de la estimación de la distancia que estas se han propagado, sería posible rastrear experimentalmente su presencia en regiones específicas, con el consecuente ahorro de energía. Por otro lado, si se modifica la magnitud del campo de tipo espín-órbita y el tiempo empleado en aumentarlo hasta su valor máximo, es posible crear una red de paredes de dominio debido a los múltiples procesos de nucleación de pares de solitones magnéticos, en los cuales cada textura magnética supermagnónica actúa como una nueva semilla. Cuando se aumenta progresivamente el estímulo externo, se produce la descompresión de la red generada debido a la aniquilación de paredes de dominio contiguas con cargas topológicas opuestas, proceso el cual está mediado por la interacción atractiva de canje de corto alcance, tras lo cual pueden permanecer algunos pares de solitones magnéticos residuales en el sistema siempre que sus constituyentes se encuentren lo suficientemente lejos entre sí. Este tipo de observaciones están en línea con los cambios de resistencia hallados experimentalmente en este tipo de

materiales tras la acción de una excitación transitoria, así como con la presencia de una señal remanente tras apagar el campo de tipo espín-órbita generado por la aplicación de una corriente eléctrica, lo cual indica que este fenómeno podría tener un origen puramente magnético, no siendo necesaria la acción del calentamiento de tipo Joule o de procesos de electromigración o de enfriamiento repentino para explicarlo. Además, debido a que el número de texturas magnéticas nucleadas depende del protocolo de excitación, no siendo uniforme la distancia entre los constituyentes que conforman un par de paredes de dominio a lo largo de la muestra, sería posible codificar información en los posibles patrones reconfigurables. Asimismo, debido a las inherentes no linealidades del sistema mediadas por la interacción de canje entre las texturas magnéticas que conforman la red generada, en conjunción con las excitaciones de gran amplitud aplicadas, este sistema podría albergar potenciales patrones caóticos. En este escenario, se podría hipotetizar que las redes generadas, conformadas por texturas magnéticas, podrían emplearse como reservorios computacionales, donde las paredes de dominio topológicamente protegidas actuarían como neuronas virtuales, debido a que este tipo de arquitecturas alcanzan su rendimiento óptimo cerca de la transición de fase entre un sistema ordenado y uno caótico. De este modo, estos esquemas neuronales reconfigurables basados en paredes de dominio antiferromagnéticas podrían ser empleados para la discriminación de señales, clasificación temporal y reconocimiento de patrones, superando las arquitecturas actuales de tipo von Neumann en términos de consumo energético, compactificación y tiempo de operación.

En el Capítulo 7, hemos investigado el resultado de la colisión de dos paredes de dominio con diferentes cargas topológicas relativas en el material antiferromagnético laminado Mn_2Au, donde el impacto es inducido por la aplicación de un campo de tipo espín-órbita generado por una corriente eléctrica. La motivación principal de este estudio se basa en la búsqueda de la producción de mayores huellas térmicas en los reservorios de electrones y fonones que los que se han obtenido a través del efecto de espín de tipo Peltier inducido por un único solitón magnético. Con esto en mente, hemos empleado simulaciones dinámicas de espines atómicos en combinación con el modelo cinético de dos temperaturas junto con métodos analíticos basados en la aproximación de coordenadas colectivas. Siendo este el caso, hemos sido capaces de deducir que:

- las reglas de selección topológicas se verifican en materiales antiferromagnéticos, las cuales están basadas en el balance de energía entre la contribución de tipo Zeeman generada por el campo de tipo espín-órbita y la interacción de canje de tipo ferromagnético entre las texturas magnéticas consideradas.
- debido a la dinámica inherentemente lorentziana, es posible obtener incrementos de hasta un 485 % de la autoenergía de canje de las paredes de dominio con respecto a su valor en reposo para el rango de estímulos externos considerado.
- además de la redistribución de energía a los reservorios de electrones y fonones del sistema como resultado de los procesos disipativos gobernados por el efecto de espín de tipo Peltier calculados a través del modelo de dos temperaturas, existe también una contribución originada por el impacto de las texturas magnéticas.
- dependiendo de las quiralidades relativas de ambos solitones magnéticos, existirá una liberación de energía mediada por topología a través del fenómeno de colisión, el cual será parcial si el proceso es elástico, debido a que ocurre una deceleración abrupta, o total si es inelástico.

- para el rango de campos de tipo espín-orbita considerado, es posible alcanzar incrementos de hasta un 51 % y de hasta un 30 % de las máximas temperaturas electrónicas y fonónicas, respectivamente, cuando las paredes de dominio se aniquilan mutuamente.

Tal y como ha sido expuesto, es posible modificar la autoenergía de canje de las texturas antiferromagnéticas a través de procesos relativistas, pudiéndose alcanzar velocidades del orden de varias decenas de km/s en regímenes dinámicos altamente estables inducidos por sus protecciones topológicas. Esto permite considerarlas como cargas dinámicas cuyas autoenergías pueden ser parcial o totalmente liberadas al medio a través de su colisión mediada por topología, lo cual se asemeja a una versión hipotética de tipo espintrónico de un condensador eléctrico. En la misma línea, sería también posible emplear los solitones magnéticos como sondas calefactoras locales no disruptivas tomando ventaja del hecho de que, al contrario de lo que sucede con otros defectos, no existe el inconveniente de tener que superar una barrera de energía para llevar a cabo la recombinación de la partícula considerada y de su antipartícula, lo cual está garantizado en los medios magnéticos debido a argumentos de tipo topológico y energético. Desde un punto de vista experimental, sería plausible emplear, por un lado, la disipación dinámica de energía a través del efecto de espín de tipo Peltier de una sola pared de dominio para caracterizar su posición en el sistema y, por otro lado, las huellas térmicas diferenciables producidas por la colisión de pares de texturas magnéticas para distinguir cuáles son sus cargas topológicas relativas usando, para ello, microscopía térmica de escaneo. Adicionalmente, el impacto de los solitones magnéticos, y los posibles resultados del proceso, pueden usarse para realizar operaciones lógicas a través de la aniquilación o prevalencia de las paredes de dominio en el sistema.

Los resultados expuestos en esta tesis se pueden hallar en las siguientes publicaciones en revistas internacionales de revisión por pares:

[1] **R. Rama-Eiroa**, R. M. Otxoa, P. E. Roy, and K. Guslienko
Steady one-dimensional domain wall motion in biaxial ferromagnets: mapping of the Landau-Lifshitz equation to the sine-Gordon equation
Phys. Rev. B **101**, 094416 (2020) arXiv:1910.13266 (2019)

[2] R. M. Otxoa, P. E. Roy, **R. Rama-Eiroa**, J. Godinho, K. Y. Guslienko, and J. Wunderlich
Walker-like domain wall breakdown in layered antiferromagnets driven by staggered spin–orbit fields
Commun. Phys. **3**, 190 (2020) arXiv:2002.03332 (2020)

[3] R. M. Otxoa, **R. Rama-Eiroa**, P. E. Roy, G. Tatara, O. Chubykalo-Fesenko, and U. Atxitia
Topologically-mediated energy release by relativistic antiferromagnetic solitons
Phys. Rev. Res. **3**, 043069 (2021) arXiv:2106.05804 (2021)

[4] **R. Rama-Eiroa**, P. E. Roy, J. González, K. Y. Guslienko, J. Wunderlich, and R. M. Otxoa
Inertial domain wall characterization in layered multisublattice antiferromagnets
J. Magn. Magn. Mater. **560**, 169566 (2022) arXiv:2109.09003 (2021)

Bibliography

[1] J. Puebla, J. Kim, K. Kondou, and Y. Otani, Commun. Mat. **1**, 24 (2020).

[2] C. Chappert, A. Fert, and F. N. Van Dau, Nat. Mat. **6**, 813 (2007).

[3] A. Sebastian, M. Le Gallo, R. Khaddam-Aljameh, and E. Eleftheriou, Nat. Nanotech. **15**, 529 (2020).

[4] S. Manipatruni, D. E. Nikonov, and I. A. Young, Nat. Phys. **14**, 338 (2018).

[5] J. Zhou and J. Chen, Adv. Electron. Mater. , 2100465 (2021).

[6] S. Bhatti, R. Sbiaa, A. Hirohata, H. Ohno, S. Fukami, and S. N. Piramanayagam, Mat. Today **20**, 530 (2017).

[7] L. Su, Y. Zhang, J.-O. Klein, Y. Zhang, A. Bournel, A. Fert, and W. Zhao, Sci. Rep. **5**, 14905 (2015).

[8] G. Finocchio, M. Di Ventra, K. Y. Camsari, K. Everschor-Sitte, P. Khalili Amiri, and Z. Zeng, J. Magn. Magn. Mat. **521**, 167506 (2021).

[9] Y. Zhang, W. Zhao, J.-O. Klein, W. Kang, D. Querlioz, Y. Zhang, D. Ravelosona, and C. Chappert, *Spintronics for Low-Power Computing* in *Design, Automation & Test in Europe Conference & Exhibition* (2014).

[10] H.-S. P. Wong and S. Salahuddin, Nat. Nanotech. **10**, 191 (2015).

[11] Z. Guo, J. Yin, Y. Bai, D. Zhu, K. Shi, G. Wang, K. Cao, and W. Zhao, Proc. IEEE (2021).

[12] R. Hunt, IEEE Trans. Magn. **7**, 150 (1971).

[13] C. Tsang, M.-M. Chen, T. Yogi, and K. Ju, IEEE Trans. Magn. **26**, 1689 (1990).

[14] E. D. Daniel, C. D. Mee, and M. H. Clark, *Magnetic Recording: the First 100 Years* (John Wiley & Sons, 1998).

[15] J. Smit, Physica **17**, 612 (1951).

[16] T. McGuire and R. L. Potter, IEEE Trans. Magn. **11**, 1018 (1975).

[17] W. Y. Lee, M. F. Toney, and D. Mauri, IEEE Trans. Magn. **36**, 381 (2000).

[18] C. L. Chien, S. Liou, D. Kofalt, W. Yu, T. Egami, and T. R. McGuire, Phys. Rev. B **33**, 3247 (1986).

[19] C. F. Majkrzak, J. W. Cable, J. Kwo, M. Hong, D. B. McWhan, Y. Yafet, J. V. Waszczak, and C. Vettier, Phys. Rev. Lett. **56**, 2700 (1986).

[20] J. Yahalom and O. Zadok, J. Mater. Sci. **22**, 499 (1987).

[21] S. Yang and J. Zhang, Chemosensors **9**, 211 (2021).

[22] M. N. Baibich, J. M. Broto, A. Fert, F. N. Van Dau, F. Petroff, P. Etienne, G. Creuzet, A. Friederich, and J. Chazelas, Phys. Rev. Lett. **61**, 2472 (1988).

[23] G. Binasch, P. Grünberg, F. Saurenbach, and W. Zinn, Phys. Rev. B **39**, 4828 (1989).

[24] B. Diény, J. Magn. Magn. Mat. **136**, 335 (1994).

[25] M. Julliere, Phys. Lett. A **54**, 225 (1975).

[26] J. S. Moodera, L. R. Kinder, T. M. Wong, and R. Meservey, Phys. Rev. Lett. **74**, 3273 (1995).

[27] T. Miyazaki and N. Tezuka, J. Magn. Magn. Mat. **139**, L231 (1995).

[28] M. A. Ruderman and C. Kittel, Phys. Rev. **96**, 99 (1954).

[29] T. Kasuya, Prog. Theor. Phys. **16**, 45 (1956).

[30] K. Yosida, Phys. Rev. **106**, 893 (1957).

[31] S. S. P. Parkin, N. More, and K. P. Roche, Phys. Rev. Lett. **64**, 2304 (1990).

[32] P. Bruno and C. Chappert, Phys. Rev. Lett. **67**, 1602 (1991).

[33] W. H. Meiklejohn and C. P. Bean, Phys. Rev. **102**, 1413 (1956).

[34] J. Nogués and I. K. Schuller, J. Magn. Magn. Mat. **192**, 203 (1999).

[35] H. J. Richter and A. Y. Dobin, J. Magn. Magn. Mat. **287**, 41 (2005).

[36] H. J. Richter, J. Phys. D Appl. Phys. **40**, R149 (2007).

[37] H.-M. Shen, L. Hu, and X. Fu, Sensors **18**, 148 (2018).

[38] S. N. Piramanayagam and K. Srinivasan, J. Magn. Magn. Mat. **321**, 485 (2009).

[39] E. Grochowski and R. F. Hoyt, IEEE Trans. Magn. **32**, 1850 (1996).

[40] B. N. Engel, J. Akerman, B. Butcher, R. W. Dave, M. DeHerrera, M. Durlam, G. Grynkewich, J. Janesky, S. V. Pietambaram, N. D. Rizzo, *et al.*, IEEE Trans. Magn. **41**, 132 (2005).

[41] J. M. Daughton, J. Appl. Phys. **81**, 3758 (1997).

[42] I. L. Prejbeanu, W. Kula, K. Ounadjela, R. C. Sousa, O. Redon, B. Dieny, and J.-P. Nozieres, IEEE Trans. Magn. **40**, 2625 (2004).

[43] I. L. Prejbeanu, M. Kerekes, R. C. Sousa, H. Sibuet, O. Redon, B. Dieny, and J. P. Nozières, J. Phys.: Condens. Matter **19**, 165218 (2007).

[44] J. C. Slonczewski, J. Magn. Magn. Mat. **159**, L1 (1996).

[45] L. Berger, Phys. Rev. B **54**, 9353 (1996).

[46] M. Tsoi, A. G. M. Jansen, J. Bass, W.-C. Chiang, M. Seck, V. Tsoi, and P. Wyder, Phys. Rev. Lett. **80**, 4281 (1998).

[47] E. B. Myers, D. C. Ralph, J. A. Katine, R. N. Louie, and R. A. Buhrman, Science **285**, 867 (1999).

[48] J. A. Katine, F. J. Albert, R. A. Buhrman, E. B. Myers, and D. C. Ralph, Phys. Rev. Lett. **84**, 3149 (2000).

[49] F. J. Albert, J. A. Katine, R. A. Buhrman, and D. C. Ralph, Appl. Phys. Lett. **77**, 3809 (2000).

[50] J. A. Katine and E. E. Fullerton, J. Magn. Magn. Mat. **320**, 1217 (2008).

[51] H. S. Choi, S. Y. Kang, S. J. Cho, I.-Y. Oh, M. Shin, H. Park, C. Jang, B.-C. Min, S.-I. Kim, S.-Y. Park, *et al.*, Sci. Rep. **4**, 5486 (2014).

[52] Z. Li and S. Zhang, Phys. Rev. B **68**, 024404 (2003).

[53] S. I. Kiselev, J. C. Sankey, I. N. Krivorotov, N. C. Emley, R. J. Schoelkopf, R. A. Buhrman, and D. C. Ralph, Nature **425**, 380 (2003).

[54] J. Torrejon, M. Riou, F. A. Araujo, S. Tsunegi, G. Khalsa, D. Querlioz, P. Bortolotti, V. Cros, K. Yakushiji, A. Fukushima, *et al.*, Nature **547**, 428 (2017).

[55] M. Romera, P. Talatchian, S. Tsunegi, F. A. Araujo, V. Cros, P. Bortolotti, J. Trastoy, K. Yakushiji, A. Fukushima, H. Kubota, *et al.*, Nature **563**, 230 (2018).

[56] D. Marković, A. Mizrahi, D. Querlioz, and J. Grollier, Nat. Rev. Phys. **2**, 499 (2020).

[57] J. D. Costa, S. Serrano-Guisan, J. Borme, F. L. Deepak, M. Tarequzzaman, E. Paz, J. Ventura, R. Ferreira, and P. P. Freitas, IEEE Trans. Magn. **51**, 1 (2015).

[58] S. Yuasa and D. D. Djayaprawira, J. Phys. D Appl. Phys. **40**, R337 (2007).

[59] M. B. Jungfleisch, W. Zhang, R. Winkler, and A. Hoffmann, *Spin-Orbit Torques and Spin Dynamics* in *Spin Physics in Semiconductors* (Springer, 2017).

[60] P. Gambardella and I. M. Miron, Philos. Trans. A Math. Phys. Eng. Sci. **369**, 3175 (2011).

[61] M. I. D'yakonov and V. I. Perel, JETP Lett. **13**, 467 (1971).

[62] J. E. Hirsch, Phys. Rev. Lett. **83**, 1834 (1999).

[63] Y. K. Kato, R. C. Myers, A. C. Gossard, and D. D. Awschalom, Science **306**, 1910 (2004).

[64] J. Wunderlich, B. Kaestner, J. Sinova, and T. Jungwirth, Phys. Rev. Lett. **94**, 047204 (2005).

[65] E. L. Ivchenko and G. E. Pikus, ZhETF Pisma Redaktsiiu **27**, 640 (1978).

[66] L. E. Vorob'ev, E. L. Ivchenko, G. E. Pikus, I. I. Farbshteĭn, V. A. Shalygin, and A. V. Shturbin, JETP Lett. **29**, 441 (1979).

[67] V. M. Edelstein, Solid State Commun. **73**, 233 (1990).

[68] A. G. Aronov and Y. B. Lyanda-Geller, JETP Lett. **50**, 431 (1989).

[69] J. Železnỳ, H. Gao, A. Manchon, F. Freimuth, Y. Mokrousov, J. Zemen, J. Mašek, J. Sinova, and T. Jungwirth, Phys. Rev. B **95**, 014403 (2017).

[70] I. M. Miron, G. Gaudin, S. Auffret, B. Rodmacq, A. Schuhl, S. Pizzini, J. Vogel, and P. Gambardella, Nat. Mat. **9**, 230 (2010).

[71] J. C. R. Sánchez, L. Vila, G. Desfonds, S. Gambarelli, J. P. Attané, J. M. De Teresa, C. Magén, and A. Fert, Nat. Commun. **4**, 2944 (2013).

[72] A. Manchon, H. C. Koo, J. Nitta, S. M. Frolov, and R. A. Duine, Nat. Mat. **14**, 871 (2015).

[73] R. Ramaswamy, J. M. Lee, K. Cai, and H. Yang, Appl. Phys. Rev. **5**, 031107 (2018).

[74] S. Fukami, C. Zhang, S. Duttagupta, A. Kurenkov, and H. Ohno, Nat. Mat. **15**, 535 (2016).

[75] Y.-W. Oh, S.-H. C. Baek, Y. M. Kim, H. Y. Lee, K.-D. Lee, C.-G. Yang, E.-S. Park, K.-S. Lee, K.-W. Kim, G. Go, *et al.*, Nat. Nanotech. **11**, 878 (2016).

[76] K. Garello, C. O. Avci, I. M. Miron, M. Baumgartner, A. Ghosh, S. Auffret, O. Boulle, G. Gaudin, and P. Gambardella, Appl. Phys. Lett. **105**, 212402 (2014).

[77] M. Finazzi, F. Bottegoni, C. Zucchetti, M. Bollani, A. Ballabio, J. Frigerio, F. Rortais, C. Vergnaud, A. Marty, M. Jamet, *et al.*, Electron. **5**, 80 (2016).

[78] F. Bloch, *Zur Theorie des Austauschproblems und der Remanenzerscheinung der Ferromagnetika* (Springer, 1932).

[79] L. D. Landau and L. M. Lifshitz, Phys. Z. Sowjetunion **8**, 153 (1935).

[80] A. Hubert and R. Schäfer, *Magnetic Domains: the Analysis of Magnetic Microstructures* (Springer Science & Business Media, 2008).

[81] H.-B. Braun, Adv. Phys. **61**, 1 (2012).

[82] S. S. P. Parkin, M. Hayashi, and L. Thomas, Science **320**, 190 (2008).

[83] A. Yamaguchi, T. Ono, S. Nasu, K. Miyake, K. Mibu, and T. Shinjo, Phys. Rev. Lett. **92**, 077205 (2004).

[84] M. Kläui, P.-O. Jubert, R. Allenspach, A. Bischof, J. A. C. Bland, G. Faini, U. Rüdiger, C. A. Vaz, L. Vila, and C. Vouille, Phys. Rev. Lett. **95**, 026601 (2005).

[85] J.-S. Kim, M.-A. Mawass, A. Bisig, B. Krüger, R. M. Reeve, T. Schulz, F. Büttner, J. Yoon, C.-Y. You, M. Weigand, *et al.*, Nat. Commun. **5**, 3429 (2014).

[86] H.-B. Braun, Phys. Rev. B **50**, 16485 (1994).

[87] A. Kunz, Appl. Phys. Lett. **94**, 132502 (2009).

[88] S. Fukami, T. Suzuki, Y. Nakatani, N. Ishiwata, M. Yamanouchi, S. Ikeda, N. Kasai, and H. Ohno, Appl. Phys. Lett. **98**, 082504 (2011).

[89] M. Hayashi, L. Thomas, C. Rettner, R. Moriya, X. Jiang, and S. S. P. Parkin, Phys. Rev. Lett. **97**, 207205 (2006).

[90] S. J. Noh, Y. Miyamoto, M. Okuda, N. Hayashi, and Y. Keun Kim, J. Appl. Phys. **111**, 07D123 (2012).

[91] N. L. Schryer and L. R. Walker, J. Appl. Phys. **45**, 5406 (1974).

[92] A. Thiaville, J. M. Garcıa, and J. Miltat, J. Magn. Magn. Mat. **242**, 1061 (2002).

[93] G. S. D. Beach, C. Nistor, C. Knutson, M. Tsoi, and J. L. Erskine, Nat. Mat. **4**, 741 (2005).

[94] S.-B. Choe, Appl. Phys. Lett. **92**, 062506 (2008).

[95] T. A. Moore, I. Miron, G. Gaudin, G. Serret, S. Auffret, B. Rodmacq, A. Schuhl, S. Pizzini, J. Vogel, and M. Bonfim, Appl. Phys. Lett. **93**, 262504 (2008).

[96] I. M. Miron, T. Moore, H. Szambolics, L. D. Buda-Prejbeanu, S. Auffret, B. Rodmacq, S. Pizzini, J. Vogel, M. Bonfim, A. Schuhl, *et al.*, Nat. Mat. **10**, 419 (2011).

[97] K.-S. Ryu, L. Thomas, S.-H. Yang, and S. Parkin, Nat. Nanotech. **8**, 527 (2013).

[98] M. Hayashi, L. Thomas, C. Rettner, R. Moriya, Y. B. Bazaliy, and S. S. P. Parkin, Phys. Rev. Lett. **98**, 037204 (2007).

[99] I. Dzyaloshinskii, J. Phys. Chem. Solid **4**, 241 (1958).

[100] T. Moriya, Phys. Rev. **120**, 91 (1960).

[101] S. Emori, U. Bauer, S.-M. Ahn, E. Martinez, and G. S. D. Beach, Nat. Mat. **12**, 611 (2013).

[102] Y. Yoshimura, K.-J. Kim, T. Taniguchi, T. Tono, K. Ueda, R. Hiramatsu, T. Moriyama, K. Yamada, Y. Nakatani, and T. Ono, Nat. Phys. **12**, 157 (2016).

[103] A. Soumyanarayanan, N. Reyren, A. Fert, and C. Panagopoulos, Nature **539**, 509 (2016).

[104] S.-W. Lee, B.-G. Park, and K.-J. Lee, Curr. Appl. Phys. **15**, 1139 (2015).

[105] J. Cao, Y. Chen, T. Jin, W. Gan, Y. Wang, Y. Zheng, H. Lv, S. Cardoso, D. Wei, and W. S. Lew, Sci. Rep. **8**, 1355 (2018).

[106] Y. Gaididei, V. P. Kravchuk, and D. D. Sheka, Phys. Rev. Lett. **112**, 257203 (2014).

[107] D. D. Sheka, V. P. Kravchuk, and Y. Gaididei, . J. Phys. A Math. Theor. **48**, 125202 (2015).

[108] M. Yan, A. Kákay, S. Gliga, and R. Hertel, Phys. Rev. Lett. **104**, 057201 (2010).

[109] M. Yan, C. Andreas, A. Kákay, F. García-Sánchez, and R. Hertel, Appl. Phys. Lett. **99**, 122505 (2011).

[110] A. Fert, V. Cros, and J. Sampaio, Nat. Nanotechnol. **8**, 152 (2013).

[111] S. Bhatti and S. N. Piramanayagam, Phys. Status Solidi R. **13**, 1800479 (2019).

[112] X. Zhang, N. Vernier, Z. Cao, Q. Leng, A. Cao, D. Ravelosona, and W. Zhao, Nanotech. **29**, 365502 (2018).

[113] M. Diegel, S. Glathe, R. Mattheis, M. Scherzinger, and E. Halder, IEEE Trans. Magn. **45**, 3792 (2009).

[114] Z. Luo, A. Hrabec, T. P. Dao, G. Sala, S. Finizio, J. Feng, S. Mayr, J. Raabe, P. Gambardella, and L. J. Heyderman, Nature **579**, 214 (2020).

[115] A. Kurenkov, C. Zhang, S. Duttagupta, S. Fukami, and H. Ohno, Appl. Phys. Lett. **110**, 092410 (2017).

[116] S. Lequeux, J. Sampaio, V. Cros, K. Yakushiji, A. Fukushima, R. Matsumoto, H. Kubota, S. Yuasa, and J. Grollier, Sci. Rep. **6**, 31510 (2016).

[117] J. Sampaio, V. Cros, S. Rohart, A. Thiaville, and A. Fert, Nat. Nanotech. **8**, 839 (2013).

[118] O. Boulle, J. Vogel, H. Yang, S. Pizzini, D. de Souza Chaves, A. Locatelli, T. O. Menteş, A. Sala, L. D. Buda-Prejbeanu, O. Klein, *et al.*, Nat. Nanotech. **11**, 449 (2016).

[119] W. Kang, Y. Huang, X. Zhang, Y. Zhou, and W. Zhao, Proc. IEEE **104**, 2040 (2016).

[120] S. Woo, K. Litzius, B. Krüger, M.-Y. Im, L. Caretta, K. Richter, M. Mann, A. Krone, R. M. Reeve, M. Weigand, *et al.*, Nat. Mat. **15**, 501 (2016).

[121] J. Zang, M. Mostovoy, J. H. Han, and N. Nagaosa, Phys. Rev. Lett. **107**, 136804 (2011).

[122] W. Jiang, X. Zhang, G. Yu, W. Zhang, X. Wang, M. B. Jungfleisch, J. E. Pearson, X. Cheng, O. Heinonen, K. L. Wang, *et al.*, Nat. Phys. **13**, 162 (2017).

[123] F. Jonietz, S. Mühlbauer, C. Pfleiderer, A. Neubauer, W. Münzer, A. Bauer, T. Adams, R. Georgii, P. Böni, R. A. Duine, *et al.*, Science **330**, 1648 (2010).

[124] T. Schulz, R. Ritz, A. Bauer, M. Halder, M. Wagner, C. Franz, C. Pfleiderer, K. Everschor, M. Garst, and A. Rosch, Nat. Phys. **8**, 301 (2012).

[125] F. Büttner, I. Lemesh, and G. S. D. Beach, Sci. Rep. **8**, 4464 (2018).

[126] D. Pinna, F. A. Araujo, J.-V. Kim, V. Cros, D. Querlioz, P. Bessière, J. Droulez, and J. Grollier, Phys. Rev. Appl. **9**, 064018 (2018).

[127] K. Gerlinger, B. Pfau, F. Büttner, M. Schneider, L.-M. Kern, J. Fuchs, D. Engel, C. M. Günther, M. Huang, I. Lemesh, *et al.*, Appl. Phys. Lett. **118**, 192403 (2021).

[128] D. Pinna, G. Bourianoff, and K. Everschor-Sitte, Phys. Rev. Appl. **14**, 054020 (2020).

[129] X. Marti, I. Fina, C. Frontera, J. Liu, P. Wadley, Q. He, R. J. Paull, J. D. Clarkson, J. Kudrnovskỳ, I. Turek, *et al.*, Nat. Mat. **13**, 367 (2014).

[130] M. B. Jungfleisch, W. Zhang, and A. Hoffmann, Phys. Lett. A **382**, 865 (2018).

[131] T. Kampfrath, A. Sell, G. Klatt, A. Pashkin, S. Mährlein, T. Dekorsy, M. Wolf, M. Fiebig, A. Leitenstorfer, and R. Huber, Nat. Phot. **5**, 31 (2011).

[132] O. Gomonay and V. M. Loktev, Low Temp. Phys. **40**, 17 (2014).

[133] O. Gomonay, T. Jungwirth, and J. Sinova, Phys. Rev. Lett. **117**, 017202 (2016).

[134] T. Shiino, S.-H. Oh, P. M. Haney, S.-W. Lee, G. Go, B.-G. Park, and K.-J. Lee, Phys. Rev. Lett. **117**, 087203 (2016).

[135] A. K. Zvezdin, JETP Lett. **29**, 553 (1979).

[136] V. G. Bar'yakhtar, B. A. Ivanov, and M. V. Chetkin, Sov. Phys. Uspekhi **28**, 563 (1985).

[137] F. D. M. Haldane, Phys. Rev. Lett. **50**, 1153 (1983).

[138] H. Yang, H. Y. Yuan, M. Yan, H. W. Zhang, and P. Yan, Phys. Rev. B **100**, 024407 (2019).

[139] R. M. Otxoa, P. E. Roy, R. Rama-Eiroa, J. Godinho, K. Y. Guslienko, and J. Wunderlich, Commun. Phys. **3**, 190 (2020).

[140] T. Jungwirth, X. Marti, P. Wadley, and J. Wunderlich, Nat. Nanotech. **11**, 231 (2016).

[141] J. Železnỳ, P. Wadley, K. Olejník, A. Hoffmann, and H. Ohno, Nat. Phys. **14**, 220 (2018).

[142] A. V. Kimel, B. A. Ivanov, R. V. Pisarev, P. A. Usachev, A. Kirilyuk, and T. Rasing, Nat. Phys. **5**, 727 (2009).

[143] O. Gomonay, M. Kläui, and J. Sinova, Appl. Phys. Lett. **109**, 142404 (2016).

[144] E. G. Tveten, T. Müller, J. Linder, and A. Brataas, Phys. Rev. B **93**, 104408 (2016).

[145] O. Gomonay and V. M. Loktev, Phys. Rev. B **81**, 144427 (2010).

[146] R. Cheng, M. W. Daniels, J.-G. Zhu, and D. Xiao, Phys. Rev. B **91**, 064423 (2015).

[147] X. Z. Chen, R. Zarzuela, J. Zhang, C. Song, X. F. Zhou, G. Y. Shi, F. Li, H. A. Zhou, W. J. Jiang, F. Pan, *et al.*, Phys. Rev. Lett. **120**, 207204 (2018).

[148] J. Železnỳ, H. Gao, K. Výbornỳ, J. Zemen, J. Mašek, A. Manchon, J. Wunderlich, J. Sinova, and T. Jungwirth, Phys. Rev. Lett. **113**, 157201 (2014).

[149] P. Wadley, B. Howells, J. Železnỳ, C. Andrews, V. Hills, R. P. Campion, V. Novák, K. Olejník, F. Maccherozzi, S. S. Dhesi, *et al.*, Science **351**, 587 (2016).

[150] P. E. Roy, R. M. Otxoa, and J. Wunderlich, Phys. Rev. B **94**, 014439 (2016).

[151] K. Olejník, T. Seifert, Z. Kašpar, V. Novák, P. Wadley, R. P. Campion, M. Baumgartner, P. Gambardella, P. Němec, J. Wunderlich, *et al.*, Sci. Adv. **4**, eaar3566 (2018).

[152] I. Fina, X. Marti, D. Yi, J. Liu, J. H. Chu, C. Rayan-Serrao, S. Suresha, A. B. Shick, J. Železnỳ, T. Jungwirth, *et al.*, Nat. Commun. **5**, 4671 (2014).

[153] K. Olejník, V. Schuler, X. Martí, V. Novák, Z. Kašpar, P. Wadley, R. P. Campion, K. W. Edmonds, B. L. Gallagher, J. Garcés, *et al.*, Nat. Commun. **8**, 15434 (2017).

[154] S. Y. Bodnar, L. Šmejkal, I. Turek, T. Jungwirth, O. Gomonay, J. Sinova, A. A. Sapozhnik, H.-J. Elmers, M. Kläui, and M. Jourdan, Nat. Commun. **9**, 348 (2018).

[155] S. Y. Bodnar, Y. Skourski, O. Gomonay, J. Sinova, M. Kläui, and M. Jourdan, Phys. Rev. Appl. **14**, 014004 (2020).

[156] J. Fischer, O. Gomonay, R. Schlitz, K. Ganzhorn, N. Vlietstra, M. Althammer, H. Huebl, M. Opel, R. Gross, S. T. B. Goennenwein, *et al.*, Phys. Rev. B **97**, 014417 (2018).

[157] L. Baldrati, A. Ross, T. Niizeki, C. Schneider, R. Ramos, J. Cramer, O. Gomonay, M. Filianina, T. Savchenko, D. Heinze, *et al.*, Phys. Rev. B **98**, 024422 (2018).

[158] A. S. Núñez, R. A. Duine, P. Haney, and A. H. MacDonald, Phys. Rev. B **73**, 214426 (2006).

[159] P. Merodio, A. Kalitsov, H. Béa, V. Baltz, and M. Chshiev, Appl. Phys. Lett. **105**, 122403 (2014).

[160] L. Šmejkal, A. B. Hellenes, R. González-Hernández, J. Sinova, and T. Jungwirth, arXiv preprint arXiv:2103.12664 (2021).

[161] A. B. Shick, S. Khmelevskyi, O. N. Mryasov, J. Wunderlich, and T. Jungwirth, Phys. Rev. B **81**, 212409 (2010).

[162] B. G. Park, J. Wunderlich, X. Martí, V. Holỳ, Y. Kurosaki, M. Yamada, H. Yamamoto, A. Nishide, J. Hayakawa, H. Takahashi, *et al.*, Nat. Mat. **10**, 347 (2011).

[163] Y. Y. Wang, C. Song, B. Cui, G. Y. Wang, F. Zeng, and F. Pan, Phys. Rev. Lett. **109**, 137201 (2012).

[164] T. Janda, J. Godinho, T. Ostatnicky, E. Pfitzner, G. Ulrich, A. Hoehl, S. Reimers, Z. Šobáň, T. Metzger, H. Reichlova, *et al.*, Phys. Rev. Mat. **4**, 094413 (2020).

[165] R. M. Otxoa, U. Atxitia, P. E. Roy, and O. Chubykalo-Fesenko, Commun. Phys. **3**, 31 (2020).

[166] S.-H. Yang, K.-S. Ryu, and S. Parkin, Nat. Nanotech. **10**, 221 (2015).

[167] W. Legrand, D. Maccariello, F. Ajejas, S. Collin, A. Vecchiola, K. Bouzehouane, N. Reyren, V. Cros, and A. Fert, Nat. Mat. **19**, 34 (2020).

[168] T. Dohi, S. Duttagupta, S. Fukami, and H. Ohno, Nat. Commun. **10**, 5153 (2019).

[169] H. Belrhazi and M. El Hafidi, Sci. Rep. **12**, 15225 (2022).

[170] Z. Kašpar, M. Surỳnek, J. Zubáč, F. Krizek, V. Novák, R. P. Campion, M. S. Wörnle, P. Gambardella, X. Marti, P. Němec, *et al.*, Nat. Electron. **4**, 30 (2021).

[171] P. Wadley, S. Reimers, M. J. Grzybowski, C. Andrews, M. Wang, J. S. Chauhan, B. L. Gallagher, R. P. Campion, K. W. Edmonds, S. S. Dhesi, *et al.*, Nat. Nanotech. **13**, 362 (2018).

[172] H. Jani, J.-C. Lin, J. Chen, J. Harrison, F. Maccherozzi, J. Schad, S. Prakash, C.-B. Eom, A. Ariando, T. Venkatesan, *et al.*, arXiv preprint arXiv:2006.12699 (2020).

[173] K. G. Rana, R. L. Seeger, S. Ruiz-Gómez, R. Juge, Q. Zhang, V. T. Pham, M. Belmeguenai, S. Auffret, M. Foerster, L. Aballe, *et al.*, arXiv preprint arXiv:2009.14796 (2020).

[174] Z. Yu, M. Shen, Z. Zeng, S. Liang, Y. Liu, M. Chen, Z. Zhang, Z. Lu, L. You, X. Yang, *et al.*, Nanoscale Adv. **2**, 1309 (2020).

[175] J. M. D. Coey, *Magnetism and Magnetic Materials* (Cambridge University Press, 2012).

[176] S. Blundell, *Magnetism in Condensed Matter* (Oxford University Press, 2014).

[177] P. A. M. Dirac, Proc. R. Soc. Lond. A **117**, 610 (1928).

[178] R. M. White, *Quantum Theory of Magnetism. Magnetic Properties of Materials* (Berlin: Springer-Verlag, 2007).

[179] T. E. Phipps and J. B. Taylor, Phys. Rev. **29**, 309 (1927).

[180] R. Beringer and M. A. Heald, Phys. Rev. **95**, 1474 (1954).

[181] J. Schwinger, Phys. Rev. **73**, 416 (1948).

[182] P. Kusch and H. M. Foley, Phys. Rev. **74**, 250 (1948).

[183] T. Aoyama, M. Hayakawa, T. Kinoshita, and M. Nio, Phys. Rev. Lett. **109**, 111807 (2012).

[184] P. J. Mohr, D. B. Newell, and B. N. Taylor, J. Phys. Chem. Ref. Data **45**, 043102 (2016).

[185] J. Sakurai and J. Napolitano, *Modern Quantum Mechanics* (Cambridge University Press, 2017).

[186] D. J. Griffiths and D. Schroeter, *Introduction to Quantum Mechanics* (Cambridge University Press, 2018).

[187] R. P. Feynman, R. B. Leighton, and M. Sands, *The Feynman Lectures on Physics. Volume II: Mainly Electromagnetism and Matter* (New York: Basic Books, 2011).

[188] A. G. Gurevich and G. A. Melkov, *Magnetization Oscillations and Waves* (CRC Press, 1996).

[189] C. A. Akosa, *Spin Transport in Ferromagnetic and Antiferromagnetic Textures* (PhD Thesis, King Abdullah University of Science and Technology, Kingdom of Saudi Arabia, 2016).

[190] R. Wieser, Eur. Phys. J. B **88**, 1 (2015).

[191] J.-P. Gazeau, *Coherent States in Quantum Physics* (Wiley-VCH, Berlin, 2009).

[192] S. Sachdev, *Quantum Phase Transitions* (Cambridge University Press, 2011).

[193] A. Messiah, *Quantum Mechanics* (North-Holland, Amsterdam, 1961).

[194] L. D. Landau and E. M. Lifshitz, *Quantum Mechanics, Non-Relativistic Theory* (Pergamon Press, New York, 1977).

[195] D. Bauer, *Atomistic Spin-Dynamics in Confined Magnetic Nanostructures* (PhD Thesis, Institut für Festkörperforschung, Forschungszentrum Jülich, Germany, 2008).

[196] M. Exler, *On Classical and Quantum Mechanical Energy Spectra of Finite Heisenberg Spin Systems* (PhD Thesis, Universität Osnabrück, Germany, 2016).

[197] D. J. Griffiths, *Introduction to Electrodynamics* (Cambridge University Press, 2017).

[198] A. Zangwill, *Modern Electrodynamics* (Cambridge University Press, 2013).

[199] J. D. Jackson, *Classical Electrodynamics* (John Wiley & Sons, 1998).

[200] J. A. Fernández-Roldán, *Micromagnetism of Cylindrical Nanowires with Compositional and Geometric Modulations* (PhD Thesis, Autonomous University of Madrid, Spain, 2019).

[201] S. Jenkins, *Spin Dynamics Simulations of Iridium Manganese Alloys* (PhD Thesis, University of York, United Kingdom, 2020).

[202] A. Auerbach, *Interacting Electrons and Quantum Magnetism* (Springer, New York, NY, 1994).

[203] R. Skomski, *Simple Models of Magnetism* (Oxford Graduate Texts, 2008).

[204] W. Nolting and A. Ramakanth, *Quantum Theory of Magnetism* (Springer-Verlag Berlin, Heidelberg, 2009).

[205] M. Voto, *Advanced Modelling of Domain Wall Dynamics for Spintronic Devices* (PhD Thesis, University of Salamanca, Spain, 2017).

[206] A. Aharoni, *Introduction to the Theory of Ferromagnetism* (Oxford Science Publications, 2001).

[207] R. C. O'Handley, *Modern Magnetic Materials: Principles and Applications* (John Wiley & Sons, 1999).

[208] G. Bertotti, I. D. Mayergoyz, and C. Serpico, *Nonlinear Magnetization Dynamics in Nanosystems* (Elsevier Science, 2009).

[209] M. Lakshmanan, Philos. Trans. Royal Soc. A **369**, 1280 (2011).

[210] F. García-Sánchez, *Modeling of Field and Thermal Magnetization Reversal in Nanostructured Magnetic Materials* (PhD Thesis, Autonomous University of Madrid, Spain, 2007).

[211] J. Miltat, G. Albuquerque, and A. Thiaville, *An Introduction to Micromagnetics in the Dynamic Regime* in *Spin Dynamics in Confined Magnetic Structures I* (Springer-Verlag Berlin, Heidelberg, 2002).

[212] T. L. Gilbert, Phys. Rev. **100**, 1243 (1955).

[213] T. L. Gilbert, IEEE Trans. Magn. **40**, 3443 (2004).

[214] W. F. Brown, *Micromagnetics* (Wiley, New York, 1963).

[215] A. Thiaville and Y. Nakatani, *Domain Wall Dynamics in Nanowires and Nanostrips* in *Spin Dynamics in Confined Magnetic Structures III* (Springer Berlin, Heidelberg, 2006).

[216] U. Atxitia, *Modeling of Ultrafast Laser-Induced Magnetization Dynamics within the Landau-Lifshitz-Bloch Approach* (PhD Thesis, Autonomous University of Madrid, Spain, 2012).

[217] E. Beaurepaire, J.-C. Merle, A. Daunois, and J.-Y. Bigot, Phys. Rev. Lett. **76**, 4250 (1996).

[218] O. Chubykalo-Fesenko, U. Nowak, R. W. Chantrell, and D. Garanin, Phys. Rev. B **74**, 094436 (2006).

[219] D. A. Garanin, Phys. Rev. B **55**, 3050 (1997).

[220] U. Atxitia, D. Hinzke, and U. Nowak, J. Phys. D Appl. Phys. **50**, 033003 (2016).

[221] O. Chubykalo-Fesenko and P. Nieves, *Landau-Lifshitz-Bloch Approach for Magnetization Dynamics Close to Phase Transition* in *Handbook of Materials Modeling. Methods: Theory and Modeling* (Springer Cham, 2020).

[222] W. F. Brown Jr, Phys. Rev. **130**, 1677 (1963).

[223] A. Lyberatos and R. W. Chantrell, J. Appl. Phys. **73**, 6501 (1993).

[224] C. Gardiner, *Stochastic Methods. A Handbook for the Natural and Social Sciences* (Springer Berlin, Heidelberg, 2009).

[225] H. B. Callen and E. Callen, J. Phys. Chem. Solids **27**, 1271 (1966).

[226] N. Kazantseva, D. Hinzke, U. Nowak, R. W. Chantrell, U. Atxitia, and O. Chubykalo-Fesenko, Phys. Rev. B **77**, 184428 (2008).

[227] P. G. Drazin and R. S. Johnson, *Solitons: An Introduction* (Cambridge University Press, 1989).

[228] C. Rebbi, Sci. Am. **240**, 92 (1979).

[229] M. Remoissenet, *Waves Called Solitons: Concepts and Experiments* (Springer, 1999).

[230] R. Rajaraman, *Solitons and Instantons. An Introduction to Solitons and Instantons in Quantum Field Theory* (North-Holland, Amsterdam, 1982).

[231] D. Chua, *Classical and Quantum Solitons* (Lecture Notes by N. S. Manton and D. Stuart, 2017).

[232] H. Năstase, *Classical Field Theory* (Cambridge University Press, 2019).

[233] J. A. Dror, *Solitons and Instantons* (Lecture Notes by C. Csaki, University of Cornell, The United States of America, 2013).

[234] N. Manton and P. Sutcliffe, *Topological Solitons* (Cambridge University Press, 2004).

[235] S. Coleman, *Aspects of Symmetry. Selected Erice Lectures* (Cambridge University Press, 1985).

[236] H. B. Braun, *Solitons in Real Space: Domain Walls, Vortices, Hedgehogs, and Skyrmions* in *Topology in Magnetism* (Springer Cham, 2018).

[237] O. Fruchart, *Lecture Notes on Nanomagnetism* (Institut Néel, France, 2012).

[238] T. Lancaster and S. J. Blundell, *Quantum Field Theory for the Gifted Amateur* (Oxford University Press, 2014).

[239] E. Fradkin, *Field Theories of Condensed Matter Physics* (Cambridge University Press, 2013).

[240] A. S. T. Pires, *A Brief Introduction to Topology and Differential Geometry in Condensed Matter Physics* (Morgan & Claypool Publishers, 2019).

[241] A. M. Kosevich, B. A. Ivanov, and A. S. Kovalev, Phys. Rep. **194**, 117 (1990).

[242] E. A. Turov, A. V. Kolchanov, V. V. Men'shenin, I. F. Mirsaev, and V. V. Nikolaev, *Symmetry and Physical Properties of Antiferromagnets* (Cambridge International Science Publishing, Cambridge, 2010).

[243] N. Papanicolaou, Phys. Rev. B **51**, 15062 (1995).

[244] A. M. Srivastava, *Topological Defects in Condensed Matter Physics* in *Field Theories in Condensed Matter Physics* (CRC Press, 2001).

[245] A. Zee, *Quantum Field Theory in a Nutshell* (Princeton University Press, 2010).

[246] D. Tong, *Quantum Field Theory, Lecture Notes* (University of Cambridge, United Kingdom, 2006).

[247] E. J. Weinberg, *Classical Solutions in Quantum Field Theory: Solitons and Instantons in High Energy Physics* (Cambridge University Press, 2012).

[248] V. G. Matyas, Notes on *Field Theory of Topological Defects. An Introduction to Solitons and Cosmology* (University of Liverpool, United Kingdom, 2017).

[249] K. Y. Guslienko, J. Nanosci. Nanotechnol. **8**, 2745 (2008).

[250] R. Antos and Y. Otani, *The Dynamics of Magnetic Vortices and Skyrmions* in *Spin Current* (Oxford Academic, 2017).

[251] S. Mühlbauer, B. Binz, F. Jonietz, C. Pfleiderer, A. Rosch, A. Neubauer, R. Georgii, and P. Böni, Science **323**, 915 (2009).

[252] Y.-f. Chen, Z.-x. Li, Z.-w. Zhou, Q.-l. Xia, Y.-z. Nie, and G.-h. Guo, J. Magn. Magn. Mater. **458**, 123 (2018).

[253] Y. Ishikawa, K. Tajima, D. Bloch, and M. Roth, Solid State Commun. **19**, 525 (1976).

[254] X. Z. Yu, N. Kanazawa, Y. Onose, K. Kimoto, W. Z. Zhang, S. Ishiwata, Y. Matsui, and Y. Tokura, Nat. Mater. **10**, 106 (2011).

[255] Z. V. Gareeva and K. Y. Guslienko, J. Phys. Commun. **2**, 035009 (2018).

[256] Y. Z. Wu, C. Won, A. Scholl, A. Doran, H. W. Zhao, X. F. Jin, and Z. Q. Qiu, Phys. Rev. Lett. **93**, 117205 (2004).

[257] J. Wu, J. Choi, C. Won, Y. Z. Wu, A. Scholl, A. Doran, C. Hwang, and Z. Q. Qiu, Phys. Rev. B **79**, 014429 (2009).

[258] S. Heinze, K. Von Bergmann, M. Menzel, J. Brede, A. Kubetzka, R. Wiesendanger, G. Bihlmayer, and S. Blügel, Nat. Phys. **7**, 713 (2011).

[259] Y. S. Lin, P. J. Grundy, and E. A. Giess, Appl. Phys. Lett. **23**, 485 (1973).

[260] S. Takao, J. Magn. Magn. Mater. **31**, 1009 (1983).

[261] G. Chen, *Magnetic Skyrmions in Thin Films* in *Topology in Magnetism* (Springer International Publishing, 2018).

[262] J. Wu, D. Carlton, J. S. Park, Y. Meng, E. Arenholz, A. Doran, A. T. Young, A. Scholl, C. Hwang, H. W. Zhao, *et al.*, Nat. Phys. **7**, 303 (2011).

[263] J. Sort, K. S. Buchanan, V. Novosad, A. Hoffmann, G. Salazar-Alvarez, A. Bollero, M. D. Baró, B. Dieny, and J. Nogués, Phys. Rev. Lett. **97**, 067201 (2006).

[264] N. Nagaosa and Y. Tokura, Nat. Nanotechnol. **8**, 899 (2013).

[265] B. Göbel, I. Mertig, and O. A. Tretiakov, Phys. Rep. **895**, 1 (2021).

[266] K. Y. Guslienko, J. Magn. **24**, 549 (2019).

[267] B. Pigeau, *Magnetic Vortex Dynamics Nanostructures* (PhD Thesis, Paris-Sud University, France, 2012).

[268] I. Kézsmárki, S. Bordács, P. Milde, E. Neuber, L. M. Eng, J. S. White, H. M. Rønnow, C. D. Dewhurst, M. Mochizuki, K. Yanai, *et al.*, Nat. Mater. **14**, 1116 (2015).

[269] H. Goldstein, C. P. Poole, and J. L. Safko, *Classical Mechanics* (Addison-Wesley, 2001).

[270] A. Deriglazov, *Classical Mechanics: Hamiltonian and Lagrangian Formalism* (Springer, 2010).

[271] R. Shankar, *Principles of Quantum Mechanics* (Springer, New York, NY, 1994).

[272] H.-B. Braun and D. Loss, Phys. Rev. B **53**, 3237 (1996).

[273] A. Altland and B. D. Simons, *Condensed Matter Field Theory* (Cambridge University Press, 2010).

[274] R. A. Duine, *Spintronics, Lecture Notes* (Utrecht University, The Netherlands, 2010).

[275] J. H. Han, *Skyrmions in Condensed Matter* (Springer, 2017).

[276] T. Lulek, W. Florek, and S. Walcerz, *Symmetry and Structural Properties of Condensed Matter. Proceedings of the 3rd International School on Theoretical Physics* (World Scientific, 1995).

[277] H.-J. Mikeska and A. K. Kolezhuk, *One-Dimensional Magnetism* in *Quantum Magnetism* (Springer Berlin, Heidelberg, 2008).

[278] R. Cheng, *Aspects of Antiferromagnetic Spintronics* (PhD Thesis, The University of Texas, The United States of America, 2014).

[279] J. M. Radcliffe, J. Phys. A **4**, 313 (1971).

[280] H. Shapourian and D. Sadri, Phys. Rev. A **93**, 013845 (2016).

[281] D. Vanderbilt, *Berry Phases in Electronic Structure Theory. Electric Polarization, Orbital Magnetization, and Topological Insulators* (Cambridge University Press, 2018).

[282] P. Coleman, *Introduction to Many-Body Physics* (Cambridge University Press, 2015).

[283] D. Tong, *Statistical Field Theory, Lecture Notes* (University of Cambridge, United Kingdom, 2017).

[284] M. V. Berry, Proc. R. Soc. A: Math. Phys. Eng. Sci. **392**, 45 (1984).

[285] S. K. Kim and O. Tchernyshyov, arXiv preprint arXiv:2208.12799 (2022).

[286] W. Döring, Z. Naturforsch. **3** (1948).

[287] J. C. Slonczewski, J. Appl. Phys. **44**, 1759 (1973).

[288] O. A. Tretiakov, D. Clarke, G.-W. Chern, Y. B. Bazaliy, and O. Tchernyshyov, Phys. Rev. Lett. **100**, 127204 (2008).

[289] S. Moretti, *Micromagnetic Study of Magnetic Domain Wall motion: Thermal Effects and Spin Torques* (PhD Thesis, University of Salamanca, Spain, 2017).

[290] J. C. Slonczewski, AIP Conf. Proc. **5**, 170 (1972).

[291] G. Tatara and R. M. Otxoa, Phys. Rev. B **101**, 224425 (2020).

[292] O. Tchernyshyov, Ann. Phys. **363**, 98 (2015).

[293] G. Tatara, H. Kohno, and J. Shibata, Phys. Rep. **468**, 213 (2008).

[294] A. Thiaville, Y. Nakatani, J. Miltat, and N. Vernier, J. Appl. Phys. **95**, 7049 (2004).

[295] A. P. Malozemoff and J. C. Slonczewski, Phys. Rev. Lett. **29**, 952 (1972).

[296] A. A. Thiele, Phys. Rev. Lett. **30**, 230 (1973).

[297] V. L. Sobolev, H. L. Huang, and S. C. Chen, J. Magn. Magn. Mat. **147**, 284 (1995).

[298] A. Mougin, M. Cormier, J. P. Adam, P. J. Metaxas, and J. Ferré, Europhys. Lett. **78**, 57007 (2007).

[299] J. Hütner, T. Herranen, and L. Laurson, Phys. Rev. B **99**, 174427 (2019).

[300] A. P. Malozemoff and J. C. Slonczewski, *Magnetic Domain Walls in Bubble Materials* (Academic Press, New York, 1979).

[301] V. Baltz, A. Manchon, M. Tsoi, T. Moriyama, T. Ono, and Y. Tserkovnyak, Rev. Mod. Phys. **90**, 015005 (2018).

[302] A. V. Kimel, A. M. Kalashnikova, A. Pogrebna, and A. K. Zvezdin, Phys. Rep. **852**, 1 (2020).

[303] A. F. Andreev and V. I. Marchenko, Sov. Phys. Uspekhi **23**, 21 (1980).

[304] E. G. Galkina and B. A. Ivanov, Low Temp. Phys. **44**, 618 (2018).

[305] A. Kamra, R. E. Troncoso, W. Belzig, and A. Brataas, Phys. Rev. B **98**, 184402 (2018).

[306] S. K. Kim, Y. Tserkovnyak, and O. Tchernyshyov, Phys. Rev. B **90**, 104406 (2014).

[307] E. G. Tveten, A. Qaiumzadeh, O. A. Tretiakov, and A. Brataas, Phys. Rev. Lett. **110**, 127208 (2013).

[308] W. Yu, J. Lan, J. Xiao, *et al.*, Phys. Rev. B **98**, 144422 (2018).

[309] Z. Y. Chen, M. H. Qin, and J.-M. Liu, Phys. Rev. B **100**, 020402 (2019).

[310] B. Göbel, *Emergent Electrodynamics in Non-Collinear Spin Textures* (PhD Thesis, Martin Luther University of Halle-Wittenberg, Germany, 2020).

[311] A. Thiaville and J. Miltat, *Topology and Magnetic Domain Walls* in *Topology in Magnetism* (Springer, Cham, 2018).

[312] K. Everschor-Sitte and M. Sitte, J. Appl. Phys. **115**, 172602 (2014).

[313] A. Thiaville, J. Miltat, and S. Rohart, *Magnetism and Topology* in *Magnetic Skyrmions and Their Applications* (Woodhead Publishing, 2021).

[314] X. J. Liu, L. Guo, H. Wang, and Z. K. Tang, AIP Adv. **10**, 075222 (2020).

[315] J. Barker and O. A. Tretiakov, Phys. Rev. Lett. **116**, 147203 (2016).

[316] X. Zhang, Y. Zhou, and M. Ezawa, Sci. Rep. **6**, 24795 (2016).

[317] M. O. A. Ellis, R. F. L. Evans, T. A. Ostler, J. Barker, U. Atxitia, O. Chubykalo-Fesenko, and R. W. Chantrell, Low Temp. Phys. **41**, 705 (2015).

[318] R. F. L. Evans, *Atomistic Spin Dynamics* in *Handbook of Materials Modeling. Applications: Current and Emerging Materials* (Springer Cham, 2020).

[319] J. Fidler and T. Schrefl, J. Phys. D Appl. Phys. **33**, R135 (2000).

[320] U. Atxitia, P. Nieves, and O. Chubykalo-Fesenko, Phys. Rev. B **86**, 104414 (2012).

[321] C. D. Stanciu, F. Hansteen, A. V. Kimel, A. Kirilyuk, A. Tsukamoto, A. Itoh, and T. Rasing, Phys. Rev. Lett. **99**, 047601 (2007).

[322] G. Grinstein and R. H. Koch, Phys. Rev. Lett. **90**, 207201 (2003).

[323] U. Nowak, *Classical Spin Models* in *Handbook of Magnetism and Advanced Magnetic Materials* (John Wiley & Sons, 2007).

[324] J. Leliaert and J. Mulkers, J. Appl. Phys. **125**, 180901 (2019).

[325] G. Chen, Nat. Phys. **13**, 112 (2017).

[326] J. M. Garcıa, A. Thiaville, J. Miltat, K. J. Kirk, J. N. Chapman, and F. Alouges, Appl. Phys. Lett. **79**, 656 (2001).

[327] A. Berger and H. P. Oepen, Phys. Rev. B **45**, 12596 (1992).

[328] M. Laufenberg, D. Backes, W. Bührer, D. Bedau, M. Kläui, U. Rüdiger, C. A. F. Vaz, J. A. C. Bland, L. J. Heyderman, F. Nolting, *et al.*, Appl. Phys. Lett. **88**, 052507 (2006).

[329] D. Navas, C. Redondo, G. A. B. Confalonieri, F. Batallan, A. Devishvili, O. Iglesias-Freire, A. Asenjo, C. A. Ross, and B. P. Toperverg, Phys. Rev. B **90**, 054425 (2014).

[330] S.-W. Cheong, M. Fiebig, W. Wu, L. Chapon, and V. Kiryukhin, npj Quantum Mater. **5**, 3 (2020).

[331] S. A. Siddiqui, J. Sklenar, K. Kang, M. J. Gilbert, A. Schleife, N. Mason, and A. Hoffmann, J. Appl. Phys. **128**, 040904 (2020).

[332] W. Wang, J. A. Mundy, C. M. Brooks, J. A. Moyer, M. E. Holtz, D. A. Muller, D. G. Schlom, and W. Wu, Phys. Rev. B **95**, 134443 (2017).

[333] Y. Shiratsuchi, S. Watanabe, S. Yonemura, T. Shibata, and R. Nakatani, AIP Adv. **8**, 125313 (2018).

[334] S. P. Bommanaboyena, D. Backes, L. S. I. Veiga, S. S. Dhesi, Y. R. Niu, B. Sarpi, T. Denneulin, A. Kovács, T. Mashoff, O. Gomonay, *et al.*, Nat. Commun. **12**, 6539 (2021).

[335] W. Roth, J. Appl. Phys. **31**, 2000 (1960).

[336] J. Baruchel, M. Schlenker, and W. L. Roth, J. Appl. Phys. **48**, 5 (1977).

[337] S. Saito, M. Miura, and K. Kurosawa, J. Phys. C **13**, 1513 (1980).

[338] A. Sapozhnik, ***Magnetic Properties of Antiferromagnetic Mn2Au: Exchange Interaction and Domain Manipulation*** (PhD Thesis, Johannes Gutenberg-Universität Mainz, Germany, 2018).

[339] A. Scholl, J. Stohr, J. Luning, J. W. Seo, J. Fompeyrine, H. Siegwart, J.-P. Locquet, F. Nolting, S. Anders, E. E. Fullerton, *et al.*, Science **287**, 1014 (2000).

[340] M. J. Grzybowski, P. Wadley, K. W. Edmonds, R. Beardsley, V. Hills, R. P. Campion, B. L. Gallagher, J. S. Chauhan, V. Novak, T. Jungwirth, *et al.*, Phys. Rev. Lett. **118**, 057701 (2017).

[341] S. Anders, A. Scholl, F. Nolting, H. A. Padmore, J. Lüning, J. Stöhr, and M. Scheinfein, AIP Conf. Proc. **521**, 7 (2000).

[342] A. Scholl, Curr. Opin. Solid State Mater. Sci. **7**, 59 (2003).

[343] H. Hopster and H. P. Oepen, *Magnetic Microscopy of Nanostructures* (Springer Berlin, Heidelberg, 2005).

[344] H. S. Nalwa, *Handbook of Surfaces and Interfaces of Materials* (Academic Press, 2001).

[345] S. Y. Bodnar, M. Filianina, S. P. Bommanaboyena, T. Forrest, F. Maccherozzi, A. A. Sapozhnik, Y. Skourski, M. Kläui, and M. Jourdan, Phys. Rev. B **99**, 140409 (2019).

[346] S. Bodnar, ***Manipulation of Néel Vector in Antiferromagnetic Mn_2Au by Electric Current and Magnetic Field Pulses*** (PhD Thesis, Johannes Gutenberg-Universität Mainz, Germany, 2020).

[347] L. Šmejkal, R. González-Hernández, T. Jungwirth, and J. Sinova, Sci. Adv. **6**, eaaz8809 (2020).

[348] S.-W. Cheong, npj Quantum Mater. **4**, 53 (2019).

[349] P. Němec, M. Fiebig, T. Kampfrath, and A. V. Kimel, Nat. Phys. **14**, 229 (2018).

[350] M. Fiebig, D. Fröhlich, G. Sluyterman v. L, and R. V. Pisarev, Appl. Phys. Lett. **66**, 2906 (1995).

[351] M. Fiebig, T. Lottermoser, D. Fröhlich, A. V. Goltsev, and R. V. Pisarev, Nature **419**, 818 (2002).

[352] J. Fischer, *Imaging and Tailoring Electric and Antiferromagnetic Textures in Multiferroic Thin Films of BiFeO* (PhD Thesis, Université Paris-Saclay, France, 2020).

[353] M. S. Wörnle, P. Welter, Z. Kašpar, K. Olejník, V. Novák, R. P. Campion, P. Wadley, T. Jungwirth, C. L. Degen, and P. Gambardella, arXiv preprint arXiv:1912.05287 (2019).

[354] T. Kosub, M. Kopte, R. Hühne, P. Appel, B. Shields, P. Maletinsky, R. Hübner, M. O. Liedke, J. Fassbender, O. G. Schmidt, *et al.*, Nat. Commun. **8**, 13985 (2017).

[355] A. Haykal, J. Fischer, W. Akhtar, J.-Y. Chauleau, D. Sando, A. Finco, F. Godel, Y. A. Birkhölzer, C. Carrétéro, N. Jaouen, *et al.*, Nat. Commun. **11**, 1704 (2020).

[356] S. H. Chew, *Photoemission Electron Microscopy for Nanoscale Imaging and Attosecond Control of Light-Matter Interaction at Metal Surfaces* (Dissertation, Ludwig-Maximilians-Universität, Germany, 2018).

[357] A. Scholl, *Thin-Film Magnetism: PEEM Studies* in *Encyclopedia of Materials: Science and Technology* (Elsevier, 2002).

[358] R. A. Duine, P. M. Haney, A. S. Núñez, and A. H. MacDonald, Phys. Rev. B **75**, 014433 (2007).

[359] Y. Wang, C. Song, G. Wang, J. Miao, F. Zeng, and F. Pan, Adv. Funct. Mater. **24**, 6806 (2014).

[360] J. Železný, ***Electronic Structure and Magnetic Properties of Antiferromagnetic Semiconductors and Metals*** (PhD Thesis, Institute of Physics of the Czech Academy of Sciences, Czech Republic, 2016).

[361] J.-H. Zheng, A. Brataas, M. Kläui, and A. Qaiumzadeh, Phys. Rev. B **102**, 184413 (2020).

[362] S. Geprägs, M. Opel, J. Fischer, O. Gomonay, P. Schwenke, M. Althammer, H. Huebl, and R. Gross, J. Appl. Phys. **127**, 243902 (2020).

[363] C. C. Chiang, S. Y. Huang, D. Qu, P. H. Wu, and C. L. Chien, Phys. Rev. Lett. **123**, 227203 (2019).

[364] P. Zhang, J. Finley, T. Safi, and L. Liu, Phys. Rev. Lett. **123**, 247206 (2019).

[365] A. Churikova, D. Bono, B. Neltner, A. Wittmann, L. Scipioni, A. Shepard, T. Newhouse-Illige, J. Greer, and G. S. D. Beach, Appl. Phys. Lett. **116**, 022410 (2020).

[366] Y. Cheng, S. Yu, M. Zhu, J. Hwang, and F. Yang, Phys. Rev. Lett. **124**, 027202 (2020).

[367] J. McCord, J. Phys. D Appl. Phys. **48**, 333001 (2015).

[368] M. Bertocchi, *First Principles Second-Harmonic Generation in Quantum Confined Silicon-Based Systems* (PhD Thesis, École Polytechnique, France, 2013).

[369] Q.-C. Sun, T. Song, E. Anderson, A. Brunner, J. Förster, T. Shalomayeva, T. Taniguchi, K. Watanabe, J. Gräfe, R. Stöhr, *et al.*, Nat. Commun. **12**, 1989 (2021).

[370] R. Wieser, E. Vedmedenko, and R. Wiesendanger, Phys. Rev. B **81**, 024405 (2010).

[371] G. Tatara, C. A. Akosa, and R. M. Otxoa, Phys. Rev. Res. **2**, 043226 (2020).

[372] B. A. Ivanov and A. K. Kolezhuk, Phys. Rev. Lett. **74**, 1859 (1995).

[373] E. Schlömann, Appl. Phys. Lett. **19**, 274 (1971).

[374] V. Eleonskii, N. Kirova, and N. Kulagin, Sov. Phys. JETP **47**, 946 (1978).

[375] V. Eleonskii, N. Kirova, and N. Kulagin, Sov. Phys. JETP **44**, 1239 (1976).

[376] E. Magyari and H. Thomas, Phys. Rev. B **29**, 6358 (1984).

[377] G. E. Khodenkov, Tech. Phys. Lett. **29**, 907 (2003).

[378] D. Hill, S. K. Kim, and Y. Tserkovnyak, Phys. Rev. Lett. **121**, 037202 (2018).

[379] E. K. Sklyanin, LOMI Prepint E3, Leningrad (1979).

[380] Y. S. Kivshar and B. A. Malomed, Rev. Mod. Phys. **61**, 763 (1989).

[381] U. Enz, Helv. Phys. Acta **37**, 245 (1964).

[382] H. J. Mikeska, J. Appl. Phys. **52**, 1950 (1981).

[383] R. K. Dodd, H. C. Morris, J. Eilbeck, and J. Gibbon, *Solitons and Nonlinear Wave Equations* (Academic Press, 1982).

[384] B. A. Ivanov and A. K. Kolezhuk, Fiz. Nizk. Temp. **21**, 355 (1995).

[385] S. M. Rezende, A. Azevedo, and R. L. Rodríguez-Suárez, J. Appl. Phys. **126**, 151101 (2019).

[386] S. Khmelevskyi and P. Mohn, Appl. Phys. Lett. **93**, 162503 (2008).

[387] V. M. T. S. Barthem, C. V. Colin, H. Mayaffre, M.-H. Julien, and D. Givord, Nat. Commun. **4**, 2892 (2013).

[388] V. G. Bar'yakhtar, M. V. Chetkin, B. A. Ivanov, and S. N. Gadetskii, *Dynamics of Topological Magnetic Solitons: Experiment and Theory* (Springer-Verlag Berlin, Heidelberg, 1994).

[389] H. Y. Yuan, W. Wang, M.-H. Yung, and X. R. Wang, Phys. Rev. B **97**, 214434 (2018).

[390] F. Chen, Z. Zhang, W. Luo, X. Yang, L. You, and Y. Zhang, J. Magn. Magn. Mat. **511**, 166995 (2020).

[391] S. Selzer, U. Atxitia, U. Ritzmann, D. Hinzke, and U. Nowak, Phys. Rev. Lett. **117**, 107201 (2016).

[392] X. F. Zhou, J. Zhang, F. Li, X. Z. Chen, G. Y. Shi, Y. Z. Tan, Y. D. Gu, M. S. Saleem, H. Q. Wu, F. Pan, *et al.*, Phys. Rev. Appl. **9**, 054028 (2018).

[393] S. Y. Bodnar, Y. Skourski, O. Gomonay, J. Sinova, M. Kläui, and M. Jourdan, Phys. Rev. Appl. **14**, 014004 (2020).

[394] V. M. T. S. Barthem, C. V. Colin, R. Haettel, D. Dufeu, and D. Givord, J. Magn. Magn. Mat. **406**, 289 (2016).

[395] A. A. Sapozhnik, M. Filianina, S. Y. Bodnar, A. Lamirand, M.-A. Mawass, Y. Skourski, H.-J. Elmers, H. Zabel, M. Kläui, and M. Jourdan, Phys. Rev. B **97**, 134429 (2018).

[396] R. Masrour, E. K. Hlil, M. Hamedoun, A. Benyoussef, A. Boutahar, and H. Lassri, J. Magn. Magn. Mat. **393**, 600 (2015).

[397] P. Wells and J. H. Smith, Acta Crystallogr. Sect. A **26**, 379 (1970).

[398] E. M. Lifshitz and L. P. Pitaevskii, *Statistical Physics, Course of Theoretical Physics, Vol. 9* (Pergamon Press, Oxford, 1980).

[399] A. K. Zvezdin and V. V. Kostyuchenko, J. Exp. Theor. Phys. **89**, 734 (1999).

[400] M. Arana, F. Estrada, D. S. Maior, J. B. S. Mendes, L. E. Fernández-Outón, W. A. A. Macedo, V. M. T. S. Barthem, D. Givord, A. Azevedo, and S. M. Rezende, Appl. Phys. Lett. **111**, 192409 (2017).

[401] I. V. Bar'yakhtar and B. A. Ivanov, Solid State Commun. **34**, 545 (1980).

[402] O. Gomonay, T. Jungwirth, and J. Sinova, Phys. Rev. B **98**, 104430 (2018).

[403] P. M. Chaikin and T. C. Lubensky, *Principles of Condensed Matter Physics* (Cambridge University Press, 1995).

[404] P. W. Anderson and W. Brinkman, Phys. Rev. Lett. **30**, 1108 (1973).

[405] D. Levine, T. C. Lubensky, S. Ostlund, S. Ramaswamy, P. J. Steinhardt, and J. Toner, Phys. Rev. Lett. **54**, 1520 (1985).

[406] J. E. S. Socolar, T. C. Lubensky, and P. J. Steinhardt, Phys. Rev. B **34**, 3345 (1986).

[407] J. M. Kosterlitz and D. J. Thouless, J. Phys. C: Solid State Phys. **5**, L124 (1972).

[408] J. Weertman, J. R. Weertman, J. Friedel, and R. G. Rhodes, Am. J. Phys. **33**, 1091 (1965).

[409] P. M. Anderson, J. P. Hirth, and J. Lothe, *Theory of Dislocations* (Cambridge University Press, 2017).

[410] J. D. Eshelby, Proc. Phys. Soc.: Sect. A **62**, 307 (1949).

[411] P. Gumbsch and H. Gao, Science **283**, 965 (1999).

[412] Q. Li and S.-Q. Shi, Appl. Phys. Lett. **80**, 3069 (2002).

[413] J. A. Y. Vandersall and B. D. Wirth, Philos. Mag. **84**, 3755 (2004).

[414] R. Rama-Eiroa, P. E. Roy, J. González, K. Y. Guslienko, J. Wunderlich, and R. M. Otxoa, J. Magn. Magn. Mat. **560**, 169566 (2022).

[415] K. Y. Guslienko, K.-S. Lee, and S.-K. Kim, Phys. Rev. Lett. **100**, 027203 (2008).

[416] S. Petit-Watelot, J.-V. Kim, A. Ruotolo, R. M. Otxoa, K. Bouzehouane, J. Grollier, A. Vansteenkiste, B. Van de Wiele, V. Cros, and T. Devolder, Nat. Phys. **8**, 682 (2012).

[417] J. R. Klauder, Phys. Rev. D **19**, 2349 (1979).

[418] M. Stone, Phys. Rev. B **53**, 16573 (1996).

[419] I. S. Gradshteyn and I. M. Ryzhik, *Table of Integrals, Series, and Products* (Academic Press, 2007).

[420] E. G. Tveten, A. Qaiumzadeh, and A. Brataas, Phys. Rev. Lett. **112**, 147204 (2014).

[421] S. Peng, Y. Wei, Z. Jin, and W. Yang, Phys. Rev. Lett. **122**, 045501 (2019).

[422] V. Nosenko, S. Zhdanov, and G. Morfill, Phys. Rev. Lett. **99**, 025002 (2007).

[423] N. Tesla, Electron. Rev. **29**, 13 (1896).

[424] M. Yan, A. Kákay, C. Andreas, and R. Hertel, Phys. Rev. B **88**, 220412 (2013).

[425] T. Matalla-Wagner, J.-M. Schmalhorst, G. Reiss, N. Tamura, and M. Meinert, Phys. Rev. Res. **2**, 033077 (2020).

[426] Y. Lytvynenko, S. Reimers, Y. Niu, E. Golias, B. Sarpi, L. Ishibe-Veiga, T. Denneulin, A. Kovacs, R. Dunin-Borkowski, M. Kläui, *et al.*, arXiv preprint arXiv:2208.04048 (2022).

[427] S. Selzer, L. Salemi, A. Deák, E. Simon, L. Szunyogh, P. M. Oppeneer, and U. Nowak, Phys. Rev. B **105**, 174416 (2022).

[428] M. Armand and J.-M. Tarascon, Nature **451**, 652 (2008).

[429] D. A. Allwood, G. Xiong, M. D. Cooke, C. C. Faulkner, D. Atkinson, N. Vernier, and R. P. Cowburn, Science **296**, 2003 (2002).

[430] E. Y. Vedmedenko and D. Altwein, Phys. Rev. Lett. **112**, 017206 (2014).

[431] Y. Tserkovnyak and J. Xiao, Phys. Rev. Lett. **121**, 127701 (2018).

[432] D. Jones, J. Zou, S. Zhang, and Y. Tserkovnyak, Phys. Rev. B **102**, 140411 (2020).

[433] D. Atkinson, D. A. Allwood, G. Xiong, M. D. Cooke, C. C. Faulkner, and R. P. Cowburn, Nat. Mater. **2**, 85 (2003).

[434] P. J. Metaxas, J. Sampaio, A. Chanthbouala, R. Matsumoto, A. Anane, A. Fert, K. A. Zvezdin, K. Yakushiji, H. Kubota, A. Fukushima, *et al.*, Sci. Rep. **3**, 1829 (2013).

[435] S. Vélez, J. Schaab, M. S. Wörnle, M. Müller, E. Gradauskaite, P. Welter, C. Gutgsell, C. Nistor, C. L. Degen, M. Trassin, *et al.*, Nat. Commun. **10**, 4750 (2019).

[436] M. Bode, E. Y. Vedmedenko, K. Von Bergmann, A. Kubetzka, P. Ferriani, S. Heinze, and R. Wiesendanger, Nat. Mater. **5**, 477 (2006).

[437] S. K. Kim, S. Takei, and Y. Tserkovnyak, Phys. Rev. B **92**, 220409 (2015).

[438] A. Ghosh, K. S. Huang, and O. Tchernyshyov, Phys. Rev. B **95**, 180408 (2017).

[439] D. Ortega and Q. A. Pankhurst, *Magnetic Hyperthermia* in *Nanoscience. Vol. 1: Nanostructures through Chemistry* (RSC Publishing, 2013).

[440] M. H. Kryder, E. C. Gage, T. W. McDaniel, W. A. Challener, R. E. Rottmayer, G. Ju, Y.-T. Hsia, and M. F. Erden, Proc. IEEE **96**, 1810 (2008).

[441] C. Kittel, *Introduction to Solid State Physics* (John Wiley & Sons, 2004).

[442] N. Bhattacharjee, A. A. Sapozhnik, S. Y. Bodnar, V. Y. Grigorev, S. Y. Agustsson, J. Cao, D. Dominko, M. Obergfell, O. Gomonay, J. Sinova, *et al.*, Phys. Rev. Lett. **120**, 237201 (2018).

[443] O. Gomonay, K. Yamamoto, and J. Sinova, J. Phys. D Appl. Phys. **51**, 264004 (2018).

[444] D. Pines, *Elementary Excitations in Solids. Lectures on Protons, Electrons, and Plasmons* (CRC Press, 1999).

[445] J. Bardeen and D. Pines, Phys. Rev. **99**, 1140 (1955).

[446] P. B. Allen, Phys. Rev. Lett. **59**, 1460 (1987).

[447] M. I. Kaganov, E. M. Lifshitz, and L. V. Tanatarov, Sov. Phys. JETP **4**, 173 (1957).

[448] N. Stojanovic, D. H. S. Maithripala, J. M. Berg, and M. Holtz, Phys. Rev. B **82**, 075418 (2010).

[449] S. Daimon, R. Iguchi, T. Hioki, E. Saitoh, and K. Uchida, Nat. Commun. **7**, 13754 (2016).

[450] K. Uchida, M. Sasaki, Y. Sakuraba, R. Iguchi, S. Daimon, E. Saitoh, and M. Goto, Sci. Rep. **8**, 16067 (2018).

[451] P. Krzysteczko, J. Wells, A. F. Scarioni, Z. Soban, T. Janda, X. Hu, V. Saidl, R. P. Campion, R. Mansell, J.-H. Lee, *et al.*, Phys. Rev. B **95**, 220410 (2017).

[452] C. Dornes, Y. Acremann, M. Savoini, M. Kubli, M. J. Neugebauer, E. Abreu, L. Huber, G. Lantz, C. A. F. Vaz, H. Lemke, *et al.*, Nature **565**, 209 (2019).

[453] D. Hinzke and U. Nowak, Phys. Rev. Lett. **107**, 027205 (2011).

[454] J. Torrejon, G. Malinowski, M. Pelloux, R. Weil, A. Thiaville, J. Curiale, D. Lacour, F. Montaigne, and M. Hehn, Phys. Rev. Lett. **109**, 106601 (2012).

[455] F. Schlickeiser, U. Ritzmann, D. Hinzke, and U. Nowak, Phys. Rev. Lett. **113**, 097201 (2014).

[456] K.-J. Kim, J.-C. Lee, S.-B. Choe, and K.-H. Shin, Appl. Phys. Lett. **92**, 192509 (2008).

[457] H. Fangohr, D. S. Chernyshenko, M. Franchin, T. Fischbacher, and G. Meier, Phys. Rev. B **84**, 054437 (2011).

[458] C.-Y. You, I. M. Sung, and B.-K. Joe, Appl. Phys. Lett. **89**, 222513 (2006).

[459] M. Meinert, D. Graulich, and T. Matalla-Wagner, Phys. Rev. Appl. **9**, 064040 (2018).

[460] A. Cappella, J.-L. Battaglia, V. Schick, A. Kusiak, A. Lamperti, C. Wiemer, and B. Hay, Adv. Eng. Mater. **15**, 1046 (2013).